POWDER SINTERING AND POTENTIAL APPLICATIONS

EDITED BY: Chao Yang and Suryanarayana Challapalli
PUBLISHED IN: Frontiers in Materials and
Frontiers in Bioengineering and Biotechnology

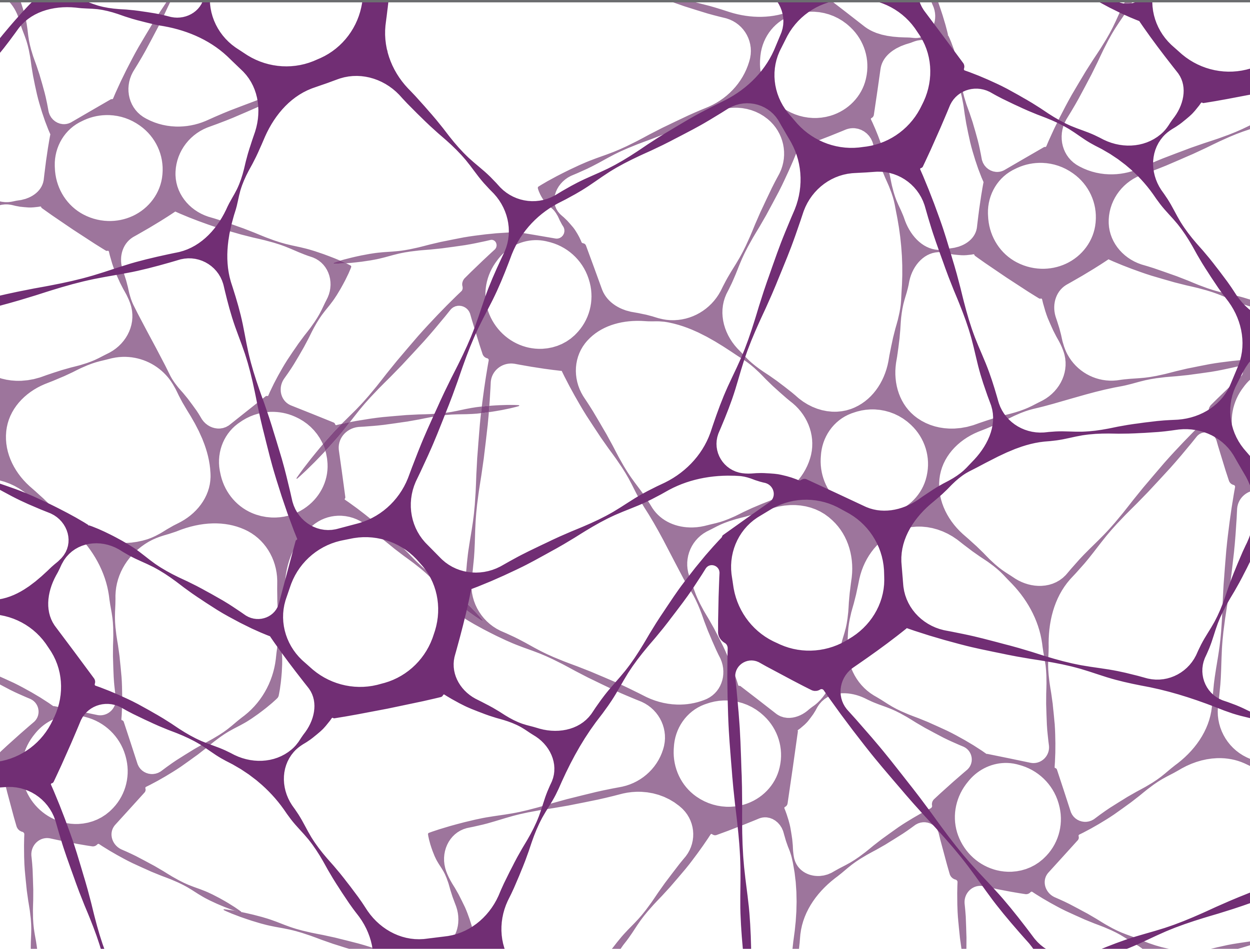

frontiers Research Topics

ISSN 1664-8714
ISBN 978-2-88971-655-5
DOI 10.3389/978-2-88971-655-5

About Frontiers

Frontiers is more than just an open-access publisher of scholarly articles: it is a pioneering approach to the world of academia, radically improving the way scholarly research is managed. The grand vision of Frontiers is a world where all people have an equal opportunity to seek, share and generate knowledge. Frontiers provides immediate and permanent online open access to all its publications, but this alone is not enough to realize our grand goals.

Frontiers Journal Series

The Frontiers Journal Series is a multi-tier and interdisciplinary set of open-access, online journals, promising a paradigm shift from the current review, selection and dissemination processes in academic publishing. All Frontiers journals are driven by researchers for researchers; therefore, they constitute a service to the scholarly community. At the same time, the Frontiers Journal Series operates on a revolutionary invention, the tiered publishing system, initially addressing specific communities of scholars, and gradually climbing up to broader public understanding, thus serving the interests of the lay society, too.

Dedication to Quality

Each Frontiers article is a landmark of the highest quality, thanks to genuinely collaborative interactions between authors and review editors, who include some of the world's best academicians. Research must be certified by peers before entering a stream of knowledge that may eventually reach the public - and shape society; therefore, Frontiers only applies the most rigorous and unbiased reviews.
Frontiers revolutionizes research publishing by freely delivering the most outstanding research, evaluated with no bias from both the academic and social point of view.
By applying the most advanced information technologies, Frontiers is catapulting scholarly publishing into a new generation.

What are Frontiers Research Topics?

Frontiers Research Topics are very popular trademarks of the Frontiers Journals Series: they are collections of at least ten articles, all centered on a particular subject. With their unique mix of varied contributions from Original Research to Review Articles, Frontiers Research Topics unify the most influential researchers, the latest key findings and historical advances in a hot research area! Find out more on how to host your own Frontiers Research Topic or contribute to one as an author by contacting the Frontiers Editorial Office: frontiersin.org/about/contact

POWDER SINTERING AND POTENTIAL APPLICATIONS

Topic Editors:
Chao Yang, South China University of Technology, China
Suryanarayana Challapalli, University of Central Florida, United States

Citation: Yang, C., Challapalli, S., eds. (2021). Powder Sintering and Potential Applications. Lausanne: Frontiers Media SA. doi: 10.3389/978-2-88971-655-5

Table of Contents

frontiers in Materials

EDITORIAL
published: 28 September 2021
doi: 10.3389/fmats.2021.737554

Editorial: Powder Sintering and Potential Applications

Chao Yang[1] *and C. Suryanarayana*[2]*

[1]*National Engineering Research Center of Near-Net-Shape Forming for Metallic Materials, South China University of Technology, Guangzhou, China,* [2]*Department of Mechanical and Aerospace Engineering, University of Central Florida, Orlando, FL, United States*

Keywords: powder sintering, applications, mechanical alloying, spark plasma sintering, composites, hydrogen-assisted processing

Editorial on the Research Topic

Powder Sintering and Potential Applications

Powder sintering is a technique that leads to bonding of powder particles together resulting in the formation of a bulk dense solid structure. The technique offers several advantages including cost effectiveness, reducing machining costs through near-net-shape forming, minimizing material losses by decreasing the number of processing steps, achieving controlled levels of porosity and superior properties. Additionally, it is possible to process materials that would otherwise be impossible to mix and also prepare materials with very high melting points. Specifically, activation and field-assisted sintering (spark plasma sintering, SPS) technologies developed in recent years have been widely employed to fabricate various kinds of bulk materials with controlled microstructures. In fact, SPS has now become “the” technique for powder consolidation. The effects of different sintering parameters on densification mechanisms and the microstructure and properties are of special importance.

Powder sintering covers various mechanisms of solid phase sintering, liquid phase sintering, pressure sintering, activation sintering, field-assisted sintering, and infiltration, etc. Thus, we have invited a strong team of researchers active in these research areas to contribute their latest research on powder sintering and its potential applications to this special issue. We have finally accepted nine manuscripts for this issue and this special collection is a compilation of these articles.

The article by Zan et al. investigated the microstructure and wear resistance of Mo_2C-doped binderless cemented carbide. By studying the effect of Mo_2C content varying between 0 and 6 wt% on cemented carbides sintered and hot isostatically pressed (HIPed), it was shown that the abrasive wear resistance has improved significantly, even though there was no change in the grain size. This was attributed to the formation of (W,Mo)C as a result of intermixing between WC and Mo_2C during sintering.

The article by Pricop et al. discussed the advantages of PM processing over ingot metallurgy (IM) processed FeMnSiCrNi shape memory alloys (SMAs). After reviewing their earlier findings in alloys processed by IM route, they investigated the processing and characterization of FeMnSiCrNi SMA by powder metallurgy and also by mixing some fraction of mechanically alloyed (MA) powder with the rest. Specifically, the formation and destabilization mechanism of unusual α'-body centered cubic thermally induced martensite during preparation process and tensile pre-straining, and the shape memory effect associated with heat treatment and hot rolling of MA powders and thermomechanical processing of bulk alloys were investigated.

The two articles by Wang et al. and Song et al. dealt with hydrogen-assisted processing of titanium alloys. While Wang et al. utilized hydrogen processing to synthesize Ti-6Al-3Nb-2Zr-1Mo alloy from blended elemental powders, Song et al. explored *in situ* synthesis of Ti/TiB composites from TiH_2 and TiB_2 powders. Especially, using TiH_2 powder instead of Ti powder as well as proper selection of sintering time-temperature conditions, minimized difficulties in the diffusion-controlled healing of the porosity and the realization of microstructural uniformity.

Edited and reviewed by:
Nicola Maria Pugno,
University of Trento, Italy

Correspondence:
C. Suryanarayana
surya_orlando@hotmail.com

Specialty section:
This article was submitted to
Mechanics of Materials,
a section of the journal
Frontiers in Materials

Received: *07 July 2021*
Accepted: *13 September 2021*
Published: *28 September 2021*

Citation:
Yang C and Suryanarayana C (2021)
Editorial: Powder Sintering and
Potential Applications.
Front. Mater. 8:737554.
doi: 10.3389/fmats.2021.737554

The article by Long et al. explored the microstructure and mechanical properties of medium-entropy and high-entropy alloys in the Fe-Co-Ni-(Cu,Al)$_x$ system prepared by mechanical alloying (MA) and SPS. It was shown that the crystal structure changed from FCC to FCC + BCC with increasing volume fraction of BCC with increasing x values. The grain size was found to change and the bulk alloy showed a high compressive strength of 1,470 MPa and a plastic strain to failure of 25% at $x = 0.6$, a very good combination indeed.

The article by Cheng et al. investigated the effect of two methods of introducing W element on the microstructure, mechanical and wear properties of sintered Fe-2Cu-0.8C-0.6Mo-2W samples. Compared with mechanically mixing the elemental powders, prediffusion treatment of Fe-W powder with 2 wt% of W in H_2 atmosphere improved the density of green compacts and sintered samples, and consequently the hardness, tensile strength and wear resistance of the sintered samples.

The article by Qin et al. compared the biological activities of unmodified titanium alloys, air-plasma-treated titanium alloys, and air-plasma-treated Sr-doped/undoped calcium phosphate (CaP) coatings on titanium alloys, which were produced by selective laser melting. The results revealed that the rapid air-plasma treatment and the Sr-CaP coating together with air-plasma treatment significantly enhanced both the biocompatibility and osteogenic differentiation of bone marrow mesenchymal stem cells.

The article by Cao et al. studied the effect of ultrafine porous boron nitride nanofiber amount on the mechanical properties, specifically hardness and toughness, of WC-Si_3N_4 composites synthesized by MA + SPS. Compared to the pure WC-Si_3N_4 composite, the boron nitride added composite showed better hardness and fracture toughness and did not show any catastrophic failure.

The article by Wu et al. reviewed the preparation methods of ultrafine (100–500 nm) WC powder, including solid-phase, liquid-phase, and vapor-phase methods according to the state of the raw materials (i.e., the W or C source). It was pointed out that the liquid-phase method had the proper preparation temperature between 500 and 800°C; the vapor-phase method has the highest purity of WC; the solid-phase method can reduce carbonization and thus has potential industrial application.

The guest editors are highly thankful to all the authors for submitting their articles and submitting them on time. We also acknowledge the great service of the reviewers who had carefully reviewed the manuscripts and made constructive suggestions to improve the quality and readability of the articles. Finally, we are very grateful to the editorial office of *Frontiers in Materials* who had worked diligently to get all the reviewed manuscripts published in this special collection in time and in a beautiful format.

AUTHOR CONTRIBUTIONS

All authors listed have made a substantial, direct, and intellectual contribution to the work and approved it for publication.

Conflict of Interest: The authors declare that the research was conducted in the absence of any commercial or financial relationships that could be construed as a potential conflict of interest.

frontiers
in Materials

REVIEW
published: 06 May 2020
doi: 10.3389/fmats.2020.00094

Preparation Technology of Ultra-Fine Tungsten Carbide Powders: An Overview

Yu-Cheng Wu[1,2,3], Yu Yang[1], Xiao-Yue Tan[2,3], Laima Luo[2,3]*, Xiang Zan[2,3], Xiao-Yong Zhu[2,3], Qiu Xu[4] and Ji-Gui Cheng[2,4]*

[1] Industry & Equipment Technology, Hefei University of Technology, Hefei, China, [2] School of Materials Science and Engineering, Hefei University of Technology, Hefei, China, [3] National–Local Joint Engineering Research Centre of Nonferrous Metals and Processing Technology, Hefei, China, [4] Institute for Integrated Radiation and Nuclear Science, Kyoto University, Osaka-fu, Japan, [5] Research Centre for Powder Metallurgy Engineering and Technology of Anhui Province, Hefei, China

Ultrafine tungsten carbide (WC) powder refers to WC powders with a particle size between 100 and 500 nm. Researchers have improved the comprehensive properties of WC-based cemented carbides by preparing ultra-fine WC powders. Because of the preparation and application of nanoscale WC powders, ultrafine-grain cemented carbides with excellent hardness and wear resistance have been successfully produced. In this paper, the preparation methods of ultra-fine WC powder are divided into solid-phase, liquid-phase, and vapor-phase methods according to the state of the raw materials (i.e., the W or C source). The liquid-phase methods could realize the preparation of WC at the temperature between 500 and 800°C. The purity of WC prepared by vapor-phase method is the highest. The solid-phase reduction carbonization method has potential industrial application.

Keywords: ultra-fine tungsten carbide, preparation method, solid-phase method, liquid-phase method, vapor-phase method

Edited by:
Chao Yang,
South China University of Technology,
China

Reviewed by:
Xuemei Liu,
Beijing University of Technology,
China
Yan Long,
South China University of Technology,
China

****Correspondence:***
Yu-Cheng Wu
ycwu@hfut.edu.cn
Laima Luo
luolaima@126.com

Specialty section:
This article was submitted to
Structural Materials,
a section of the journal
Frontiers in Materials

Received: *18 December 2019*
Accepted: *27 March 2020*
Published: *06 May 2020*

Citation:
Wu Y-C, Yang Y, Tan X-Y, Luo L, Zan X, Zhu X-Y, Xu Q and Cheng J-G (2020) Preparation Technology of Ultra-Fine Tungsten Carbide Powders: An Overview.
Front. Mater. 7:94.
doi: 10.3389/fmats.2020.00094

INTRODUCTION

Cemented carbides using tungsten carbide (WC) as main raw materials with high hardness and excellent wear resistance are widely used in drill, mold, needle, cutting tool, and other special processing industries. Due to the high bonding strength and fine microstructure between ultrafine WC particles and metal binder phase, ultrafine-grain cemented carbide combines the characteristics of ceramics and metal at the same time, which has high toughness, good strength and excellent hardness. Thus, a large number of studies on the optimal preparation of composite powders, the most suitable proportions of bonding phases, the effects of doping with other elements, and the best size and morphology of WC grains, among others, have been conducted to improve the hardness and toughness of cemented carbides (Zheng et al., 2015; Wang et al., 2017). Among many factors, the size of WC particles generates the greatest impact on the mechanical properties of cemented carbides. As shown in **Figure 1**, the hardness and bending strength of cemented carbides increase as the proportion of fine WC particles increases (Akhtar et al., 2007). The conventional and ultrafine WC particles' size is 4, 0.2 μm, respectively. The samples were prepared by mixing two kinds of WC powders with different mass ratio between conventional and ultrafine powders. The particle size of WC powders directly determines the size of WC grain

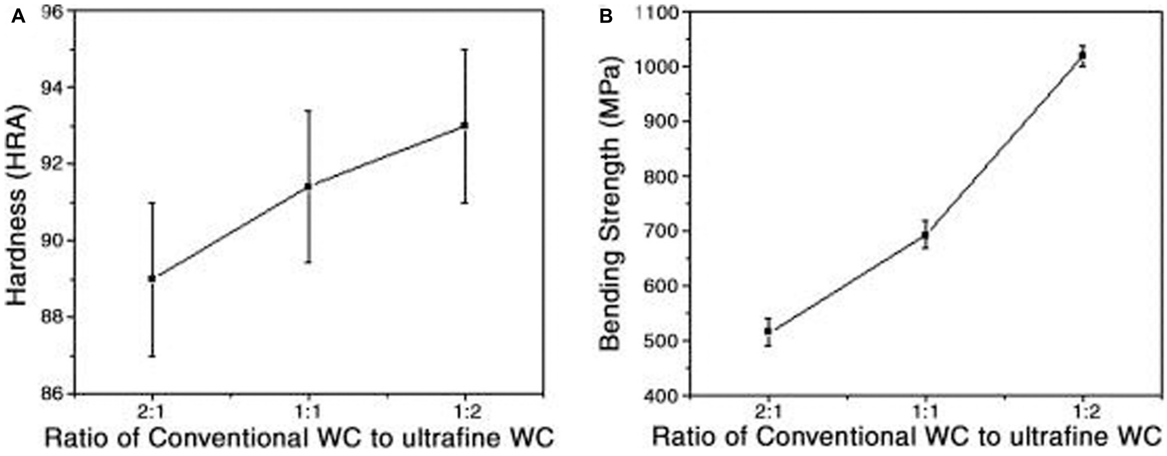

FIGURE 1 | Changes in the **(A)** hardness and **(B)** bending strength of cemented carbides with increasing proportion of coarse and fine grained WC (Akhtar et al., 2007) [Figure 3 of Akhtar et al. (2007), Copyright Elsevier Ltd].

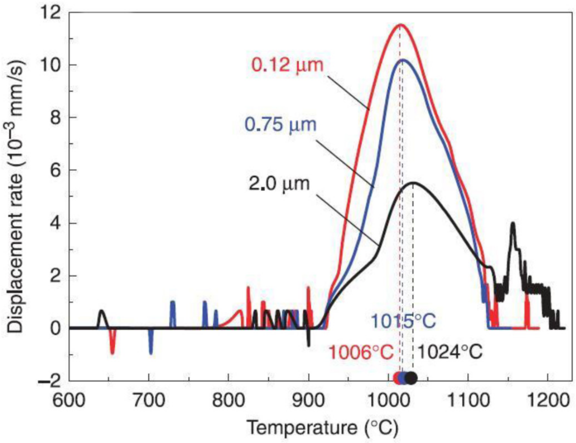

FIGURE 2 | Displacement rates of sintering of WC powder with different particle sizes (Liu et al., 2010) [Figure of Liu et al. (2010), Copyright The American Ceramic Society].

in cemented carbide during the sintering process. And the grain size of WC is related to the mechanical properties of sintered cemented carbides. Hardness of cemented carbide increased with the mass fraction of ultrafine WC particles. The bending strength presented the same trend as the hardness.

Ultrafine WC powders improve sintering performance and enhance the mechanical properties of the cemented carbide (Liu et al., 2010; Emani et al., 2015). As shown in **Figure 2**; Liu et al. (2010) carried out studies on the displacement rate curve of WC–10 wt% Co powder samples by taking WC powders of different particle sizes and Co powder of equal particle sizes as sintering materials and found that smaller WC particle sizes result in higher displacement rates and degrees of densification of powder sintering.

Maheshwari et al. (2007) carried out a comprehensive study by sintering WC–10Co powders with different initial particle sizes. **Figure 3** shows the relationship between the sintering densification and sintering temperature of WC powders of different initial particle sizes. The entire sintering temperature range decreased gradually as the initial average particle size decreased from 30 μm to 10 nm. When the initial particle size was 10 nm, the densification of the alloy was up to 90% approximately.

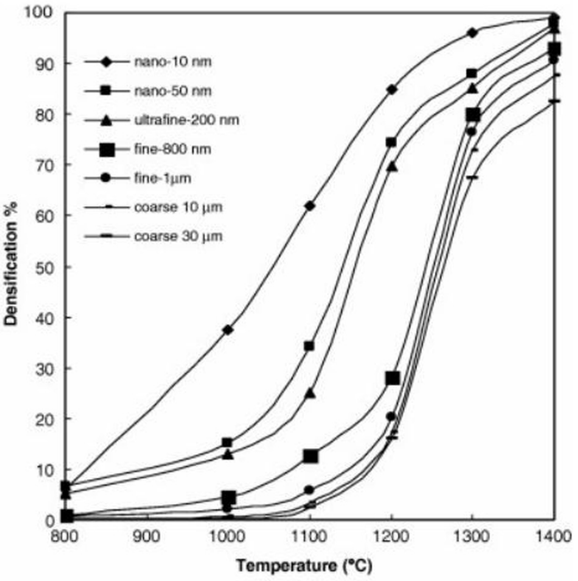

FIGURE 3 | Relationship between sintering temperature and sintering densification of powders with different initial particle sizes (Maheshwari et al., 2007) [Figure 2 of Maheshwari et al. (2007), Copyright Amer Powder Metallurgy Inst].

Some researchers have proved that ultrafine WC powders have better activation in plating binder-phase mental coat on the WC particles. Such as, Luo et al. (2011) have studied the activation

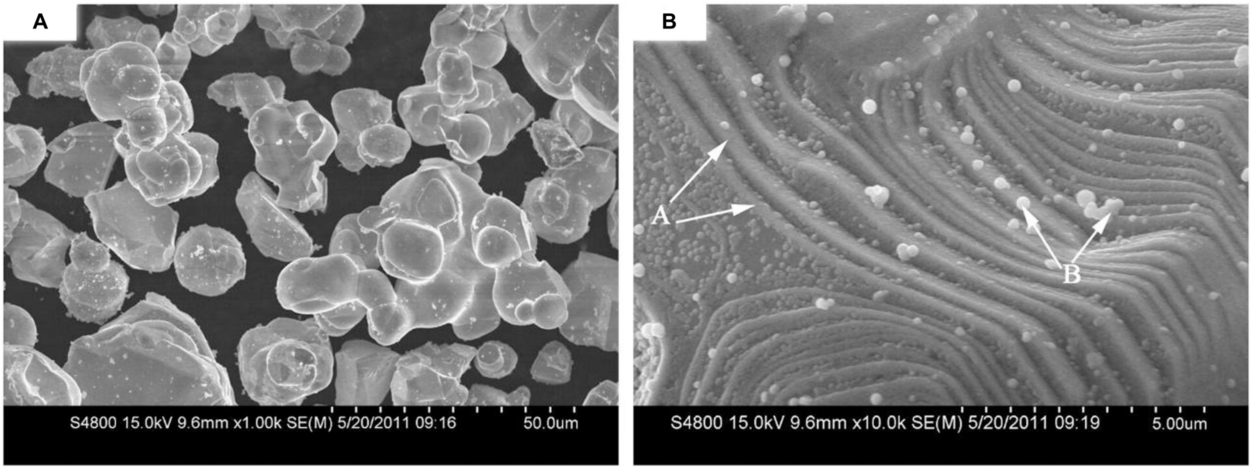

FIGURE 4 | Surface appearance of Ni-coated WC powders after 30 min of electroplating: **(A)** Low-power image; **(B)** high-power image (The Ni particles prioritized nucleation and growth at the surface step defects (arrow A in panel **B**). The uncompleted Ni coating showed a cell structure with some free-formed Ni particles (arrow B in panel **B**) (Luo et al., 2011) [Figure 3 of Luo et al. (2011), Copyright Elsevier B.V.].

technique of ultra-fine powders and prepared a uniform Ni-coated WC composite powder, taking less than 1 μm WC as a matrix. As shown in **Figure 4B**, ultrafine WC powders after ultrasonic-assisted electroless plating appear step-like defects on the surface of WC particles. These defect make nucleation and growth of Ni cell generate on the activated WC particle surface more effectively. Further studies showed that the thinner the WC powder, the better the Ni coating (Luo et al., 2011; Chen H. Y. et al., 2017).

Some scholars have carried out further theoretical studies to figure out how ultra-fine WC powders can improve the comprehensive performance of cemented carbides (Chuvil'deev et al., 2015; Postek and Sadowski, 2018). The most consistent view at present is that the use of ultra-fine WC powders decreases the average thickness of the bonding phase, which increases the dispersion of the former through the latter and, thus, improves the strength and toughness of the resulting alloy (Zhang et al., 2012). Several studies have focused on the preparation method and industrial production of ultra-fine WC (Xu et al., 2018; Luo et al., 2019). A number of methods to prepare ultra-fine WC powder, such as mechanical alloying (Li et al., 2019), *in situ* carburizing reduction (Li et al., 2019), direct reduction of carbonization (Chen L. J. et al., 2018), gas-phase reaction synthesis (Zhang et al., 2018), and spray conversion (Guo et al., 2015), have been proposed. These methods can generally be summarized into three synthesis categories, namely, solid-phase methods, vapor-phase methods, and liquid-phase methods, based on the initial state of the reactants.

SOLID-PHASE METHOD

When preparing tungsten carbide by the solid-phase method, WO_3 is usually taken as the W source. Carbonization of WO_3 can be divided into reduction carbonization and direct carbonation according to the generation of elemental W; it can also be divided into mechanical alloying and high temperature carbonization according to the temperature of carbonization.

Reduction Carbonization

Reduction carbonization is a traditional WC preparation process that is commonly used for the high-volume industrial production of WC (Borchardt et al., 2012). A typical synthesis route is: W source [Ammonium paratrungstate (APT) or ammonium metatungstate (AMT)] calcination → WO_3 → hydrogen reduction → ultrafine W powders → carbonization → ultrafine WC powders.

Ma and Zhu, 2010 calcined a mechanically activated WO_3 and graphite mixture at 1215°C under vacuum conditions and achieved the solid C thermal reduction of WO_3 to nano-WC particles. The specific preparation process was as follows: WO_3 (purity 99.9%) and graphite (purity 99%) powders as raw materials were mixed at a molecular weight of 1:4 and then ball milled under an Ar atmosphere for 10 h. The composite powder was placed in a ceramic vessel, first heated to 741°C and then heated to 1215°C in a vacuum tube furnace at a rate of 10°C/min, finally kept in the temperature for 1 h.

Ma and Zhu (2010, analyzed ultrafine WC particles' generation based on homogeneity increase and associated decrease during the diffusion period of mechanical milling. Besides, formation of some intermediates, such as $WO_{2.72}$ and WO_2, are also responsible for the successful production of ultra-fine WC powders. Thermodynamic calculations for reactions that may occur during the calcination process have accurately detected the reaction process and generation phase, and the results are shown in **Figure 5**. As the calcination temperature increases, WO_3 is reduced to other lower-valence WO_3 types, such as $WO_{2.72}$ and WO_2. These low valence WO_3 forms are called Magneli-phase WO_3 (meta-stable phase WO_3) (Ma and Zhu, 2010; Lee et al., 2019). When the temperature is higher than 273, 346, or 489°C, the solid-phase carbothermal

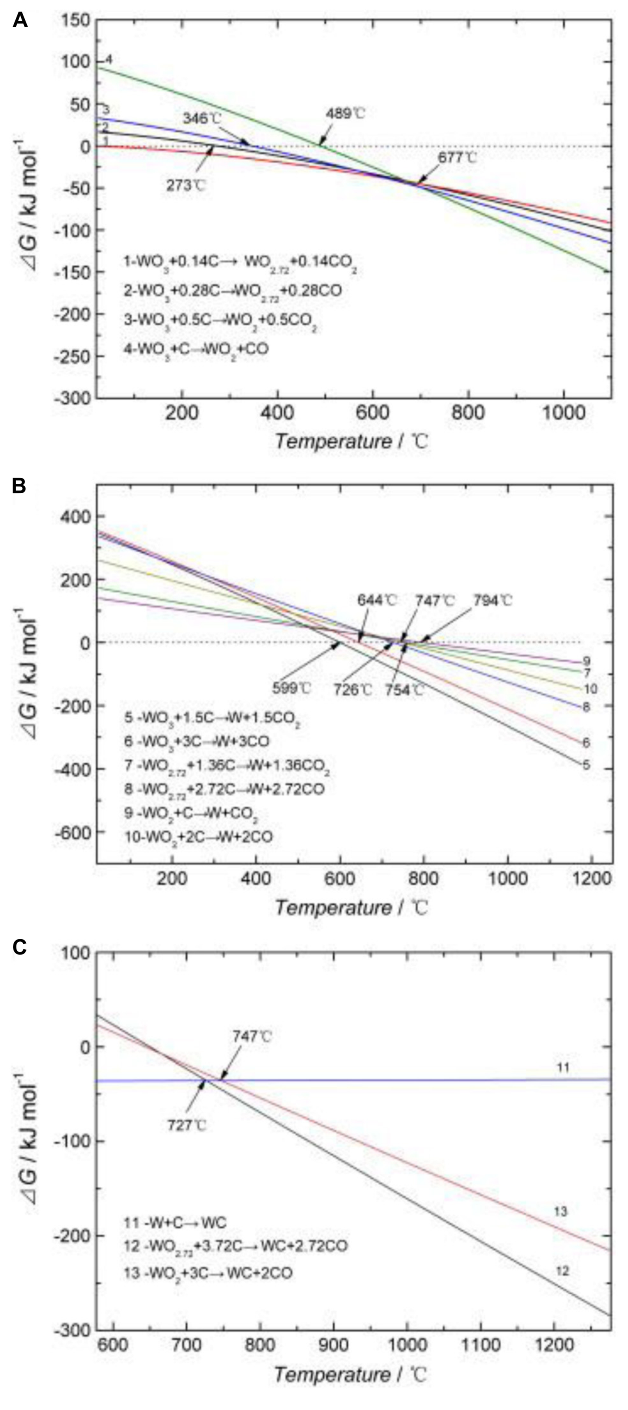

FIGURE 5 | Changes of ΔG with the temperature of different tungsten oxides when reacting with graphite: **(A)** Magneli-phase WO_3 formation; **(B)** W formation; **(C)** WC formation (Ma and Zhu, 2010) [Figure 4 of Ma and Zhu (2010), Copyright Elsevier Ltd.].

reaction of WO_3 generates these Magneli phases. Magneli-phase WO_3 is reduced to elemental W by graphite when the temperature is 599–794°C. X-ray diffractometry (XRD) of the samples was carried out at 741°C, and only the diffraction peaks of mesophase $WO_{2.72}$, WO_2, and W were found; no diffraction peaks of WO_3 were observed, likely due to the initial reaction temperature of 599–644°C, which fully reduces the metal oxide to $WO_{2.72}$, WO_2, and W (Ma and Zhu, 2010). The peaks of $WO_{2.72}$ and WO_2 were still present at 741°C because the initial reaction temperatures of $WO_{2.72}$ and WO_2 are 726–754°C and 747–794°C, respectively, or slightly higher than 741°C. As the temperature continues to increase, W reacts with graphite to generate WC. The reaction route can be summarized as $WO_3 + C \rightarrow W + WO_2 + WO_{2.72} + C \rightarrow WC$ (Ma and Zhu, 2010).

Using ammonium paratungstate (APT) as a raw material, Ryu et al. (2009) prepared nano-WC powders by using the thermal plasma method. The preparation process was divided into three stages:

Stage 1: Thermal decomposition of ammonium paratungstate (APT):

$$(NH_4)_{10}W_{12}O_{41} \cdot xH_2O \rightarrow 12WO_3 + 10NH_3(g) + (5 + x)H_2O(g) \tag{1}$$

Stage 2: Hydrogen reduction:

$$WO_3 + 3H_2(g) \rightarrow W + 3H_2O(g) \tag{2}$$

Stage 3: CH_4 carbonization:

$$WO_3 + H_2(g) + CH_4(g) \rightarrow W_2C, WC_{1-x}, WC + H_2O(g) \tag{3}$$

In the thermal plasma reaction system, APT generates a nano-WC_{1-x} powder which the powders sometimes contain a small amount of the W_2C phase after the period of thermal decomposition, reduction, and carburization. By using this way to prepare WC, the particle size of the prepared WC_{1-x} powder is less than 20 nm. The synthetic powder is heated by hydrogen to fully carburize the WC_{1-x} and W_2C phases to WC. After removing excess C, we could obtain WC powders whose particle size is less than 100 nm, as shown in **Figure 6**.

Direct Carbonization

Direct carbonization to prepare WC is known as a one-step method. Researchers have developed different techniques for the one-step preparation of WC powder. For example, Won et al. (2010) prepared WC powders with particle size of 50–100 nm through carbonization at a high temperature by using WO_3 and C powder as raw materials and NaN_3 as a combustion agent (Won et al., 2010; Lin et al., 2013). Lee et al. (2003) converted WO_3 into WC by heating WO_3 to 300–700°C in He atmosphere; here, −HX, −NaX, and −KX were added to WO_3 powder as catalysts, and CO gas was used as the C source. He and Tang (2011) had prepared ultra-fine WC powders with particle size of 0.3 μm through direct reduction and carbonization of AMT by

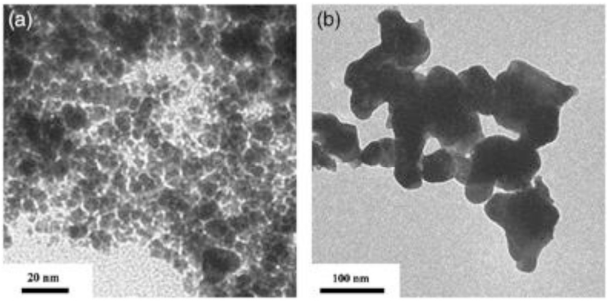

FIGURE 6 | TEM micrographs of WC_{1-x} powders obtained **(a)** from the plasma reactor and **(b)** after 3 h of hydrogen heat treatment at 900°C (Ryu et al., 2009) [Figure 8 of Ryu et al. (2009), Copyright The American Ceramic Society].

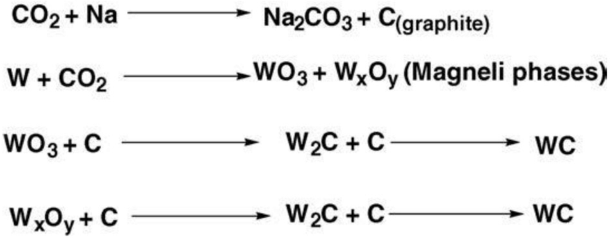

FIGURE 7 | Reaction scheme of the CO_2 heat treatment method (Wang et al., 2006) [Scheme 1 of Wang et al. (2006), Copyright Elsevier B.V.].

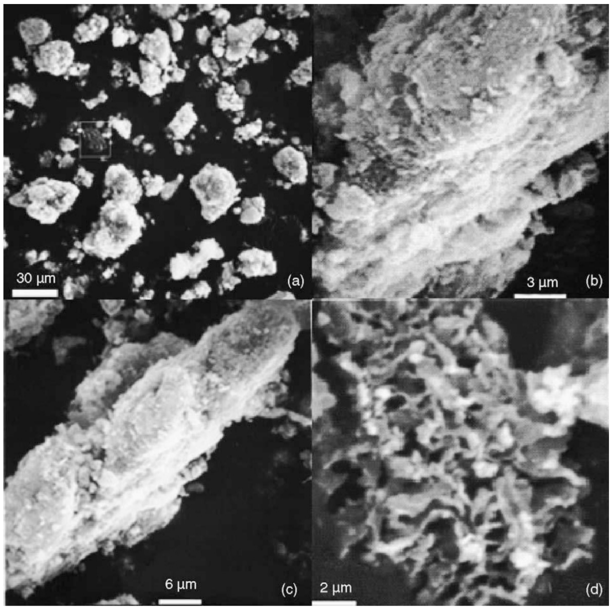

FIGURE 8 | (a) Low-resolution SEM image of the WC sample, **(b)** cross-sectional morphology of typical WC particles, **(c)** surface morphology of WC particles, and **(d)** SEM image of the residual graphite network (Wang et al., 2006) [Figure 2 of Wang et al. (2006), Copyright Elsevier B.V.].

using carbon-black as the C source in N_2 atmosphere. The direct carbonization method utilizes the reducibility of C to conduct direct reduction of WO_3 and generate WC. During the reduction process, only Magneli phases W is generated, and eventually WC powder particles are difficult to gather. In the traditional method, W powder is prepared and then carbonized to generate WC via hydrogen reduction of WO_3. During the reduction process, hydrates of WO_3, such as $WO_2(OH)_2$ and $WO_x{\cdot}H_2O$, are generated, and these compounds cause W powder particles to grow. Thus, the carbonized WC powder yields large particles that must be ground to obtain a fine WC powder (Venables and Brown, 1996; Gu et al., 2002).

Wang et al. (2006) invented a supercritical CO_2 heat treatment method to prepare WC based on the direct carbonation method. The reaction route of this method is shown in **Figure 7**, and the reaction could divide into two stages. In Stage 1, dense CO_2 is reduced to graphite sheets by Na, and metal W is oxidized into WO_3 by excess CO_2; in Stage 2, WO_3 reacts with the graphite sheets and then converted into WC.

Based on the reaction route described above, Wang et al. realized the carbonization of W powder at a moderate temperature of 600°C by placing W powder, dry ice, and Na metal in an autoclave, which was then sealed and heated in a heating furnace to 600°C at a heating rate of 10°C/min with insulation for 20 h. Black solid products were obtained when the furnace was finally cooled to room temperature. Dilute HCl was added to the product, which was subsequently heated to remove Na_2CO_3. Finally, the solid product was washed with distilled water and dried at 80°C for 2 h. The resultant WC powder is shown in **Figure 8**; Wang et al. (2006).

Mechanical Alloying

Mechanical alloying involves the high-speed and long-running transmission of mechanical energy to the powder through a high-energy ball mill to improve the powder activity. During the ball milling process, the ball in the milling jar repeatedly collides with the powder, thus subjecting it to various forces, such as impact, compression, friction, and shearing. The powder is further refined, crushed, and cold welded into dispersed ultra-fine particles and then alloyed at room temperature. The basic principle behind powder alloying at room temperature is the repeated mixing, crushing, and cooling of weld powder particles through high-energy ball milling. The mixed powder in the ball mill can form high-density dislocations, and the particles are gradually refined to the nanoscale level. Increases in powder activity accelerate the mutual diffusion of atoms. Under certain conditions, alloy phase nuclei are formed through ball milling and gradually grow into an alloy phase until all elemental powders are consumed (Dai et al., 2013; Maat et al., 2018; Sadeghi et al., 2018).

By using the ball-milling method, Wu et al. (2009) mixed pure WO_3, graphite, and Mg powder according to a certain atomic ratio at room temperature and characterized the resulting powder through SEM, XRD and TEM. As shown in **Figure 9**, the XRD peaks of MgO and WC could be clearly detected after 4.5 h of ball milling. These results show that a redox reaction occurs between

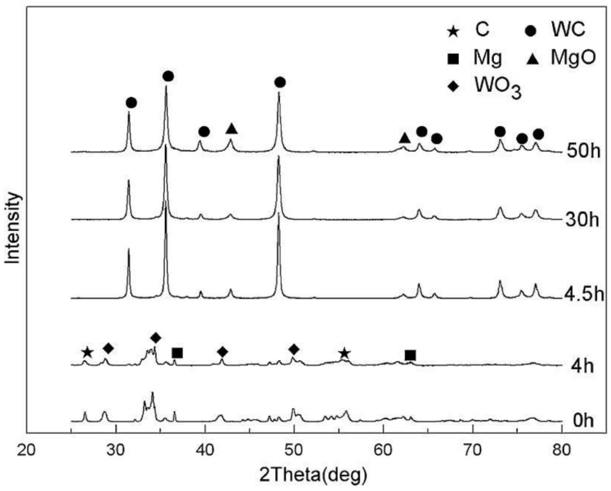

FIGURE 9 | XRD patterns of composite powders at different ball milling time (Wu et al., 2009) [Figure 1 of Wu et al. (2009), Copyright Elsevier B.V.].

the WO_3 powder, Mg, and graphite during ball milling to form MgO and WC via the following reaction:

$$WO_3 + 3Mg + C \rightarrow WC + 3MgO$$

The powder was further refined with ball milling going on. As shown in **Figure 10**, after 80 h ball- milling, nanocrystalline WC particles (25 nm) were embedded in the fine MgO matrix, thus forming a nanoscale MgO–WC composite powder with diameters close to 100 nm. This process could overcome the shortcomings of the high-cost preparation of WC by using MgO instead of Co, Ni, and Fe which are the conventional binder. Besides, the newly developed binder could be used for other carbide substrates.

High-Temperature Carbonization

The high-temperature carbonization of solid metal W essentially involves the diffusion reaction of C in W. When the temperature is above 1000°C, C atoms can be soluble into W particles to form WC phase which the process called C diffusion reaction, which is also the basic principle in high-temperature carbonization. C diffusion is based on the formation of a thin polycrystalline WC layer around W particles; this layer gradually develops toward the core, thus enabling the growth of polycrystalline WC by extending toward the center of the W particles and moving to the grain boundary of WC (Yang et al., 2015). Although the principle of high-temperature carbonization of metal W is similar, researchers have developed different methods to prepare ultra-fine WC. For instance, Li (2013) used AMT and violet tungsten as raw materials to prepare W powders with a minimum particle size of about 30 nm through hydrogen reduction; thereafter, the scholar prepared a nano-WC powder with a minimum particle size of 60 nm after carbonization at 1200°C and microwave heating (Li, 2013). Chen Z. et al. (2017) combined C with W, Co, Cr_3C_2, and VC as raw materials and then placed this mixture into a combustion reaction chamber for carbonization with burning; finally, WC powders with a grain size of 30–100 nm were obtained.

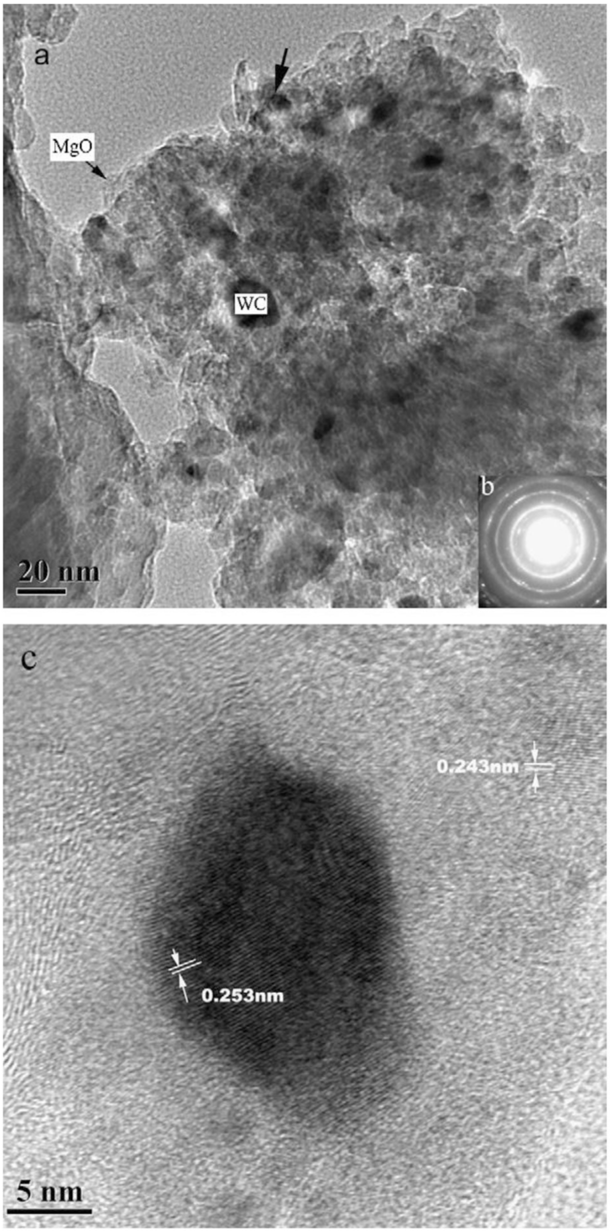

FIGURE 10 | High-power microscopic image of WC powders after 80 h of ball milling: **(a)** High power micrograph; **(b)** the selected-area diffraction pattern; **(c)** enlarged micrograph of selected-area (Wu et al., 2009) [Figure 3 of Wu et al. (2009), Copyright Elsevier B.V.].

Wang et al. (2018) studied the effects of as on the growth of WC powders by adding As element into the high-temperature carbonization process of nano-W. The experimental process is as follows: First, the W–As composite powder was mixed with C black at 100 rpm for 1 h by a planetary mill. Next, the mixed powder of W, As, and C was placed in a graphite boat and placed into a tube furnace for high-temperature carbonization

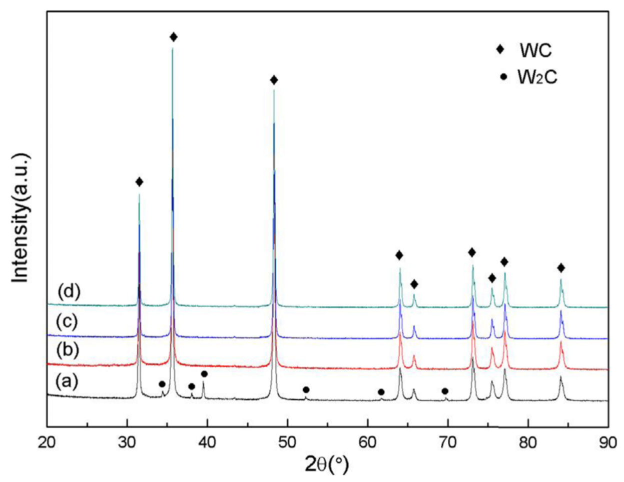

FIGURE 11 | XRD patterns of: **(a)** W powder at 1300°C; **(b)** W-As powder at 1300°C; **(c)** W powder at 1400°C; **(d)** W-As powder at 1400°C (Wang et al., 2018) [Figure 3 of Wang et al. (2018), Copyright Elsevier B.V. and The Society of Powder Technology Japan].

at 1300, 1400, 1500, and 1600°C with a controlled heating rate of 5°C/min.

Figure 11 shows the XRD patterns of the samples obtained by carbonization of W powder and W–As powder at 1300 and 1400°C. The diffraction peak shown in **Figure 11A** reveals the presence of a W_2C phase in the WC powder after carbonization of the W powder at 1300°C. As shown in **Figure 11C**, W_2C phase was not observed in the diffraction peak after the carbonization at 1400°C, contrasting to **Figure 11A**, which indicate that pure W powder was not fully carbonized at 1300°C but was totally carbonized at 1400°C. According to the diffraction peaks in **Figures 11B,D**, only WC could be detected, and no W_2C phase was found. Comparison of the peaks of the two composite powders after carbonization at high temperature reveals that addition of As have decreased the temperature of complete carbonization (Wang et al., 2018).

As shown in **Figure 12**, the average particle size of the WC–As powder is less than that of WC at the same temperature, which indicates that addition of arsenic has decreased the concentration of WC during the carbonization process. Wang provided the following explanation for this phenomenon: during carbonization, W and As generate a WAs_2 mesophase, which attaches to the grain boundaries of WC and hinder the growth of WC grains through migration of these boundaries. Therefore, uniform WC composite powders could be obtained even at high carbonization temperatures.

LIQUID-PHASE METHOD

The traditional liquid-phase method refers to the coprecipitation of tungstate and cobaltate in the liquid phase, and then makes the sediment completely decomposed at a low temperature. The precursor of the highly dispersed and highly active W–Co compound is prepared to generate ultra-fine WC–Co composite powders through reduction and carbonization in a fixed or fluidized bed. This method is also called chemical precipitation (Yang et al., 2018). Compared with other methods, chemical precipitation presents the advantages of simple equipment and easy process control; moreover, the prepared nano-WC–Co powders have small particle size, uniform distribution, and high reaction activity. However, chemical precipitation method also have a number of issues need to be overcome, such as introduction of impurities during the preparation process, physical statement change of the generated sediment, high difficulty in filtering and washing the product, high preparation cost, and poor scaling to batch production. All advantages mentioned above have limited the technique's applications (Fan et al., 2013).

Several researchers have developed a solvothermal method to prepare WC powder. Solvothermal method is a synthetic method that uses organic or non-aqueous solvents as solvents to react the original mixture with the solution at a certain temperature under the spontaneous pressure in a closed system (Hosokawa, 2016).

Preparation of WC powder via the solvothermal method generally takes WO_3 as the W source and C-based organic solvents as the C source. The raw materials are mixed proportionally and then react by heating to 500–800°C after addition of a reducing agent to the reactor. This method can be used to generate WC at low temperatures, but the subsequent processing of reaction products is often complex. Indeed, high-purity WC can only be obtained after several cycles of removal of the reducing agent, distillation drying, immersion, and filtration with ethanol (Kumar et al., 2010).

Zeng et al. (2008) took Mg as a reducing agent, anhydrous ethanol and WO_3 as C and W sources, respectively. He synthesized WC nanocrystals using a simple solvothermal method. The effect of reaction temperature on the synthesis of WC was discussed. **Figure 13** shows the XRD patterns of products obtained at different reaction temperatures. There are WO_3 and $MgWO_4$ existing at different temperature. The peaks of WO_3 disappear at 550°C and the peaks of $MgWO_4$ disappear at 650°C. With the increase of temperature, the peaks of WO_3 and $MgWO_4$ disappeared gradually, while the peak intensity of WC increased obviously. The activity of C and W atoms increased with the increase of reaction temperature which made the reaction more completely and WC crystallization more completely. The pressure produced in the high pressure reactor greatly reduces the synthesis temperature of WC. When the temperature was 500°C, hexagonal WC phases with particle sizes of about 40–70 nm could be synthesized.

Singla et al. (2015) prepared WC nanoparticles with a particle size between 30–80 nm by using Mg, acetone (C_3H_6O), and WO_3 as raw materials. During the reaction, acetone was used as a hot solvent and C source, Mg acted as the catalyst, and the mixed raw material was placed in an electric furnace to heat to 600°C and kept warm for different periods of time. Then, it was cooled to room temperature using an autoclave. The product was washed with dilute HCl to remove MgO, leached, and washed

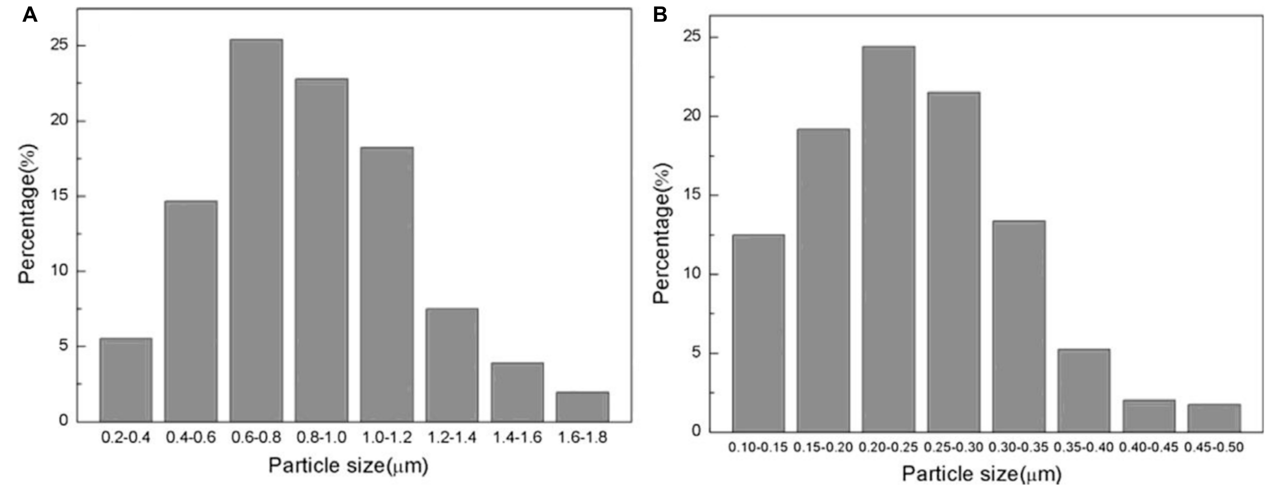

FIGURE 12 | Particle distributions of **(A)** WC and **(B)** WC-As powders after 2 h of carbonization at 1400°C (Wang et al., 2018) [Figure 13 of Wang et al. (2018), Copyright Elsevier B.V. and The Society of Powder Technology Japan].

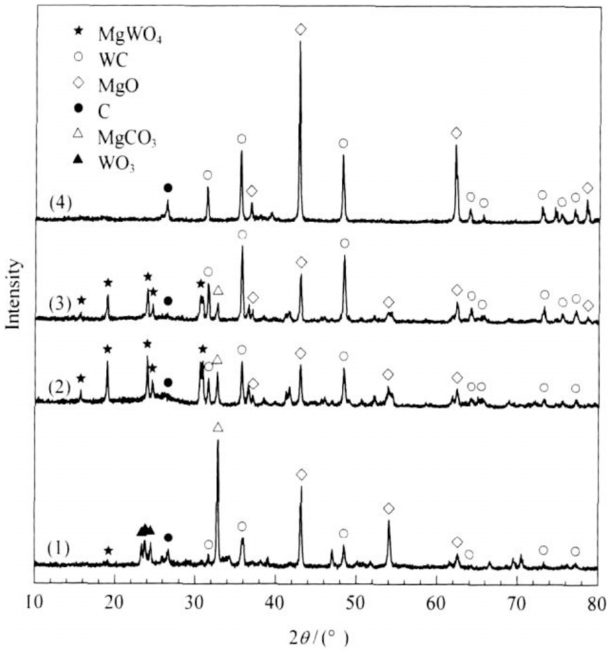

FIGURE 13 | XRD patterns of WC powders synthesized at different temperatures for 15 h: (1) 500°C; (2) 550°C; (3) 600°C; (4) 650°C (Zeng et al., 2008) [Figure 1 of Zeng et al. (2008), Copyright Science Press].

with distilled water several times to remove the acid. Finally, the product was washed with acetone and then dried under vacuum at 100°C. The synthesized WC powder had plate- or sphere-shaped grains that dispersed without aggregation, and ultra-fine WC powders could be obtained without pulverization. However, because the oxygen content of the powders increased with increasing insulation time, control of the insulation time is the key to prepare high-quality WC via this method.

VAPOR-PHASE METHOD

The chemical vapor-phase synthesis (CVS) of WC powder refers to the preparation of WC powders via hydrogen and hydrocarbon vapor reduction precursors (Dushik et al., 2018). If WCl_6 is used as a precursor, CH_4 and hydrogen are taken as the C source and reducing agent, respectively, and the reaction temperature is set to 1200°C, the following reaction takes place (Aneela and Srikanth, 2018):

$$WCl_6(g) + H_2(g) + CH_4(g) \rightarrow WC(s) + 6HCl(g)$$

WCl_6, WF_6, and $W(CO)_6$ are preferred W sources for preparing WC because these raw materials have a low volatilization temperature and are easy to reduce or thermally dissociate by hydrogen; hydrocarbon gases often used as C sources such as methane, ethylene and propane (Wu et al., 2018). The preparation of WC powders via the vapor-phase method can result in uniform and controllable particle sizes; moreover, because no other solid products are generated, the WC purity is usually higher than that obtained from other methods. However, this kind of method requires raw materials and substrates with high initial purity, and the use of flammable gases presents significant risk during mass production.

The plasma chemical vapor deposition method is a widely used to prepare nano-WC. The raw material is quickly heated to above 1500°C using plasma as the heat source, and the raw materials decompose, react, and synthesize the product. The raw materials are generally W or WO_3, and the C source is usually CH_4 or acetylene. The plasma chemical vapor deposition method can also be used to produce other nano-powders, such as TiC, TiN, and Si_3N_4 (Morimitsu et al., 2013; Chen L. et al., 2018).

Using WCl_6 as raw materials, Sohn et al. prepared nano-WC by plasma heating to ultra-high temperature. In this experiment, H_2 and CH_4 were used as reducing and carburizing agents,

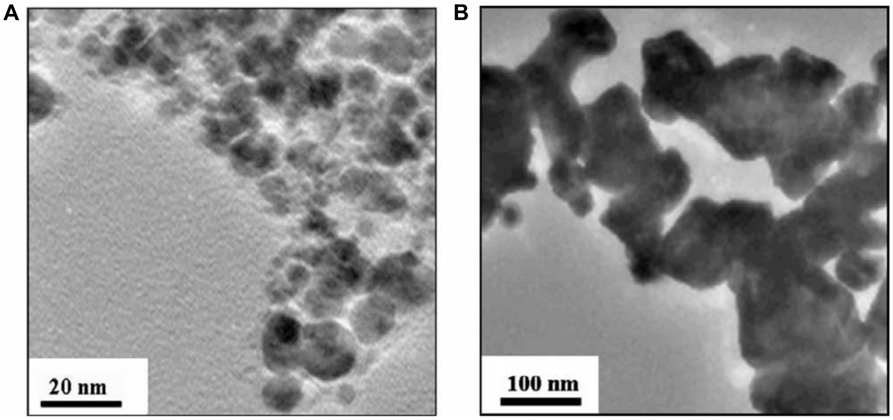

FIGURE 14 | TEM micrographs of **(A)** WC_{1-x} powder synthesized by plasma-assisted CVS from WCl_6 and **(B)** WC powders obtained after 5 h of hydrogen heat treatment of WC_{1-x} powders at 900°C (Sohn et al., 2007) [Figure 1 of Sohn et al. (2007), Copyright Elsevier Ltd].

TABLE 1 | Comparison of characteristics of WC prepared by different methods.

Preparation method		Raw materials	Particle size of WC powders	Intermediate product
Soild-phase method	Reduction carbonization	WO_3, graphite (Ma and Zhu, 2010)	100–200 nm	WO_2, $WO_{2.72}$, W
		APT, H_2, CH_4 (Ryu et al., 2009)	20–100 nm	W_2C, WC_{1-x}, W
	Direct carbonization	CO_2, Na, W (Wang et al., 2006)	Less than 150 nm	W_xO_y, W_2C
	Mechanical alloying	WO_3, Mg, C (Wu et al., 2009)	25–100 nm	MgO
	High-temperature carbonization	W, As, C (Wang et al., 2018)	100–500 nm	WAs_2
Liquid-phase method		WO_3, Mg, anhydrous ethanol (Zeng et al., 2008)	40–70 nm	$MgWO_4$, MgO, $MgCO_3$
		WO_3, Mg, acetone (Singla et al., 2015)	30–80 nm	MgO
Vapor-phase method		WCl_6, H_2, CH_4 (Sohn et al., 2007; Ryu et al., 2008)	30–100 nm	HCl

respectively. WC_{1-x} with a particle size of less than 30 nm was obtained. The particle size of this product increased with increasing plasma transmitter power and decreasing plasma flow rate. Hydrogen was used for the heat treatment of the WC_{1-x} powder. The C content was reduced to stoichiometric levels and the WC_{1-x} phase was fully carburized to generate the WC phase. However, the particle size of the powder increased from 30 nm to approximately 100 nm after hydrogen heat treatment, as shown in **Figure 14**; Sohn et al. (2007).

Ryu et al. (2008) taking WCl_6 as a precursor, reduced and carbonized it by using CH_4-H_2 mixed gas, and then prepared nano-WC powder by the thermal plasma method. His team also studied the effects of other factors on the product composition and particle size, such as molar ratio of the reaction gas, plasma torch power, plasma gas flow rate and addition of a secondary plasma gas. Results showed that nano-WC_{1-x} powder containing WC and W_2C phases could be synthesized by using the thermal plasma method with WCl_6 and CH_4 as the W and C sources, respectively. The content of W_2C in the product decreased with increasing plasma torch power and plasma gas flow rate. In addition, the particle size of WC_{1-x} was affected by the plasma torch power, plasma gas flow rate, and addition of a secondary plasma gas (H_2) but is not subject to the CH_4 concentration within the range tested. The generated WC_{1-x} and W_2C phases were carburized into the fully carbidized WC phase, and excess C in the product was removed completely by hydrogen heat treatment at 900°C. The particle size of WC_{1-x} obtained by the thermal plasma process was less than 20 nm, and the particle size of the WC powder obtained after hydrogen heat treatment was between 40 and 100 nm. Since the plasma process can operate continuously, it is also suitable for the mass production of nano-WC powders.

Table 1 lists different WC preparation methods in the literature. Compared with the liquid-phase and vapor-phase method, the solid-phase method on preparing WC powders have a more wider range of particle size which means that the accuracy of WC particle size is not easy to control in the period of carbonization by the solid-phase method. Except for mechanical alloying, the intermediate products of other solid-phase methods are all related to tungsten compounds which could be carbonize completely by promoting the temperature of carbonization.

CONCLUSION AND EXPECTATIONS

In general, high-quality ultra-fine WC powders are often evaluated with some characteristic like these: (a) Tungsten needs to be completely carbonized. The amount of material that is not completely carbonized, such as W_xO_y and W_2C, should be as small as possible; (b) The content of impurities should be as low as possible; () The particle size distribution should be as uniform as possible. The precipitation methods which have mentioned in the literature are able to make the WC powders meet these characteristics, but some of them have some problems in the period of preparation.

Using reduction carbonization to prepare ultra-fine WC powders needs to generate simple-substance W, and then make W powders carbonize to WC powders. The particle size of WC depends on the W powder. If size of W particle during preparation of WC was not as small as possible, WC nanoparticles may be failed to produce. The other methods in the Soild-phase methods, which have taken Na, Mg, and, As as catalyst or inhibitor, WC can be prepared directly, but the effect of additions on crystallization of tungsten carbide during the sintering period need to be made further research. Besides, using solid-phase methods to prepare WC often proceed in the high temperature environment and need to keep the high temperature for a long time in order to completely carbonize. However, the liquid-phase method could prepare WC powders at low temperatures. Zeng et al. (2008), researchers achieved preparation of WC at 500°C which had greatly decreased the temperature of carbonization. But the liquid-phase method in preparing WC powders often generates other by-products. In order to remove these intermediates, it is necessary to add other solvents to dissolve them which may increase the difficulty of WC preparation. The vapor-phase method could get high-purity ultrafine WC powders. But the cost of large-scale preparation of WC by vapor-phase method is higher than others which limit its application and development. Compared with the vapor-phase method, the solid-phase reduction carbonization method has potential industrial application. Because it is much closer to current commercial production mode of tungsten carbide, which just replaces graphite to CH_4 as the C source comparing to the traditional method to produce WC.

Throughout all methods mentioned above, useful studies have been made on the option of W and C sources around the refinement of WC particles, which has laid a foundation for the industrial production of ultrafine WC powders. The preparation technology of ultra-fine WC powders is an interesting branch of nanotechnology that shows the importance of this field in the research and development of new materials. Although different methods have been developed to prepare nano-WC powder, the approaches proposed are often limited to laboratory-scale production. Thus, the large-scale industrial production of ultra-fine WC powders remains a very important direction for future research.

AUTHOR CONTRIBUTIONS

Y-CW, YY, and LL drafted the manuscript. Y-CW and LL supervised the experiments. X-YT, LL, XZ, X-YZ, QX, and J-GC were involved in the data analysis and discussions.

FUNDING

This work was supported by the National Key Research and Development Program of China (2017YFE0302600), the National Natural Science Foundation of China (21671145), the State Key Laboratory of Powder Metallurgy, the Foundation of Laboratory of Non-ferrous Metal Material and Processing Engineering of Anhui Province (15CZS08031), and the 111 Project (B18018).

REFERENCES

Akhtar, F., Humail, I. S., Askari, S. J., Tiana, J., and Shijua, G. (2007). Effect of WC particle size on the microstructure, mechanical properties and fracture behavior of WC-(W, Ti, Ta) C-6 wt% Co cemented carbides. *Int. J. Refrac. Met. Hard Mater.* 25, 405–410. doi: 10.1016/j.ijrmhm.2006.11.005

Aneela, R., and Srikanth, V. S. (2018). Thermodynamic aspects of co-formation of different condensed phases from CH4-WCl6 gas mixtures diluted in H2. *Appl. Phys. A Mater.* 124, 9–14.

Borchardt, L., Hoffmann, C., Oschatz, M., Mammitzsch, L., Petasch, U., Herrmannb, M., et al. (2012). Preparation and application of cellular and nanoporous carbides. *Chem. Soc. Rev.* 41, 5053–5067.

Chen, L., Chen, N. N., Wu, H. M., Li, W., Fang, Z., Xu, Z., et al. (2018). Flexible design of carbon nanotubes grown on carbon nanofibers by PECVD Chock for enhanced Cr(VI) adsorption capacity. *Sep. Purif. Technol.* 207, 406–415. doi: 10.1016/j.seppur.2018.06.065

Chen, L. J., Xie, Z. H., Wang, R. X., Tian, L., and Nie, H.-P. (2018). Reduction carbonization mechanism analysis of tungsten oxide powder and preparation of ultrafine tungsten carbide powder. *Rare Met. Cement. Carb.* 46, 14–20.

Chen, Z., Qin, M. L., Chen, P. Q., Huang, M., Li, R., Zhao, S., et al. (2017). WC-Co-Cr3C2-VC nanocomposite powders fabricated by solution combustion synthesis and carbothermal reduction. *Ceram. Int.* 43, 68–72.

Chen, H. Y., Wang, Z. C., Luo, L. M., Liu, Z., Zhibiaob, T., and Yuchengac, W. (2017). Effect of Ni Content on Microstructure and Properties of WC-Ni Composites Prepared by Electroless Plating and Powder Metallurgy. *Rare. Metal. Mat. Eng.* 46, 2820–2824. doi: 10.1016/s1875-5372(18)30013-4

Chuvil'deev, V. N., Blagoveshchenskii, Y. V., Sakharov, N. V., and Boldin, M. (2015). Preparation and investigation of ultrafine-grained tungsten carbide with high hardness and fracture toughness. *Dokl. Phys.* 60, 288–291. doi: 10.1134/s1028335815070095

Dai, L. Y., Lin, S. F., Chen, J. F., and Wang, W. C. (2013). Synthesis of nano-WC by high-energy ball milling. *Mater. Sci. Forum* 745, 327–334. doi: 10.4028/www.scientific.net/msf.745-746.327

Dushik, V. V., Rozhanskii, N. V., Lifshits, V. O., Rybkina, T. V., and Kuzmin, V. P. (2018). The formation of tungsten and tungsten carbides by CVD synthesis and the proposed mechanism of chemical transformations and crystallization processes. *Mater. Lett.* 228, 164–167. doi: 10.1016/j.matlet.2018.06.003

Emani, S. V., Wang, C. L., Shaw, L. L., and Shaw, L. L. (2015). On the hardness of submicrometer-sized WC-Co materials. *Mat. Sci. Eng. A Struct.* 628, 98–103. doi: 10.1016/j.msea.2014.12.106

Fan, P., Fang, Z. Z., and Guo, J. (2013). A review of liquid phase migration and methods for fabrication of functionally graded cemented tungsten carbide. *Int. J. Refract. Met. Hard Mater.* 36, 2–9. doi: 10.1016/j.ijrmhm.2012.02.006

Gu, G., Zheng, B., Han, W. Q., Roth, S., and Liu, J. (2002). Tungsten oxide nanowires on tungsten substrates. *Nano Lett.* 2, 849–851. doi: 10.1021/nl025618g

Guo, S. D., Yang, J. G., Lü, J., Zhu, E., Chen, H., and Zhang, X. (2015). Morphology of nanophase WC/6Co composite powder prepared by spray conversion method. *Chin. J. Rare Metals* 39, 43–48.

He, L. M., and Tang, S. C. (2011). Preparation of ultrafine WC powders by direct reduction and carbonization process. *Min. Metallurg. Eng.* 31, 57–63.

Hosokawa, S. (2016). Synthesis of metal oxides with improved performance using a solvothermal method. *J. Ceram. Soc. Jpn.* 124, 870–874. doi: 10.2109/jcersj2.16109

Kumar, A., Singh, K., and Pandey, O. P. (2010). Optimization of processing parameters for the synthesis of tungsten carbide (WC) nanoparticles through solvo thermal route. *Phys. E.* 42, 2477–2483. doi: 10.1016/j.physe.2010.06.002

Lee, J. D., Jun, J. H., and Park, N. K. (2003). The effect of zeolite NaX, HX and KX on the reduction-carburization of WO3. *Appl. Chem.* 7, 253–256.

Lee, Y. J., Lee, T. H., and Soon, A. (2019). Phase stability diagrams of group 6 magneli oxides and their implications for photon-assisted applications. *Chem. Mater.* 31, 4282–4290. doi: 10.1021/acs.chemmater.9b01430

Li, J., Ni, J. J., Huang, B. X., Liao, S., Wang, C., Luo, W., et al. (2019). Long-term ball milling and hot pressing of in-situ nanoscale tungsten carbides reinforced copper composite and its characterization. *Mater. Charact.* 152, 134–140. doi: 10.1016/j.matchar.2019.04.014

Li, T. (2013). *Research on Microwave Carbonization Process, And Properties Of Nano-Tungsten Carbide Powder*. Nanchang: Nanchang University.

Lin, H., Tao, B. W., Xiong, J., Li, Q., and Li, Y. (2013). Tungsten carbide (WC) nanopowders synthesized Via novel core-shell structured precursors. *Ceram. Int.* 39, 2877–2881. doi: 10.1016/j.ceramint.2012.09.061

Liu, X. M., Song, X. Y., Zhao, S. X., and Zhang, J. (2010). Spark plasma sintering densification mechanism for cemented carbides with different WC particle sizes. *J. Am. Ceram. Soc.* 93, 3153–3158. doi: 10.1111/j.1551-2916.2010.03862.x

Luo, L. M., Wu, Y. C., Li, J., and Zheng, Y. (2011). Preparation of nickel-coated tungsten carbide powders by room temperature ultrasonic-assisted electroless plating. *Surf. Coat. Tech.* 206, 1091–1095. doi: 10.1016/j.surfcoat.2011.07.078

Luo, W. Y., Liu, Y. Z., and Shen, J. J. (2019). Effects of binders on the microstructures and mechanical properties of ultrafine WC-10%AlxCoCrCuFeNi composites by spark plasma sintering. *J. Alloy. Compd.* 791, 540–549. doi: 10.1016/j.jallcom.2019.03.328

Ma, J., and Zhu, S. G. (2010). Direct solid-state synthesis of tungsten carbide nanoparticles from mechanically activated tungsten oxide and graphite. *Int. J. Refract. Met. Hard Mater.* 28, 623–627. doi: 10.1016/j.ijrmhm.2010.06.004

Maat, N., Larde, R., Nachbaur, V., Le Breton, J. M., Isnard, O., Pop, V., et al. (2018). Investigation by mossbauer spectroscopy and atom probe tomography of the phase transformation of Nd-Fe-B alloys after high-energy ball milling. *J. Appl. Phys.* 12:22.

Maheshwari, P., Fang, Z. G. Z., and Sohn, H. Y. (2007). Early-stage sintering densification and grain growth of nanosized WC-Co powders. *Int. J. Powder. Metall.* 43, 41–47.

Morimitsu, L. C. A., Ospina, R. O., and Carmona, J. M. G. (2013). Deposition and computational analysis of WC thin films grown by PAPVD. *Rev. Mex. Fis.* 59, 106–111.

Postek, E., and Sadowski, T. (2018). Qualitative comparison of dynamic compressive pressure load and impact of WC/Co composite. *Int. J. Refract. Met. Hard Mater.* 77, 68–81. doi: 10.1016/j.ijrmhm.2018.07.009

Ryu, T., Sohn, H. Y., Hwang, K. S., and Fang, Z. Z. (2009). Plasma synthesis of tungsten carbide nanopowder from ammonium paratungstate. *J. Am. Ceram. Soc.* 92, 655–660. doi: 10.1111/j.1551-2916.2009.02961.x

Ryu, T., Sohn, H. Y., Hwang, K. S., and Zhigang, Z. (2008). Tungsten carbide nanopowder by plasma-assisted chemical vapor synthesis from WCl6-CH4-H2 mixtures. *J. Mater. Sci.* 43, 5185–5192. doi: 10.1007/s10853-008-2741-8

Sadeghi, N., Akbarpour, M. R., and Aghajani, H. (2018). A novel two-step mechanical milling approach and in-situ reactive synthesis to fabricate TiC/Graphene layer/Cu nanocomposites and investigation of their mechanical properties. *Mat. Sci. Eng. A Struct.* 734, 164–170. doi: 10.1016/j.msea.2018.07.101

Singla, G., Singh, K., and Pandey, O. P. (2015). Effect of Processing Variables on WC Nanoparticles Synthesized by Solvothermal Route. *Particul. Sci. Technol.* 33, 47–52. doi: 10.1080/02726351.2014.933147

Sohn, H. Y., Ryu, T., Choi, J. W., Hwang, K. S., Han, G., Choi, Y. J., et al. (2007). The chemical vapor synthesis of inorganic nanopowders. *JOM* 59, 44–49. doi: 10.1007/s11837-007-0151-z

Venables, D. S., and Brown, M. E. (1996). Reduction of tungsten oxides with carbon. *Thermochim. Acta* 10, 251–264. doi: 10.1016/0040-6031(95)02814-5

Wang, Q., Cao, F. Y., and Chen, Q. W. (2006). Synthesis of hexagonal tungsten carbide in tungsten-sodium and supercritical carbon dioxide system. *Mater. Chem. Phys.* 95, 113–116. doi: 10.1016/j.matchemphys.2005.06.008

Wang, W., Lu, Z. C., Zeng, M. Q., Bao, X., and Zhu, M. (2017). Achieving high transverse rupture strength of WC-8Co hardmetals through forming plate-like WC grains by plasma assisted milling. *Mater. Chem. Phys.* 190, 128–135. doi: 10.1016/j.matchemphys.2017.01.010

Wang, X. R., Tan, D. Q., Zhu, H. B., He, W., Ouyang, C., Zou, Z., et al. (2018). Effect mechanism of arsenic on the growth of ultrafine tungsten carbide powder. *Adv. Powder Technol.* 29, 291348–291356.

Won, H. I, Nersisyan, H. H., and Won, C. W. (2010). Combustion synthesis of nano-sized tungsten carbide powder and effects of sodium halides. *J. Nanopart. Res.* 12, 493–500. doi: 10.1007/s11051-009-9736-5

Wu, C., Zhu, S. G., Ma, J., and Zhang, M. L. (2009). Synthesis and formation mechanisms of nanocomposite WC-MgO powders by high-energy reactive milling. *J. Alloy. Compd.* 478, 615–619. doi: 10.1016/j.jallcom.2008.11.100

Wu, Y. J., Dang, J., Lv, Z. P., and Zhang, R. (2018). The preparation of tungsten carbides and tungsten powders by reaction of tungsten trioxide with methanol. *Int. J. Refract. Met. Hard Mater.* 76, 99–107. doi: 10.1016/j.ijrmhm.2018.06.002

Xu, Z. F., Zhou, X. K., Wang, K., and Wang, Q. (2018). Fabrication of ultrafine-grained gradient cemented carbide by SPS pre-sintered method. *J. Northeastern Univer.* 39:1593.

Yang, Q. M., Yang, J. G., Wen, Y., Zhang, Q., Chen, L., and Chen, H. (2018). A novel route for the synthesis of ultrafine WC-15wt %Co cemented carbides. *J. Alloy. Compd.* 748, 577–582. doi: 10.1016/j.jallcom.2018.03.197

Yang, T. M., Wei, Q. P., Qi, Y., and Yu, Z. (2015). The diffusion behavior of carbon in sputtered tungsten film and sintered tungsten block and its effect on diamond nucleation and growth. *Diam. Relat. Mater.* 52, 49–58. doi: 10.1016/j.diamond.2014.12.009

Zeng, J. H., Yuan, D. S., Liu, Y. L., Chen, J., and Tan, S. (2008). Synthesis of tungsten carbide nanocrystals and its electrochemical properties. *Chin. J. Catal.* 29, 607–611.

Zhang, H. C., Yu, X. D., Nie, Z. H., Tan, C., Wang, F., and Cai, H. (2018). Microstructure and growth mechanism of tungsten carbide coatings by atmospheric CVD. *Surf. Coat. Tech.* 344, 85–92. doi: 10.1016/j.surfcoat.2018.03.011

Zhang, L., Chen, S., Shan, C., and Cheng, X. (2012). Effects of cobalt additions on WC grain growth. *Powder Metall.* 55, 200–205. doi: 10.1179/1743290111y.0000000009

Zheng, H. C., Fan, J. L., Yang, W. H., Zhang, Z., and Liu, T. (2015). Influence of VC/Cr3C2 and mixed carbon content on microstructure and properties of ultrafine WC-0.5Co cemented carbide. *Rare Metal. Mat. Eng.* 44, 912–917.

Conflict of Interest: The authors declare that the research was conducted in the absence of any commercial or financial relationships that could be construed as a potential conflict of interest.

frontiers
in Bioengineering and Biotechnology

ORIGINAL RESEARCH
published: 12 May 2020
doi: 10.3389/fbioe.2020.00367

Improved Osteogenesis of Selective-Laser-Melted Titanium Alloy by Coating Strontium-Doped Phosphate With High-Efficiency Air-Plasma Treatment

Haiyuan Xing*[1†]*, *Ruiyan Li*[1†]*, *Yongjie Wei*[2]*, *Boda Ying*[1]*, *Dongdong Li*[2*]* and *Yanguo Qin*[1*]

[1] Department of Orthopedics, The Second Hospital, Jilin University, Changchun, China, [2] Key Laboratory of Automobile Materials of MOE, Department of Materials Science and Engineering, Jilin University, Changchun, China

OPEN ACCESS

Edited by:
Chao Yang,
South China University of Technology,
China

Reviewed by:
Yan Xu,
Northeastern University, China
Zhiyong Zhang,
Guangzhou Medical University, China

***Correspondence:**
Dongdong Li
lidongdong@jlu.edu.cn
Yanguo Qin
qinyg@jlu.edu.cn

†These authors have contributed equally to this work

Specialty section:
This article was submitted to Biomaterials,
a section of the journal
Frontiers in Bioengineering and Biotechnology

Received: *22 February 2020*
Accepted: *02 April 2020*
Published: *12 May 2020*

Citation:
Xing H, Li R, Wei Y, Ying B, Li D and Qin Y (2020) Improved Osteogenesis of Selective-Laser-Melted Titanium Alloy by Coating Strontium-Doped Phosphate With High-Efficiency Air-Plasma Treatment.
Front. Bioeng. Biotechnol. 8:367.
doi: 10.3389/fbioe.2020.00367

Surface treatment and bioactive metal ion incorporation are effective methods for the modification of titanium alloys to be used as biomaterials. However, few studies have demonstrated the use of air-plasma treatment in orthopedic biomaterial development. Additionally, no study has performed a direct comparison between unmodified titanium alloys and air-plasma-treated alloys with respect to their biocompatibility and osteogenesis. In this study, the biological activities of unmodified titanium alloys, air-plasma-treated titanium alloys, and air-plasma-treated strontium-doped/undoped calcium phosphate (CaP) coatings were compared. The strontium-doped CaP (Sr-CaP) coating on titanium alloys were produced by selective laser melting (SLM) technology as well as micro-arc oxidation (MAO) and air-plasma treatment. The results revealed that rapid air-plasma treatment improved the biocompatibility of titanium alloys and that Sr-CaP coating together with air-plasma treatment significantly enhanced both the biocompatibility and osteogenic differentiation of bone marrow mesenchymal stem cells (BMSCs). Overall, this study demonstrated that low temperature air-plasma treatment is a fast and effective surface modification which improves the biocompatibility of titanium alloys. Additionally, air-plasma-treated Sr-CaP coatings have numerous practical applications and may provide researchers with new tools to assist in the development of orthopedic implants.

Keywords: air-plasma treatment, strontium, calcium phosphate, biocompatibility, osteogenesis

INTRODUCTION

Titanium alloys are widely used as orthopedic implants for bone defects but the lack of osseointegration is a barrier to their application. Therefore, treatment methods to enhance the bioactivity of the material surface should be employed. Air-plasma treatment enhances the surface properties of materials and has been utilized in agricultural production, waste management, as well as surface cleaning and disinfection (Petlin et al., 2017; Messerle et al., 2018; Saberi et al., 2018; Thana et al., 2019). The main advantages of this process are thin film deposition, increased wettability, induced cross-linking, and surface activation of the material. Additionally, compared to wet chemical coating techniques, this process is more economical (Canal et al., 2004; Yoo et al., 2009; Hagiwara et al., 2013; Yoshida et al., 2013; Cheng et al., 2014; Zhang et al., 2019). Recently, air-plasma treatment has been implemented to improve the surface properties of biomaterials used in tissue engineering and drug delivery (Yoo et al., 2009; D'Sa et al., 2010; Chen et al., 2019). The key features of optimal biomaterials are as follows: surface protection, biocompatibility, antimicrobial and anti-tumor properties, as well as directed differentiation of stem/progenitor cells (Yoshida et al., 2013; Zhang et al., 2019). Utilizing air-plasma treatment for coatings has been shown to enhance the wear resistance and corrosion resistance of substrate surfaces (Fenker et al., 2002; Khorasanian et al., 2011; Tsunekawa et al., 2011; Wang et al., 2011; Hussein et al., 2017). Recently, various reports have demonstrated the enhanced biocompatibility of surfaces modified with air-plasma treatment (Liu et al., 2005; Lu et al., 2012). Jeong et al. reported that the hydrophilicity of the amine plasma-treated titanium alloy plate was increased relative to the control. They suggest that this treatment had a positive effect on biocompatibility (Jeong et al., 2019). Wong et al. (2013) reported that oxygen plasma surface modification in combination with aluminum enhanced cell adhesion and viability. In summary, previous studies demonstrated that air-plasma treatment significantly improved the biocompatibility of biomaterial surfaces in a quick and efficient manner.

However, ideal biomaterials not only require good biocompatibility but they must demonstrate suitable bioactivity. Air-plasma treatment has been shown to promote limited osteogenesis, as well as enhance cell proliferation and adhesion (Griffin et al., 2019). This means it is necessary to perform customized surface modification on the titanium alloy substrate in order to improve the bioactivity and osteogenesis of the implant surface. Coatings containing calcium phosphate (CaP), the main component of natural bone tissue, can promote osteogenic differentiation of stem/progenitor cells. Various ceramics, nanoparticles, and scaffolds developed with CaP have been shown to enhance osteogenesis (de Jonge et al., 2010; Alghamdi et al., 2014; Zhou et al., 2017; Othman et al., 2019). The osteogenic nature of CaP is attributed to its ability to regulate both the extracellular $Ca^{2+}/PO_4{}^{3-}$ ions (Wu et al., 2003) and the adsorption/release of osteoinductive growth factors such as bone morphogenetic proteins (BMPs) (Begam et al., 2017). Furthermore, strontium (Sr)-doped CaP (Sr-CaP) coatings have been shown to have better osteogenic activity than undoped CaP coatings (Huang et al., 2017; Yu et al., 2017; Basu et al., 2019; Khalifehzadeh and Arami, 2019). Sr can increase osteoblast number, stimulate bone formation, reduce bone resorption rate, and reduce osteoclast activity and number (Yang et al., 2011; Raucci et al., 2015; Kargozar et al., 2017; Glenske et al., 2018). Together, these studies demonstrate that CaP coatings, especially the Sr-CaP coatings, are pro-osteogenic. Therefore, utilizing both plasma surface modification and Sr-CaP coating on the surface of the titanium alloys has the potential to improve the biocompatibility and osteogenesis, respectively.

Selective laser melting (SLM) has a high degree of forming freedom for titanium alloy. Based on computer reconstructed bone models, SLM can be utilized to produce orthopedic implant products with mechanical properties that are more compatible with original bones, making it possible for orthopedic clinical application (de Wild et al., 2013; Wang et al., 2019). Meanwhile, SLM technology has broad application prospects in high-strength titanium alloys and 4D printing (Kang and Yang, 2019; Lu et al., 2019), potentially leading the frontiers of orthopedic implants. In this work, we designed titanium alloy substrates (produced using SLM) modified with air-plasma surface treatment combined with Sr-CaP coating to simulate *in vivo* conditions. Titanium alloys were sintered and manufactured using SLM equipment. Sr ions were doped to the coating via micro-arc oxidation (MAO) and various assays were performed to evaluate the feasibility of these approaches to design orthopedic implants. These varied surface treatments and coating combinations allowed us to determine the optimal biomaterial surface to enhance biocompatibility and induce osteogenesis.

MATERIALS AND METHODS

Materials

Titanium alloy disks (12 mm in diameter and 1 mm thick) were manufactured from a commercially available SLM device (Dimetal 280, Syndaya, China) using a laser power of 150 watts (W) and laser scanning speed of 500 mm/s. The device was equipped with a 500 W Yb:YAG fiber laser (spot size = 80 μm). All the disks were polished with abrasive papers and ultrasonically washed with acetone and distilled water before used.

Preparation of Ceramic Coatings

The experimental settings for preparing the ceramic coatings were as follows: pulse frequency (500 Hz), duty cycle (10%), duration time (3 min), forward voltage (350 V), and negative voltage (50 V). During the reaction, the temperature of the electrolytes was maintained below 24°C using cooled water. The MAO electrolytes were divided into two groups depending on compositions: Group 1 (Sr-doped and labeled Sr-CaP): 0.085 M calcium acetate $[(CH_3COO)_2Ca]$, 0.01 M β-glycerophosphate (β-GP) disodium, and 0.03 M strontium acetate $[(C_2H_3O_2)_2Sr]$; and Group 2 (undoped and labeled CaP): 0.085 M calcium acetate $[(CH_3COO)_2Ca]$ and 0.01 M β-GP disodium. After the procedure, coatings were washed with water to remove any impurities.

Air-Plasma Treatment

After MAO, all the samples were plasma-treated by using the active component (ion, atom, active group, photon, etc.). Air-plasma treatment was performed using a plasma surface treatment processor (PT-03-LF, Tiankechuangda Co. Ltd., China) to produce hydroxyl groups. The experimental settings were as follows: frequency (13.56 MHz), electric power (100 W), and airflow at 10 sccm at 0.05 T for 10 min. The plasma surface modification technique was applied to titanium alloy (TC4), CaP, Sr-CaP and the new surfaces were labeled TC4-p, CaP-p, and Sr-CaP-p, respectively.

Surface Characterization

The morphology of the thin film coatings was observed using field emission scanning electron microscopy (FE-SEM, Hitachi8010, Japan). The mean elemental composition of each surface coating and the Ca:P atomic ratio of crystals with various morphologies was analyzed. This was done using an energy dispersive X-ray spectrometer (EDS) incorporated into the scanning electron microscope (SEM) under "area scanning" mode. The crystalline phase composition and structure of the bioceramic coatings was evaluated using an X-ray diffractometer (XRD, D8 DISCOVER, Germany) which had a monochromatic CuKa radiation source generated at 30 mA and 40 kV and a scanning speed of 4°/min with a scanning range between 15° and 60°.

Cell Culture

Rabbit bone marrow stromal cells (rBMSCs) were obtained from the 28-day-old white rabbits (Jilin University, China). The rabbits were dissected, long bone limbs were isolated, and rBMSCs were harvested by extracting bone marrow cavities using previously described methods (Li et al., 2017). The rBMSCs were cultured in Dulbecco's Modified Eagle's medium with low glucose (Low/DMEM, Hyclone, United States), containing 10% fetal bovine serum (FBS, Gibco, United States) and 1% penicillin/streptomycin (Hyclone, United States) at 37°C in a humidified atmosphere of 95% air and 5% CO_2. The medium was replaced every 2 days and cells at passage 4 were used in the following experiments. The animal procedures were performed in strict accordance with the laboratory animal regulations of the State Council of the People's Republic of China (No. [2017] 676) and approved by the ethics committee of Jilin University.

Cell Adhesion and Morphology

To assess cell adhesion, the rBMSCs were seeded on TC4, TC4-p, CaP-p, and Sr-CaP-p at a density of 1×10^5 cells/ml in 24-well plates (Corning, United States). After 2 h of incubation, the number of adherent cells was quantified using the Cell Counting Kit-8 (CCK-8, Dojindo, Japan). The suspension was added into 96-well plates (Corning, United States) to facilitate detection using a microplate reader. To assess cell morphology, the rBMSCs were seeded at a density of 4×10^4 cells/ml in 24-well plates. The cytoskeleton and cell nuclei were stained using the following protocol: (i) Incubate cells for 2 h; (ii) Wash samples with phosphate-buffered solution (PBS); (iii) Fix samples with 4% paraformaldehyde (Sangon, China) for 10 min at 4°C and stain with 50 mg/ml rhodamine phalloidin (Sigma, United States) for 1 h and 4,6-diamidino-2-phenylindole (DAPI, Sigma, United States) for 5 min at room temperature (25°C). All samples were washed with PBS between each step and each sample was visualized using a confocal laser scanning microscope (Olympus LX81-ZDC, Japan).

A separate group of cell-seeded samples at a density of 1×10^4 cells/ml was fixed in 2.5% v/v glutaraldehyde at 4°C overnight. After washing with PBS, the fixed samples were dehydrated through an ethanol concentration gradient (30, 50, 75, 80, 90, 95, and 99.5%), critical-point dried, and finally sputtered with platinum. The samples were observed through the FE-SEM (XL-30 ESEM FEG Scanning Electron Microscope, FEI Company, United States).

Cell Proliferation

The rBMSCs were seeded on different surfaces at a density of 4×10^4 cells/ml in 24-well plates. At 1, 4, and 7 days, the samples were moved to fresh 24-well plates, respectively, before being gently washed by PBS. Cell proliferation was assessed using CCK-8 kit (CCK-8:DMEM = 10:100) according to the manufacturer's instructions (2 h incubation at 37°C) and was quantified using optical density (OD) values at 450 nm on a microplate reader (Varioskan Flash, Thermo Scientific, United States).

Cell Viability

The rBMSCs were seeded at a density of 2×10^4 cells/ml and incubated for 1 day. Apoptosis was evaluated using Cell Viability Assays (Invitrogen, Life Technologies, Carlsbad, CA, United States) and quantification was performed using the FR-1800 luminescent and fluorescent biological image analysis system (Furi Science and Technology Co., China).

Alkaline Phosphatase (ALP) Activity Assay

The rBMSCs were seeded on samples at a density of 6×10^4 cells/ml in 24-well plates and incubated until blank group cells had mostly adhered. Subsequently, the cells were cultured with the osteogenic medium supplemented with 50 mg/l ascorbic acid, 10^{-8} M dexamethasone, and 10 mM β-glycerol phosphate (Sigma, United States). The medium was changed every 2 days. Alkaline phosphatase (ALP) staining was performed 7 days after the addition of the osteogenic medium using the BCIP/NBT ALP Color Development Kit (Beyotime, China). To quantify ALP activity, the samples were washed with PBS and cells were disrupted using RIPA lysis buffer (Beyotime, China). The cell lysate was collected for determining both the ALP and total protein concentration using ALP Assay Kit (Beyotime, China) and BCA Assay Kit (Beyotime, China), respectively. After 30 min incubation at 37°C, the ALP concentration and total protein concentration were measured using a microplate reader (Varioskan Flash, Thermo Scientific) at wavelengths of 405 and 562 nm, respectively. The ALP concentration was calculated according to a standard curve and normalized to total protein concentration while the ALP activity was normalized to incubation time. Specifically, the following equation was used to calculate ALP activity.

ALP activity (nmol/min/mg) = (ALP concentration/total protein concentration)/incubation time.

Alizarin Red Staining

After incubation for 7 and 14 days with osteogenic medium, the samples were fixed with 4% paraformaldehyde for 10 min at 4°C and stained with alizarin red (pH = 4.2) at room temperature (25°C). Images were visualized using a zoom stereo microscope.

Statistical Analysis

All the assays in this study were performed in triplicate. Data was presented as the mean ± standard deviation (SD). Statistical analysis was performed using multiple t-tests with the

GraphPad Prism software. The value $p < 0.05$ was considered statistically significant.

RESULTS

Characterization

The morphological features of the coated titanium alloy samples were characterized by SEM. **Figure 1** shows SEM images of the specimen surfaces: TC4, TC4-p, CaP-p, and Sr-CaP-p. The surface morphology of TC4 exhibited an irregular shape with numerous artificial scratches due to the mechanical polishing process (**Figure 1**). There was no change in the topographic characteristics (morphology or average roughness values) of TC4 surfaces after plasma treatment. After MAO modification, a volcanic eruptive microporous structure was observed on the sample. The pore diameter of the coating was about 1–3 μm and distributed at regular intervals. At higher magnifications, the surface of the coating was observed to be quite smooth. The introduction of strontium ion did not change the morphology of the coatings.

The chemical composition of Sr-CaP-p was analyzed by EDS. The element mapping diagrams were consistent with the surface topography of Sr-CaP-p, suggesting that all the elements were evenly distributed (**Supplementary Figure S1**). The element Ti is incorporated into the coating from the substrate, and the elements Ca, P, Sr originated from the electrolyte solution. The percent by weight (wt%) of Ca and P in Sr-CaP-p was 6.17 and 4.25 wt%, respectively. The Ca:P ratio was approximately 1.12, which is close to the Ca:P stoichiometric ratio of HA at 1.67. Bioactive surface coatings containing CaP, which mimic *in vivo* bone tissue, have been widely developed for load-bearing implant applications. The introduction of Sr ions into the coatings can accelerate the formation and calcification of bone tissue, thereby reducing fracture healing time. The wt% of Sr in Sr-CaP-p is approximately 1.97 wt%.

The osseointegration of implants is strongly related to their surface composition (Zhang et al., 2015). The XRD patterns of the different coatings are shown in **Figure 2**. TC4 and TC4-p had similar peaks after plasma treatment and this suggested to us that this modification did not change the structure and composition of materials. The main substance in the coating of CaP-p and Sr-CaP-p is the diffraction peak of anatase and rutile with low crystallinity, and the diffraction peak of titanium alloy is derived from the TC4 matrix. Rutile and anatase peaks can be clearly detected due to the MAO process, which was in conformance with JCPDS 96-900-7433 and JCPDS 1-86-1156, respectively, demonstrating their potential biocompatibility.

The potentiodynamic polarization curves of TC4 before and after modification are shown in **Figure 3**. The E_{corr} of TC4-p (-0.287 V) is slightly more positive compared to TC4 substrates (-0.304 V), suggesting that plasma treatment can improve the corrosion resistance of the substrate. The MAO coating of CaP-p, and Sr-CaP-p had higher E_{corr} (-0.109 and -0.026 V) compared to titanium alloy, suggesting improved corrosion resistance of TC4 resulting from MAO and plasma treatment. This improved corrosion resistance in the human body is essential for metal implant development.

Hydrophilicity is critical for the biological activity of bone tissue implants (Albrektsson and Wennerberg, 2019). Knowing this, we measured the water contact angle just before cell incubation. The water contact angles on the surfaces of the TC4 and customized coatings are shown in **Figure 4**. The static contact angle of water droplets on the original, as-polished Ti

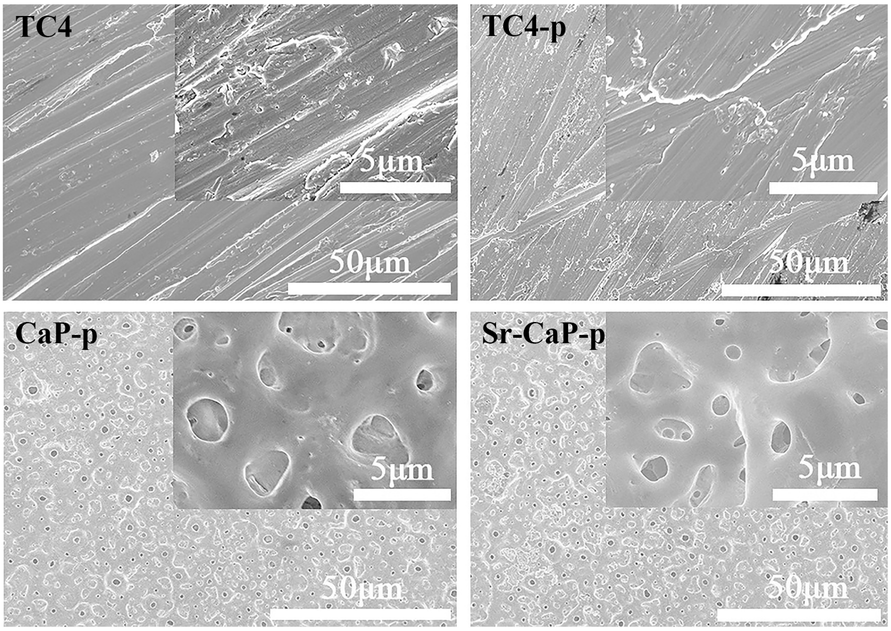

FIGURE 1 | SEM images of TC4, TC4-p, CaP-p, and Sr-CaP-p.

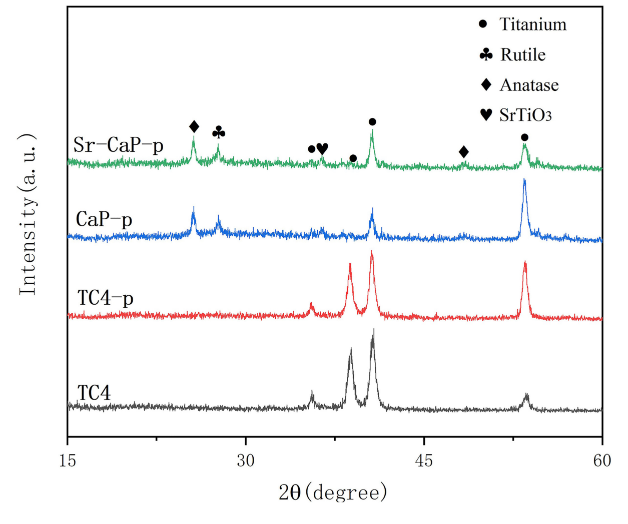

FIGURE 2 | XRD spectra for TC4, TC4-p, CaP-p, and Sr-CaP-p.

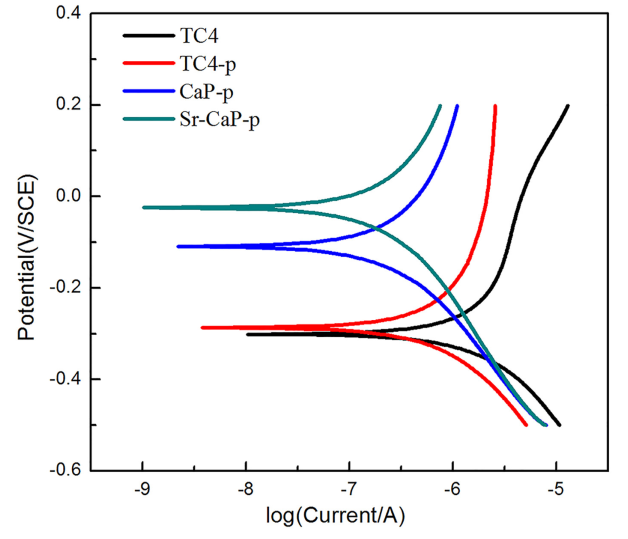

FIGURE 3 | Potential dynamic polarization curves of TC4, TC4-p, CaP-p, and Sr-CaP-p.

disk was approximately 73.0 ± 3.0°. After plasma treatment, the water contact angle changed to 44.3 ± 1.2°, suggesting that the obtained coating had hydrophilic properties. After the MAO process, the water contact angles of CaP-p and Sr-CaP-p decreased to 18.2 ±3.4° and 12.2 ± 0.8°, respectively. The micro/nano hierarchical structure exhibited a powerful capillary function, which resulted in increased contact area and accelerated water droplet spread. These results suggest that the excellent wettability may be beneficial for protein adsorption, adhesion, and spreading of cells.

Cell Proliferation and Cell Viability

Cell proliferation on days 1, 4, and 7 was measured for cells grown on TC4, TC4-p, CaP-p, and Sr-CaP-p (**Figure 5A**).

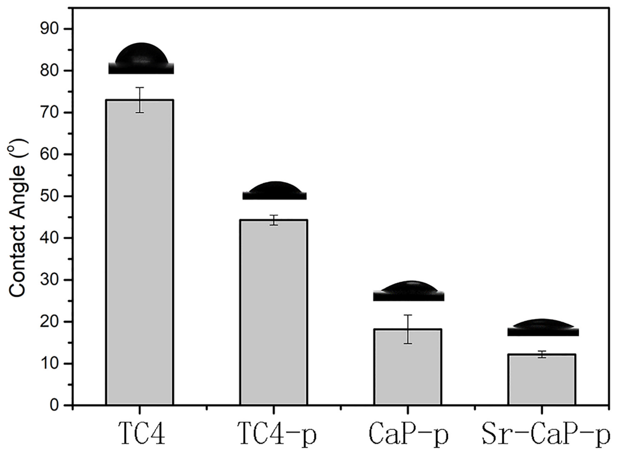

FIGURE 4 | Contact angle measurement of water on the surface of different samples.

All groups show a tendency to increase in cell mass, indicating that they provide the feasibility of suitable substrates of cell growth environment. On day 1, there was no difference in cell proliferation among the groups. While on day 4, the proliferation rate of the Sr-CaP-p group was significantly higher than those of the other three groups. Lastly, on day 7, the proliferation rate of the TC4-p group was significantly higher than that of the TC4 group, and the rate of the Sr-CaP-p group was significantly higher than that of theTC4-p group. These results demonstrate that Sr-CaP-p promotes the highest rate of cell proliferation. To evaluate the cytotoxicity of the coated samples, live-dead cell staining (red dots = dead cells; green dots = live cells) was performed. Cell viability was assessed using fluorescence microscopy (**Figure 5B**). All groups were observed under the same magnification. Samples tested from all four groups showed low cytotoxicity indicated by the low number of red dots (dead cells) observed.

Cell Adhesion

Short-term cell adhesion can be quantified by cell viability (**Figure 6A**). Cells were allowed to adhere for 2 h before quantification was performed (similar to a previous study, Zhang et al., 2018). The number of adherent cells on TC4-p was higher than those on the CaP-p and Sr-CaP-p groups, which had nearly identical OD values (which represent the relative cell number). Additionally, initial cell adhesion behavior was assessed by visualizing the rhodamine-labeled phalloidin-stained cytoskeleton, and DAPI-stained nuclei using confocal microscopy (**Figure 6B**). rBMSCs were shown to adhere to all the samples. Notably, cells adhered to the Sr-CaP-p had many intercellular connections, as well as clear and well-ordered cytoskeleton/microfilaments. Additionally, there was an obvious rearrangement of the cytoskeleton and good directionality.

To avoid the effect of fluorescent dye adsorption, showing the micropores clearer, we used a SEM to observe the passage of cells on the coating (**Figure 6C**). Morphologically, at higher magnification (1000X, 2000X), cells in the TC4 group had a flat

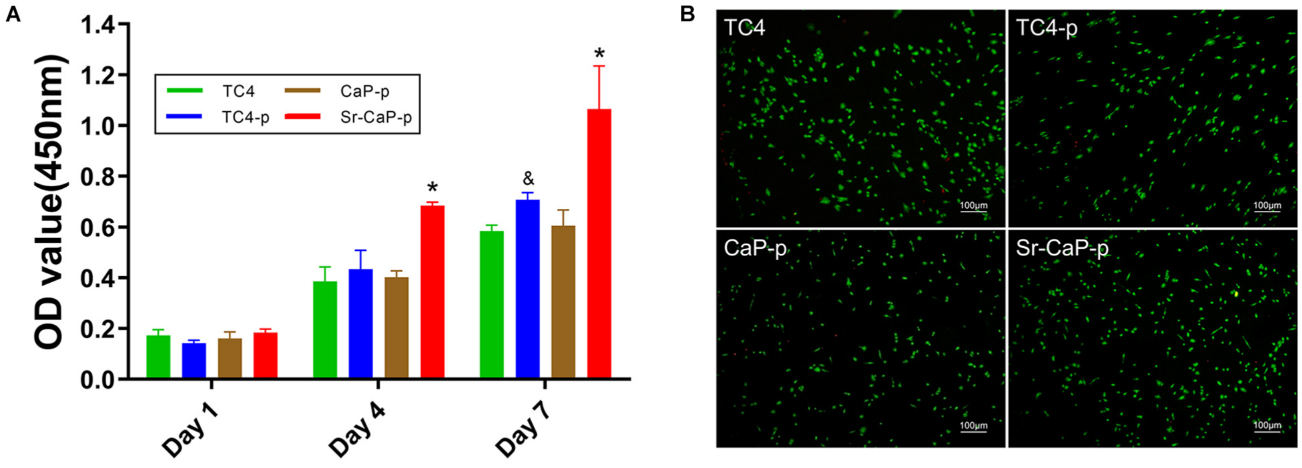

FIGURE 5 | (A) Cell proliferation of rBMSCs on TC4, TC4-p, CaP-p, Sr-CaP-p at 1, 4, and 7 days. (* indicates statistical significance $p < 0.05$ vs. TC4-p and & indicates statistical significance $p < 0.05$ vs. TC4). **(B)** Cell viability of rBMSCs on different groups at 24 h. Live cells were stained with green dots and dead cells were stained with green dots. Scale: 100 μm.

structure and the intercellular connections between cells were almost invisible. Cells in the TC4-p group exhibited a typical fusiform shape with clear pseudopods, and intercellular filaments could clearly be seen. In the CaP-p group, a longer irregular fusiform structure was observed. The pseudopods are extended directionally to micropores. For the Sr-CaP-p group, there is an extended structure with some cell–cell interactions, and the extended pseudopods with multi-direction attach well to the micropores. These results show that TC4-p, CaP-p, and Sr-CaP-p all demonstrated better cell adhesion than TC4, while Sr-CaP-p has the highest performance.

Osteogenic Differentiation

Alkaline phosphatase staining was performed to detect ALP expression. Cells seeded on TC4, TC4-p, CaP-p, and Sr-CaP-p were all stained (**Figure 7A**) and day 7 was chosen to represent early-stage differentiation. The nodules in the deep-stained area of TC4 were scattered, while those of the other three coating groups were closer. From the perspective of the denseness, nodules in CaP-p and Sr-CaP-p have deeper staining. Osteogenesis was accurately measured by quantifying the ALP activity (a measure of the differentiation level of osteoblasts). Early osteogenesis was measured at days 4 and 7 in quantification. As time progressed, the ALP activity expression increased (**Figure 7B**). At day 4 and 7, the highest ALP activity expression was observed in the Sr-CaP-p group. This result was consistent with the staining result (**Figure 7A**). Overall, the Sr-CaP-p group had the best ALP activity during early osteogenesis.

The formation of mineralized nodules is one of the most important phenomena at the end stage of osteoblast differentiation and represents the maturation of osteoblasts. To assay this, alizarin red staining is performed to measure the extent of mineralization (Gregory et al., 2004). Alizarin red staining was conducted on day 7 and 14 (**Figure 7C**). The number of stained red spots (representing calcium nodules) was used to quantify alizarin red staining. Generally, more calcified nodules are observed at the advanced stage (21 days) compared to the middle stage (14 days) in each group. Specifically, the number of calcified nodules in the TC4-p group on days 14 and 21 was higher compared to the TC4 group. On days 14 and 21, nodules in Sr-CaP-p were increased compared to the CaP-p group. Moreover, the Sr-CaP-p group had significantly more nodules on days 14 and 21 compared to every other group. We conclude that among the groups, Sr-CaP-p possessed the greatest osteogenesis.

DISCUSSION

Biomaterials with osteogenesis and enhanced biocompatibility are important for the production of orthopedic implants. In this study, we used SLM technology to prepare titanium alloys. SLM technology has a high degree of processing freedom (unlike traditional design) making it possible to produce medical devices of various shapes and structures. The basic principle of SLM technology is that metal powder is completely melted under the heat of laser beam, and formed after cooling and solidification. SLM can quickly prepare orthopedic implants. To further enhance the biocompatibility and osteogenesis of the orthopedic implant, suitable modification is necessary. In this study, we fabricated and characterized a coating treated with air-plasma and MAO. To investigate the biocompatibility and osteogenesis of the coating, rBMSCs were cultured on the coating surface and various assays were performed to determine the suitability of the coatings.

Biocompatibility and osteogenesis are effective evaluation methods for orthopedic implants (Constantin et al., 2019). When assessing the biocompatibility of a biomaterial, cytotoxicity is an important early measure that can be used to qualitatively and quantitatively determine the potential biological risks.

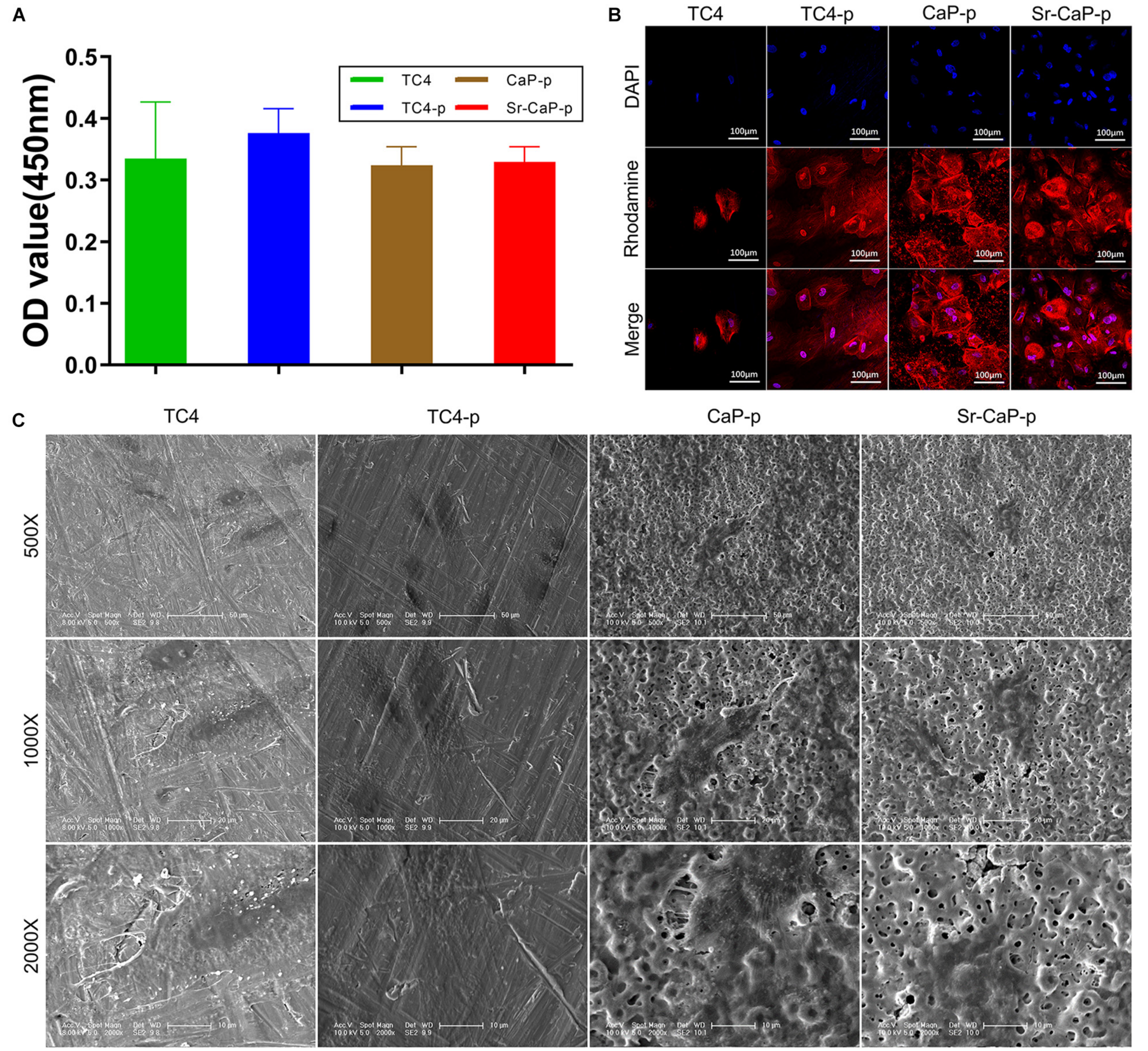

FIGURE 6 | (A) Cell adhesion of rBMSCs on different groups at 2 h. **(B)** Confocal laser scanning microscopy images of rBMSCs on different groups at 2 h (red, rhodamine-phalloidin for F-actin; blue, DAPI for nucleus). Scale: 100 μm. **(C)** SEM micrographs of rBMSCs on different groups at 12 h. Scale: 50 μm (500 Scale), 20 μm (1000 Scale), 10 μm (2000×).

Cell adhesion and cell proliferation are also effective for the determination of a material's biocompatibility. At the cellular level, assessment of osteogenic capacity can be performed using both ALP and alizarin red staining. This staining demonstrates some of the key proteins in the stem cell osteogenesis signaling pathway (Aminian et al., 2016).

The suitability of air-plasma-treated titanium alloy for stem cell culture has not been directly tested; therefore, we first performed a biocompatibility verification on a single air-plasma-treated titanium alloy. Cell proliferation, cell adhesion, and cell viability experiments demonstrated faster cell growth, more extended cytoskeleton, clearer cell morphology, and lower cytotoxicity on TC4-p compared to TC4. Specifically, there was a significant difference in cell proliferation on day 7. Spreading cell morphology was clearly observed in cells grown on the TC4-p coating which aids in promoting cluster growth and proliferation of rBMSCs. Although ALP activity of TC4-p is not significantly higher than that of TC4, the results of ALP and alizarin red staining (as shown in **Figures 7A,C**) show that single air-plasma coating enhances the osteogenic activity. This evidence demonstrates that air-plasma treatment can significantly improve the biocompatibility of inorganic implants and may be conducive

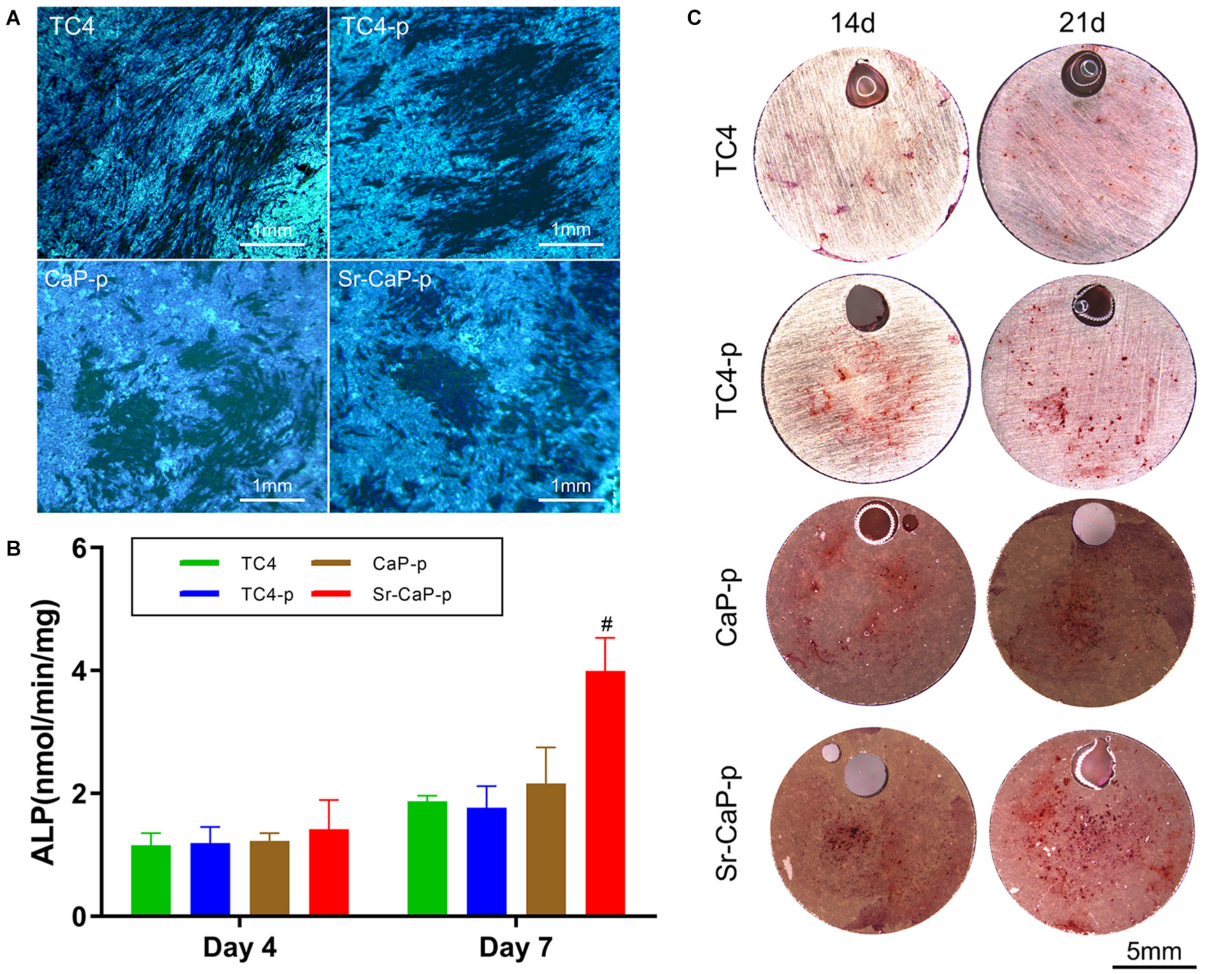

FIGURE 7 | (A) Locally magnified picture of ALP staining images at 7 days. Scale: 1 mm. **(B)** ALP activity at 4 and 7 days (# indicates statistical significance $p < 0.05$ vs. CaP-p). **(C)** Alizarin red staining images of different groups at 14 days. Scale: 5 mm.

for osteogenesis. After air-plasma treatment, hydroxyl radicals are added to the treated surface (Tsougeni et al., 2015; Kurzyp et al., 2017; Sathish et al., 2019; Wieland et al., 2020; Zhang et al., 2020), further reducing water contact angle shown in **Figure 4**, which forms an adsorption effect with adhesion proteins and enhances biocompatibility. Hydrophilicity is critical for the bioactivity of bone tissue implants and can improve cell adhesion and proliferation. It has been reported that the surface energy and hydrophilicity would affect the biocompatibility positively by changing the adsorption capability of the surface (Fan and Guo, 2020). Cell adhesion, migration, and growth are related to the degree of roughness and hydrophilicity of the biomaterial's surface. These properties may explain the improved biocompatibility of TC4-p. When hydroxyl radicals are formed on the treated surface, the OH^- attracts Ca^{2+} ions to the film surface and increases the calcium ions concentration on the surface of the TC4-p sample. As the calcium ions accumulate, then combine the PO_4^{3-} in the DMEM to form CaP apatite. Thus, the CaP apatite formed on the TC4-p sample may improve the osteogenic activity (Huang et al., 2015). Since both TC4-p and CaP-p groups promote osteogenesis via the osteoinduction effect of the CaP, they have a similar performance on the *in vitro* osteogenesis experiment, especially the mineralization of extracellular matrix (**Figure 7C**). Osteogenesis is enhanced in both the TC4-p and CaP-p groups. However, the enhancement of osteogenesis by air-plasma treatment is limited, and it is necessary to introduce a coating that is beneficial to osteogenesis.

To further enhance the osteogenesis of the implant material, active ion-doping can be performed. Strontium has a long history of being utilized as an active component of orthopedic implants and bone tissue engineering materials (Pilmane et al., 2017). Whether as a substrate or modification, strontium has excellent osteogenesis. In this work, the Sr-CaP-p group enhanced osteogenic activity better than any other group, which indicates a beneficial role for Sr. Our previous studies have also shown that Sr ion-exchange zeolite-A coatings can remarkably enhance the osteoinductive ability of porous titanium alloys (Wang et al., 2018). Peng et al. (2009) also found that Sr promoted osteogenic differentiation of MSC by activating Ras/MAPK signaling pathway and downstream transcription factor Runx2.

Overall, we found that the use of strontium in the coating could enhance the osteogenesis of the implant.

The comparison of TC4-p and TC4 confirms that air-plasma treatment enhances biocompatibility. To improve osteogenesis, CaP was chosen to be an incorporation coating for strontium. Strontium-doped or -undoped CaP was combined with air-plasma treatment to study the induction of osteogenesis. With regard to biocompatibility, the cell proliferation results showed excellent cell growth capability on Sr-CaP-p. It is worth noting that the enhancement of cell proliferation in the CaP-p group is not significant, which is consistent with some reports (Klymov et al., 2016; Nguyen et al., 2019). Confocal microscopy images showed that cells in the CaP-p group spread well with clear microfilaments while cells in the Sr-CaP-p group had a spindle-shaped cell morphology with actively-dividing cells. Electron micrographs of the two groups of cells show obvious pseudopods that extended to the micropores, which were not observed in the TC4 and TC4-p groups. This is due to the micro-scale pores formed on the surface by the MAO method which is conducive to cell attachment and provides a suitable microenvironment for early bone repair as previously reported (Alves et al., 2019). In terms of osteogenesis, both ALP activity (**Figure 7B**) and alizarin red staining (**Figure 7C**) show that Sr-CaP-p has the best osteogenesis at both the early and advanced stages. A comprehensive comparison of each group shows that the biocompatibility and osteogenesis of Sr-CaP-p are significantly improved. In summary, air-plasma treatment introduces a large number of hydroxyl groups and reduces the water contact angle, thus enhancing protein adsorption and promoting stable protein release. Additionally, Sr-CaP coating potentially works in concert with air-plasma treatment to improve biocompatibility and induction of osteogenesis.

CONCLUSION

In this study, we demonstrated the biocompatibility and osteogenesis of air-plasma-treated strontium-doped phosphate coating. It had been successfully developed and characterized after applying MAO and air-plasma treatment on SLM-produced titanium alloys. Air-plasma treatment does not change the structure and composition of materials but it improves the wettability and corrosion resistance of the substrate. To investigate the biocompatibility and osteogenesis of TC4-p and Sr-CaP-p, various assays measuring cell proliferation, cell adhesion morphology and quantification, cell viability, ALP staining and quantification, and alizarin red staining were performed. Overall, rBMSCs adhered, proliferated, and induced osteogenesis throughout the culture period. Pure air-plasma treatment enhanced biocompatibility and slightly promoted osteogenesis. The results also showed that strontium-doped phosphate coating significantly enhanced both biocompatibility and osteogenesis. Therefore, these results show that (i) air-plasma treatment can be an efficient method to enhance the biocompatibility of a titanium alloy; and (ii) manufactured Sr-CaP-p can be a beneficial modification to enhance the biocompatibility and osteogenesis of a titanium alloy.

DATA AVAILABILITY STATEMENT

All datasets generated for this study are included in the article/**Supplementary Material**.

AUTHOR CONTRIBUTIONS

HX and RL collected the experimental data, performed data analysis, and wrote the manuscript. YW and BY performed a part of data analysis. DL and YQ oversaw the project and performed the overall editing of the manuscript.

FUNDING

We greatly acknowledge the support from the National Natural Science Foundation of China (81772456 and 51627805), Scientific research planning project of Jilin Provincial Department of Education (No. JJKH20190148KJ), the Project supported by PHD Interdisciplinary Research Fund of Jilin University (No. 10183201845), and the Training Program of Outstanding Doctoral PhD for Norman Bethune Health Science Center of Jilin University (No. 470110000644).

SUPPLEMENTARY MATERIAL

The Supplementary Material for this article can be found online at: https://www.frontiersin.org/articles/10.3389/fbioe.2020.00367/full#supplementary-material

REFERENCES

Albrektsson, T., and Wennerberg, A. (2019). On osseointegration in relation to implant surfaces. *Clin. Implant Dent. Relat. Res.* 21, 4–7. doi: 10.1111/cid.12742

Alghamdi, H. S., Bosco, R., Both, S. K., Iafisco, M., Leeuwenburgh, S. C. G., Jansen, J. A., et al. (2014). Synergistic effects of bisphosphonate and calcium phosphate nanoparticles on peri-implant bone responses in osteoporotic rats. *Biomaterials* 35, 5482–5490. doi: 10.1016/j.biomaterials.2014.03.069

Alves, A. C., Thibeaux, R., Toptan, F., Pinto, A. M. P., Ponthiaux, P., and David, B. (2019). Influence of macroporosity on NIH/3T3 adhesion, proliferation, and osteogenic differentiation of MC3T3-E1 over bio-functionalized highly porous titanium implant material. *J. Biomed. Mater. Res. B Appl. Biomater.* 107, 73–85. doi: 10.1002/jbm.b.34096

Aminian, A., Shirzadi, B., Azizi, Z., Maedler, K., Volkmann, E., Hildebrand, N., et al. (2016). Enhanced cell adhesion on bioinert ceramics mediated by the osteogenic cell membrane enzyme alkaline phosphatase. *Mater. Sci. Eng. C Mater. Biol. Appl.* 69, 184–194. doi: 10.1016/j.msec.2016.06.056

Basu, S., Ghosh, A., Barui, A., and Basu, B. (2019). Epithelial cell functionality on electroconductive Fe/Sr co-doped biphasic calcium phosphate. *J. Biomater. Appl.* 33, 1035–1052. doi: 10.1177/0885328218821549

Begam, H., Nandi, S. K., Kundu, B., and Chanda, A. (2017). Strategies for delivering bone morphogenetic protein for bone healing. *Mater. Sci. Eng. C Mater. Biol. Appl.* 70, 856–869. doi: 10.1016/j.msec.2016.09.074

Canal, C., Molina, R., Bertran, E., and Erra, P. (2004). Wettability, ageing and recovery process of plasma-treated polyamide 6. *J. Adhes. Sci. Technol.* 18, 1077–1089. doi: 10.1163/1568561041257487

Chen, Z., Visalakshan, R. M., Guo, J., Wei, F., Zhang, L., Chen, L., et al. (2019). Plasma deposited poly-oxazoline nanotextured surfaces dictate osteoimmunomodulation towards ameliorative osteogenesis. *Acta Biomater.* 96, 568–581. doi: 10.1016/j.actbio.2019.06.058

Cheng, Q., Komvopoulos, K., and Li, S. (2014). Plasma-assisted heparin conjugation on electrospun poly(L-lactide) fibrous scaffolds. *J. Biomed. Mater. Res. A* 102, 1408–1414. doi: 10.1002/jbm.a.34802

Constantin, C. P., Aflori, M., Damian, R. F., and Rusu, R. D. (2019). Biocompatibility of polyimides: a mini-review. *Materials* 12:3166. doi: 10.3390/ma12193166

de Jonge, L. T., Leeuwenburgh, S. C. G., van den Beucken, J. J. J. P., te Riet, J., Daamen, W. F., Wolke, J. G. C., et al. (2010). The osteogenic effect of electrosprayed nanoscale collagen/calcium phosphate coatings on titanium. *Biomaterials* 31, 2461–2469. doi: 10.1016/j.biomaterials.2009.11.114

de Wild, M., Schumacher, R., Mayer, K., Schkommodau, E., Thoma, D., Bredell, M., et al. (2013). Bone regeneration by the osteoconductivity of porous titanium implants manufactured by selective laser melting: a histological and micro computed tomography study in the rabbit. *Tissue Eng. Part A* 19, 2645–2654. doi: 10.1089/ten.tea.2012.0753

D'Sa, R. A., Burke, G. A., and Meenan, B. J. (2010). Protein adhesion and cell response on atmospheric pressure dielectric barrier discharge-modified polymer surfaces. *Acta Biomater.* 6, 2609–2620. doi: 10.1016/j.actbio.2010.01.015

Fan, H., and Guo, Z. (2020). Bioinspired surfaces with wettability: biomolecule adhesion behaviors. *Biomater. Sci.* 8, 1502–1535. doi: 10.1039/c9bm01729a

Fenker, M., Balzer, M., Jehn, H. A., Kappl, H., Lee, J. J., Lee, K. H., et al. (2002). Improvement of the corrosion resistance of hard wear resistant coatings by intermediate plasma etching or multilayered structure. *Surf. Coat. Technol.* 150, 101–106. doi: 10.1016/s0257-8972(01)01506-7

Glenske, K., Donkiewicz, P., Kowitsch, A., Milosevic-Oljaca, N., Rider, P., Rofall, S., et al. (2018). Applications of metals for bone regeneration. *Int. J. Mol. Sci.* 19:826.

Gregory, C. A., Gunn, W. G., Peister, A., and Prockop, D. J. (2004). An Alizarin red-based assay of mineralization by adherent cells in culture: comparison with cetylpyridinium chloride extraction. *Anal. Biochem.* 329, 77–84. doi: 10.1016/j.ab.2004.02.002

Griffin, M. F., Ibrahim, A., Seifalian, A. M., Butler, P. E. M., Kalaskar, D. M., and Ferretti, P. (2019). Argon plasma modification promotes adipose derived stem cells osteogenic and chondrogenic differentiation on nanocomposite polyurethane scaffolds; implications for skeletal tissue engineering. *Mater. Sci. Eng. C Mater. Biol. Appl.* 105:110085. doi: 10.1016/j.msec.2019.110085

Hagiwara, K., Hasebe, T., and Hotta, A. (2013). Effects of plasma treatments on the controlled drug release from poly(ethylene-co-vinyl acetate). *Surf. Coat. Technol.* 216, 318–323. doi: 10.1016/j.surfcoat.2012.11.064

Huang, B. L., Tian, Y., Zhang, W. J., Ma, Y. F., Yuan, Y., and Liu, C. S. (2017). Strontium doping promotes bioactivity of rhBMP-2 upon calcium phosphate cement via elevated recognition and expression of BMPR-IA. *Colloid Surf. B Biointerfaces* 159, 684–695. doi: 10.1016/j.colsurfb.2017.06.041

Huang, Q. L., Yang, X., Zhang, R. R., Liu, X. J., Shen, Z. J., and Feng, Q. L. (2015). Enhanced hydrophilicity and in vitro bioactivity of porous TiO2 film through the incorporation of boron. *Ceram. Int.* 41, 4452–4459. doi: 10.1016/j.ceramint.2014.11.137

Hussein, R., Nie, X., and Northwood, D. (2017). "Plasma electrolytic oxidation coatings on Mg-alloys for improved wear and corrosion resistance: material performance and cathodic protection," in *Corrosion: Material Performance and Cathodic Protection*, ed. S. Syngellakis (Southampton: WIT Press), 133–147. doi: 10.2495/978-1-78466-249-3/012

Jeong, Y. W., Jung, S., Han, J. J., Park, H. J., Kim, R. Y., Kim, B. H., et al. (2019). Effectiveness of surface treatment with amine plasma for improving the biocompatibility of maxillofacial plates. *Materials* 12:2581. doi: 10.3390/ma12162581

Kang, L. M., and Yang, C. (2019). A review on high-strength titanium alloys: microstructure, strengthening, and properties. *Adv. Eng. Mater.* 21:1801359. doi: 10.1002/adem.201801359

Kargozar, S., Lotfibakhshaiesh, N., Ai, J., Mozafari, M., Milan, P. B., Hamzehlou, S., et al. (2017). Strontium- and cobalt-substituted bioactive glasses seeded with human umbilical cord perivascular cells to promote bone regeneration via enhanced osteogenic and angiogenic activities. *Acta Biomater.* 58, 502–514. doi: 10.1016/j.actbio.2017.06.021

Khalifehzadeh, R., and Arami, H. (2019). DNA-templated strontium-doped calcium phosphate nanoparticles for gene delivery in bone cells. *ACS Biomater. Sci. Eng.* 5, 3201–3211. doi: 10.1021/acsbiomaterials.8b01587

Khorasanian, M., Dehghan, A., Shariat, M. H., Bahrololoom, M. E., and Javadpour, S. (2011). Microstructure and wear resistance of oxide coatings on Ti-6Al-4V produced by plasma electrolytic oxidation in an inexpensive electrolyte. *Surf. Coat. Technol.* 206, 1495–1502. doi: 10.1016/j.surfcoat.2011.09.038

Klymov, A., Song, J., Cai, X., Te Riet, J., Leeuwenburgh, S., Jansen, J. A., et al. (2016). Increased acellular and cellular surface mineralization induced by nanogrooves in combination with a calcium-phosphate coating. *Acta Biomater.* 31, 368–377. doi: 10.1016/j.actbio.2015.11.061

Kurzyp, M., Girard, H. A., Cheref, Y., Brun, E., Sicard-Roselli, C., Saada, S., et al. (2017). Hydroxyl radical production induced by plasma hydrogenated nanodiamonds under X-ray irradiation. *Chem. Commun.* 53, 1237–1240. doi: 10.1039/c6cc08895c

Li, R. Y., Qin, Y. G., Liu, G. C., Zhang, C. X., Liang, H. J., Qing, Y. A., et al. (2017). Tantalum nitride coatings prepared by magnetron sputtering to improve the bioactivity and osteogenic activity for titanium alloy implants. *Rsc Adv.* 7, 55408–55417. doi: 10.1039/c7ra09032c

Liu, X., Xie, Y., Ding, C., and Chu, P. K. (2005). Early apatite deposition and osteoblast growth on plasma-sprayed dicalcium silicate coating. *J. Biomed. Mater. Res. A* 74, 356–365. doi: 10.1002/jbm.a.30273

Lu, H. Z., Yang, C., Luo, X., Ma, H. W., Song, B., Li, Y. Y., et al. (2019). Ultrahigh-performance TiNi shape memory alloy by 4D printing. *Mater. Sci. Eng. A* 763:138166. doi: 10.1016/j.msea.2019.138166

Lu, T., Qiao, Y. Q., and Liu, X. Y. (2012). Surface modification of biomaterials using plasma immersion ion implantation and deposition. *Interface Focus* 2, 325–336. doi: 10.1098/rsfs.2012.0003

Messerle, V. E., Mosse, A. L., and Ustimenko, A. B. (2018). Processing of biomedical waste in plasma gasifier. *Waste Manag.* 79, 791–799. doi: 10.1016/j.wasman.2018.08.048

Nguyen, T. T., Jang, Y. S., Lee, M. H., and Bae, T. S. (2019). Effect of strontium doping on the biocompatibility of calcium phosphate-coated titanium substrates. *J. Appl. Biomater. Funct. Mater.* 17:2280800019826517. doi: 10.1177/2280800019826517

Othman, Z., Fernandes, H., Groot, A. J., Luider, T. M., Alcinesio, A., Pereira, D. D., et al. (2019). The role of ENPP1/PC-1 in osteoinduction by calcium phosphate ceramics. *Biomaterials* 210, 12–24. doi: 10.1016/j.biomaterials.2019.04.021

Peng, S. L., Zhou, G. Q., Luk, K. D. K., Cheung, K. M. C., Li, Z. Y., Lam, W. M., et al. (2009). Strontium promotes osteogenic differentiation of mesenchymal stem cells through the Ras/MAPK signaling pathway. *Cell. Physiol. Biochem.* 23, 165–174. doi: 10.1159/000204105

Petlin, D. G., Tverdokhlebov, S. I., and Anissimov, Y. G. (2017). Plasma treatment as an efficient tool for controlled drug release from polymeric materials: a review. *J. Control. Release* 266, 57–74. doi: 10.1016/j.jconrel.2017.09.023

Pilmane, M., Salma-Ancane, K., Loca, D., Locs, J., and Berzina-Cimdina, L. (2017). Strontium and strontium ranelate: historical review of some of their functions. *Mater. Sci. Eng. C Mater. Biol. Appl.* 78, 1222–1230. doi: 10.1016/j.msec.2017.05.042

Raucci, M. G., Giugliano, D., Alvarez-Perez, M. A., and Ambrosio, L. (2015). Effects on growth and osteogenic differentiation of mesenchymal stem cells by the strontium-added sol-gel hydroxyapatite gel materials. *J. Mater. Sci. Mater. Med.* 26:90.

Saberi, M., Modarres-Sanavy, S. A. M., Zare, R., and Ghomi, H. (2018). Amelioration of photosynthesis and quality of wheat under non-thermal radio frequency plasma treatment. *Sci. Rep.* 8:11655. doi: 10.1038/s41598-018-30200-7

Sathish, S., Ishizu, N., and Shen, A. Q. (2019). Air plasma-enhanced covalent functionalization of poly(methyl methacrylate): high-throughput protein immobilization for miniaturized bioassays. *ACS Appl. Mater. Interfaces* 11, 46350–46360. doi: 10.1021/acsami.9b14631

Thana, P., Wijaikhum, A., Poramapijitwat, P., Kuensaen, C., Meerak, J., Ngamjarurojana, A., et al. (2019). A compact pulse-modulation cold air plasma jet for the inactivation of chronic wound bacteria: development and characterization. *Heliyon* 5:e02455. doi: 10.1016/j.heliyon.2019.e02455

Tsougeni, K., Petrou, P. S., Awsiuk, K., Marzec, M. M., Ioannidis, N., Petrouleas, V., et al. (2015). Direct covalent biomolecule immobilization on plasma-nanotextured chemically stable substrates. *ACS Appl. Mater. Interfaces* 7, 14670–14681. doi: 10.1021/acsami.5b01754

Tsunekawa, S., Aoki, Y., and Habazaki, H. (2011). Two-step plasma electrolytic oxidation of Ti-15V-3Al-3Cr-3Sn for wear-resistant and adhesive coating. *Surf. Coat. Technol.* 205, 4732–4740. doi: 10.1016/j.surfcoat.2011.04.060

Wang, H., Su, K. X., Su, L. Z., Liang, P. P., Ji, P., and Wang, C. (2019). Comparison of 3D-printed porous tantalum and titanium scaffolds on osteointegration and osteogenesis. *Mater. Sci. Eng. C* 104:109908. doi: 10.1016/j.msec.2019.109908

Wang, S., Li, R. Y., Li, D. D., Zhang, Z. Y., Liu, G. C., Liang, H. J., et al. (2018). Fabrication of bioactive 3D printed porous titanium implants with Sr ion-incorporated zeolite coatings for bone ingrowth. *J. Mater. Chem. B* 6, 3254–3261. doi: 10.1039/c8tb00328a

Wang, Z. X., He, Z. Y., Wang, Y. Q., Liu, X. P., and Tang, B. (2011). Microstructure and tribological behaviors of Ti6Al4V alloy treated by plasma Ni alloying. *Appl. Surf. Sci.* 257, 10267–10272. doi: 10.1016/j.apsusc.2011.07.040

Wieland, F., Bruch, R., Bergmann, M., Partel, S., Urban, G. A., and Dincer, C. (2020). Enhanced protein immobilization on polymers-a plasma surface activation study. *Polymers* 12:104. doi: 10.3390/polym12010104

Wong, H. M., Zhao, Y., Tam, V., Wu, S., Chu, P. K., Zheng, Y., et al. (2013). In vivo stimulation of bone formation by aluminum and oxygen plasma surface-modified magnesium implants. *Biomaterials* 34, 9863–9876. doi: 10.1016/j.biomaterials.2013.08.052

Wu, X. M., Itoh, N., Taniguchi, T., Nakanishi, T., and Tanaka, K. (2003). Requirement of calcium and phosphate ions in expression of sodium-dependent vitamin C transporter 2 and osteopontin in MC3T3-E1 osteoblastic cells. *Biochim. Biophys. Acta* 1641, 65–70. doi: 10.1016/s0167-4889(03)00065-x

Yang, F., Yang, D. Z., Tu, J., Zheng, Q. X., Cai, L. T., and Wang, L. P. (2011). Strontium enhances osteogenic differentiation of mesenchymal stem cells and in vivo bone formation by activating Wnt/catenin signaling. *Stem Cells* 29, 981–991. doi: 10.1002/stem.646

Yoo, H. S., Kim, T. G., and Park, T. G. (2009). Surface-functionalized electrospun nanofibers for tissue engineering and drug delivery. *Adv. Drug Deliv. Rev.* 61, 1033–1042. doi: 10.1016/j.addr.2009.07.007

Yoshida, S., Hagiwara, K., Hasebe, T., and Hotta, A. (2013). Surface modification of polymers by plasma treatments for the enhancement of biocompatibility and controlled drug release. *Surf. Coat. Technol.* 233, 99–107. doi: 10.1016/j.surfcoat.2013.02.042

Yu, W. L., Sun, T. W., Qi, C., Ding, Z. Y., Zhao, H. K., Chen, F., et al. (2017). Strontium-doped amorphous calcium phosphate porous microspheres synthesized through a microwave-hydrothermal method using fructose 1,6-bisphosphate as an organic phosphorus source: application in drug delivery and enhanced bone regeneration. *ACS Appl. Mater. Interfaces* 9, 3306–3317. doi: 10.1021/acsami.6b12325

Zhang, J., Barbieri, D., ten Hoopen, H., de Bruijn, J. D., van Blitterswijk, C. A., and Yuan, H. (2015). Microporous calcium phosphate ceramics driving osteogenesis through surface architecture. *J. Biomed. Mater. Res. A* 103, 1188–1199. doi: 10.1002/jbm.a.35272

Zhang, Q., Ma, L., Zheng, S., Wang, Y., Feng, M., Shuai, Y., et al. (2019). Air-plasma treatment promotes bone-like nano-hydroxyapatite formation on protein films for enhanced in vivo osteogenesis. *Biomater. Sci.* 7, 2326–2334. doi: 10.1039/c9bm00020h

Zhang, W., Yang, P., Luo, M., Wang, X., Zhang, T., Chen, W., et al. (2020). Fast oxygen, nitrogen co-functionalization on electrospun lignin-based carbon nanofibers membrane via air plasma for energy storage application. *Int. J. Biol. Macromol.* 143, 434–442. doi: 10.1016/j.ijbiomac.2019.11.237

Zhang, Y., Li, R., Wu, W., Qing, Y., Tang, X., Ye, W., et al. (2018). Adhesion and proliferation of osteoblast-like cells on porous polyetherimide scaffolds. *Biomed Res. Int.* 2018:1491028. doi: 10.1155/2018/1491028

Zhou, Z. F., Sun, T. W., Chen, F., Zuo, D. Q., Wang, H. S., Hua, Y. Q., et al. (2017). Calcium phosphate-phosphorylated adenosine hybrid microspheres for anti-osteosarcoma drug delivery and osteogenic differentiation. *Biomaterials* 121, 1–14. doi: 10.1016/j.biomaterials.2016.12.031

Conflict of Interest: The authors declare that the research was conducted in the absence of any commercial or financial relationships that could be construed as a potential conflict of interest.

frontiers in Materials

ORIGINAL RESEARCH
published: 30 June 2020
doi: 10.3389/fmats.2020.00191

Microstructure and Abrasive Wear Resistance of Mo_2C Doped Binderless Cemented Carbide

Xiuqi Zan[1,2], *Kaihua Shi*[2]*, *Kailin Dong*[2], *Jun Shu*[2] *and Jun Liao*[2]

[1] *State Key Laboratory of Powder Metallurgy, Central South University, Changsha, China,* [2] *Zigong Cemented Carbide Corp, Ltd., Zigong, China*

Binderless cemented carbide contains very little (<0.5 wt.%) or no metal binder and has an incomparable excellent wear resistance, corrosion resistance, excellent polishing, and oxidation resistance compare to traditional cemented carbide (Imasato et al., 1995). For now, many studies were focusing on the influence of Mo/Mo_2C on the microstructure and mechanical properties of traditional cemented carbide (Guo et al., 2008; Wang et al., 2010; Yu et al., 2015). However, to our knowledge, no report was found studying on Mo/Mo_2C added binderless cemented carbide. In this work, a series of binderless cemented carbides with diverse Mo_2C addition amounts (0–6 wt.%) were prepared by sintering and then hot isostatic pressing (HIP) at 2000°C under an isostatic pressure of 70 MPa. The microstructure and abrasive wear resistance of the obtained samples were systemically investigated. The grain size does not change with the increase of Mo_2C addition amount, while the abrasive wear resistance of the cemented carbide increases obviously. The data of the abrasive wear test show the wear volume loss of the cemented carbide reduces from 7.32 to 0.02 $cm^3/10^5r$ when the Mo_2C addition amount change from 0 to 6.0 wt.%. The superior abrasion resistance of samples with higher Mo_2C content and the smoother appearance of the worn surfaces with no definite pullout of grains compared with other samples were result from the forming of (W,Mo)C because of the intermixing between WC and Mo_2C caused by high temperature sintering.

Keywords: microstructure, binderless, cemented carbide, wear, Mo

OPEN ACCESS

Edited by:
Suryanarayana Challapalli,
University of Central Florida,
United States

Reviewed by:
Qiao Yanxin,
Jiangsu University of Science and Technology, China
Dongchan Jang,
Korea Advanced Institute of Science and Technology, South Korea

****Correspondence:***
Kaihua Shi
kaihua_shi@outlook.com

Specialty section:
This article was submitted to Mechanics of Materials, a section of the journal Frontiers in Materials

Received: *11 December 2019*
Accepted: *25 May 2020*
Published: *30 June 2020*

Citation:
Zan X, Shi K, Dong K, Shu J and Liao J (2020) Microstructure and Abrasive Wear Resistance of Mo_2C Doped Binderless Cemented Carbide. Front. Mater. 7:191. doi: 10.3389/fmats.2020.00191

INTRODUCTION

WC-Co cemented carbides have a wide range of industrial applications, being used in cutting tools, forming tools, impact resistant mold, and wear resistant parts due to their exceptionally high hardness, wear resistance, and good toughness (Shi et al., 2014; García et al., 2019). The properties of cemented carbides depend primarily on binding phase content and WC grain size. Typical WC-Co cemented carbides contain less than 30 wt% cobalt, and the WC grain size ranges from submicron levels to a few microns (Wu et al., 2016). The binding phase such as Co is good for fracture toughness and strength increase, but at the same time, it will also reduce the hardness, corrosion resistance, and wear resistance. What's more, because of the different thermal expansion coefficient compare to WC, cobalt may also cause thermal stress, which limits its application in high temperature and harsh conditions (Suzuki, 1986). Therefore, binderless cemented carbide has received growing research attention over recent years.

Binderless cemented carbide has excellent properties such as wear resistance and corrosion resistance etc. due to it's contains very little or no metal binder (Imasato et al., 1995). These advantages ensure it can be used in the production of milling cutter, reamer, high precision mold, water sand tube, fracturing nozzle, glass cutter knife, valves, water cannon, textiles, and tape cutter, etc. (Poetschke et al., 2012). Owing to the high melting point (2870°C) of the WC, a high sintering temperature up to 1700–2000°C should be adopted in order to get high density of non-bonded WC cemented carbide. At present, many sintering methods, such as discharge plasma sintering method, hot pressing method, pressure and pressureless sintering method etc. have been used to produce binderless WC cemented carbides (Zhang et al., 2009; Tsai et al., 2010; Kornaus et al., 2017). In recent years, many researches and exploration have been carried out in the field of binderless WC based cemented carbide, mainly focus on densifying and properties improvement. It was reported that the smaller the average particle size of WC powder is, the higher the hardness and bending strength are (Li and Liu, 2005). Furthermore, the presence of cobalt accelerated the sintering densification process of binderless WC cemented carbide, which also resulted in the obvious anisotropic non-continuous grain growth of WC grains (Zhang et al., 2011).

Mo and Mo_2C added traditional cemented carbides have been studied for many years because Mo has similar structure and properties to that of Yu et al. (2015) studied the effect of Mo content on the microstructure and properties of WC-8-(Fe-Co-Ni) cemented carbide. The results show that the increase of Mo content can reduce the solubility of WC in the liquid phase, so that the grain growth is refined and the hardness of the cemented carbide is significantly improved. Because of the solid solution strengthening of Mo, the bending strength of the cemented carbide is improved. The WC-8(Fe-Co-Ni) cemented carbide get the best comprehensive performance when the Mo content increased to 5 wt%. Wang et al. (2010) studied the effect of Mo addition on the microstructure and properties of WC-2Co cemented carbide. The results show that a small amount of Mo addition can refine WC grains, improve the relative density and hardness of the cemented carbide, but reduce the bending strength of the cemented carbide. When the amount of Mo addition is 2.4 wt%, the microstructure and comprehensive properties of the sample are the best. Guo et al. (2008) studied the effect of Mo_2C on the microstructure and properties of WC-Ti-Ni cemented carbide. The results show that Mo_2C is an effective inhibitor of grain growth. With the increase of Mo_2C addition (0→ 1.2 wt%), the grains of the alloy become finer, the hardness and bending strength increase. In addition, Mo_2C can improve the wettability of bonding phase Ni to WC. Surprisingly, there has been relatively little investigation of the effect of Mo/Mo_2C addition on the microstructure and properties of binderless cemented carbide.

In this work, a series of Non-bond cemented carbide with various Mo_2C doping amounts were prepared using traditional PM route. The effect of Mo_2C doping amount on microstructure and abrasive wear properties of the as-prepared samples were studied.

TABLE 1 | Compositions of WC-0.3Co-xMo_2C samples.

	WC(wt.%)	Co(wt.%)	Mo_2C(wt.%)
Sample 1	99.70	0.30	0
Sample 2	98.50	0.30	1.20
Sample 3	97.30	0.30	2.40
Sample 4	96.10	0.30	3.60
Sample 5	94.90	0.30	4.80
Sample 6	93.70	0.30	6.00

EXPERIMENTAL

In the research, three different analytical reagent grade powders (WC (≈0.4 μm), Mo_2C and Co) were mixed by ball milling to form initial powder mixture. The chemical compositions of the designed samples with different Mo_2C addition amount are given in **Table 1**. In this work, raw powders with a certain weight ratio were mixed in a rolling ball mill machine for 30 h at room temperature, using WC-6 wt%Co (ISO: K20) balls with a diameter of 6.35 mm as grinding media. The ball-to-powder mass ratio was 4:1 and the rotational speed was 80 rpm. Next, the slurry was dried in a 60°C oven for 60 min to obtain the powders for pressing. The powders were then pressed into green compacts with a radius of 25 ± 0.5 mm and rectangular specimens of 57 × 26 × 6 mm in dimension were also pressed for abrasive wear resistance tests.

All the samples were placed on a graphite tray and sintered in a HIP furnace (QIH-15, USA) with the maximum sintering temperature of 2000°C for a dwell time of 90 min. During the maximum sintering temperature, an isostatic pressure of 70 MPa was applied to the samples using Ar.

Microstructural features of the specimens as well as the compositional analysis of certain phases were examined by optical microscopy (Leica DMI 5000 M) and scanning electron microscopy (EVO-18) equipped with an X-Max-20 X-ray energy dispersive spectroscopy (EDS) system. A D/max2550pc X-ray diffractometer was utilized to obtain the X-ray diffraction (XRD) patterns of the as-prepared specimens.

The abrasive wear resistance of the cemented carbide was conducted under wet conditions with Al_2O_3 (particle size: 500–560 μm) and water as the abrasive media at room temperature (20 ± 2°C) using MLS-40 instrument (Shi et al., 2015). The test was done at a load of 196 N and rotation number of 5,000 r. The rotational speed was 120 $r \cdot min^{-1}$.

RESULTS AND DISCUSSION

Microstructure

Figure 1 shows the XRD patterns of the WC-0.3Co-xMo_2C alloys after sintering. The peaks of the six group of samples are similar, which are identified as two main phases corresponding to WC and Mo_2C. However, the Bragg peaks for "WC" of the sintered samples tend to shift toward higher angles with increasing Mo_2C addition amount, as shown in XRD patterns (**Figures 1A,B**). This is mainly because "MoC" and WC have

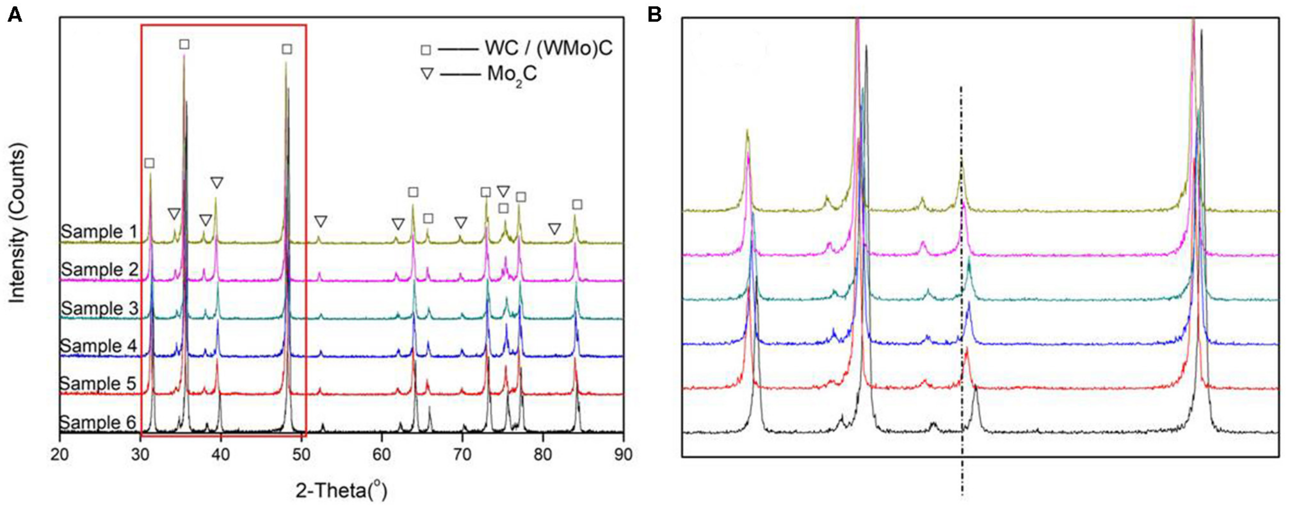

FIGURE 1 | XRD patterns of **(A)** WC-0.3Co-xMo$_2$C alloys after sintering and **(B)** region of interest in **Figure 2**.

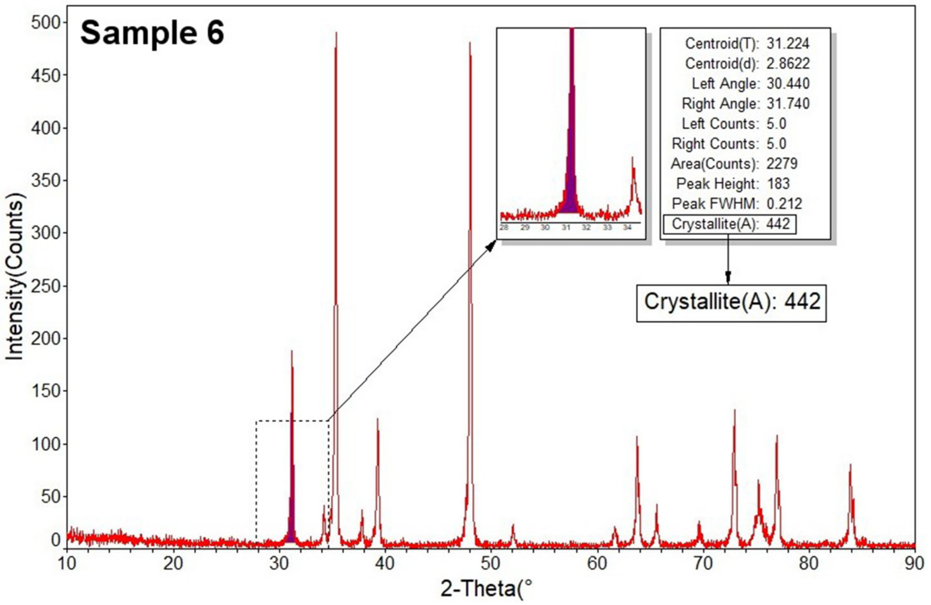

FIGURE 2 | XRD patterns of sample 6 with 6.0 wt.% Mo$_2$C content.

very similar crystallographic structures. A complete range of solid solution exists between WC and "MoC" below 1180°C (Shi et al., 2015). The sintering temperature used in this study is up to 2000°C. A possible reaction path for the formation of mixed WC-Mo$_2$C-C grains could be $Mo_2C+C+WC\rightarrow$ (W,Mo)C (Rudy et al., 1978; Schwarz et al., 2016; Shi et al., 2017). The lattice parameter value "a" of "MoC" is 2.9030 Å, which is lower than that of WC (2.9063 Å). Thus, it seems reasonable that the shifting of "WC" peaks to higher angles is caused by the shrinking lattice.

The XRD results can also be used to evaluate the grain sizes of the samples. **Figure 2** shows the fitting of the peaks in low angle of sample 6, which gives us some information including the WC crystallite dimension. The crystallite WC of other samples was analyzed by this method and the results show that the crystallite WC of all samples is 452, 431, 440, 427, 455, and 442 Å, separately. It means that there is no significant difference between them.

Figures 3A–F shows the SEM images of the polished surfaces of the sintered samples after etching. The images were converted to binary images using a freeware image analysis Image-J (NIH, http://rsb.info.nih.gov/ij/) in order to observe the WC grains' boundaries. For binary images converting, the original images were first opened and convert to 8-bit files. Then threshold values

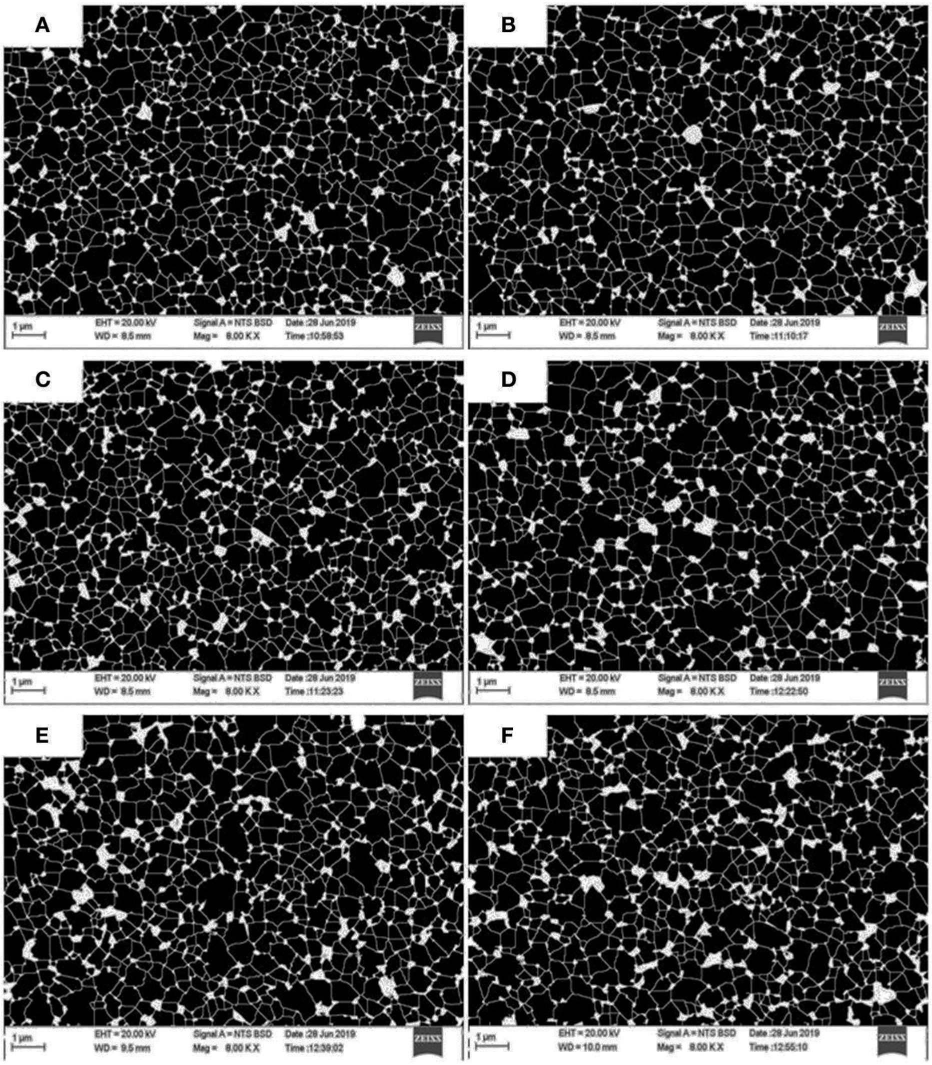

FIGURE 3 | Binary images of the alloys with different Mo_2C addition amount: **(A)** 0% Mo_2C; **(B)** 1.2% Mo_2C; **(C)** 2.4% Mo_2C; **(D)** 3.6% Mo_2C; **(E)** 4.8% Mo_2C; **(F)** 6.0% Mo_2C.

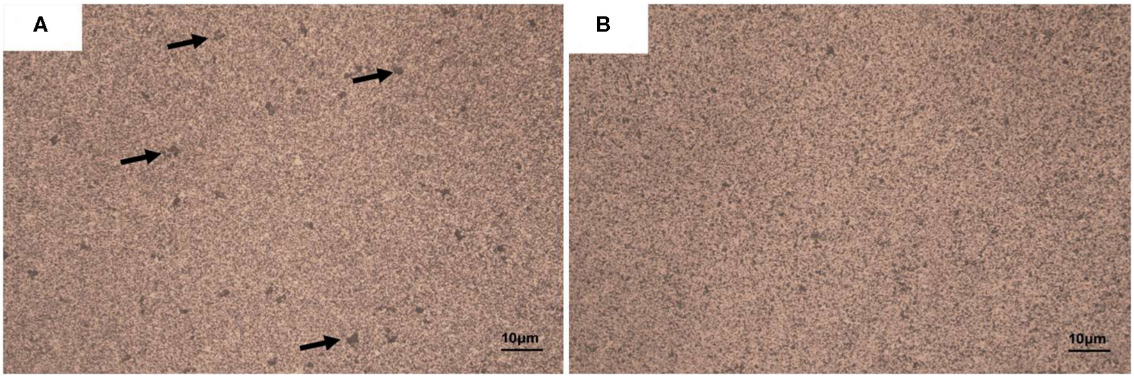

FIGURE 4 | The photomicrographs of the alloys with different Mo_2C addition amount: **(A)** 0% Mo_2C; **(B)** 6.0% Mo_2C.

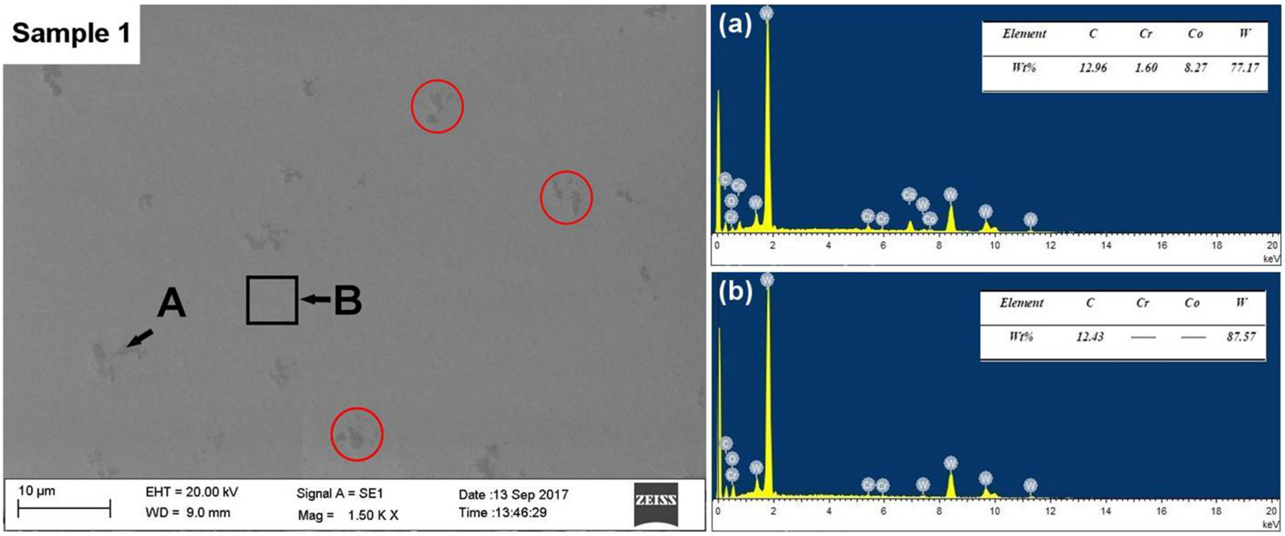

Element	C	Cr	Co	W
Wt%	12.96	1.60	8.27	77.17

Element	C	Cr	Co	W
Wt%	12.43	—	—	87.57

FIGURE 5 | SEM microstructure and EDX results of certain areas on the polished surface of sample 1: **(a)** Point A; **(b)** Area B.

were determined empirically by selecting a setting, which gave the most accurate binary image for analysis. Watershed was chosen for processing to get the final images with clear grain boundaries. As shown in the pictures, there is no significant difference of WC grains size between the samples with different Mo_2C content. This indicates that Mo_2C has little effect on WC grain growth in binderless cemented carbide under the adopted HIP sintering process parameters.

There are two theories about the effect of Mo_2C as a WC grain growth inhibitor. One is that Mo_2C acts a barrier to the WC growth because Mo_2C might precipitate in the WC grains interface. Therefore, it is difficult for WC grains to grow to incorporate those Mo_2C impurity atoms (Bosio et al., 2018). Nevertheless, according to the discussion about solid solution between molybdenum carbide and tungsten carbide earlier in this paper, it is reasonable that a reaction of mixed WC-Mo_2C-C grains exists. Therefore, this theory is not suitable for this study. The other theory is based on WC grain abnormal growth mechanism. Morton et al. (2005) reported that WC grain abnormal growth occurs during liquid phase sintering due to re-precipitations of the small WC dispersed in Co on the large solid WC grains (Ostwald ripening). The main driving force of the mentioned phenomenon is mainly the reduction in surface energy of the solid particles during sintering. Many reports (Kang et al., 2002; Morton et al., 2005; Fang et al., 2009; Zhao et al., 2015) believed that Mo_2C dissolves in binder phase can restrain the dissolution and re-precipitation of WC in binder phase during liquid phase sintering process, thus inhibit the individual growth of WC grains. If there is limit binder phase, the effect of Mo_2C on WC individual grain growth may be not significant, which is the case of this study.

Figures 4A,B show the photomicrographs of the sintered samples with 0 and 6.0 wt.% Mo_2C content, separately. Bright areas correspond to WC. Both of the alloys contain "dark areas" look like large pores (see arrows in **Figure 4A**). Meanwhile, the size and quantity of the "dark areas" decrease with the Mo_2C content increasing. In order to find out the morphology and chemical composition of the "dark areas," SEM and EDS are employed for the analysis of the chemical composition at fixed points on the polished surface of the alloy, and the results of sample 1 (other results of the samples are similar) are shown in **Figures 5a,b**.

From **Figure 5**, it can be ensured that the "dark areas" are not pores but liquid phase concentration. The EDX result of the "dark area" of sample 1 in **Figure 5** indicates that the area contains mainly Co and some elements dissolve in it. The size of the "dark areas" in **Figures 4A,B** decreases as Mo_2C content increasing, which means that the Co distribution becomes more uniform in the sample. This is because that after addition of Mo_2C, Mo dissolved in liquid Co and reduced wetting angle, thereby improving the wettability of Co relative to the WC phase (Balbino et al., 2017).

Abrasion Resistance

Figures 6, **7** show the images of the sample surface after abrasive wear testing, and their representative cross-section profile of worn surface, separately. According to **Figure 6**, the morphology of the wear scratches in sample 1∼4 are consist of many narrow grooves, while those of sample 5 and 6 are almost flat. It is obviously that the wear area of the samples decreasing against Mo_2C content increases. This change indicates that Mo_2C addition amount is a primary factor in the abrasive wear behavior of the samples. The morphology details of the wear scratches including width and depth of the samples are shown in cross-section profiles in **Figures 7A–F**. The difference between them is obvious in the images where the depth of the scratch of sample 1 with 0 wt.% Mo_2C addition is more than 0.5 mm, which is much deeper than that of other samples. For sample 5 with 4.8 wt.%

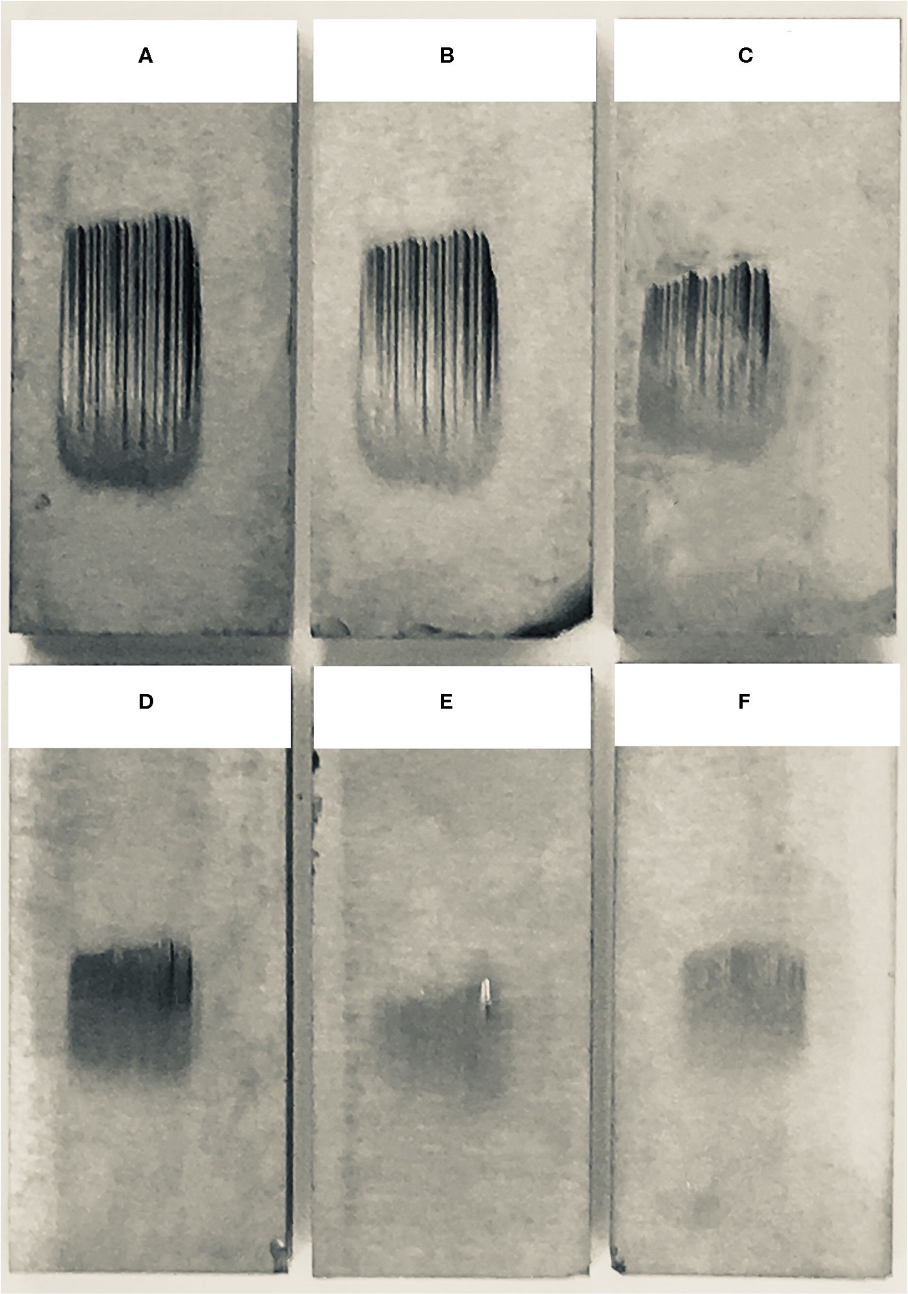

FIGURE 6 | Photos of the alloys with different Mo_2C addition amount after abrasive wear testing: **(A)** 0% Mo_2C; **(B)** 1.2% Mo_2C; **(C)** 2.4% Mo_2C; **(D)** 3.6% Mo_2C; **(E)** 4.8% Mo_2C; **(F)** 6.0% Mo_2C.

Mo_2C, the depth of scratch significantly decreases from 0.25 mm to ∼0.05 mm in comparison to sample 3 with 2.4 wt.% Mo_2C content. In sample 6 (**Figure 6F**), it can be seen that it is hard to obtain the cross-section profile because of the slight wear scratch result from the maximum Mo_2C addition amount (6.0 wt.%) in the sample.

The wear volume loss of different samples is shown in **Figure 8**. It can be seen in the picture that the wear volume tends to decrease with the Mo_2C content which is in accordance with the images in **Figures 6**, **7**. The wear volume loss decreases from 7.32 $cm^3/10^5 \cdot r$ for sample 1 to 0.04 $cm^3/10^5 \cdot r$ for sample 5 with 4.8 wt.% Mo_2C. However, the wear volume loss of the sample 6 containing 6.0 wt.% Mo_2C decreases slightly to 0.02 $cm^3/10^5 \cdot r$.

The SEM images of surface scratches of all the samples at low and high magnification are shown in **Figures 9A–F**. It is well-known that the wear resistance is usually determined in accordance with the wear mechanisms, which can be identified the worn surfaces analysis. Wear behavior in homogeneous

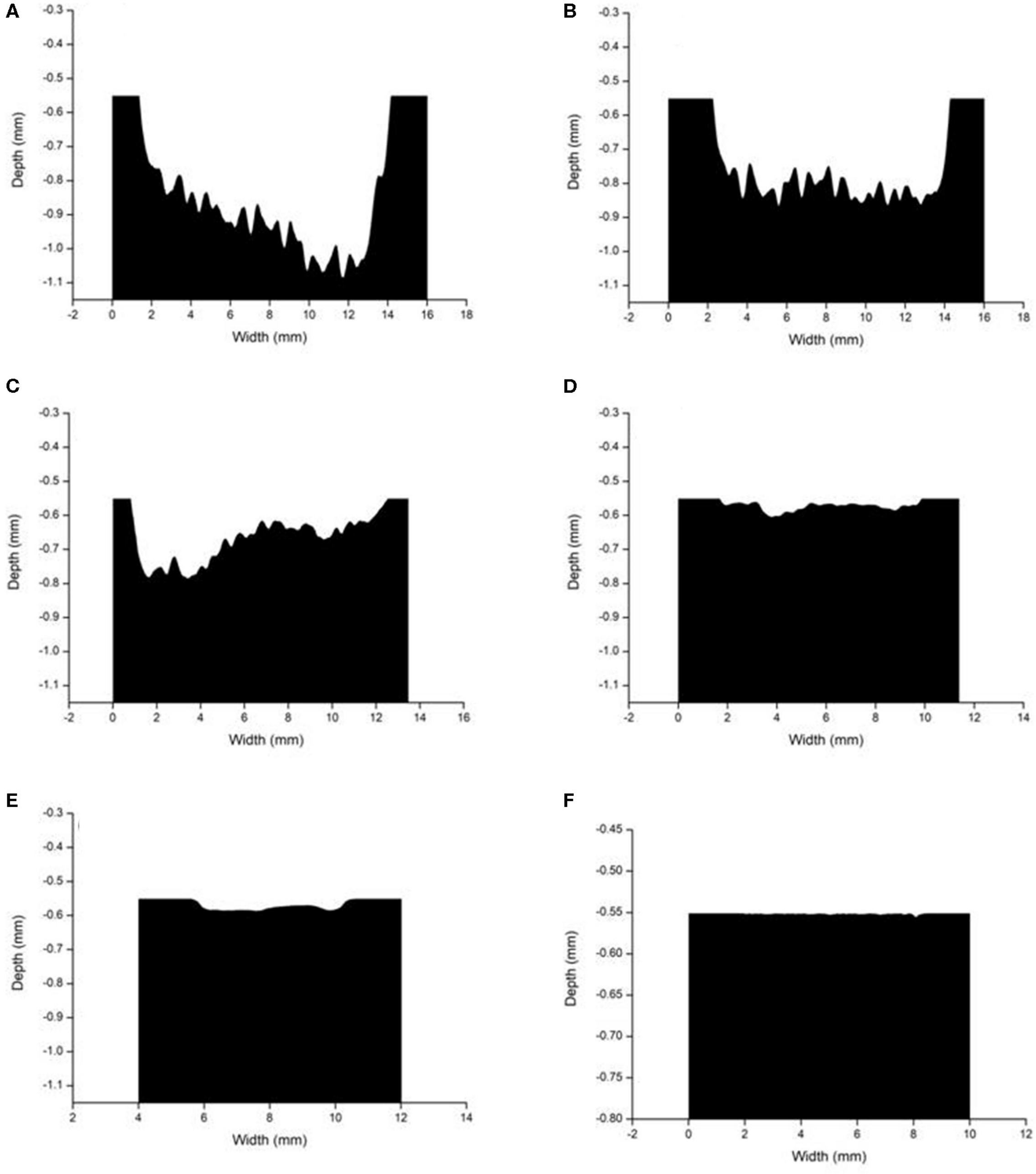

FIGURE 7 | Cross profiles of the samples' worn surfaces with different Mo_2C addition amount: **(A)** 0% Mo_2C; **(B)** 1.2% Mo_2C; **(C)** 2.4% Mo_2C; **(D)** 3.6% Mo_2C; **(E)** 4.8% Mo_2C; **(F)** 6.0% Mo_2C.

materials can be explained by adhesion, plastic deformation, delamination, plowing, microcracks, grain fragmentation and pull-out etc., and is dependent on their chemical and physical properties (Suh et al., 2008; Lee et al., 2010; Wang et al., 2010, 2018). In the abrasive wear testing process, several complex wear mechanisms may exist at the same time. **Figures 9A–D** shows the scratches images of samples with less Mo_2C content. Plowing and pullout of entire WC grains can be observed obviously in high magnification images in **Figure 9**. With Mo_2C content increasing from 4.8 to 6.0 wt.% in **Figures 9E,F**, the plowing and WC grain spalling gradually disappears. The worn surface presented a smooth wear track with no apparent damage in **Figures 9E,F**, which means that the wear behaviors of sample with 6.0 wt.% Mo_2C content is consistent with the mild wear regime, which explained little wear volume loss in **Figure 8**.

Mo_2C addition can improve the wettability of Co relative to the WC phase, strengthen grain boundaries and phase boundaries (Zhang et al., 2011), thus avoid grain fragmentation

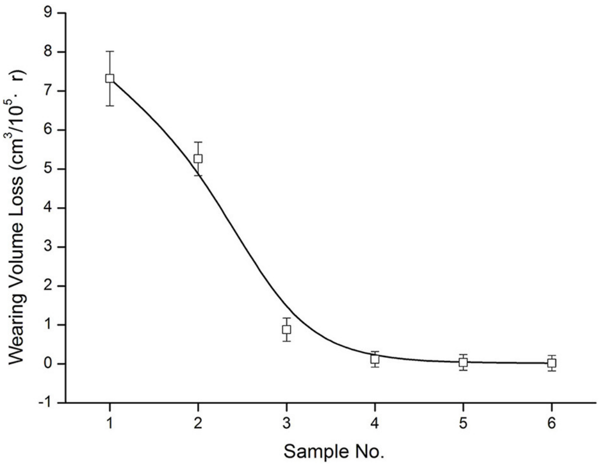

FIGURE 8 | Relationship of wearing volume loss against Mo_2C content:(1) 0% Mo_2C; (2) 1.2% Mo_2C; (3) 2.4% Mo_2C; (4) 3.6% Mo_2C; (5) 4.8% Mo_2C; (6) 6.0% Mo_2C.

and pull-out to some extent and enhance the wear resistance. According to the discussion of the foregoing, the liquid phase concentration in the sample decreases because Co distribution becomes more uniform as Mo_2C content increasing, thereby improving the binding force between WC and Co. However, it seems that this cannot be the only reason of the superior abrasion resistance of the samples with higher Mo_2C content because there is limit binder phase in all the samples.

It has been discussed earlier in this paper that the forming of (W,Mo)C due to the intermixing between Mo and W carbides when sintering at a high temperature is high due to the very similar crystallographic structures of WC-"MoC" and W_2C-Mo_2C (Shi et al., 2015). The superior abrasion resistance and smoother worn surfaces with less pullout of grains of samples with higher Mo_2C content are mainly result from the better grain boundaries due to the intermixing between Mo and W carbides (Engqvist et al., 2000). The wear volume loss results also show that binderless carbides with higher Mo_2C content have lower wear rate among the samples. According to previous study (Su et al., 2019), the bonding between the WC grains is the dominant

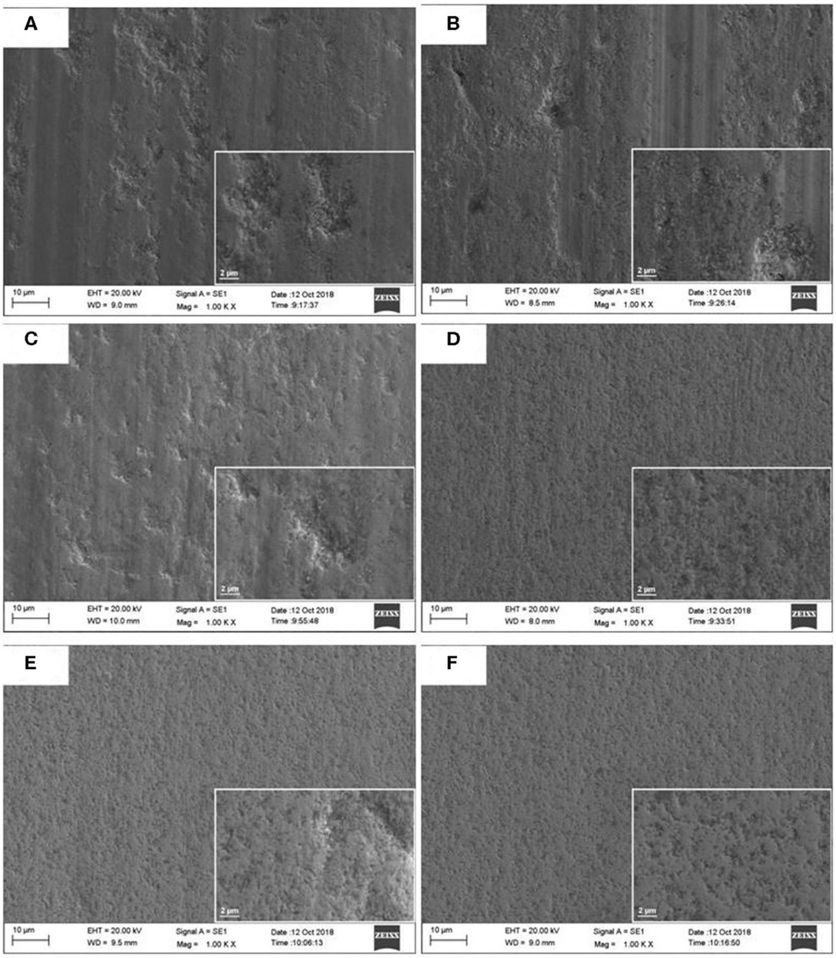

FIGURE 9 | SEM microstructures at low and high magnification of wear areas of the alloys with different Mo_2C addition amount (on the lower right of the figures are SEM images at 5000 times magnification): **(A)** 0% Mo_2C; **(B)** 1.2% Mo_2C; **(C)** 2.4% Mo_2C; **(D)** 3.6% Mo_2C; **(E)** 4.8% Mo_2C; **(F)** 6.0% Mo_2C.

factor of wear results of the binderless carbides. In this study, sample with 6.0 wt% Mo_2C is the best candidate due to its good WC-WC grains bonding.

CONCLUSIONS

In this paper, the effects of a small amount of Mo_2C on the microstructure and abrasion wear resistance properties of binderless cemented carbides were investigated. The results show that the addition of 1.2∼6.0 wt.% Mo_2C has little effect on WC grain growth because only 0.3% binder phase in the samples. The addition of Mo_2C could decrease the size of cobalt pool formation in the sample and promote the uniform distribution of binder phase. Moreover, the volume loss, cross-section profiles and the surface scratches show the abrasion resistances of the binderless cemented carbides with higher Mo_2C addition amount are superior to those of cemented carbides without or with less Mo_2C addition. This may result from the forming of (W,Mo)C due to the intermixing between WC and Mo_2C after sintering at a high temperature due to the very similar crystallographic structures of Mo and W carbides. In consequence, the cemented carbide has more wear-resistant because of the better grain boundaries caused by WC-"MoC" and W_2C-Mo_2C intermixing.

DATA AVAILABILITY STATEMENT

The raw data supporting the conclusions of this article will be made available by the authors, without undue reservation, to any qualified researcher.

AUTHOR CONTRIBUTIONS

KS, XZ, and KD were work together on the experiment. JS and JL gave help on the microstructure observation and properties testing. XZ and KS wrote this manuscript together. All authors contributed to the article and approved the submitted version.

REFERENCES

Balbino, N. A. N., Correa, E. O., Valeriano, L. C., and Amâncio, D. A. (2017). Microstructure and mechanical properties of 90WC-8Ni-2Mo_2C cemented carbide developed by conventional powder metallurgy. *Int. J. Refract. Metals Hard Mater.* 68, 49–53. doi: 10.1016/j.ijrmhm.2017.06.009

Bosio, F., Bassini, E., Oñate Salazar, C. G., Ugues, D., and Peila, D. (2018). The influence of microstructure on abrasive wear resistance of selected cemented carbide grades operating as cutting tools in dry and foam conditioned soil. *Wear* 394–395, 203–216. doi: 10.1016/j.wear.2017.11.002

Engqvist, H., Botton, G. A., Axe'n, N., and Hogmark, S. (2000). Microstructure and abrasive wear of binderless carbides. *J. Am. Ceram. Soc.* 83, 2491–2496. doi: 10.1111/j.1151-2916.2000.tb01580.x

Fang, Z. Z., Wang, X., Ryu, T., Hwang, K. S., and Sohn, H. Y. (2009). Synthesis, sintering, and mechanical properties of nanocrystalline cemented tungsten carbide e a review. *Int. J. Refract. Metals Hard Mater.* 27, 288–299. doi: 10.1016/j.ijrmhm.2008.07.011

García, J., Ciprés, V., C., Blomqvist, A., and Kaplan, B. (2019). Cemented carbide microstructures: a review. *Int. J. Refract. Metals Hard Mater.* 80, 40–68. doi: 10.1016/j.ijrmhm.2018.12.004

Guo, Z. X., Xiong, J., Yang, M., Song, X. Y., and Jiang, C. J. (2008). Effect of Mo_2C on the microstructure and properties of WC–TiC–Ni cemented carbide. *Int. J. Refract. Metals Hard Mater.* 26, 601–605. doi: 10.1016/j.ijrmhm.2008.01.007

Imasato, S., Tokumoto, K., and Kitada, T. (1995). Properties of urtra-fine grain binderless cemented carbide 'RCCFN'. *Int. J. Refract. Metals Hard Mater.* 13, 305–312. doi: 10.1016/0263-4368(95)92676-B

Kang, M. K., Kim, D. Y., and Hwang, N. M. (2002). Ostwald ripening kinetics of angular grains dispersed in a liquid phase by two-dimensional nucleation and abnormal grain growth. *J. Eur. Ceram. Soc.* 22, 603–612. doi: 10.1016/S0955-2219(01)00370-3

Kornaus, K., Raczka, M., Gubernat, A., and Zientara, D. (2017). Pressureless sintering of binderless tungsten carbide. *J. Eur. Ceram. Soc.* 37, 4567–4576. doi: 10.1016/j.jeurceramsoc.2017.06.008

Lee, C. W., Han, H. J., Yoon, J., Shin, M. C., and Kwun, S. I. (2010). A study on powder mixing for high fracture toughness and wear resistance of WC-Co-Cr coatings sprayed by HVOF. *Surf. Coat. Tech.* 204, 2223–2229. doi: 10.1016/j.surfcoat.2009.12.014

Li, R. Q., and Liu, T. M. (2005). Effects of processing parameters on the properties of Non-bond Cemented Carbide. *Cement. Carbide* 22, 23–26. doi: 10.3969/j.issn.1003-7292.2005.01.006

Morton, C. W., Wills, D. J., and Stjernberg, K. (2005). The temperature ranges for maximum effectiveness of grain growth inhibitors in WC-Co alloys. *Int. J. Refract. Metals Hard Mater.* 23, 287–293. doi: 10.1016/j.ijrmhm.2005.05.011

Poetschke, J., Richter, V., and Holke, R. (2012). Influence and effectivity of VC and Cr3C2 grain growth inhibitors on sintering of binderless tungsten carbide. *Int. J. Refract. Metals Hard Mater.* 31, 218–223. doi: 10.1016/j.ijrmhm.2011.11.006

Rudy, E., Kieffer, B. F., and Baroch, E. (1978). HfN coatings for cemented carbides and new hard-facing alloys on the basis (Mo,W)C–$(Mo,W)_2C$. *Planseeber Pulvermetall.* 26, 105–115.

Schwarz, V., Shi, K., and Lengauer, W. (2016). *Metallurgy and Properties of Mo-doped WC-Co and (W,Mo)C-Co Hardmetals*. Hamburg: WorldPM.

Shi, K., Schwarz, V., and Lengauer, W. (2017). "Preparation and properties of (W,Mo)C powders and (W,Mo)C-Co cemented carbides," in *19th Plansee Seminar* (Reutte).

Shi, K., Zhou, K., Li, Z., and Zan, X. (2014). Optimization of initial WC grain-size distribution in WC-6Ni cemented carbides. *J. Mater. Eng. Perform.* 23, 3222–3228. doi: 10.1007/s11665-014-1117-2

Shi, K., Zhou, K., Li, Z., Zan, X. Q., Dong, K. L., and Jiang, Q. (2015). Microstructure and properties of ultrafine WC–Co–VC cemented carbides with different Co contents. *Rare Metals*. doi: 10.1007/s12598-014-0424-y. [Epub ahead of print].

Su, Q. D., Zhu, S. G., Ding, H., Bai, Y. F., and Di, P. (2019). Comparison of the wear behaviors of advanced and conventional cemented tungsten carbides. *Int. J. Refract. Metals Hard Mater.* 79, 18–22. doi: 10.1016/j.ijrmhm.2018.10.019

Suh, M. S., Chae, Y. H., and Kim, S. S. (2008). Friction and wear behavior of structural ceramics sliding against zirconia. *Wear* 264, 800–806. doi: 10.1016/j.wear.2006.12.079

Suzuki, H. (1986). *Cemented Carbide and Sintered Hard Materials*. Tokyo: Maruzen Publishing Company.

Tsai, K. M., Hsieh, C. Y., and Lu, H. H. (2010). Sintering of binderless tungsten carbide. *Ceram. Int.* 36, 689–692. doi: 10.1016/j.ceramint.2009.10.017

Wang, H. B., Hou, C., Liu, X. M., Liu, X. W., and Song, X. Y. (2018). Wear resistance mechanisms of near-nanostructured WC-Co coatings. *Int. J. Refract. Metals Hard Mater.* 71, 122–128. doi: 10.1016/j.ijrmhm.2017.11.013

Wang, L. L., Li, H. Y., and Liu, N. (2010). Effect of Mo addition on microstructure and mechanical property of WC-Co-based carbides. *Rare Metals Cemen. Carb.* 38, 31–35. doi: 10.3969/j.issn.1004-0536.2010.02.008

Wu, C. C., Chang, S. H., Tang, T. P., Peng, K. Y., and Chang, W. C. (2016). Study on the properties of WC-10Co alloys adding Cr_3C_2 powder via various vacuum sintering temperatures. *J. Alloys Compd.* 686, 810–815. doi: 10.1016/j.jallcom.2016.06.221

Yu, J. M., Feng, X., and Lu, L. (2015). Effect of molybdenum content on structure and properties of WC-8(Fe-Co-Ni) cemented carbide. *Jiangxi Sci.* 33, 888–893. doi: 10.13990/j.issn1001-3679.2015.06.023

Zhang, J., Zhang, G., Zhao, S., and Song, X. (2009). Binder-free WC bulk synthesized by spark plasma sintering. *J. Alloys Compd.* 479, 427–431. doi: 10.1016/j.jallcom.2008.12.151

Zhang, L., Chen, S., and Huang, F. J. (2011). Effects of small amount of cobalt addition on densification and WC grain growth during sintering of binderless cemented tungsten carbide. *Cement. Carbide* 28, 271–275. doi: 10.3969/j.issn.1003-7292.2011.05.001

Zhao, Z. Y., Liu, J. W., Tang, H. G., Ma, X. F., and Zhao, W. (2015). Effect of Mo addition on the microstructure and properties of WCeNieFe hard alloys. *J. Alloys Compd.* 646, 155–160. doi: 10.1016/j.jallcom.2015.05.277

Conflict of Interest: The authors declare that the research was conducted in the absence of any commercial or financial relationships that could be construed as a potential conflict of interest.

frontiers
in Materials

REVIEW
published: 31 July 2020
doi: 10.3389/fmats.2020.00247

Powder Metallurgy: An Alternative for FeMnSiCrNi Shape Memory Alloys Processing

Bogdan Pricop[1], Ahmet U. Söyler[2,3], Burak Özkal[3] and Leandru G. Bujoreanu[1]*

[1] Gheorghe Asachi Technical University of Iaşi, Iaşi, Romania, [2] TETA Glass Technologies, Istanbul, Turkey, [3] Istanbul Technical University, Istanbul, Turkey

In the case of quintenary Fe-Mn-Si-Cr-Ni shape memory alloys (SMAs), ingot metallurgy (IM) has technological shortcomings concerning compositional segregation, imperfect melt-incorporation of Si, demanganization during heating and cooling-induced cracking, which can be effectively surmounted by combining powder metallurgy (PM) with mechanical alloying (MA). The paper reviews the results reported in the processing and characterization of PM-MA'ed FeMnSiCrNi SMAs, with special emphasis on the findings obtained by present authors in the last decade. Specimens with nominal chemical compositions Fe-18Mn-3Si-7Cr-4Ni and Fe-14Mn-6Si-9Cr-5Ni (mass %) were produced by IM and PM. In the latter case various volume fractions of as-blended powders were MA'ed under protective atmosphere, before being pressed and sintered. Further compacting, up to 5% porosity degrees, was achieved by hot rolling. Structural analysis, performed by X-ray diffraction and scanning electron microscopy, revealed the formation of unusually large amounts of α'-body centred cubic (bcc) thermally induced martensite. This undesirable martensite seemed to be destabilized by tensile pre-straining, and enabled PM specimens to reach higher stresses than IM ones. The formation and accumulation of α'-bcc stress induced martensite was enhanced by tensile pre-straining, mechanical cycling and augmentation of MA'ed powder fraction. It has been argued that the optimization of technological processing parameters of heat treatment (HT) and hot rolling (HR) combined with MA'ed powder fraction caused the augmentation of shape memory effect (SME) magnitude. DMA-temperature scans revealed an increasing tendency of internal friction ($\tan\delta$) with MA'ed powder fraction, as well as the presence of two $\tan\delta$ maxima ascribed to antiferromagnetic-paramagnetic transition and martensite reversion to austenite, respectively. DMA-strain sweeps emphasized the occurrence of a plateau on the storage modulus vs. strain amplitude variation which was associated with stress-induced formation of ε hexagonal close-packed (hcp)-martensite. In spite of large α'-bcc amounts, PM-MA'ed Fe-14Mn-6Si-9Cr-5Ni experienced free-recovery SME which was enhanced by thermomechanical training. Coupling rings, meant to connect vibrating pipes that transport turbulent fluids, being able to mitigate vibrations that could accidentally open the connection, were manufactured and tested.

Keywords: Fe-Mn-Si alloys, martensite, mechanical alloying, internal friction, coupling ring

OPEN ACCESS

Edited by:
Chao Yang,
South China University of Technology, China

Reviewed by:
Chenglin Li,
Wuhan University, China
Laima Luo,
Hefei University of Technology, China

****Correspondence:***
Leandru G. Bujoreanu
lgbujor@tuiasi.ro

Specialty section:
This article was submitted to Mechanics of Materials, a section of the journal Frontiers in Materials

Received: *07 May 2020*
Accepted: *07 July 2020*
Published: *31 July 2020*

Citation:
Pricop B, Söyler AU, Özkal B and Bujoreanu LG (2020) Powder Metallurgy: An Alternative for FeMnSiCrNi Shape Memory Alloys Processing. Front. Mater. 7:247. doi: 10.3389/fmats.2020.00247

INTRODUCTION

Amongst Intelligent Materials, Shape Memory Alloys (SMAs) form a distinctive group able to restore their original shape by heating or magnetic field application (Ma and Karaman, 2010). Within SMAs class, NiTi-based, CuZn-based, CuAl-based and FeMnSi-based alloys have become of commercial use (Sun et al., 2012). The interest for FeMnSi-based SMAs is due to their lower price, better workability and the perspective to take advantage of the technological development of iron working industry (Dunne, 2012). In FeMnSi-based SMAs, the occurrence of free-recovery shape memory effect (SME) is due to the thermally induced reversion to γ (face centered cubic, fcc) austenite of stress-induced ε (hexagonal close-packed, hcp) martensite (Kajiwara, 1999). Besides ε – hcp, α′ (body centered cubic, bcc) martensite can be generated by cooling, at low Mn amount (Bracke et al., 2006) or by applying high stress levels, where it is stress-induced at the intersection ε plates (Arruda et al., 1999). α′-bcc occurrence is considered as detrimental for the magnitude of SME (Li et al., 2000).

The history of FeMnSi-based SMAs begun in 1982, with the report of SME occurrence in the single crystals of Fe-30Mn-1Si (mass %, as hereinafter, throughout the text) (Sato et al., 1982). The development of polycrystalline alloys was reported 5 years later by Murakami et al. who: (i) discussed the role of Si in reducing the temperature of antiferromagnetic-paramagnetic transition (Murakami et al., 1987c); (ii) obtained a good SME value (above 50%) in the composition range Fe-(28.34) Mn-(4–6.5) Si (Murakami et al., 1987b) and (iii) improved the SME of Fe-32Mn-6Si by means of a combination of pre-strain and heat treatment (Murakami et al., 1987a). In the subsequent 3–4 years, corrosion resistance was improved owing to the benefits of Cr and Ni additions and thus two FeMnSi-based SMA grades were developed in the commercial field: Fe-28Mn-6Si-5Cr (Otsuka et al., 1990) and Fe-l4Mn-6Si-9Cr-5Ni (Moriya et al., 1991).

One of the main drawbacks of FeMnSi-based SMAs was their recoverable strains limited to 5%, even after the application of suitable "training" thermomechanical processing (Stanford et al., 2008) and various attempts, the mentioning of which is beyond the purpose of this paper, were done in order to increase these values. A series of successful results were remarkably obtained through suppressing the formation of the twin boundaries (Wen et al., 2014), associated with austenitic grain coarsening (Peng et al., 2017), which enabled "giant" tensile recoverable strains (Peng et al., 2018) of the order of 7.6–7.7%.

The most prominent practical applications of Fe-Mn-Si-based SMAs include lock rings for bicycle frame pipes (Otsuka, 1991), pipe coupling rings (Druker et al., 2014), fishplates for crane rail fastening (Maruyama et al., 2008), concrete pre-straining rods (Sawaguchi et al., 2006) and embedded stripes for concrete beam curvature control (Shahverdi et al., 2016). More recently, truncated cone modules, produced by high speed – high pressure torsion, were proposed for self-adjustable axial preloading of angular contact bearings (Paleu et al., 2018).

All the above mentioned results were obtained on FeMnSi-based alloy samples produced by ingot metallurgy (IM), comprising melt casting, multiple remelting to achieve the target chemical composition, heat treatment prolonging to homogenize the chemical composition, and slow cooling to avoid contraction cracking (Berns and Theisen, 2008).

As recently pointed out, powder metallurgy (P/M) associated with mechanical alloying (MA), are prone to control both the chemical composition and grain size (Dang et al., 2019), achieving near-final forming parts (Bahador et al., 2020), as well as to minimize secondary processing, thus reducing the amount of generated waste (Aydogmus and Bor, 2011). Nevertheless, as compared to other alloy systems, such as NiTi-based (Bahador et al., 2017) or Cu-based SMA (Mazzer et al., 2017), only few reports exist on the preparation of Fe-Mn-Si-based SMA by P/M-MA processing.

It has been argued that, in spite of the potential embrittlement caused by pores (Xu et al., 2015), applying P/M-MA at FeMnSi-based SMAs enabled an accurate control of chemical composition (Zhang et al., 2003), especially at quintenary Fe-Mn-Si-Cr-Ni SMAs where most of crystal faults were eliminated (He et al., 2006). Moreover, P/M-MA enhanced the solubility of alloying elements into Fe matrix (Liu et al., 1999), reduced the oxide formation tendency (Oro et al., 2014), assisted the occurrence of ε-hcp martensite (Saito et al., 2014) and increased the density of the alloy (Xu et al., 2016).

As opposed to the above mentioned reports, the present authors separately initiated the research-development of P/M-MA'ed FeMnSiCrNi SMAs more than 10 years ago, the first results being communicated at ESOMAT 2009, Prague (Bujoreanu et al., 2009). The present review mainly summarizes the results reported by present authors during the past decade.

PROCESSING PROCEDURES AND STRUCTURE OF P/M-MA'ed FeMnSiCrNi SMAs

The preparation of prealloyed powders is possible via advanced atomization technics. Compared to the variety of elemental powders, in the market only a few specific composition having commercial importance are available as masteralloy or prealloyed forms offered by powder producers. Same scarceness is true for SMA compositions and therefore many researchers who chose to study P/M route, applied mechanical milling or mechanical alloying (MA) methodology to obtain a powdered material having desired composition in nearly almost each of its particles. Indeed, it is obvious that mechanical alloying is quite logical in order to attain shorter diffusion distances between the constituting elements compared to their elemental powder mixture case.

For fabricating Fe–20Mn–6Si–9Cr alloy powders, it was found that the optimum ball-milling time, at 300 rpm, was 20 h (Dogan and Arslan, 2012). The present authors studied the effect of MA time, up to 8 h for Fe-14Mn-6Si-9Cr-5Ni, using stainless steels milling media in a SPEX-D8000 high energy ball mill at 1,200 rpm. In addition to powder state properties, compatibility and sinterability of these powders were studied and it was concluded that 4 h MA time is optimum since green and sintered densities of the powders started to decreased after this point

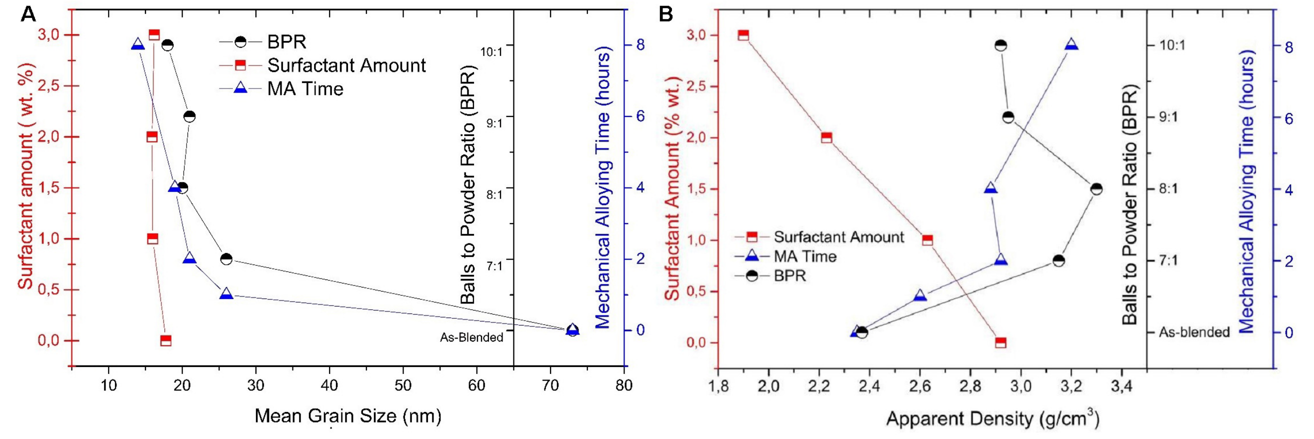

FIGURE 1 | Effect of ball to powder ratio (BPR), surfactant amount and mechanical alloying time on **(A)** mean grain size, **(B)** apparent density (modified after Söyler et al., 2010, 2011).

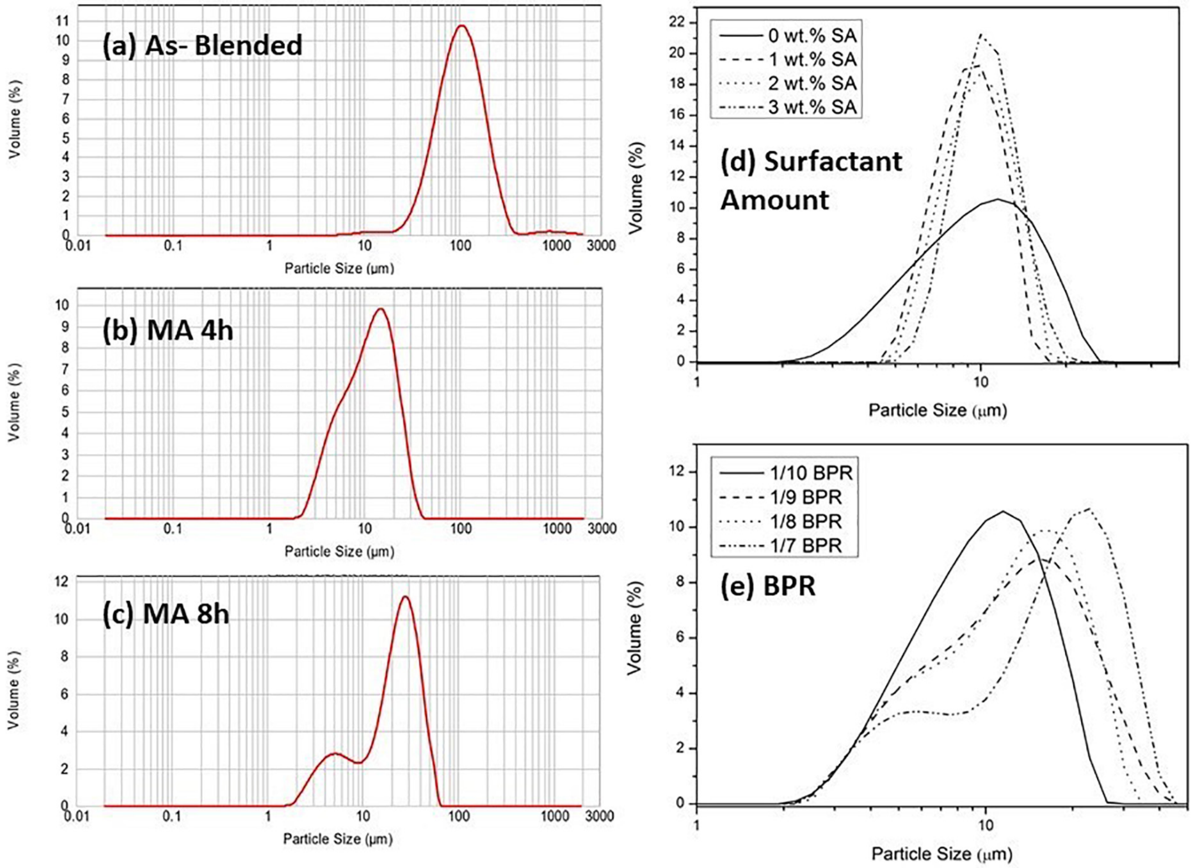

FIGURE 2 | Particle size analysis as a function of MA parameters: **(a)** As-blended powders (MA 0 h), **(b)** MA 4 h, **(c)** MA 8 h, **(d)** surfactant amount and **(e)** ball to powder ratio (BPR) (modified after Söyler et al., 2010, 2011).

(Söyler et al., 2010). The effects of ball to powder ratio (BPR), within 10:1 to 7:1 range and amount of surfactant (stearic acid, SA), between 0 and 3% range, were also studied for Fe-14Mn-6Si-9Cr-5Ni, at constant MA time of 4 h (Söyler et al., 2011).

The effect of BPR, surfactant amount and MA time are shown against mean grain size, as calculated from XRD, in **Figure 1A**. Grain size values decreased with increasing BPR and MA time, but a slight increase is observed with the use of surfactant

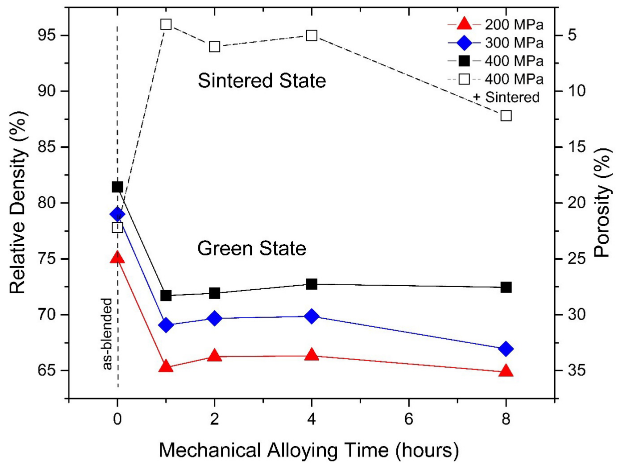

FIGURE 3 | Relative density and retained porosity values of the samples after compaction (green state) and after sintering (modified after Söyler et al., 2010).

and with the increase of surfactant amount. The effect of these parameters on apparent density of the powders is shown in **Figure 1B**. While increasing the amount of SA led to a steady decrease for apparent density values, higher BPR and longer MA time led to increase, as compared to the apparent density of as-blended case. Overall effects of these parameters on particle size distributions of the mechanical alloyed powders are also summarized in **Figure 2**. As compared to as-blended case, finer particle sizes are obtained with increasing MA time **Figures 2a–c**. Compared to initial particle size distribution of processed powders without surfactant addition, the use of surfactant and the increase of the surfactant amount led to narrower particle size distributions (**Figure 2d**). Also increasing BPR during MA seems useful for obtaining finer particle sizes without changing the general particle size distribution trends.

For reaching desired level of microstructural homogenization during MA, many parameters should be adjusted in order to maximize the energy input to be delivered to the powders and to minimize the processing time. It is also obvious from the upper discussion that based on energy input provided by milling equipment, the milling conditions should be optimized. On the other hand, utilization of these materials as in powder state is quite rare and subsequent consolidation is necessary to convert them into bulk materials, in order to use them in different engineering applications. Therefore, in addition to the powders state properties, the compaction and sintering behaviors of these powders gain importance. Effect of MA time on compaction and sintering response of these powders were also studied by Söyler et al. (2010). A comparative graph is given in **Figure 3** which shows that the compressibility of the processed powders decreases with increasing MA time. Although better green densities can be obtained with increasing compaction pressure, excessive MA deteriorates the densification during sintering. But in all cases MA has lead to better sintering densification compared to as-blended powders. It should also be noted that full densification at this stage is not necessary or preferably from the perspective of many shape memory alloy compositions, since most of them require post-processing like hot-rolling for training purposes. During post-processing steps further densification can also be compensated and initial sintered microstructure is open for alterations. Therefore, an overall strategy should be applied during MA, considering the final grain size and the relative density of the shape memory material attained at the end.

The importance of grinding time during MA, on the formation of martensite in FeMnSiCrNi SMAs, was also emphasized by other researchers. For instance, Dogan et al. showed that, in the initial stage of ball milling of Fe-20Mn-6Si-9Cr powders, a solid solution of all component elements mainly formed which gradually disappeared with increasing ball milling time. Thus, with the accumulation of lattice strain and process energy, during 20 h-ball milling, particle size decreased to about 100 nm and a large amount of ε (hcp) was generated (Dogan and Arslan, 2012).

However, these phase transformations were observed when subsequent annealing was applied to MA'ed powders at higher temperatures. In the case of P/M-MA'ed FeMnSiCrNi SMAs studied by present authors no newly formed phase was noted, up to 8 h, and most of the diffraction peaks of Mn, Si, Ni, and Cr disappeared in time (Söyler et al., 2010).

On the other hand, a transition from initial α-phase to γ-phase was observed, by Saito et al., during MA of Fe-30Mn-6Si composition. After 20 h MA, the initial α-phase totally transformed γ-phase and this XRD observation was supported with Mössbauer spectra also. Moreover, they mentioned that in the case when no MA was applied, initial Mn peaks can be still observed in the XRD plots even after sintering (Saito et al., 2014).

Both as-blended and MA'ed powders were compacted using uniaxial hydraulic press at 500 MPa in a rectangular prism mold having cross section of 4 mm × 40 mm. Compacted samples were sintered under argon atmosphere at 1,150°C for 2 h using high-temperature furnace and H_2 is used at 800°C for 30 min for reduction of the oxides from samples (Söyler et al., 2014).

Sintered P/M-MA'ed specimens with chemical compositions Fe-18Mn-3Si-7Cr-4Ni and Fe-14Mn-6Si-9Cr-5Ni were hot rolled between 1,000 and 1,100°C, with a thickness reduction degree of 20% per pass, until an approximate final thickness of 1 mm. The porosity degree accordingly decreased from 16.85% at 0_MA to 2.51% at 50_MA. The temperature of the last rolling pass was altered, in the case of Fe-14Mn-6Si-9Cr-5Ni at four different values: (i) room temperature (RT), (ii) 600°C, (iii) 800 and 1,100°C (Pricop et al., 2014). After hot rolling, the specimens were heat treated at 700, 800, 900, 1,000 and 1,100°C/5 min/water, in order to relieve internal stresses and to enhance martensite formation. The specimens were further designated with the volume fraction of as blended powder substituted with mechanically alloyed (MA'ed) particles and the heat treatment temperature (e.g., 0_MA_700 describes the specimen sintered from as-blended powders and heat treated at 700°C while 40_MA_1100 designates the specimen with 40%$_{\text{vol}}$ MA'ed powder which was heat treated at 1,100°C).

By means of simultaneous thermal analysis (STA), powder mixtures of Fe-14Mn-6Si-9Cr-5Ni, were subjected to three heating-cooling cycles, between RT and 400°C, under two

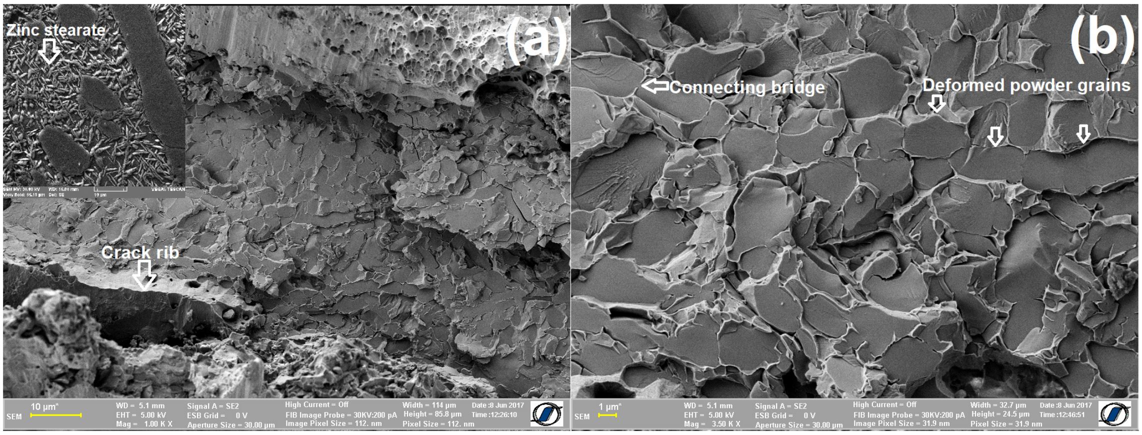

FIGURE 4 | SEM micrographs illustrating sintering effects on 0_MA_700 specimen: **(a)** brittle general fractographic aspect with detail of an area with Zn stearate segregation; **(b)** magnified view of an area with connection bridges between deformed powder grains (reproduced after Mocanu et al., 2018, with permission granted by Springer Nature).

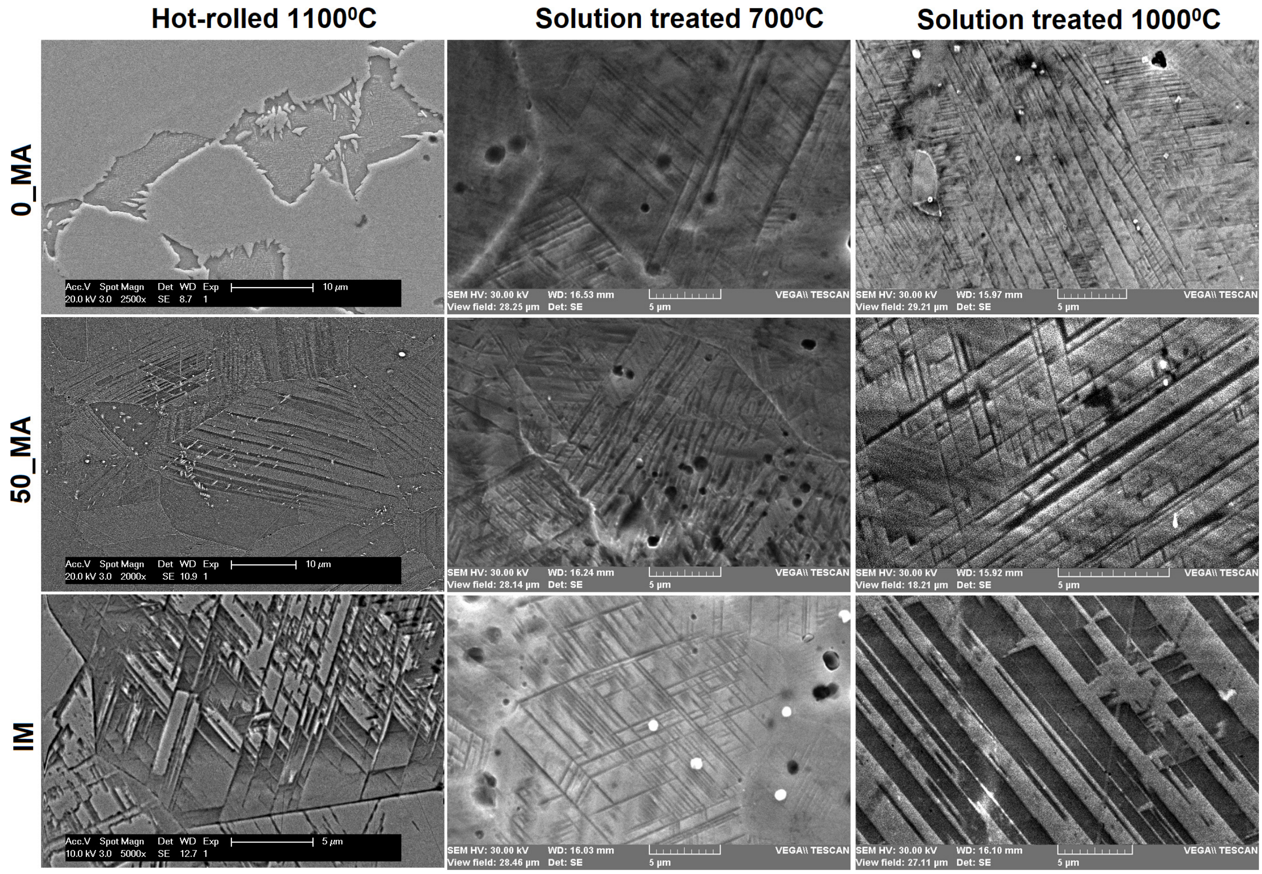

FIGURE 5 | SEM micrographs illustrating the evolution of initial hot rolled structure of P/M specimens sintered from pressed as blended powders (0_MA), 50% as blended powders substituted with MA'ed powders (50_MA) and ingot metallurgy specimens (14 Mn), which were subjected to solution treatments at 700 and 1,100°C (adapted after Pricop et al., 2015a, © owned by the authors).

forms: (i) as-blended (0_MA) and (ii) with equal amounts of as-blended and MA'ed powders (50_MA). During each heating and cooling stages, the ferromagnetic-paramagnetic transition of Ni was identified, by means of an exothermic and an endothermic step, respectively. Their thermal ranges experienced an increasing tendency with the number of thermal cycles and

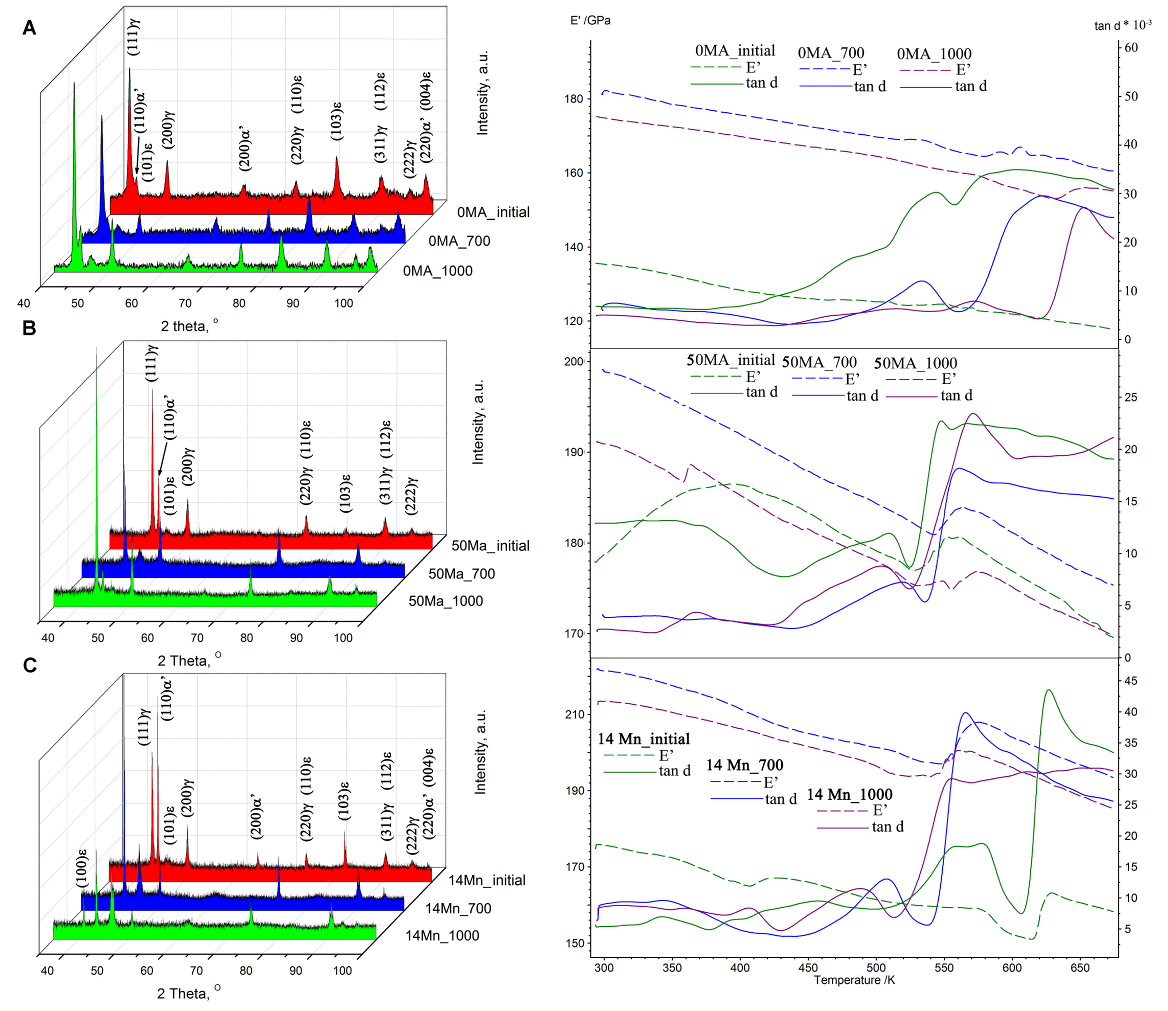

FIGURE 6 | Solution treatment effects on the structure and dynamic behavior of: **(A)** P/M specimens sintered from pressed as blended powders (0_MA), **(B)** 50% as blended powders substituted with MA'ed powders (50_MA) and **(C)** ingot metallurgy specimens (14 Mn) (adapted after Pricop et al., 2015a, © owned by the authors).

were higher at 50_MA powders. Besides magnetic transition of Ni, glass transition of amorphous regions was emphasized in MA'ed powders as well as the surface oxidation of as-blended pure Fe particles (Pricop et al., 2011). The powder mixtures were also subjected to heating-cooling cycles in the thermal chamber of a scanning electron microscope equipped with focused ion beam (SEM-FIB), the effects being evaluated by SEM and X-ray diffraction (XRD). The former emphasized the presence of iron oxides under the form of micrometer-size length cilia-like outgrowth and the latter highlighted the partial crystallization of amorphous regions in 50_MA powder mixtures (Pricop et al., 2012).

After pressing and sintering, the powders were aggregated into single compacts the density of which was further increased by hot rolling. It was noticed that the specimens obtained from sintered as-blended powders remained highly brittle, even after hot rolling and heat treatment. The brittle character of the specimens could be revealed by fractographic observations such as the example illustrated, in **Figure 4**, in the case of a 0_MA_700 specimen.

Figure 4a shows long crack ribs and an area with Zn stearate segregation. **Figure 4b** displays the presence of connection bridges between elongated powder grains, as an effect of rolling (Mocanu et al., 2018).

The main shortcoming seems to be the high brittleness of sintered powder compacts due to a porosity degree of 16.85%. Future efforts will be focused on the optimization of MA processing parameters, considering the initial particle size of the powders and energy provided by high energy milling equipment.

THERMOMECHANICAL PROCESSING AND PRE-STRAINING EFFECTS

Most of our work consisted in comparing the effects of hot rolling and heat treatments upon structure and properties of IM and P/M specimens, while substituting various amounts of as-blended with MA'ed powder fractions, in the latter case.

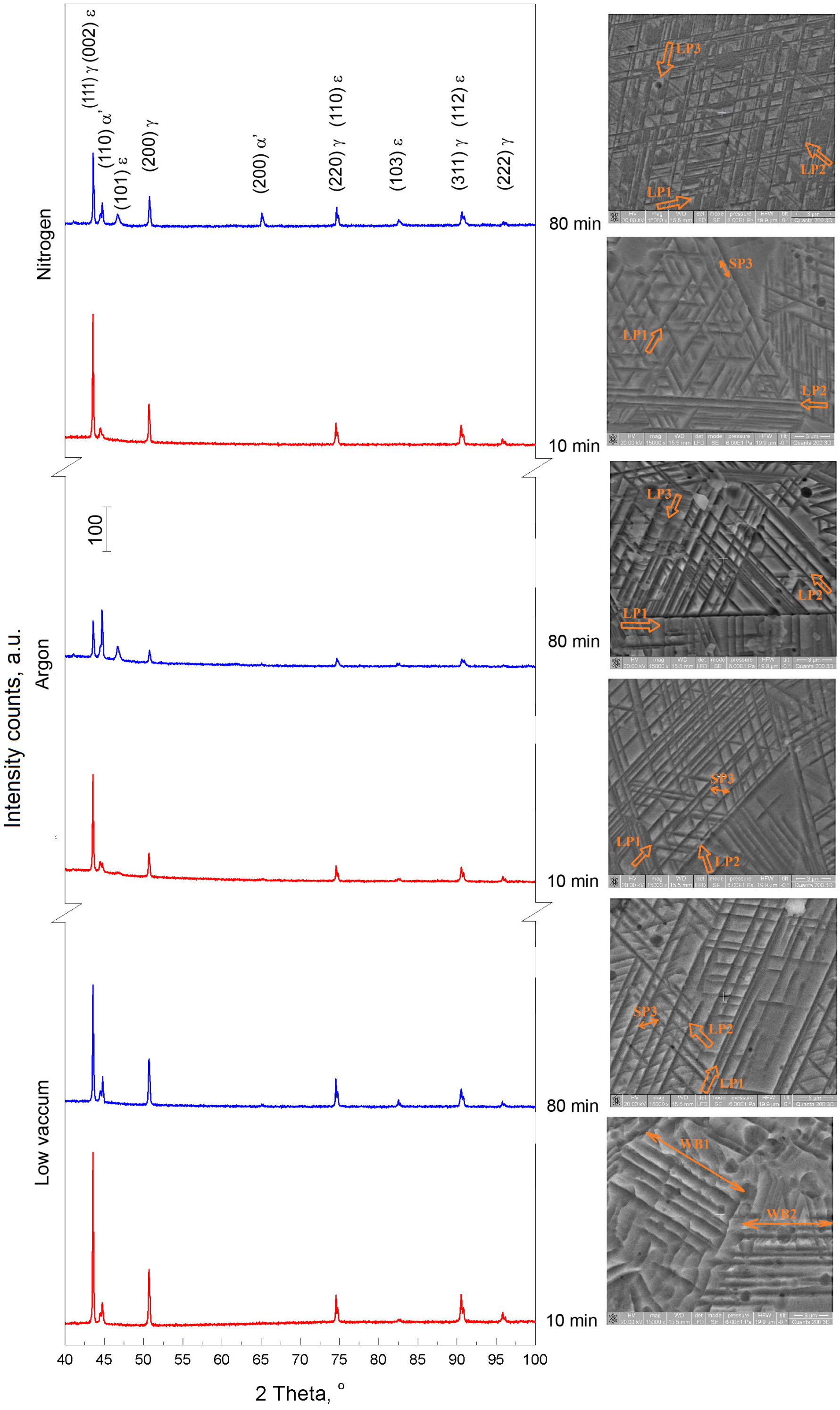

FIGURE 7 | Effects of holding environment (protective atmosphere: low vacuum, argon and nitrogen) and time (10, 80 min) on the structure of 50_MA specimens heat treated at 1,200°C (reproduced after Pricop et al., 2016, with permission granted by Springer Nature).

The first investigations were performed on IM and P/M-MA'ed specimens Fe-18Mn-3Si-7Cr-4Ni SMA. Firstly, when subjected to tensile cycling, it was noticed that both IM and P/M specimens experienced transformation induced plasticity, within the first tensile loading cycle and slip induced plasticity during the subsequent ones. Yet IM specimens preserved their

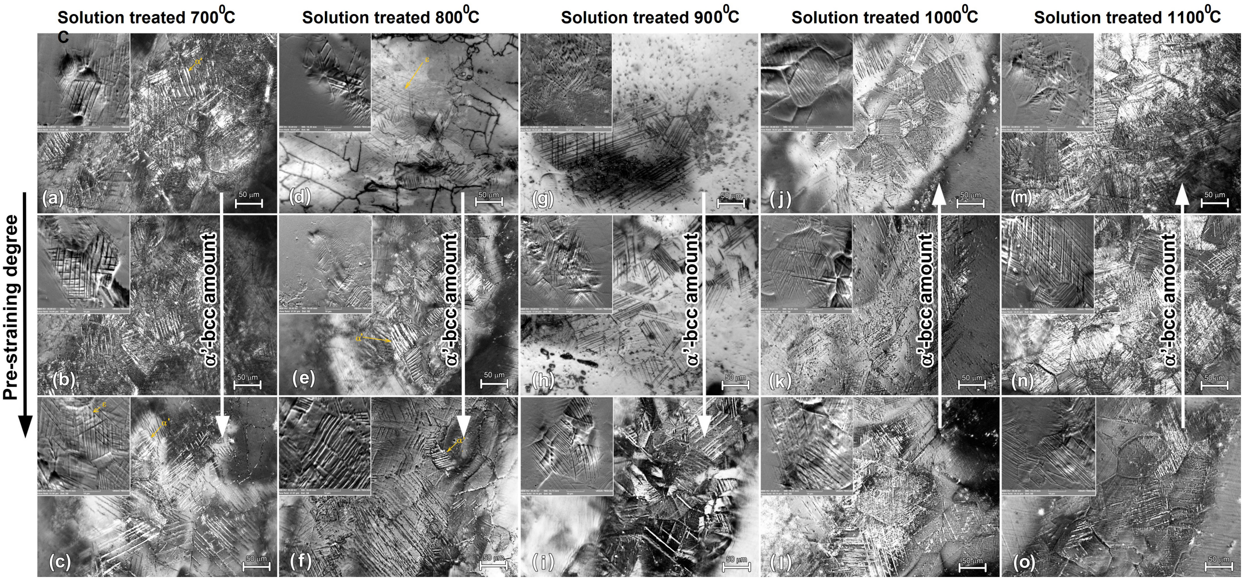

FIGURE 8 | Dark-field OM micrographs with SEM insets illustrating the formation of thermally induced martensite with increasing solution treatment temperature (from 700 to 1,100°C) and the occurrence of stress induced martensite with increasing pre-strain degree (from 0% to max. 4.2%) at specimens sintered from as-blended powders, 0_MA_700 at **(a)** 0%; **(b)** 0.7%; **(c)** 2%; 0_MA_800 at: **(d)** 0%; **(e)** 2.1%; **(f)** 3.3%; 0_MA_900 at: **(g)** 0%; **(h)** 1.8%; **(i)** 3.4%; 0_MA_1000 at: **(j)** 0%; **(k)** 1.7%; **(l)** 4.2%; 0_MA_1100 at: **(m)** 0%; **(n)** 1.1%; **(o)** 3.8% (reproduced after Pricop et al., 2015b, Open Acess).

pseudoelastic character even after total strains of 25% while P/M ones were tougher, due to the presence of larger amounts of α′-bcc stress induced martensite. The elongated gauges of tensile specimens were further analyzed by dilatometry (DIL) and XRD. The former revealed a solid state transition occurring during first heating, that increased in intensity with the maximum applied strain, while the latter confirmed the presence of larger amounts, i.e., 10–13%, of α′-bcc stress induced martensite in P/M-MA'ed specimens (Bujoreanu et al., 2009). Aiming to further investigate the stress induced formation of α′-bcc martensite and its thermally induced reversion to γ-fcc austenite, a study was performed on P/M Fe-18Mn-3Si-7Cr-4Ni specimens sintered from as-blended powders with Zn stearate binder (P/M -Zn) and from MA'ed powders without binder (P/M-MA). At P/M - Zn specimens, XRD patterns revealed that the amount of α′-bcc stress induced martensite increased with the number of tensile cycles, exceeding 34% after 20 cycles. On the other hand, at P/M-MA specimens, XRD emphasized a decreasing tendency of α′-bcc martensite with increasing the number of tensile mechanical cycling. It was demonstrated that none of P/M-MA Fe-18Mn-3Si-7Cr-4Ni specimens revealed ε-hcp martensite on their XRD patterns. Nevertheless, a slight contraction was observed by DIL, at about 360°C, during heating of the gauge of the tensile specimen subjected to five mechanical cycles. It has been assumed that this low-intensity SME (since an elongated specimen tends to reduce its length during heating) could be caused by the thermally induced reversion of α′-bcc stress induced martensite (Pricop et al., 2010).

The greatest part of experiments were performed on specimens with chemical composition Fe-14Mn-6Si-9Cr-5Ni. Three specimens in each state, 0_MA, 50_MA and IM, respectively, were hot rolled and then one specimen was heat treated at 700°C and the other at 1,000°C. The nine resulting representative microstructures, recorded by SEM, are summarized in **Figure 5** (Pricop et al., 2015a).

In hot rolled state, martensite plates are noticeable only at specimens 50_MA and IM, which has an average grain size of 74.4 μm, much larger than 17.8 μm, the corresponding value for P/M specimens. After solution treatment at 700°C, the density of martensite plates obviously increased. At IM specimen, average grain size decreased to 29.4 μm, due to recrystallization and this caused a refinement of martensite plates. Increasing heat treatment temperature to 1,000°C produced finer preferentially oriented martensite plates, in 0_MA and 50_MA specimens but caused the increase of martensite plates widths at IM specimen, since a slight grain coalescence occurred, causing average grain size increase to 40.3 μm. The identification of phase structure was performed by XRD and the dynamic behavior of the nine specimens under study was evaluated by dynamic mechanical analysis (DMA), using three-point-bending specimen holder, as summarized in **Figure 6** (Pricop et al., 2015a).

In **Figure 6A**, on the XRD pattern of 0_MA specimen in hot rolled state, designated as "initial," the relative intensities of the diffraction maxima corresponding to ε-hcp and α′-bcc martensite plate variants are rather low. After heat treatment, the intensities of $(101)_{\varepsilon}$ and $(110)_{\alpha'}$ planes that correspond to the main maxima of the two martensites, increased and the effect is more obvious at 0_MA_1000. These XRD patterns of 0_MA specimens confirm the absence of martensite plates at hot rolled specimen and their presence in heat treated states. The DMA thermograms from **Figure 6A** illustrate a continuous decrease of storage modulus (E') during heating at all specimens,

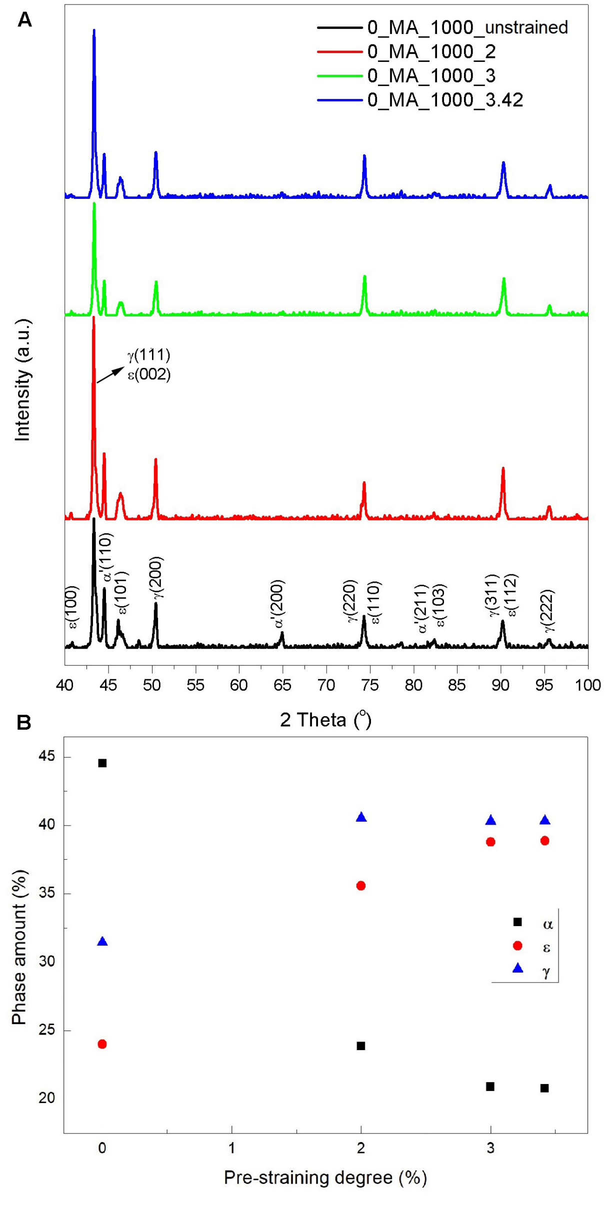

FIGURE 9 | Effects of pre-straining degree increase at 0_MA_1000 specimens: **(A)** XRD patterns and **(B)** phase amounts of α′-bcc martensite, ε-hcp martensite and γ-fcc austenite (reproduced after Pricop et al., 2018, with permission granted by Taylor & Francis).

since martensite is stiffer than austenite and two internal friction (tanδ) maxima, associated with the successive reversions to γ (fcc) austenite of α′-bcc and ε-hcp martensites, respectively (Pricop et al., 2015a). More recent studies corroborated the variations of storage modulus and magnetization, during heating. By associating storage modulus and magnetization increases, observed during heating (Mocanu et al., 2018), it was suggested that the occurrence of the first tanδ maximum could be a composed effect of overlapping α′-(bcc) →γ (fcc) reverse martensitic transformation and antiferromagnetic → paramagnetic transition at Néel temperature (T_N) (Pricop et al., 2018). At 50_MA specimens, the main diffraction maxima of martensite are more prominent than in the case of 0_MA, in good agreement with the micrographs from **Figure 5**. In addition, some maxima are broader, in **Figure 6B**, which could indicate either small crystallite size along the direction normal to the specified planes or distortions of crystalline structure, as an effect of MA. Due to the higher amount of martensite, the internal friction maxima are obviously more prominent in **Figure 6B** than in **Figure 6A** and storage modulus experiences an obvious increase, ($\Delta E'_{\max}$ = 19 GPa). When comparing the three XRD patterns from **Figure 6C**, recorded at IM specimens designated as 14 Mn, it is noticeable that the hot rolled state presents a large $(110)_{\alpha'}$ diffraction maximum, that sustains the presence of α′-(bcc) martensite in this specimen, while no diffraction maxima belonging to α′-(bcc) martensite could be identified, in heat treated specimens. However, the storage modulus of hot rolled (initial) 14 Mn specimen experienced an increase of $\Delta E'$ = 12 GPa, in spite of its general low values. It was noticed that heat treatment caused an increase of maximum storage modulus values, and a decrease of maximum internal friction, from 0_MA, to 50_MA and finally to 14 Mn (Pricop et al., 2015a).

It was also noticed that martensite plate variants became more diversified with the increase of MA fraction and more complexly intersected, as more γ-fcc austenite transformed to α′-bcc and ε-hcp stress-induced martensites (Bulbuc et al., 2019).

In the particular case of 50_MA specimens, the effects of holding environment (protective atmosphere) and time, during the heat treatment at 1,200°C followed by water quenching, were investigated, as summarized in **Figure 7** (Pricop et al., 2016).

The XRD patterns reveal that the heat treatments performed during 80 min, in nitrogen or argon atmospheres, caused the occurrence of ε-hcp martensite, while α′-(bcc) martensite is present in all specimens, ranging between 17 and 65%. The semi-quantitative analysis was performed based on the ratio of the intensities of the non-overlapping peaks $(110)_{\alpha'}$, $(101)_{\varepsilon}$, $(200)_{\gamma}$, $(200)_{\alpha'}$, $(103)_{\varepsilon}$ and $(222)_{\gamma}$ (Sawaguchi et al., 2008). The amount of ε-hcp martensite represents 8–20%, after the heat treatment performed during 80 min, and this could sustain the presence of SME, in these specimens. Even if the ε-hcp martensite could not be detected on XRD patterns, the SEM micrographs display “triangular” morphologies” formed by martensite plates oriented over three directions $\{111\}_{\gamma}$, marked with indexes 1, 2, and 3. The specimen heat treated for 10 min in low vacuum presents wide martensite plates (WB1 and WB2) while those treated in argon and nitrogen display thinner bands. Typical structures comprise long plates of two variants (LP1 and LP2) and a shorter plate (SP3) separated by the long ones. These results sustain the conclusion that MA promotes the formation of α′-(bcc) martensite, after heat treatment at 1,200°C in low vacuum, argon or nitrogen, both at short and long holding periods, while ε-hcp martensite formed only after 80 min holding in argon or nitrogen (Pricop et al., 2016).

On the other hand, the highest structural homogeneity degree was achieved after 80 min holding in low vacuum (Spiridon et al., 2013).

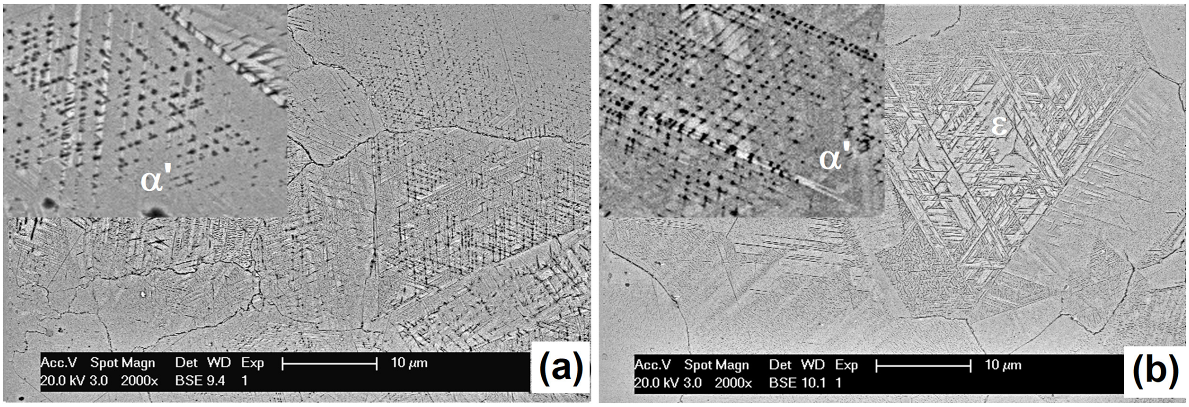

FIGURE 10 | Influence of MA degree on the microstructure of specimens pre-strained with 4%: **(a)** 0_MA_1100 and **(b)** 50_MA_1100, with thermally induced ε-hcp martensite. The insets display the effects of 4% pre-straining on stress-induced formation of α′-bcc martensite (modified after Pricop et al., 2013).

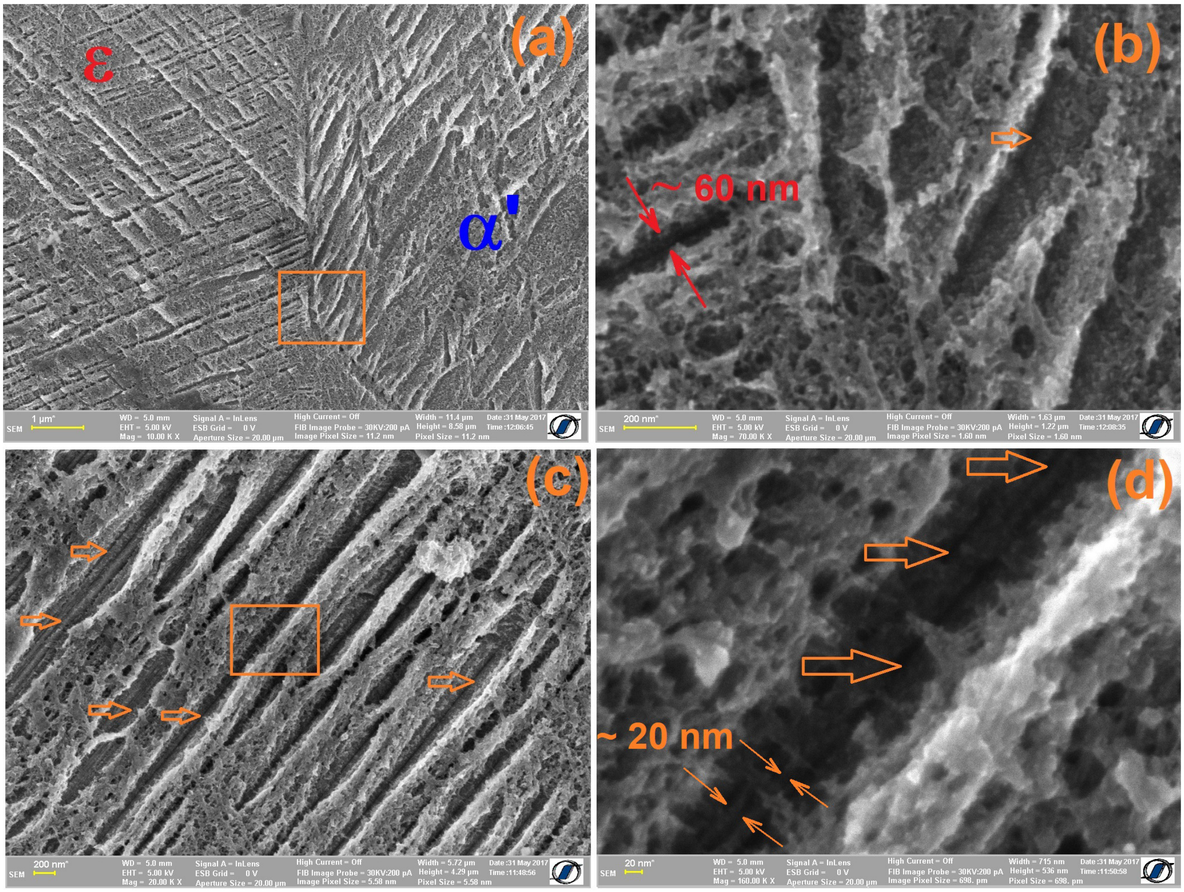

FIGURE 11 | (Sub)structural particularities of specimen 0_MA_1100 illustrated by HR-SEM: **(a)** grain boundary between neighboring regions with α′-bcc and ε-hcp thermally induced martensite; **(b)** detail of the grain boundary from panel **(a)** with typical dimension of a ε-hcp martensite plate and one internal sub-band of α′-bcc martensite; **(c)** multiple sub-bands identified within α′-bcc martensite plates with single orientation and **(d)** detail from panel **(c)** typical dimension of identified α′-bcc martensite sub-bands from panel **(c)** (reproduced after Pricop et al., 2018, with permission granted by Taylor & Francis).

The cumulated effects of heat treatments and tensile pre-straining degrees were investigated on the hot rolled specimens sintered from as-blended powders, designated as 0_MA_700, 0_MA_800, 0_MA_900, 0_MA_1000 and 0_MA_1100. The XRD patterns showed that, with increasing heat treatment temperature, the amount of α′-bcc martensite experienced

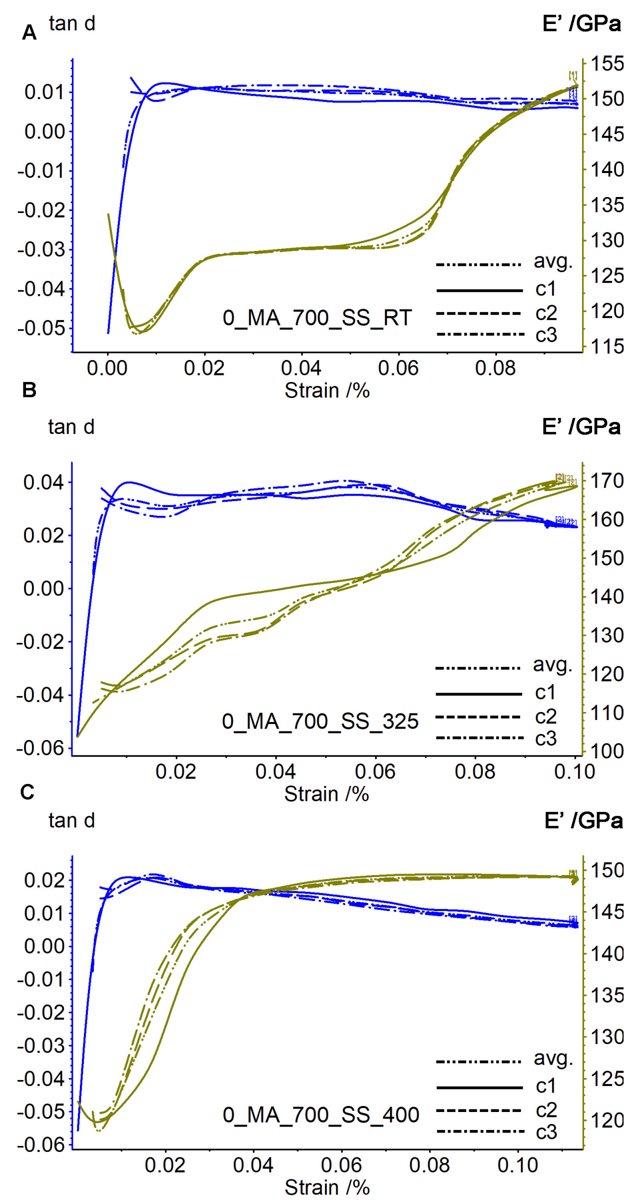

FIGURE 12 | Influence of test temperature on the dynamic behavior of 0_MA_700 specimens, during DMA SS, at: **(A)** T_1 = RT; **(B)** T_2 = 325°C and **(C)** T_3 = 400°C (reproduced after Pricop et al., 2018, with permission granted by Taylor & Francis).

an increasing tendency reaching a maximum at 1,100°C. The further application of tensile pre-straining revealed two opposing tendencies: (i) at specimens 0_MA_700, 0_MA_800 and 0_MA_900 the amount of α′-bcc martensite increased with pre-straining degree and (ii) at specimens 0_MA_1000 and 0_MA_1100 it decreased. This situation is summarized in **Figure 8** (Pricop et al., 2015b).

As mentioned above, ε-hcp martensite is visible due to its typical "triangular" morphology caused by the $\{111\}_\gamma$ habit planes and its narrow plates that completely cross austenite grains, from one border to the other. α′-bcc martensite, with shorter bands with either lenticular or lath shape, does not cross austenite grains and is better emphasized in dark field. By means of EDS measurements, it has been proved that the bcc phase identified on XRD patterns is martensite and not a ferrite, because no chemical composition fluctuations were detected, which could be caused by the substitutional diffusion, necessary for the formation of α ferrite instead of α′-bcc martensite. The global microstructural evolution, at the specimens 0_MA_1000 and 0_MA_1100, reflect the general decreasing tendency of the amount of α′-bcc martensite with increasing of pre-straining degree (Pricop et al., 2015b).

Aiming to overlap MA on the effects of heat treatment and pre-straining degree, fifteen sets of specimens, with three fractions of mechanically alloyed powders (0, 10, and 20 vol.%), were heat treated to the above five temperatures (700, 800, …, 1,100°C) before being pre-strained with various deformation degrees up to 4%. The formation of thermally induced α′-bcc martensite was revealed, as a particularity of these P/M-MA'ed alloys. Martensite plates became finer with the increase of MA'ed fraction, which enhanced a global increasing tendency of the amount of α′-bcc martensite on behalf of the amount of γ-fcc austenite (Mihalache et al., 2015). It has been concluded that internal friction, determined statically and dynamically, experienced an increasing trend with pre-straining degree, heat treatment temperature and MA'ed fraction (Mihalache et al., 2017).

A closer look was taken to the unusual decrease of α′-bcc martensite amount, with the increase of pre-straining degree at the specimens sintered from as-blended powders and heat treated to elevated temperatures. XRD patterns were recorded on specimens 0_MA_1000, in initial state and pre-strained with 2, 3, and 3.42%, as illustrated in **Figure 9** (Pricop et al., 2018).

In initial state, the amount of α′-bcc martensite is over 44%, much larger than that of ε-hcp martensite, 24%. With the increase of pre-straining degree to 2, 3, and 3.42%, the amount of α′-bcc martensite decreased to 23.9, 20.9, and 20.8% while that of ε-hcp martensite increased to 36, 38.8, and 38.9%, respectively. These data suggest ε-hcp martensite is stress-induced during pre-straining while thermally induced α′-bcc martensite is detwinned and reverts to γ-fcc austenite (Pricop et al., 2018). Similar results were obtained by Saito et al. and Amini et al. The former observed the formation of the γ-fcc and ε-hcp phases from the α-bcc phase due to diffusion of Mn and Si atoms into the Fe matrix (Saito et al., 2014) and the latter performed MA on Fe-32Mn-6Si and found that the α′→γ phase transition occurred during the ball milling process (Amini et al., 2013).

The main shortcomings are related to the higher amount of α′-bcc martensite in the specimens sintered from MA'ed powders while those sintered from as-blended powders experienced opposing variation tendencies of thermally induced α′-bcc martensite: to increase, at specimens heat treated below 900°C and to decrease, at specimens heat treated above 1,000°C. Nevertheless, since MA contributed to porosity degree decrease, martensite plate refinement and internal friction increase, further studies must be focused on the effects of pre-straining degree and heat treatment temperature to the tendency of thermally induced α′-bcc martensite to become detwinned and to revert to γ-fcc austenite.

PARTICULARITIES OF α′-bcc MARTENSITE

The typical aspect of α′-bcc martensite is represented under the form of intersection areas between ε-hcp martensite plates. At P/M-MA'ed FeMnSiCrNi, heat treated at 1,100°C, this morphology is influenced by MA degree, as exemplified by **Figure 10** (Pricop et al., 2013).

Pre-strained specimens 0_MA_1100 and 50_MA_1100 were etched with a solution of 1.2% $K_2S_2O_5 + 1\%\ NH_4HF_2$ in 100 ml distilled water and covered with Au film by an EDWARDS S150 deposition device. The SEM micrographs show a typical aspect of ε-hcp martensite and some dark regions, at the intersection of ε plates, which were associated with α′-bcc martensite. Obviously, the structure of 50_MA_1100 specimen, from **Figure 10b**, reveals a larger amount of α′-bcc martensite (Pricop et al., 2013).

An explanation for the decreasing tendency of the amount of α′-bcc martensite, with increasing pre-straining degree at specimens 0_MA_1100, was observed by investigating their substructure by HR-SEM, as shown in **Figure 11** (Pricop et al., 2018).

The grain boundary between α′-bcc and ε-hcp martensite regions, from **Figure 11a** is magnified in **Figure 11b**. Besides the typical spacing of 60 nm, between ε-hcp martensite plates, an internal sub-band is identified by an orange arrow in α′-bcc martensite. When analyzing the parallel array of α′-bcc martensite plates, from **Figure 11c**, the high resolution detail from **Figure 11d** reveals a spacing of 20 nm between internal sub-bands. We assumed that these sub-bands, in thermally induced α′-bcc martensite, hinder the nucleation and growth of α′ stress-induced martensite (Pricop et al., 2018).

A series of systematic measurements, performed by AFM, revealed a thinning tendency of martensite plate widths, from 1 to 2 μm at 0_MA specimens, to 0.78–0.97 μm at 20_MA specimens. This refining tendency, caused by the increase of MA'ed powder fraction is in good agreement with the structural analysis results observed by HR-SEM (Pricop et al., 2018). In addition, it was noticed that the chemical composition of the martensite plates is independent of the heat treatment temperature and thermally induced martensite plates preferably formed in Fe-rich, Mn-depleted regions (Cimpoesu et al., 2018).

The main shortcoming of present common scientific belief on α′-bcc martensite, in FeMnSi-based SMAs, is its detrimental effect of shape memory recovery. Further research need to be focused of the substructure of thermally induced α′-bcc martensite. The effects of its internal 20 nm-spaced sub-bands on the nucleation and growth of α′ stress-induced martensite require in-depth high resolution microscopy observations.

DYNAMIC BEHAVIOR

The dynamic behavior of P/M-MA'ed FeMnSiCrNi specimens, hot rolled and heat treated, was investigated by DMA in temperature scan (TS) and strain sweep (SS) modes. Typical TS-DMA diagrams were presented in **Figure 6**, displaying the variations with temperature of storage modulus (E') and internal friction (tanδ). The former experienced a local hardening ($\Delta E'$) and the latter displayed two maxima associated with: (i) antiferromagnetic-paramagnetic transition overlapped with the reversion to γ (fcc) austenite of α′-(bcc) martensite and (ii) the reversion of ε-hcp martensite reversion to γ-fcc austenite. SS-DMA tests were performed at three constant temperatures: T_1 = RT, (ii) $T_2 < A^{\varepsilon}_{50}$ and (iii) $T_3 > A^{\varepsilon}_{50}$ (the temperature of second tan δ maximum). The variations of E' and tanδ with strain amplitude, in the case of specimen 0_MA_700, are summarized in **Figure 12** (Pricop et al., 2018).

The curves correspond to three SS cycles, *c1*, *2*, *3* as well as their average value, *avg*. At RT, in **Figure 12A** the storage modulus plateau noticed between 0.02 and 0.06 strain amplitudes can be associated with the stress-induced formation of ε-hcp martensite because, as long as martensite is stress induced, E' value remained almost constant at about 128 GPa. In the other figures there are steeper increases of E' and no plateaus are noticeable, since no martensite can be stress induced above A^{ε}_{50}. The specimen tested at $T_2 < A^{\varepsilon}_{50}$, contains a mixture of martensitic and austenitic phases, experienced the highest values of tanδ and E' in **Figure 12B** (Pricop et al., 2018). The presence of this modulus plateau recommends P/M-MA'ed Fe-Mn-Si-Cr-Ni SMAs as potential candidates for RT-dampers, under the form of coupling rings of vibrating pipes (Popa et al., 2019).

The main shortcoming is the difficulty to increase internal friction at room temperature by creating bi-phasic structures (martensite/austenite). Since the single present solution for internal friction enhancement are stress-induced martensitic transformations, further studies are necessary in order to explain the in-depth relationship between stress-induced formation of martensite, storage modulus plateau and internal friction.

SHAPE MEMORY EFFECT AND APPLICATIONS

Due to the lack of thermoelasticity, Fe-Mn-Si-based SMAs are unable to deliver work-generating SME. Yet, they are successful in developing free-recovery SME, with great potential for self-healing phenomena (Lutz et al., 2016) and constrained-recovery SME, applicable for couplings development.

The succession of bending-heating-cooling represents the most practical way to emphasize free-recovery SME. A lamellar specimen is bent, at RT, around a cylindrical caliber then heated at 600°C and SME is expressed as a function of the rotation angles (Söyler et al., 2014) or the successive positions of the free end of the specimen, monitored by video control. In order to get a better SME response, a training procedure can be applied by repetitively applying the bending-heating-cooling succession (Pricop et al., 2018).

The evolution of a lamellar 40_MA_1000 specimen, containing 46.8% α′-bcc and 25.5% ε-hcp martensite, is illustrated in **Figure 13**, during five training cycles (Mocanu et al., 2018).

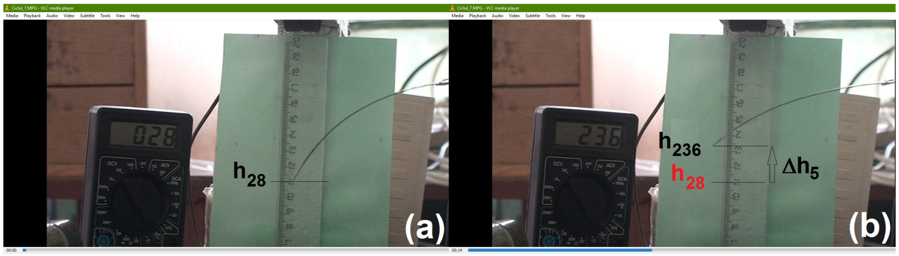

FIGURE 13 | Free-recovery SME training of a 40_MA_1000 lamellar specimen subjected to bending: **(a)** the start of 1st cycle; **(b)** the end of 5th cycle (reproduced after Mocanu et al., 2018, with permission granted by Springer Nature).

TABLE 1 | Evolution of training parameters.

Cycle number	Temperature increase, ΔT (°C)	Maximum heating time, Δt (s)	Maximum vertical displacement, Δh (mm)	Average displacement rate	
				in time, $\Delta h/\Delta t$ (mm/s)	with temperature, $\Delta h/\Delta T$ (mm/°C)
1	228	9	15	1.07	0.066
2	270	21	16	0.76	0.059
3	135	36	19	0.53	0.141
4	219	17	20.5	1.21	0.094
5	208	14	24	1.71	0.115

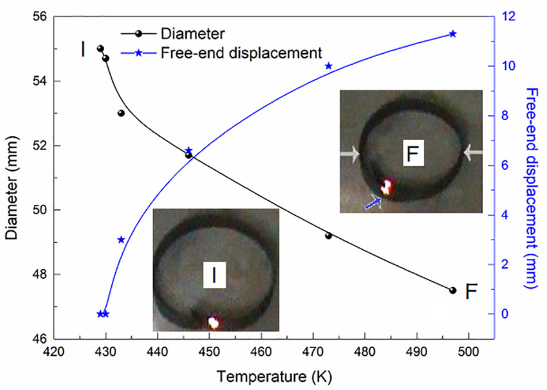

FIGURE 14 | Details of the training procedure applied to a 50_MA pipe-coupling ring subjected to free recovery SME, with opposite gray horizontal arrows indicating diameter shrinkage and blue tilted arrow emphasizing free-end displacement, from initial (I) to final (F) stages and variations of diameter and free-end displacement, during heating (modified after Bujoreanu, 2015).

Figure 13a shows the position of specimen's free end at 28°C, designated at h_{28}. During each cycle, a mobile gas lamp was used to heat up the specimen and a water spray to cool it down, both being moved along its entire length. Then the specimen was released and bent again against the caliber. The evolution of the training parameters: ΔT-temperature increase, Δt-maximum heating time, Δh-maximum vertical displacement, and average displacement rates in time ($\Delta h/\Delta t$) and with temperature ($\Delta h/\Delta T$) are summarized in **Table 1**, for the five cycles. In **Figure 13b**, during heating up to 236°C, in the 5th cycle, the free end reached the position designated h_{236}, which gives a total displacement $\Delta h_5 = 24$ mm and an average displacement rate of 1.71 mm/s (Mocanu et al., 2018).

As mentioned above, P/M-MA'ed FeMnSiCrNi SMAs have the potential to be used for the development of coupling rings, meant to connect vibrating pipes that transport turbulent fluids, where dynamic stiffness is one of the key properties, because vibration could contribute to the accidental opening of coupling ring.

Pipe-coupling rings were produced by gradually heating lamellar specimens and rounding them, between outer and inner calibers. One example of the training procedure of a pipe coupling manufactured from a 50_MA lamellar specimen is shown in **Figure 14** (Bujoreanu, 2015).

Figure 14 illustrates the initial and final training stages of the ring. The evolutions of rings diameter and free-end displacement with temperature, indicated by arrows, were monitored by cinematographic analysis and shown in the **Figure 14**.

The main shortcoming is related to the low value of shape recovery degree determined according to the beam bending model (Park et al., 2015). Further studies are necessary in order to increase the strokes developed by free-recovery SME and to develop fastening systems with advanced damping capacity, meant to safely connect oscillating part ends.

CONCLUDING REMARKS AND FUTURE TRENDS

By summarizing the results reviewed in the above sections the following concluding remarks can be drawn, concerning P/M-MA'ed Fe-14Mn-6Si-9Cr-5Ni SMAs:

1. The use of over 8:1 BPR values and minimum 4 h of milling, in the presence of surfactant are found useful to obtain compositionally homogeneous composite particles having an average particle size of 10–20 μm which may easily be consolidated into bulk materials having enough relative density.
2. In thermally cycled powder mixtures, MA increased the thermal ranges of magnetic transition of Ni while the sintered powder compacts remained highly brittle, even after hot rolling and heat treatment, due to a porosity degree of 16.85%.
3. As an effect of increasing the fraction of MA'ed powders, porosity degree decreased to 2.51% at 50_MA, martensite plate variants became more diversified and more complexly intersected since more γ-fcc austenite transformed mostly to α'-bcc martensite during heat treatment, at temperatures as high as 1,200°C, both at short and long holding periods of time in low vacuum, argon or nitrogen.
4. At the specimens sintered from as-blended powders, the increase of pre-straining degree caused opposing variation tendencies of α'-bcc martensite: (i) to increase, at specimens 0_MA_700, 0_MA_800 and 0_MA_900 and (ii) to decrease, at specimens 0_MA_1000 and 0_MA_1100. At 0_MA_1000, ε-hcp martensite was stress-induced during pre-straining while thermally induced α'-bcc martensite was detwinned and reverted to γ-fcc austenite. Internal friction, determined statically and dynamically, experienced an increasing trend with pre-straining degree, heat treatment temperature and MA'ed fraction.
5. The substructure of thermally induced α'-bcc martensite contained internal sub-bands with 20 nm-spacing which hindered the nucleation and growth of α' stress-induced martensite. Increasing the fraction of MA'ed powders, from 0 to 20%vol. caused a thinning tendency of martensite plate widths, from 1–2, to 0.78–0.97 μm.
6. DMA performed during heating emphasized a local increase of storage modulus ($\Delta E'_{\max}$ = 19 GPa) and two internal friction maxima associated with: (i) antiferromagnetic-paramagnetic transition overlapped with the reversion to γ (fcc) austenite of α'-(bcc) martensite and (ii) the reversion of ε-hcp martensite reversion to γ-fcc austenite. DMA performed isothermally at RT highlighted a storage modulus plateau, between 0.02 and 0.06 strain amplitude, associated with the stress-induced formation of ε-hcp martensite because.
7. After five thermomechanical training cycles, a 40_MA_1000 lamellar specimen, containing 46.8% α'-bcc and 25.5% ε-hcp martensites, developed a total displacement $\Delta h_5 = 24$ mm and an average displacement rate of 1.71 mm/s.
8. Coupling rings with advanced damping capacity, meant to connect vibrating pipes that transport turbulent fluids, were produced and trained from lamellar specimens.
9. Further research efforts are necessary in order to develop the advanced processing, characterization and implementation of P/M-MA'ed Fe-14Mn-6Si-9Cr-5Ni SMAs which have the potential to contribute to the production of simple high damping fastening systems.

AUTHOR CONTRIBUTIONS

BP organized the figures and requested the utilization permissions from corresponding publishing houses. BÖ and AS organized the section concerning P/M-MA processing. LB arranged the manuscript and managed the correspondence. All authors contributed to the article and approved the submitted version.

REFERENCES

Amini, R., Shamsipoor, A., Ghaffari, M., Alizadeh, M., and Okyay, A. K. (2013). Phase transformation during mechano-synthesis of nanocrystalline/amorphous Fe-32Mn-6Si alloys. *Mater. Char.* 84, 169–174. doi: 10.1016/j.matchar.2013.07.017

Arruda, G. J., Buono, V. T. L., and Andrade, M. S. (1999). The influence of deformation on the microstructure and transformation temperatures of Fe–Mn–Si–Cr–Ni shape memory alloys. *Mater. Sci. Eng. A* 273–275, 528–532. doi: 10.1016/s0921-5093(99)00393-7

Aydogmus, T., and Bor, A. S. (2011). Production and characterization of porous TiNi shape memory alloys. *Turkish J. Eng. Env. Sci.* 35, 69–82. doi: 10.3906/muh-1007-1127

Bahador, A., Hamzah, E., Kondoh, K., Kawahito, Y., Junko, U., and Abu Bakar, T. A. (2017). Mechanical and superelastic properties of disk-laser welded Ti-Ni shape-memory alloys produced by powder metallurgy. *J. Mater. Proc. Tech.* 248, 198–206. doi: 10.1016/j.jmatprotec.2017.05.019

Bahador, A., Junko, U., Mizutani, M., Hamzah, E., Yusof, F., and Kondoh, K. (2020). High-brightness and high-power laser welding of powder metallurgy shape memory alloy: welding-parameter-dependent microstructure. *J. Mater. Eng. Perform.* 29:987. doi: 10.1007/s11665-020-04597-0

Berns, H., and Theisen, W. (2008). *Ferrous Materials: Steel and Cast Iron*. Berlin: Springer, 190–207.

Bracke, L., Mertens, G., Penning, J., De Cooman, B. C., Liebeherr, M., and Akdut, N. (2006). Influence of phase transformations on the mechanical properties of high-strength austenitic Fe-Mn-Cr steel. *Metall. Mater. Trans. A* 37A, 307–317. doi: 10.1007/s11661-006-0002-5

Bujoreanu, L. G. (2015). Development of shape memory and superelastic applications of some experimental alloys. *J Optoelectron. Adv. M.* 17, 1437–1443.

Bujoreanu, L. G., Stanciu, S., Ozkal, B., Comaneci, R. I., and Meyer, M. (2009). "Comparative study of the structures of Fe-Mn-Si-Cr-Ni shape memory alloys obtained by classical and by powder metallurgy, respective1y," in *ESOMAT 2009 - European Symposium on Martensitic Transformations*, eds P. Šittner, L. Heller, and V. Paidar (Paris: EDP Sciences), 05003. doi: 10.1051/esomat/200905003

Bulbuc, V., Pricop, B., Popa, M., Mihalache, E., Özkal, B., and Bujoreanu, L. G. (2019). Thermomechanical processing effects on the structure and properties of Fe-based SMAs. I. Evolution of phase structure. *IOP Conf. Series* 485:012004. doi: 10.1088/1757-899x/485/1/012004

Cimpoesu, N., Mihalache, E., Lohan, N. M., Suru, M. G., Comăneci, R. I., Özkal, B., et al. (2018). Structural-morphological fluctuations induced by thermomechanical treatment in a Fe – Mn – Si shape memory alloy. *Met. Sci. Heat Treat.* 60, 471–477. doi: 10.1007/s11041-018-0303-5

Dang, S., Li, Y., Zou, Q., Wang, M., Xiong, J., and Luo, W. (2019). Progress in Fe-Mn-Si based shape memory alloys prepared by mechanica1 alloying and powder metallurgy. *J. Mater. Eng.* 47, 18–25.

Dogan, A., and Arslan, H. (2012). Effect of ball-milling conditions on microstructure during production of Fe-20Mn-6Si-9Cr shape memory alloy powders by mechanical alloying. *J. Therm. Anal. Ca1orim*. 109, 933–938. doi: 10.1007/s10973-011-1809-x

Druker, A., Perotti, A., Esquivel, I., and Malarría, J. (2014). A manufacturing process for shaft and pipe couplings of Fe–Mn–Si–Ni–Cr shape memory alloys. *J. Mater. Design* 56:878. doi: 10.1016/j.matdes.2013.11.032

Dunne, D. (2012). "Shape memory in ferrous alloys," in *Diffusionless Transformations, High Strength Steels, Modelling and Advanced Analytical Techniques. Phase Transformations in Steels*, Vol. 2, eds E. Pereloma and D. V. Edmonds (Cambridge: Woodhead), 83–125. doi: 10.1533/9780857096111.1.83

He, Q., Jia, C., and Meng, J. (2006). Inf1uence of iron powder particle size on the microstructure and properties of Fe3Al intermetallics prepared by mechanical alloying and spark plasma sintering. *Mater. Sci. Eng. A*. 428, 314–318. doi: 10.1016/j.msea.2006.05.024

Kajiwara, S. (1999). Characteristic features of shape memory effect and related transformation behavior in Fe-based alloys. *Mat. Sci. Eng. A* 273–275, 67–88. doi: 10.1016/s0921-5093(99)00290-7

Li, J. C., Zhao, M., and Jiang, Q. (2000). Alloy design of Fe-Mn-Si-Cr-Ni shape-memory alloys related to stacking-fault energy. *Metall. Mater. Trans. A* 31, 581–584.

Liu, T., Liu, H. Y., Zhao, Z. T., Ma, R. Z., Hu, T. D., and Xie, Y. N. (1999). Mechanical alloying of Fe- Mn and Fe-Mn-Si. *Mater. Sci. Eng. A*. 271, 8–13. doi: 10.1016/s0921-5093(98)01022-3

Lutz, A., Van den Berg, O., Wielant, J., De Graeve, I., and Terryn, H. (2016). A multiple-action self-healing coating. *Front. Mater.* 2:73.

Ma, J., and Karaman, I. (2010). Expanding the repertoire of shape memory alloys. *Science* 327, 1468–1469. doi: 10.1126/science.1186766

Maruyama, T., Kurita, T., Kozaki, S., Andou, K., Farjami, S., and Kubo, H. (2008). Innovation in producing crane rail fishplate using Fe–Mn–Si–Cr based shape memory alloy. *J. Mater. Sci. Technol.* 24, 908–912. doi: 10.1179/174328408x302585

Mazzer, E. M., Gargarella, P., Cava, R. D., Bolfarini, C., Galano, M., and Kiminami, C. S. (2017). Effect of dislocations and residual stresses on the martensitic transformation of Cu-Al-Ni-Mn shape memory alloy powders. *J. Alloy Compd.* 723, 841–849. doi: 10.1016/j.jallcom.2017.06.312

Mihalache, E., Pricop, B., Comăneci, R. I., Suru, M. G., Lohan, N. M., Mocanu, M., et al. (2017). Structural Effects of Thermomechanical Processing on the Static and Dynamic Responses of Powder Metallurgy Fe-Mn-Si Based Shape Memory Alloys. *Adv. Sci. Technol.* 97, 153–158. doi: 10.4028/www.scientific.net/ast.97.153

Mihalache, E., Pricop, B., Suru, M. G., Lohan, N. M., Comăneci, R. I., Istrate, B., et al. (2015). Factors influencing martensite transitions in Fe-based shape memory alloys, Matec Web of Conferences. *Paris EDP Sci.* 33:04002. doi: 10.1051/matecconf/20153304002

Mocanu, M., Mihalache, E., Pricop, B., Borza, F., Grigoraş, M., Comăneci, R. I., et al. (2018). "The Influence of α′(bcc) Martensite on the Dynamic and Magnetic Response of Powder Metallurgy Fe-Mn-Si-Cr-Ni Shape Memory Alloys," in *Proceedings of the International Conference on Martensitic Transformations*, eds A. P. Stebner and G. B. Olson (Chicago: Springer), 99–108. doi: 10.1007/978-3-319-76968-4_16

Moriya, Y., Kimura, H., Ishizaki, S., Hashizume, S., Suzuki, S., Suzuki, H., et al. (1991). Properties of Fe-Cr-Ni-Mn-Si (-Co) shape memory alloys. *J. Phys. IV C* 4, 433–437.

Murakami, M., Otsuka, H. H., and Matsuda, S. (1987a). Improvement in shape memory effect for Fe-Mn-Si alloys. *Trans. ISIJ* 27:B89.

Murakami, M., Otsuka, H., Suzuki, H., and Matsuda, S. (1987b). Effect of alloying content, phase and magnetic transformation on shape memory effect of Fe-Mn-Si alloys. *Trans. ISIJ* 27:B88.

Murakami, M., Suzuki, H., and Nakamura, Y. (1987c). Effect of silicon on the shape memory effect of polycrystalline Fe-Mn-Si alloys. *Trans. ISIJ* 27:B87.

Oro, R., Hryha, E., Campos, M., and Torralba, J. M. (2014). Effect of processing conditions on microstructural features in Mn-Si sintered steels. *Mat. Char.* 95, 105–117. doi: 10.1016/j.matchar.2014.06.011

Otsuka, H. (1991). Fe-Mn-Si Based Shape Memory Alloys. *MRS Proc.* 246:309. doi: 10.1557/PROC-246-309

Otsuka, H., Yamada, H., Maruyama, T., Tanahashi, H., Matsuda, S., and Murakami, M. (1990). Effects of alloying additions on Fe-Mn-Si shape memory alloys. *Trans. ISIJ* 30, 674–679. doi: 10.2355/isijinternational.30.674

Paleu, V., Gurău, G., Comăneci, R. I., Sampath, V., Gurău, C., and Bujoreanu, L. G. (2018). A new application of Fe-28Mn-6Si-5Cr (mass%) shape memory alloy, for self adjustable axial preloading of ball bearings. *Smart Mater. Struct.* 27:075026. doi: 10.1088/1361-665X/aac4c5

Park, J., Headings, L. M., Dapino, M. J., Baur, J. W., and Tandon, G. P. (2015). Investigation of interfacial shear stresses, shape fixity, and actuation strain in composites incorporating shape memory polymers and shape memory alloys. *Front. Mater.* 2:12. doi: 10.3389/fmats.2015.00012

Peng, H., Chen, J., Wang, Y., and Wen, Y. (2017). Key factors achieving large recovery strains in po1ycrystalline Fe-Mn-Si based shape memory alloys: a review. *Adv. Eng. Mater.* 20, 1–18.

Peng, H., Wang, G., Wang, S., Chen, J., Mac Laren, I., and Wen, Y. (2018). Key criterion for achieving giant recovery strains in polycrystalline Fe-Mn-Si based shape memory alloys. *Mater. Sci. Eng. A*. 712, 37–49. doi: 10.1016/j.msea.2017.11.071

Popa, M., Pricop, B., Bulbuc, V., Mihalache, E., Özkal, B., and Bujoreanu, L. G. (2019). Thermomechanical processing effects on the structure and properties of Fe-based SMAs. II. Evolution of damping behavior. *IOP Conf. Series* 485:012023. doi: 10.1088/1757-899x/485/1/012023

Pricop, B., Mihalache, E., Lohan, N. M., Istrate, B., Mocanu, M., Özkal, B., et al. (2015a). Powder metallurgy and mechanical alloying effects on the formation of thermally induced martensite in an FeMnSiCrNi SMA. *Matec Web Conf. Paris EDP Sci.* 33:04004. doi: 10.1051/matecconf/20153304004

Pricop, B., Söyler, U., Özkal, B., Suru, M. G., Lohan, N. M., Comaneci, R. I., et al. (2015b). A study of martensite formation in powder metallurgy Fe-Mn-Si-Cr-Ni shape memory alloys. *Mater. Today Proc.* 2, 789–792.

Pricop, B., Mihalache, E., Stoian, G., Borza, F., Özkal, B., and Bujoreanu, L. G. (2018). Thermo-mechanical effects caused by martensite formation in powder metallurgy FeMnSiCrNi shape memory alloys. *Powder Met.* 61, 348–356. doi: 10.1080/00325899.2018.1492773

Pricop, B., Özkal, B., Söyler, U., Van Humbeeck, J., Lohan, N. M., Suru, M. G., et al. (2014). Influence of mechanically alloyed fraction and hot rolling temperature in the last pass on the structure of Fe-14Mn-6Si-9Cr-5Ni (mass.%) shape memory alloys processed by powder metallurgy. *Optoelectron. Adv. Mat.* 8, 247–250.

Pricop, B., Özkal, B., Söyler, U., Van Humbeeck, J., Lohan, N. M., Suru, M. G., et al. (2016). Structural changes caused by high-temperature holding of powder shape memory alloy Fe-14Mn-6Si-Cr-5Ni. *Met. Sci. Heat Treat.* 57, 553–558. doi: 10.1007/s11041-016-9921-y

Pricop, B., Söyler, U., Comaneci, R. I., Özkal, B., and Bujoreanu, L. G. (2010). Mechanica1 cycling effects at Fe-Mn-Si-Cr-Ni SMAs obtained by powder metallurgy. *Phys. Proc.* 10, 125–131.

Pricop, B., Söyler, U., Lohan, N. M., Özkal, B., Bujoreanu, L. G., Chicet, D., et al. (2012). Therma1 behavior of mechanically alloyed powders used for producing an Fe- Mn-Si-Cr-Ni shape memory alloy. *J. Mater. Eng. Perform.* 21, 2407–2416.

Pricop, B., Söyler, U., Lohan, N. M., Özkal, B., Chicet, D., David, A., et al. (2011). Mechanica1 alloying effects on the thermal behavior of a Fe-Mn-Si-Cr-Ni shape memory alloy under powder form. *Optoelectron. Adv. Mat.* 5, 555–561.

Pricop, B., Söyler, U., Özkal, B., Lohan, N. M., Paraschiv, A. L., Suru, M. G., et al. (2013). Inf1uence of Mechanical Alloying on the Behavior of Fe-Mn-Si-Cr-Ni Shape Memory Alloys Made by Powder Metallurgy. *Materials Science Forum.* 739, 237–241.

Saito, T., Kapusta, C., and Takasaki, A. (2014). Synthesis and characterization of Fe-Mn-Si shape memory alloy by mechanical alloying and subsequent sintering. *Mater. Sci. Eng. A*. 592, 88–94.

Sato, A., Chishima, E., Soma, K., and Mori, T. (1982). Shape memory effect in y ↔ ε transformation in Fe-30Mn-1Si alloy single crystals. *Acta Metall.* 30, 1177–1183.

Sawaguchi, T., Bujoreanu, L. G., Kikuchi, T., Ogawa, K., and Yin, F. (2008). Effects of Nb and C in Solution and in NbC form on the transformation-related internal friction of Fe–17Mn (mass%) alloys. *ISIJ* 48, 99–106.

Sawaguchi, T., Kikuchi, T., Ogawa, K., Kajiwara, S., Ikeo, Y., Kojima, M., et al. (2006). Development of prestressed concrete using Fe-Mn-Si-based shape memory alloys containing NbC. *Mater. Trans.* 47, 580–583.

Shahverdi, M., Czaderski, C., and Motavalli, M. (2016). Iron-based shape memory alloys for prestressed near surface mounted strengthening of reinforced concrete beams. *Constr. Build. Mater.* 112, 28–38.

Söyler, A. U., Özkal, B., and Bujoreanu, L. G. (2010). Sintering Densification and Microstructural Characterization of Mechanical Alloyed Fe-Mn-Si based Powder Metal System, TMS 2010. *Suppl. Proc.* 3, 785–792.

Söyler, A. U., Özkal, B., and Bujoreanu, L. G. (2011). Investigation of Mechanical Alloying Process Parameters on Fe-Mn-Si Based System, TMS 2011. *Suppl. Proc.* 1, 577–583.

Söyler, A. U., Özkal, B., and Bujoreanu, L. G. (2014). Improved shape memory characteristics of Fe-14Mn-6Si-9Cr-5Ni alloy via mechanical alloying. *J. Mater. Eng. Perf.* 23, 2357–2361.

Spiridon, I. P., Pricop, B., Suru, M. G., Paraschiv, A. L., Lohan, N. M., and Bujoreanu, L. G. (2013). The influence of heat treatment atmosphere and maintaining period on the homogeneity degree of a Fe-Mn-Si-Cr-Ni shape memory alloy obtained through powder metallurgy. *J. Optoelectron. Adv. M.* 15, 730–733.

Stanford, N., Dunne, D., and Li, H. (2008). Re-examination of the effect of NbC precipitation on shape memory in Fe–Mn–Si-based alloys. *Scripta Mater.* 58, 583–586.

Sun, L., Huang, W. M., Ding, Z., Zhao, Y., Wang, C. C., Purnawali, H., et al. (2012). Stimulus-responsive shape memory materials: A review. *Mater Design.* 33, 577–640.

Wen, Y.H., Peng, H. B., Raabe, D., Gutierrez-Urrutia, I., Chen, J., and Du, Y. Y. (2014). Large recovery strain in Fe-Mn-Si-based shape memory steels obtained by engineering annealing twin boundaries. *Nature Comm.* 5:4964. doi: 10.1038/ncomms5964

Xu, Z., Hodgson, M. A., and Cao, P. (2015). A comparative study of powder metallurgical (PM) and wrought Fe-Mn-Si alloys. *Mater. Sci. Eng. A.* 630, 116–124.

Xu, Z., Hodgson, M. A., and Cao, P. (2016). Effects of mechanical milling and sintering temperature on the densification, microstructure and tensile properties of the Fe-Mn-Si powder compacts. *J. Mater. Sci. Technol.* 32, 1161–1170.

Zhang, Z., Sandstroma, R., Frisk, K., and Salwen, A. (2003). Characterization of intermetallic Fe-Mn-Si powders produced by casting and mechanical ball milling. *Powder Tech.* 137, 139–147.

Conflict of Interest: AS has been employed by company TETA Glass Technologies.

The remaining authors declare that the research was conducted, between 2009 and 2019, in the absence of any commercial or financial relationships that could be construed as a potential conflict of interest.

frontiers in Materials

ORIGINAL RESEARCH
published: 25 August 2020
doi: 10.3389/fmats.2020.00291

Microstructure and Properties of Ti80 Alloy Fabricated by Hydrogen-Assisted Blended Elemental Powder Metallurgy

Baicheng Wang[1]*, Peng Lei[1], Guangyu Ma[1], Dongdong Li[1], Dmytro Savvakin[1,2,3] and Orest Ivasishin[1,2,3]

[1] College of Materials Science and Engineering, Jilin University, Changchun, China, [2] International Center of Future Science, Jilin University, Changchun, China, [3] G. V. Kurdyumov Institute for Metal Physics, Kyiv, Ukraine

Ti80 (Ti-6Al-3Nb-2Zr-1Mo) is a recently developed near-α titanium alloy that is generally applied in marine applications. In this study, the feasibility of producing the Ti80 alloy via the blended elemental powder metallurgy (BEPM) press-and-sinter method was demonstrated. Generally, the presence of elements with low diffusion mobility in titanium (Mo, Nb) creates difficulties with diffusion-controlled healing of the porosity and the realization of microstructural uniformity. These issues were minimized by using titanium hydride powder instead of titanium powder to activate the sintering, as well as by the proper selection of complex alloying powders rather than elemental powders to promote alloy uniformity. The sintering time-temperature conditions to obtain a chemically and microstructurally homogeneous and nearly-dense alloy microstructure were determined. Special attention was given to the microstructural peculiarities of the sintered material to regulate its mechanical characteristics. Finally, the processing parameters were determined to reach the properties required by alloy specifications. This enabled both the fully beta transformed lamellar microstructure inherent to beta phase field sintering and one that could be modified via post sintering thermomechanical processing.

Keywords: Ti80, powder metallurgy, sintering, microstructure, mechanical properties

Edited by:
Chao Yang,
South China University of Technology,
China

Reviewed by:
Jianan Hu,
Sente Software Ltd., United Kingdom
Chenglin Li,
Wuhan University, China

****Correspondence:***
Baicheng Wang
b.c.wang@foxmail.com

Specialty section:
This article was submitted to
Mechanics of Materials,
a section of the journal
Frontiers in Materials

Received: *19 June 2020*
Accepted: *03 August 2020*
Published: *25 August 2020*

Citation:
Wang B, Lei P, Ma G, Li D,
Savvakin D and Ivasishin O (2020)
Microstructure and Properties of Ti80
Alloy Fabricated by
Hydrogen-Assisted Blended
Elemental Powder Metallurgy.
Front. Mater. 7:291.
doi: 10.3389/fmats.2020.00291

INTRODUCTION

The development of materials and corresponding manufacturing technologies for marine and aerospace applications has attracted growing attention. Titanium alloys are widely used in notable applications because of their good corrosion resistance, high strength to weight ratio, and other well balanced mechanical characteristics. One of the titanium alloys used for marine application is Ti80 (Ti-6Al-3Nb-2Zr-1Mo, mass%), a new alloy developed in China, which shows a good combination of strength and weldability characteristics (Huang et al., 2011).

However, titanium products manufactured with traditional ingot metallurgy processing are generally at least 20 times more expensive than carbon steels and ∼4–5 times more expensive than stainless steels (Fang et al., 2017). The increased cost of titanium ingot metallurgy products is a result of the complicated processing required, which includes multi step vacuum remelting, hot deformation, and, finally, machining with significant material waste.

In contrast, powder metallurgy enables significant cost reduction because expensive operation steps such as vacuum remelting can be avoided and because of near net shape manufacturing of the titanium alloy products. At the same time, powder technologies have issues related to protecting the material from impurities, which could degrade the mechanical properties. The high reactivity of titanium with oxygen, nitrogen, and carbon requires significant efforts to protect the titanium powder with a high specific surface area. Furthermore, chlorine impurities are inevitably present in titanium sponge and powders because of the Kroll manufacturing process; they remain in powder metallurgy materials in the absence of melting operations during processing, resulting in compromised mechanical properties.

A particularly low cost but effective method to achieve titanium alloys with sufficient performance is the blended elemental powder metallurgy (BEPM) method, which includes compaction and vacuum sintering of powder blends comprising the titanium base powder and master alloys (Ivasishin et al., 2000). For BEPM, using titanium hydride TiH_2 powder to replace Ti powder is beneficial in some ways. Titanium hydride is a brittle low strength material and a fine powder of the desired size can be obtained more easily than for ductile titanium. During vacuum sintering, dehydrogenation of the material with a $TiH_2 \rightarrow Ti + 2H$ phase transformation takes place, creating lots of defects in the titanium crystal lattice. This allows for accelerated diffusion, which is beneficial for improved sintering and better homogenization of the powder blends (Cao et al., 2017; Chen et al., 2017; Paramore et al., 2017). Reports have also shown that hydrogen dissolved in the crystal lattices of various metals, including titanium, promotes faster diffusion (Fukai, 2003). Furthermore, highly active atomic hydrogen emitted from the titanium crystal lattice is able to reduce surface oxides via the following reaction:

$$TiO_2 + 2H \rightarrow Ti + H_2O$$

Hydrogen also reacts with C and Cl impurities, thus, cleaning the material and provides an acceptable impurity (O, Cl, C) content in the sintered products. Finally, hydrogen is removed from the material after providing its beneficial effects during sintering and alloy formation; hence, the mechanical properties of the produced alloy are not negatively affected by the presence of hydrogen.

Previous work by Ivasishin (Ivasishin et al., 2000; Ivasishin et al., 2008; Ivasishin et al., 2012; Ivasishin and Moxson, 2015) reported various titanium alloy materials with good mechanical characteristics can be manufactured using the press-and-sinter BEPM approach with TiH_2-based powder blends. Each individual alloy composition needs careful optimization of the starting powders, including the size and chemical composition of alloying powders, compaction parameters, and time-temperature sintering regimes to achieve a desirable alloy microstructure, which is responsible for a good balance of mechanical characteristics. Earlier work on Ti80 dedicated to the influence of alloying element addition on material performance was carried out by Huang et al. (2011). This notable study demonstrated that the alloy could be produced via powder metallurgy, but failed to obtain adequate mechanical properties using TiH_2 powder, especially for elongation. This negative result could be because of the selected processing parameters, which resulted in a suboptimal microstructure and impurity content in the produced Ti80 alloy.

Given the advantages of TiH_2 powder over Ti powder for the BEPM approach, the main challenge in this work was to achieve sufficient mechanical properties for the Ti80 alloy using TiH_2 -based powder blends as a starting material. The Ti80 alloy contains elements with a low diffusion mobility in titanium (Mo, Nb). The presence of elements with a low mobility creates difficulties with diffusion-controlled healing of the porosity and achieving microstructural uniformity during BEPM fabrication (Liu et al., 2006). The present investigation was aimed at realizing a desirable microstructure and acceptable impurity content, and, hence, lead to the production of a Ti80 alloy with good mechanical properties.

MATERIALS AND METHODS

Powder Preparations

Titanium sponge from BaoTi HuaShen Titanium Industry Co., Ltd. (**Table 1**) and casted bulk 50%Al-25%Nb-16.7%Zr-8.3%Mo (mass.%) master alloy were used as starting materials in the present investigation to produce the Ti80 alloy.

Titanium sponge was hydrogenated under laboratory conditions using the prescribed heat treatment under a hydrogen atmosphere (Ivasishin and Moxson, 2015). The produced titanium hydride sponge and bulk master alloy ingot were crushed into smaller pieces; then, they were individually treated via ball milling in the planetary ball mill device to produce powders of the desired sizes. TiH_2 (~0–65 μm) and master alloy (~0–45 μm) powder size fractions were sieved and selected for the experiments. The selected powders were blended under an Ar atmosphere for 4 h. The morphology of the initial powders is shown in **Figure 1**.

A malvern 3000 Laser analyzer was used to investigate the size distribution of the initial powders. The size distribution of the sieved powders obeyed a Gaussian distribution, as shown in **Figure 2**, and both curves show Dx (50) in the proper section.

Consolidation of Ti-6Al-3Nb-2Zr-1Mo

The powder blends were compacted at room temperature via die pressing at 600 MPa. For this, 25 g was used for each sample to produce green compacts with a rectangular shape (65 mm in length, 10 mm in wide, and 11.25 ± 0.10 mm in height), which is convenient for further machining and tensile testing.

Various temperatures (1100, 1150,1200, 1250°C) were tested for sintering the powder compacts. The green compacts were heated in vacuum (10^{-3}Pa) with a rate of 10°C/min up to the selected temperature. Sintering duration of 3 and 4 h was chosen following our previous experience, such duration is usually enough to achieve microstructure homogeneity and sufficient

TABLE 1 | Chemical composition of the used titanium sponge.

Ti	Si	Fe	Cl	C	N	O	Mn	Mg	H
99.7	0.005	0.019	0.038	0.010	0.003	0.047	0.008	0.003	0.001

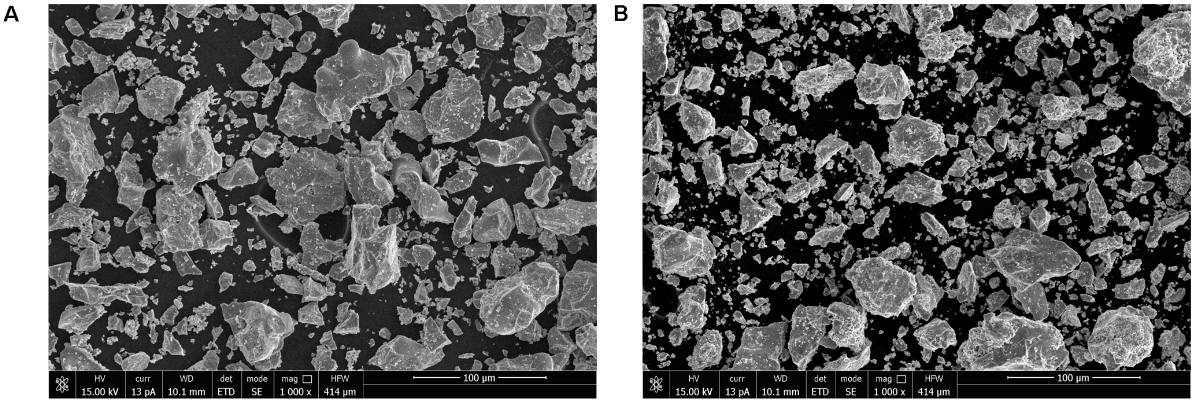

FIGURE 1 | SEM pictures showing the morphology of the starting powders of the selected sizes: **(A)** TiH2 and **(B)** 50%Al-25%Nb-16.7%Zr-8.3%Mo master alloy.

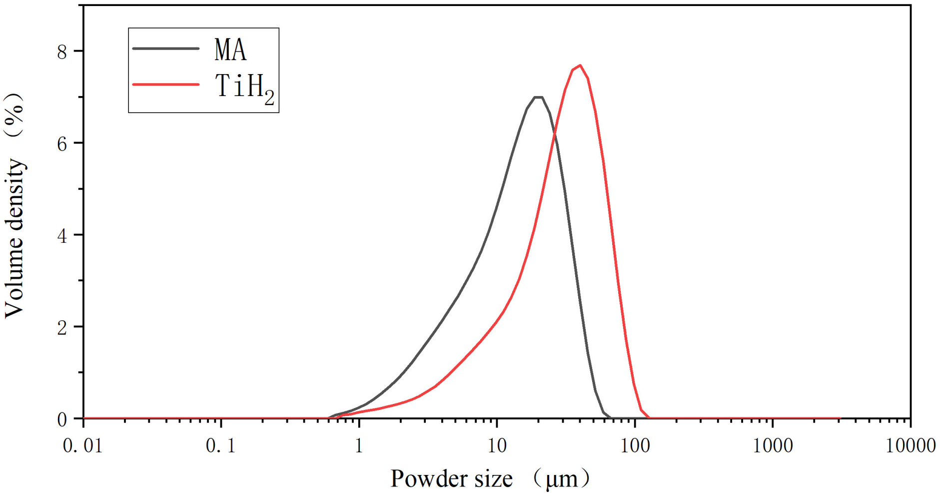

FIGURE 2 | Size distribution curve of TiH_2 and master alloy (MA) powders.

density level. After sintering, materials were cooled in the furnace down to room temperature.

To investigate the potential of post-sintering hot deformation for microstructure improvement, cylindrical green compacts of 29 mm in diameter and 140 mm long, which are suitable for hot deformation, were produced via Cold isostatic Pressing (CIP) under 300 MPa for 10 min. The CIP-treated powder blend preforms were vacuum sintered at 1200°C for 4 h, such sintering regime provides formation of uniform microstructure with minimized porosity. The as-sintered Ti80 billets were then treated by hot rolling in air at 950°C.

Characterization of Sintered Materials

Scanning electron microscopy (SEM, Vega 3 TESCAN) and optical microscopy (Leika Zeiss) were used to study the microstructures of the samples sintered following the above procedure. The Kroll reagent (3%HF, 6%HNO_3, 91%H_2O) was used to reveal the constituent microstructure for light microscopy. The density of the sintered materials was measured via Archimedes' technique and the residual porosity was determined via optical microscopy on the polished cross-sections of the sintered samples. The oxygen, nitrogen, and hydrogen contents in the sintered materials were measured using a LECO 836 system. The chemical composition of the produced alloy was determined by Xi'an Hantang Analysis & Test Co., Ltd. To evaluate the mechanical properties following the various sintering regimes, tensile testing was performed at room temperature using turned cylindrical samples with a gauge diameter of 5 mm, length of 25 mm.

RESULTS AND DISCUSSION

Chemical Composition of Sintered Ti80 Materials

Inductively coupled plasma (ICP) analysis of the sintered material revealed that its average chemical composition was comparable with the proportions expected for the Ti80 alloy (**Table 2**).

The average oxygen (0.18–0.21 wt%), nitrogen (0.0085–0.023 wt%), and hydrogen (0.21–3.7 ppm) contents for the samples sintered with all the tested regimes were at admissible levels. Usually, a 0.15–0.2 wt% content of oxygen in titanium alloys is desirable, a higher value would lower the ductility, while insufficient oxygen content negatively affects the alloy strength. Residual atmospheric impurities (oxygen and nitrogen) present in the sintering chamber, even at relatively good vacuum conditions, are scavenged by titanium; hence, the content of these impurities has a tendency to slightly increase with increasing sintering time and temperature. The reverse trend for hydrogen cleaning of the powder compacts was realized during vacuum heating within the range of 300 − 600°C (Ivasishin et al., 2012), when the majority of hydrogen is emitted from the material. Then, hydrogen completely escapes from titanium if the vacuum heating cycle is sufficiently long. For the temperature, time, and vacuum conditions used in our experiments, the hydrogen content decreased to a sufficient level to avoid hydrogen embrittlement (usually, the standard requirements for hydrogen content in titanium alloys are $<$ 0.01 wt%). Therefore, all the tested sintering regimes provided acceptable impurity (O, N, H) levels in the final samples, which is a necessary condition to achieve good mechanical properties.

Microstructure Analysis and Density Measurement

To select the optimized sintering regime and obtain superior material properties, a set of experiments was carried out to explore the relationship between the microstructure, density (i.e., residual porosity), and temperature-time condition.

To achieve a good balance of mechanical properties, the sintered material should demonstrate a completely uniform microstructure, minimized volume fraction of spherical residual pores, and a fine grain size. Usually, a longer duration at a higher sintering cycle temperature promotes chemical and microstructure uniformity of the material, a higher sintered density, and a desirable spherical morphology of residual pores, however, this simultaneously results in an increased grain size, which negatively affects the tensile elongation. Furthermore, insufficient sintering time and a low temperature results in a decrease in the relative density, inadequate time for pore healing, and potentially unfinished diffusion redistribution of the alloying elements in the titanium matrix, which results in considerable microstructure inhomogeneity. Such sintered microstructures are unsuitable because they naturally result in markedly poorer mechanical performance.

Taking into consideration the above points and the results of earlier studies dedicated to BEPM production of other titanium compositions (Ivasishin et al., 2008; Ivasishin and Moxson, 2015), we selected sintering temperatures in the range of 1100 − 1250°C which corresponds to the single-phase β field. At lower sintering temperatures α stabilizing aluminum is able to block diffusion redistribution of the β stabilizers (Nb, Mo) in the titanium matrix (Ivasishin et al., 2008) from the alloying particles, while temperatures > 1250°C create a risk for excessive grain growth. The realization of chemical uniformity of the alloyed titanium matrix usually takes ∼2 h or more, and this is considerably dependent on the size and chemical composition of the alloying powder used as well as on temperature. Taking into consideration the relatively low diffusion mobility of Nb and Mo in titanium (Kale and Patil, 1994; Thibon et al., 1998; Laik et al., 2006), we tested sintering times of 3 and 4 h.

TABLE 2 | Chemical composition of sintered material (wt.%).

Al	Mo	Zr	Nb	Fe	Ti
5.78	0.97	1.83	2.94	0.23	balanced

The microstructures of the sintered materials are shown in **Figures 3a–e**. An important observed result is that all the used time-temperature sintering regimes realized sufficient microstructural uniformity; thus, the transformation of the heterogeneous powder blend into a homogeneous alloy was achieved. The as-sintered Ti80 materials demonstrated a typical lamellar α + β microstructure, which formed during cooling to room temperature after sintering within the β phase field. It should be noted that the α lamellae precipitated inside β grains were nearly the same size for all sintering regimes; this can be attributed to the same post-sintering cooling rate. An exception is the presence of some relatively coarse isolated α-phase crystallites of near equiaxed shape located among the lamellar α + β structure, which can be seen at the lowest sintering temperature of 1100°C (**Figures 3a,b**).

Coarse α-phase precipitates also clearly formed at some of the locations with increased concentration of α stabilizers (Al, as well as O and N impurities); this could either be attributed to remnants of the α phase that were not totally transformed into the β phase during sintering at 1100°C, or, more probably, they formed during cooling because of the higher rate of α nucleation and growth at these locations.

Time-temperature parameters of the sintering clearly affected the size of the β grains and the residual porosity. The relationship of the β grain size and the sintered density are shown in **Figures 4**, **5**. It can be observed from the corresponding microstructures (**Figure 3**) that grain growth increases alongside increasing sintering temperature, resulting in coarser β grains. Additionally, the grain size is naturally coarser for longer sintering times (sintering for 4 h compared with the 3 h group, **Figure 4**).

The density values markedly increased with temperature and time with a corresponding decrease in the residual porosity. The increased density demonstrated a non-linear behavior with temperature, with noticeable densification as the temperature increased from 1150 to 1200°C. Low sintering temperatures (1100 and 1150°C) led to the lowest density values for both 3 and 4 h sintering durations (**Figure 5**). From **Figure 3**, it can be seen that the sintering temperatures resulted in a wider size distribution of residual pores and their shape was far from spherical (**Figure 3a** as an example). The evolution of the pore structure on densification began with extensive healing of the pores during material heating and at the very beginning stages of

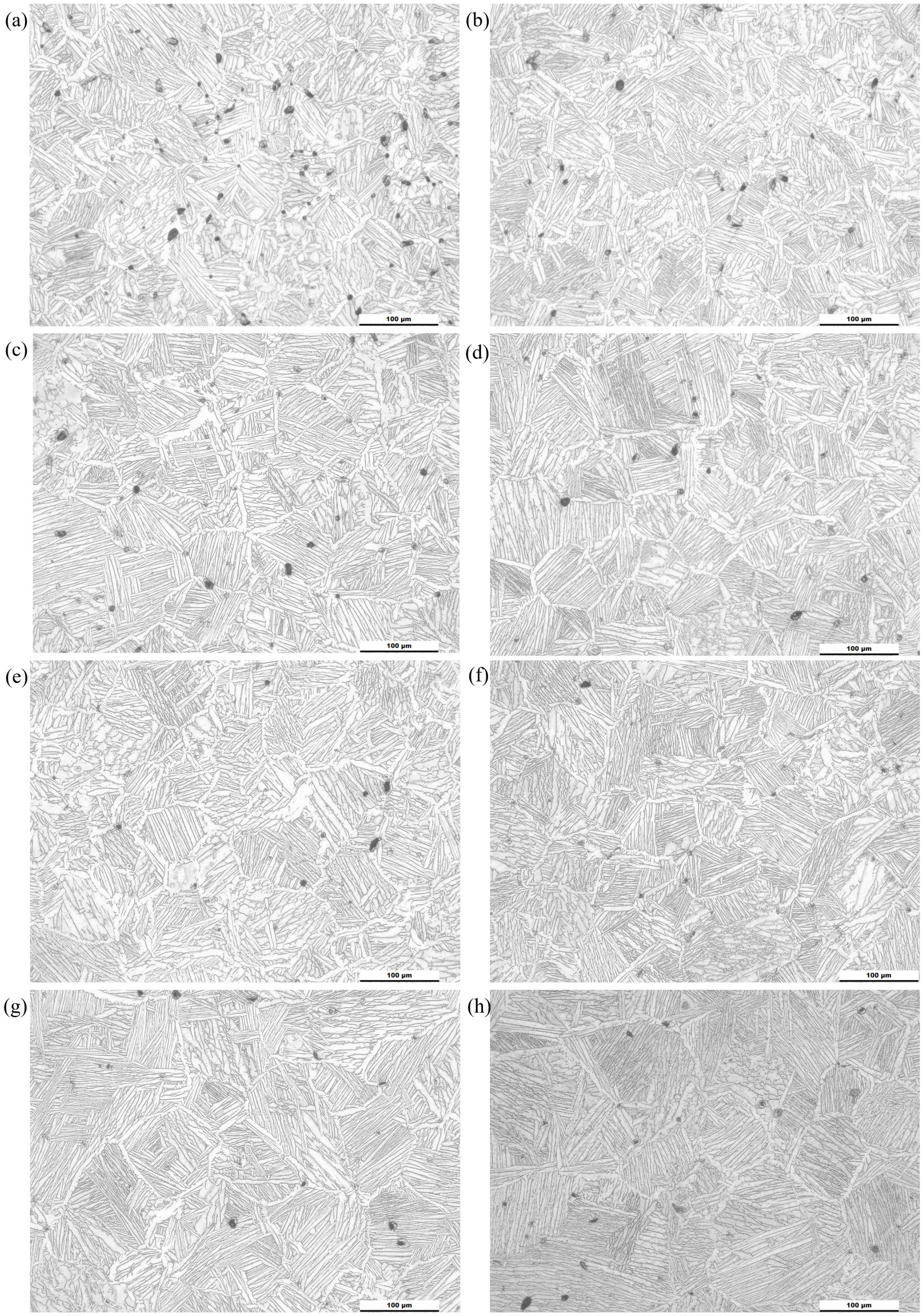

FIGURE 3 | Microstructure of sintered material: **(a,c,e,g)** represent 3 h at 1100, 1150, 1200, 1250°C; **(b,d,f,h)** represent 4 h at 1100, 1150, 1200, 1250℃, respectively.

isothermal sintering, then, this process slowed down. Because the pores are effective barriers for grain boundary movement, which restricts grain merging and growth, grain growth was minimal in these stages. A gradual decrease in the volume fraction of the pores with time led to more pronounced grain growth (**Figure 3b**), while densification slowed. There was minimal possibility for intragrain pores to be eliminated in the coarse grained structures via the vacancy flowing mechanism, which is because of the large distance from the pores to the nearest grain boundaries where vacancies annihilate. Hence, instead of

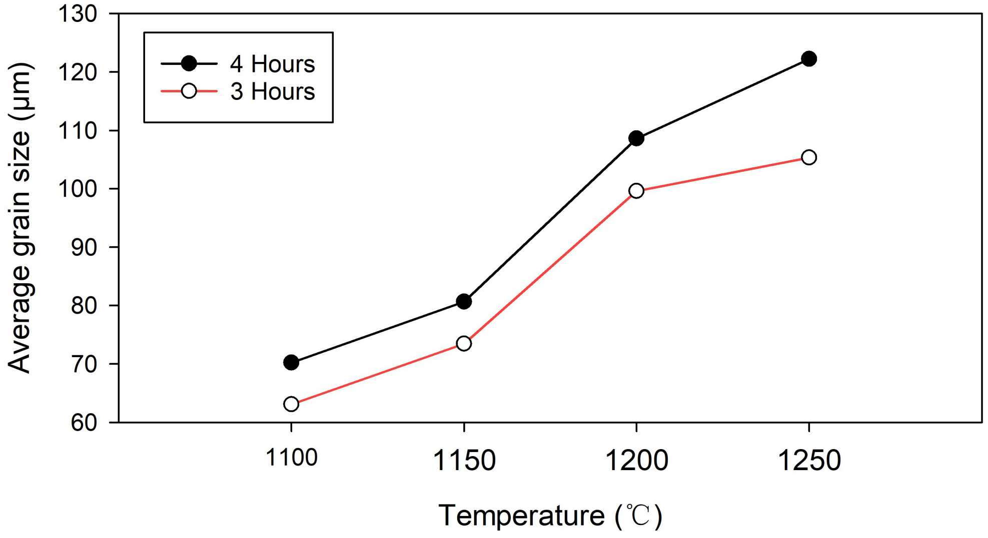

FIGURE 4 | The average β grain size depending on time-temperature sintering conditions.

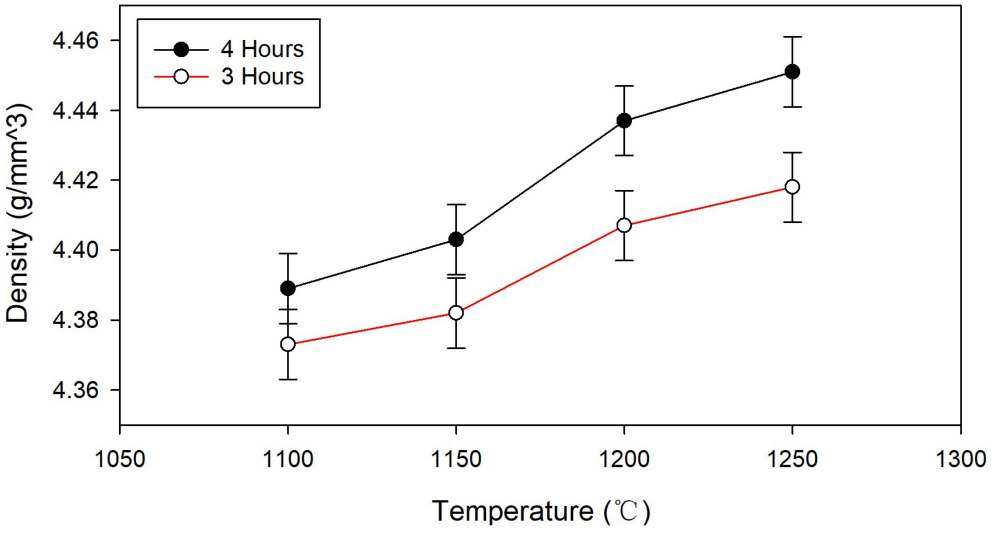

FIGURE 5 | Density of the Ti80 materials depending on sintering temperature and time.

pore healing, pore coalescence became more probable in the coarse-grained structures (small pores merged into a larger one inside the coarse grain).

Insufficient time and temperature have a noticeable impact on the pore healing process, which caused the difference in **Figure 3**. At relatively low temperatures (1100 – 1150°C) densification was hindered and remained far from realization of the full potential density, with preservation of the increased volume fraction of pores (2.7–3.1%, **Figures 3a,b**). The pores heal with increasing temperature and sintering time (**Figure 6**), while their shape gradually transformed from an irregular shape (**Figure 6A**) to a spherical one with increased sintering (**Figure 6B**). The lowest porosity measured was 1.3% for the regime at 1250°C for 4 h.

Irregular pore morphology (elongated with sharp corners) is detrimental to the mechanical properties. The locations with such pores become a weak area during loading and deformation. For achievement of high overall performance, residual pores with a spherical morphology and small size are preferable.

The non-linear dependence of the density growth (**Figure 5**) once more confirms the inability to achieve dense (poreless) structures with increased temperature and sintering time. The retardation of the densification process can be caused by gases trapped in the pores, while pore channels between the powder particles close. It should be noted that hydrogen emission from the titanium hydride powder and the emission of other volatile impurities usually takes place at relatively low temperatures (below ∼ 800°C) when the pore channels are not yet closed, thus, eliminating the noted negative effect on densification in present case. However, lengthening the sintering time or rise temperature would not effectively help the density, otherwise it would result in noticeably larger beta grain size, which is undesirable in most cases.

Tensile Properties

The typical stress-strain behavior lines of the 4-h-sintered Ti80 materials are displayed in **Figure 7**. It can be seen that all the samples demonstrated an acceptable balance of strength and ductility. On increasing the sintering temperature from 1100 to 1250°C, the ultimate tensile strength and yield stress values increased. This behavior can be attributed mainly to the useful decrease in residual porosity with increased sintering temperature, while simultaneous increase in grain size as well as analog intragrain $\alpha + \beta$ microstructure and grain boundary α layers formed due to similar cooling conditions for all materials does not noticeably affect strength characteristics.

In more detail, the relationship of the ultimate tensile strength (UTS) and elongation of different Ti80 materials is shown in **Figure 8**. Both the tensile strength and ductility increased with increased sintering time, but a drop in tensile elongation is

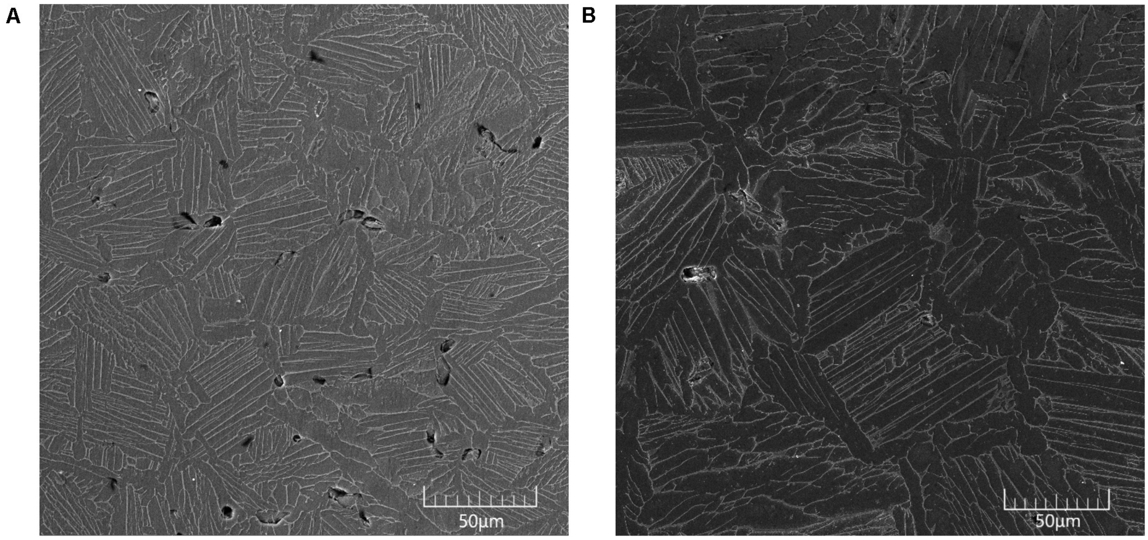

FIGURE 6 | Transformation of porosity in sintered Ti80 alloy depending on sintering temperature: **(A)** 1100°C 4 h and **(B)** 1250°C 4 h (SEM).

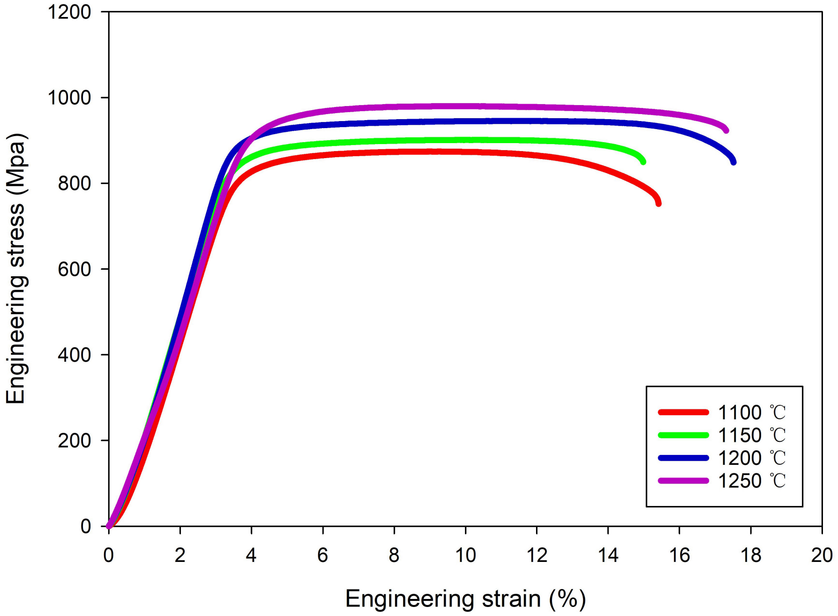

FIGURE 7 | Stress-Strain curves for the Ti80 samples sintered at different temperatures for 4 h.

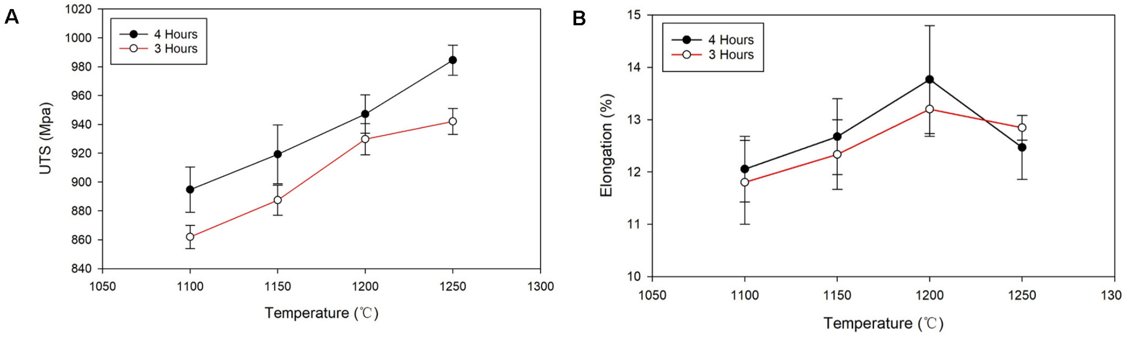

FIGURE 8 | UTS **(A)** and elongation **(B)** of sintered Ti80.

observed from 1200 to 1250°C. This can be explained by the simultaneous effect of the residual porosity and grain size on the mechanical characteristics (**Table 3**). A longer sintering time and higher temperature result in a decrease in residual porosity (from ∼3 to 1%) along with simultaneous β grain growth (from 63 to 122 μm). A lower porosity with fine residual pores and a spherical shape is preferable for both strength and elongation characteristics. However, the formation of coarse grains is detrimental for ductility, while having a negligible effect on strength. This is why the structure with minimized porosity demonstrated an effective improvement in the strength independently on coarse grains formation. The elongation demonstrated a similar trend as the temperature increased up to 1200°C; further increasing the temperature resulted in the reverse trend compared with the UTS. The ductility decreased for the highest sintering temperature of 1250°C; this is because the negative effect of the coarse (122 μm) grains was more significant than the positive contribution afforded by the reduced porosity. It should be noted, some difference in tensile characteristics for similar samples (error values noted in **Table 3**) with corresponding error bars shown in **Figure 8** can be explained mainly with random distribution of pores over the material. Non-uniformity in size, morphology and locations of residual pores slightly affects strength characteristics, while becomes more significant for tensile elongation.

It can be concluded that the optimal balance of tensile characteristics is realized with the microstructure obtained with sintering at 1200°C for 4 h, which gives an optimized grain size and reduced porosity. However, if specific conditions of practice application of produced Ti80 materials need highest possible strength without rigid requirements to ductile characteristics, the sintering temperature should be increased to 1250°C.

TABLE 3 | Room temperature tensile properties and microstructure characteristics of the Ti80 alloys.

	UTS (MPa)	Elongation (%)	Average residual porosity (%)	Average β grain size (μm)
1100°C-4 h	890 ± 15	12.2 ± 0.5	2.7%	70.2
1100°C-3 h	863 ± 17	11.9 ± 0.6	3.1%	63.1
1150°C-4 h	920 ± 20	12.7 ± 0.6	2.4%	80.75
1150°C-3 h	884 ± 14	12.1 ± 0.9	2.9%	73.7
1200°C-4 h	948 ± 12	14.0 ± 0.8	1.6%	108.6
1200°C-3 h	926 ± 14	13.2 ± 0.5	2.3%	99.6
1250°C-4 h	987 ± 8	12.4 ± 0.6	1.3%	122.2
1250°C-3 h	943 ± 8	12.7 ± 0.4	2.0%	105.3

Figure 9 shows an SEM images of the fracture surface with sintering at 1200 and 1100°C for 4 h after tensile testing at room temperature. Both (a) and (b) show a dimple fracture of the material; but (b) clearly shows a coarse surface and larger dimples than a), which indicated that the structure in (b) has inferior ductility.

Hot Deformation

To investigate the possibility of obtaining a modified poreless microstructure for the Ti80 alloy via post-sintering treatment, bars of CIP-treated samples at 300 MPa with sintering at 1200°C for 4 h were used. The as-sintered CIP TI80 shows an average density of 4.39g/cm^3, which is close to the value of 4.42 g/cm^3 obtained under the same sintering condition after uniaxial die compaction at 600 MPa. Sintered bars 26.5 ± 0.5 mm in diameter were hot rolled at 950°C, lower than phase transformation point (Yuan et al., 2013), with a diameter reduction to 15.5 ± 1 mm; thus, the reduction in the cross sectional area indicates ∼66% deformation occurred.

In **Figure 10**, the optical microscopy microstructure after rolling indicated that the lamellar α + β structure had been substantially broken and most of the pores were eliminated. Archimedes' technique revealed that the average density reached ∼4.49 g/cm^3, such an increase in density is in accordance with the less than 0.4% fine pore content observed in the microstructure (**Figure 10**). With the crushed structure, the grain boundaries could be hardly recognized, however, a refined basket weave structure with a relatively low residual porosity is promising for further improvement of the mechanical properties, such as the tensile strength, elongation, and fatigue characteristics. A reduction in the deformation temperature is a potential route to produce a poreless equiaxed microstructure. Thus, post-sintering hot deformation of Ti80 alloy can be recommended for some specific applications to meet rigid requirements for the mechanical characteristics.

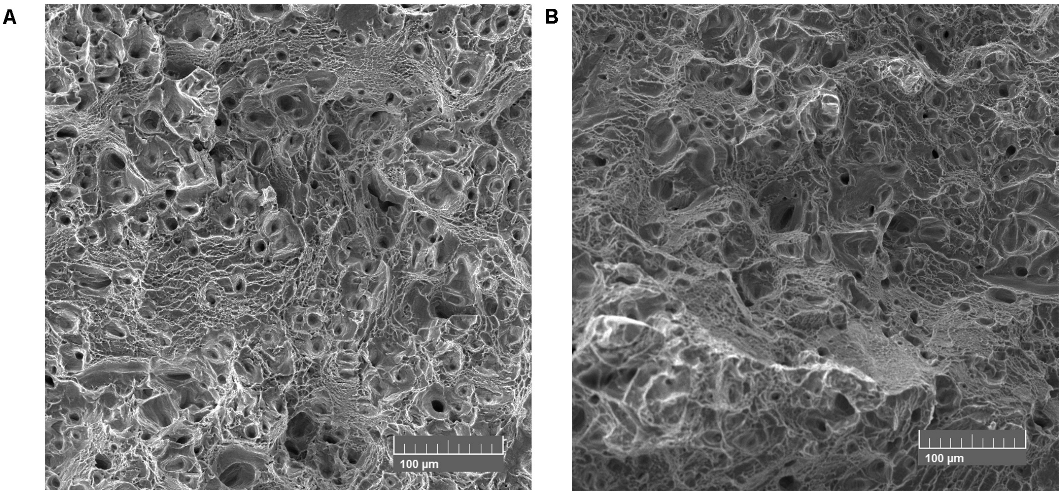

FIGURE 9 | Fracture surfaces of the Ti80 alloys produced with 4 h sintering at: **(A)** 1200℃ and **(B)** 1100°C.

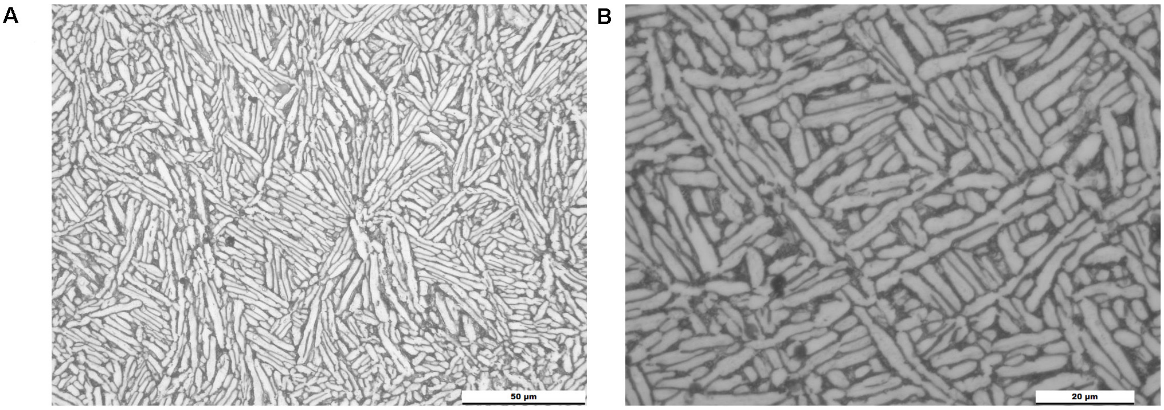

FIGURE 10 | As-rolled Ti80 microstructures via optical microscop at ×500 **(A)** and ×1000 **(B)** magnification.

CONCLUSION

1. In this work, a uniform low-porous Ti80 alloy with an acceptable impurity content was produced via the press-and-sinter BEPM approach using blends of TiH_2 and Al-Zr-Nb-Mo master alloy powders.
2. The influence of different time-temperature sintering parameters on the microstructure, including the residual porosity, grain size, and mechanical properties was carefully analyzed. The microstructure produced with sintering at 1200°C for 4 h shows the best balance of strength/ductility characteristics owing to the reduced residual porosity (1.6%) and relatively fine (108 μm) grain size.
3. The achieved balance of strength (UTS 948 ± 12 MPa) and ductile characteristics (elongation 14.0 ± 0.8%) is promising to consider practical application of the Ti80 alloy manufactured using the notably cost-effective BEPM approach.
4. Post-sintering hot deformation treatment, like rolling, can be recommended to form a dense Ti80 alloy ($< 0.4\%$ pores) with a refined $\alpha + \beta$ microstructure. Hot-deformed microstructures are promising for further improvement of mechanical characteristics.

DATA AVAILABILITY STATEMENT

All datasets presented in this study are included in the article/supplementary material.

AUTHOR CONTRIBUTIONS

BW collected the experimental data, performed the data analysis, and wrote the manuscript. PL and GM were involved in the work of rolling. DL, DS, and OI supervised the experiments and overall editing of the manuscript. All authors contributed to the article and approved the submitted version.

REFERENCES

Cao, F., Chandran, K. S. R., and Kumar, P. (2017). New approach to achieve high strength powder metallurgy Ti-6Al-4V alloy through accelerated sintering at β-transus temperature and hydrogenation-dehydrogenation treatment. *Scr. Mater.* 130, 22–26. doi: 10.1016/j.scriptamat.2016.11.005

Chen, G., Liss, K. D., Auchterlonie, G., Tang, H., and Cao, P. (2017). Dehydrogenation and sintering of TiH2: an in situ study. *Metall. Mater. Trans. A* 48, 2949–2959. doi: 10.1007/s11661-017-4043-8

Fang, Z. Z., Paramore, J. D., Sun, P., Chandran, K. S. R., Zhang, Y., Xia, Y., et al. (2017). Powder metallurgy of titanium – past, present, and future. *Int. Mater. Rev.* 63, 407–459. doi: 10.1080/09506608.2017.1366003

Fukai, Y. (2003). Formation of superabundant vacancies in M–H alloys and some of its consequences: a review. *J. Alloys Compd.* 356-357, 263–269. doi: 10.1016/s0925-8388(02)01269-0

Huang, Y., Tang, H., Jia, W., Liu, H., and He, W. (2011). Influence of element addition ways on the performance of Ti-6Al-3Nb-2Zr-1Mo Alloy. *Rare Metal Mater. Eng.* 40, 163–167.

Ivasishin, O. M., Anokhin, V. M., Demidik, A. N., and Savvakin, D. G. (2000). Cost-effective blended elemental powder metallurgy of titanium alloys for transportation application. *Key Eng. Mater.* 188, 55–62. doi: 10.4028/www.scientific.net/KEM.188.55

Ivasishin, O. M., Eylon, D., Bondarchuk, V. I., and Savvakin, D. G. (2008). Diffusion during powder metallurgy synthesis of titanium alloys. *Defect Diffus. Forum* 277, 177–185. doi: 10.4028/www.scientific.net/DDF.277.177

Ivasishin, O. M., and Moxson, V. S. (2015). Low-cost titanium hydride powder metallurgy. *Titanium Powder Metall.* 2015, 117–148. doi: 10.1016/b978-0-12-800054-0.00008-3

Ivasishin, O. M., Savvakin, D. G., Gumenyak, M. M., and Bondarchuk, O. B. (2012). Role of surface contamination in titanium PM. *Key Eng. Mater.* 520, 121–132. doi: 10.4028/www.scientific.net/KEM.520.121

Kale, G. B., and Patil, R. V. (1994). Chemical diffusion in titanium-molybdenum system. *Mater. Trans. Jim* 35, 439–444. doi: 10.2320/matertrans1989.35.439

Laik, A., Kale, G. B., and Bhanumurthy, K. (2006). Interdiffusion studies between a Mo-based alloy and Ti. *Metall. Mater. Trans. A* 37, 2919–2926. doi: 10.1007/s11661-006-0173-0

Liu, Y., Chen, L. F., Tang, H. P., Liu, C. T., Liu, B., and Huang, B. Y. (2006). Design of powder metallurgy titanium alloys and composites. *Mater. Sci. Eng. A* 418, 25–35.

Paramore, J. D., Fang, Z. Z., Dunstan, M., Sun, P., and Butler, B. G. (2017). Hydrogen-enabled microstructure and fatigue strength engineering of titanium alloys. *Sci. Rep.* 7:41444. doi: 10.1038/srep41444

Thibon, I., Ansel, D., Boliveau, M., and Debuigne, J. (1998). Interdiffusion in the β Mo - Ti Solid Solution at High Temperatures. *Zeitschrift Für Metallkunde* 89, 187–191.

Yuan, M., Cao, Y., Zhang, Y., Jiangtao, Y., Ji, L. I., and Zhang, L. (2013). Measurement for phase transformation Point of Ti80 Alloy. *Hot Work. Technol.* 42, 57–59. doi: 10.14158/j.cnki.1001-3814.2013.14.036

Conflict of Interest: The authors declare that the research was conducted in the absence of any commercial or financial relationships that could be construed as a potential conflict of interest.

The handling editor declared a past co-authorship with one of the authors OI.

frontiers
in Materials

ORIGINAL RESEARCH
published: 29 October 2020
doi: 10.3389/fmats.2020.537812

Fine-Grained FeCoNi(CuAl)$_x$ High Entropy Alloys: Phase Transformation, Microstructure Evolution and Mechanical Properties

Yan Long[1]*, Guiqi Li[2], Xiaobiao Liang[2] and Haiyan Peng[1]

[1]*Guangdong Key Laboratory for Advanced Metallic Materials, School of Mechanical and Automotive Engineering, South China University of Technology, Guangzhou, China,* [2]*National Near-Net-Shape Forming Engineering Research Center for Metallic Materials, Guangzhou, China*

OPEN ACCESS

Edited by:
Suryanarayana Challapalli,
University of Central Florida,
United States

Reviewed by:
Ho Jin Ryu,
Korea Advanced Institute of Science and Technology, South Korea
Peter K Liaw,
The University of Tennessee,
United States

***Correspondence:**
Yan Long
ylong1@scut.edu.cn

Specialty section:
This article was submitted to Mechanics of Materials, a section of the journal Frontiers in Materials

Received: *25 February 2020*
Accepted: *23 September 2020*
Published: *29 October 2020*

Citation:
Long Y, Li G, Liang X and Peng H (2020) Fine-Grained FeCoNi(CuAl)$_x$ High Entropy Alloys: Phase Transformation, Microstructure Evolution and Mechanical Properties. Front. Mater. 7:537812. doi: 10.3389/fmats.2020.537812

A series of fine-grained FeCoNi(CuAl)$_x$ (x = 0, 0.4, 0.6, 0.8, 1.0) medium-entropy alloy (MEA) and high-entropy alloys (HEAs) were fabricated by Mechanical Alloying (MA) and Spark Plasma Sintering (SPS). The effect of Al and Cu content (x) on phase composition, microstructure, and mechanical properties of the alloys was investigated. Experimental results show that the crystal structure of FeCoNi(CuAl)$_x$ alloy transforms from single (face-centered cubic) FCC phase for $x = 0$ to FCC + BCC duplex phases for $x = 0.4$~1.0, with the fraction of (body-centered cubic) BCC phase gradually increasing with the increase of x. Adding a low content of Al and Cu elements to FeCoNi alloy can significantly hinder the grain growth during sintering process, the average grain size of FCC phase decreases from 0.95 to 0.30 μm at $x = 0.4$. However, the grain sizes of FCC and BCC phases gradually grow up when x increases from 0.4 to 1.0. The variation in grain size indicates that the atomic diffusion rate of sintered alloy may be influenced by the sluggish diffusion effect in HEA as well as the content of Al and Cu with lower melting points. Mechanical properties of the HEAs are mainly affected by the volume fraction of BCC phase. The compressive yield strength and hardness of HEAs are improved at first and then slightly reduced, while the plasticity drops down continuously with the increase of x. The bulky HEA achieved excellent comprehensive mechanical properties with a compressive yield strength of 1,467.7 MPa and plastic strain to failure of 24.9% at $x = 0.6$, due to the fine duplex microstructure.

Keywords: high-entropy alloys, phase transformation, fine-grained, mechanical properties, spark plasma sintering

INTRODUCTION

Different from traditional alloy design strategies, the concept of high-entropy alloys (HEAs) was first proposed by Yeh et al. in 2004. Generally, HEAs consist of at least five constituents in equimolar or near equimolar proportions, with atomic concentration ranging between 5% and 35% (Yeh et al., 2004; Ye et al., 2016; Miracle and Senkov, 2017). Due to their special multiple-principal-element composition and high configurational entropy, HEAs generally tend to form simple solid solution phases like face-centered cubic (FCC), body-centered cubic (BCC), hexagonal close-packed (HCP) phases or a mixture of them. In addition, some HEAs have promising properties, such as excellent mechanical properties (Zhang et al., 2014; Fu et al., 2018; Lei et al., 2018; Long et al., 2019; Zhang et al., 2020), oxidation resistance (Nong et al., 2018), high-temperature mechanical properties (Senkov et al., 2018a; Senkov et al., 2018b; Senkov et al., 2018c), outstanding wear resistance (Ye et al., 2018; Li et al., 2019) and corrosion resistance (Fujieda et al., 2017; Luo et al., 2018; Zhou et al., 2019), and so on. This new alloy system has been extensively researched in recent years.

FeCoNiCr-based HEA is one of the earliest proposed and most intensively investigated alloy systems. They usually consist of single-phase FCC structure or FCC + BCC dual-phase structure. Generally, single FCC-phase HEAs are ductile but soft (Li et al., 2017; Xiang et al., 2019), and single BCC-phase HEAs have high strength but are less ductile (Senkov et al., 2011; Zhang et al., 2012), while a combination of these two phases can make a good balance between strength and ductility (Lu et al., 2014). The general strengthening method of FeCoNiCr HEA is adding other elements (Al, Ti, Mn, Cu, Mo, etc.) to study their effects on the phase composition and mechanical properties [such as FeCoNiCrCu (Zhang et al., 2011), FeCoNiCrAl (Tian et al., 2019), FeCoNiCrMn (Han et al., 2019), FeCoNiCrMo$_x$ (Liu et al., 2016), etc.]. Tong et al. (2019) prepared a precipitation-strengthened FeCoNiCrTi$_{0.2}$ high-entropy alloy using arc melting and casting methods. It exhibits a great increase in yield strength ($\sigma_{0.2}$) and ultimate tensile strength (σ_{UTS}), with little loss in ductility at room temperature compared with the single-phase FeCoNiCr parent alloy; in addition, at cryogenic temperatures, its $\sigma_{0.2}$ and σ_{UTS} are increased from 700 MPa to 1.24 GPa to 860 MPa and 1.58 GPa, respectively, associated with a ductility improvement from 36% to 46%. In recent years, systematic studies on FeCoNiCuAl HEA and its variant alloys prepared by different methods have been carried out. Zhuang et al. (2012) and Zhuang et al. (2013) studied the microstructure and mechanical properties of a series of FeCoNiCuAl high-entropy alloys in as-cast and heat-treated conditions. During the casting process of FeCoNiCuAl HEA, Cu element tends to segregate to interdendritic regions, which affects the comprehensive properties of the material. Fu et al. (2016) prepared a CoNiFeAl$_{0.3}$Cu$_{0.7}$ HEA with single-phase FCC structure by a combination method of Mechanical Alloying (MA) and Spark Plasma Sintering (SPS). Its yield strength and hardness were 1795 MPa and 454 Hv, respectively. Compared with the casting method, the combination of MA + SPS has advantages of low-temperature sintering, rapid sintering, multi-field coupling, etc., which makes the prepared alloys have the characteristics of high density, fine grains, uniform microstructure and less segregation.

According to earlier researches (Tung et al., 2007; Li et al., 2010; Yang et al., 2015; Matusiak et al., 2019), in FeCoNiCuAl HEAs, Al element can promote the formation of BCC phase, while Cu element can stabilize FCC phase. Actually, the addition of Al and Cu into FeCoNi medium-entropy alloy (MEA) might not only increase the entropy of alloy, lead to the phase transformation, but also influence the diffusion rate and grain growth of the alloy at elevated temperature. In the present work, the competitive influence of Al and Cu elements on the phase formation of the alloy was researched, bulky FeCoNi(CuAl)$_x$ (x = 0~1, means the content of Cu and Al elements) MEA and HEA samples with fine grains were prepared by powder metallurgy method (MA + SPS), the mechanical alloying behavior of powders during ball milling process and the phase formation of bulky MEA and HEAs during sintering were analyzed; the grain sizes in various sintered samples were measured in order to evaluate the atomic diffusion rate of HEAs; meanwhile, the effects of Al and Cu content on phase formation, microstructure evolution and mechanical properties of FeCoNi(CuAl)$_x$ (x = 0, 0.4, 0.6, 0.8, 1.0) MEA and HEAs were also investigated.

EXPERIMENTAL

In the present experiment, five kinds of elemental powders, Fe, Co, Ni, Cu and Al, with purity greater than 99.9 wt%, were used as raw materials. Their physical properties are shown in **Table 1**. These five elements were mixed with each other in proportions of FeCoNi(CuAl)$_x$ (x = 0, 0.4, 0.6, 0.8, 1.0), the mixing enthalpy among the relative elements are shown in **Table 2**.

The mixed powders were then placed in a stainless-steel ball mill tank at a ball-to-material ratio of 12:1 and the MA process was performed under the protection of high purity argon atmosphere. In the vacuum glove box, a small amount of powders ball-milled for 10, 20, 30 and 40 h were taken out for analysis. The powders ball milled for 40 h were subsequently consolidated in a graphite die by a spark plasma sintering (SPS) machine (Sumitomo Coal Mining Co., Ltd., Japan) at 1,100°C for 10 min in vacuum atmosphere. The sintering pressure was 50 MPa. The powders were heated to the sintering temperature at the heating rate of 100°C min^{-1}. The fabricated bulky HEA samples were cylinders with a diameter of 20 mm and height of 10 mm.

The phase analysis of ball milled powders and sintered samples were conducted by a Bruker D8 ADVANCE X-ray diffractometer (XRD) with a rotating Cu anode and cross-beam optics selection Cu-K$_\alpha$ ($\lambda_{\alpha1}$ = 1.54059 Å, $\lambda_{\alpha2}$ = 1.54441 Å). Its scanning step was 0.02° and the angular 2θ range was $20° < 2\theta < 100°$. The thermal analysis of the alloy powders milled for 40 h were performed in the Differential Scanning Calorimeter (DSC, NETZSCH STA 449C) from room temperature to 1,280°C with a heating rate of 10 K min^{-1} under flowing high purity argon atmosphere. Microstructures of sintered samples were observed by Scanning Electron Microscope (SEM, Nova Nano SEM 430, United States). The phase composition and microstructure of bulk alloys were analyzed by Transmission Electron Microscope (TEM, TECHNAL G2 F20 S-TWIN, United States) with an EDS. Specimens for TEM tests were thinned by mechanical polishing and then via ion beam thinning. After that, the samples were cleaned with acetone first and then with absolute ethyl alcohol. The electron back-scattered diffraction (EBSD) was used to investigate the phase distribution of sintered samples, mechanically polished and ion polished specimens were used for observation. Densities of consolidated alloy samples were measured by Archimedes principle method. The measuring medium was deionized water. The hardness test (according to the Chinese national standard-GB/T 4340.1-2009) was carried out by a digital Micro Hardness (Tester HVS-1000 Vickers hardness apparatus) at a load of 500 gf holding for 20 s. Ten

TABLE 1 | Characteristic parameters of alloy elements.

Element	Molar mass (g mol^{-1})	Lattice constant (Å)	Atomic radius (Å)	Electronegativity	Melting point (K)	Density (g cm^{-3})	Crystal structure
Fe	55.85	2.87	1.26	1.83	1,811	7.87	BCC
Co	58.93	2.51	1.25	1.88	1,768	8.9	HCP
Ni	58.69	3.52	1.24	1.91	1,728	8.91	FCC
Cu	63.55	3.61	1.28	1.90	1,358	8.96	FCC
Al	26.89	4.05	1.43	1.61	933	2.70	FCC

TABLE 2 | Mixing enthalpy of atomic pairs (kJ mol^{-1}).

Element	Fe	Co	Ni	Cu	Al
Fe	—	−1	−2	13	−11
Co	—	—	0	6	−19
Ni	—	—	—	4	−22
Cu	—	—	—	—	−1
Al	—	—	—	—	—

points were evenly selected on the sample for measurement to obtain the average value, with each indent spaced about 0.5 mm from one another. The samples for XRD, SEM, Density and Hardness test were cut to the size of 6 × 6 × 8 mm, then mechanically polished and ultrasonic cleaned. Compressive properties at room temperature were measured by a universal testing machine (AG-100 KNx, Shimadzu Corporation, Japan) at a strain rate of 10^{-3} s^{-1} using cylinder specimens with the size of Φ3 × 6 mm and three compression specimens were measured for each component. In order to avoid the influence of carbon diffusion during sintering, the surface of sintered samples were cut off by 1 mm by wire electrical discharge machining before sampling and analyzing.

RESULTS AND DISCUSSION

Phase Transformation and Microstructure Evolution

X-ray diffraction (XRD) patterns illustrate the mechanical alloying process of pre-mixed elemental powders with different compositions during ball milling and their phase compositions, as shown in **Figure 1**. It is found that with the increase of milling time, the intensities of diffraction peaks of original elements decrease sharply and meanwhile peaks of a new solid solution phase emerge. After ball milling for 20~40 h, single FCC phases are identified as basic crystal structure in the mechanically alloyed powders. It is noticed that when the content of Al and Cu elements increases from 0 to 1.0, the mechanical alloying rate becomes slower, indicating that the addition of Al and Cu elements to Fe-Co-Ni powders slows down the process of mechanical alloying and increases the time required to form a solid solution phase, without affecting the final solid solution structure. According to **Table 1**, Fe, Co, and Ni have similar electronic structure and atomic radius, so these three elements tend to form substitutional solid solution easily in the process of mechanical alloying. When Cu and Al elements are added, due to their relatively large atomic radius, large lattice distortion would be introduced during the alloying process, and the number of elements also increases, which might hinder the mechanical alloying process. In high-entropy alloys, the formation of a new phase depends on the cooperative diffusion of many different kinds of atoms, the interaction between different kinds of atoms and the severe lattice distortion would decrease the effective diffusion rate in HEAs and thus the mechanical alloying time needed to form a solid solution phase would increase. Furthermore, the grain size and lattice strain of the respective powders ball milled for 40 h are calculated from the diffraction peak widths by Williamson-Hall equation (Williamson and Hall, 1953) and are given in **Table 3**. After ball milling for 40 h, the average grain sizes of powders are reduced to 12.71~29.83 nm.

DSC curves for FeCoNi(CuAl)$_x$ alloy powders milled for 40 h are shown in **Figure 2**. There are no obvious exothermic or endothermic peaks in the DSC curve for $x = 0$, which means during the heating process the powder has good thermal stability and remains the single FCC structure. In the range of $0.4 \le x \le 0.8$, the DSC curves exhibit obvious endothermic and exothermic peaks, indicating the occurrence of phase transformation, i.e., precipitation and solid dissolution of second phase during the heating process. As x reaches 1.0, it can be seen that the DSC curve has a clear exothermic peak at 313.7°C, while the endothermic peak is hardly visible. Comparing the exothermic peaks of various FeCoNi(CuAl)$_x$ alloy powders in **Figure 2**, it is found that with the increase of Al and Cu content, the FCC solid solution generated by mechanical alloying becomes more unstable and the precipitation temperature of the second phase is descending.

Figure 3 shows XRD results of bulky MEA and HEA sintered samples. It is revealed that the sintered samples remain the single FCC crystal structure in the FeCoNi MEA; but while the content of Cu and Al increases, BCC phase is generated from the FCC matrix during the sintering process and the sintered HEAs exhibit BCC + FCC dual-phase structures. The XRD results of the sintered samples confirm the phase transformation shown in **Figure 2**. The exothermic peaks observed in **Figure 2** correspond to the precipitation of BCC phase from the supersaturated FCC alloy powders at a lower temperature and the endothermic peaks in it indicate partial solid solution of BCC phase into FCC matrix at a higher temperature.

According to the diffraction peak strength of FCC and BCC phases shown in **Figure 3**, it is clearly seen that the fraction of BCC phase increases obviously with the increase of Al and Cu contents. It is suggested that the increase of Al and Cu contents will promote the formation of BCC phase in FeCoNi(CuAl)$_x$ alloys, and make its structure change from single FCC phase to

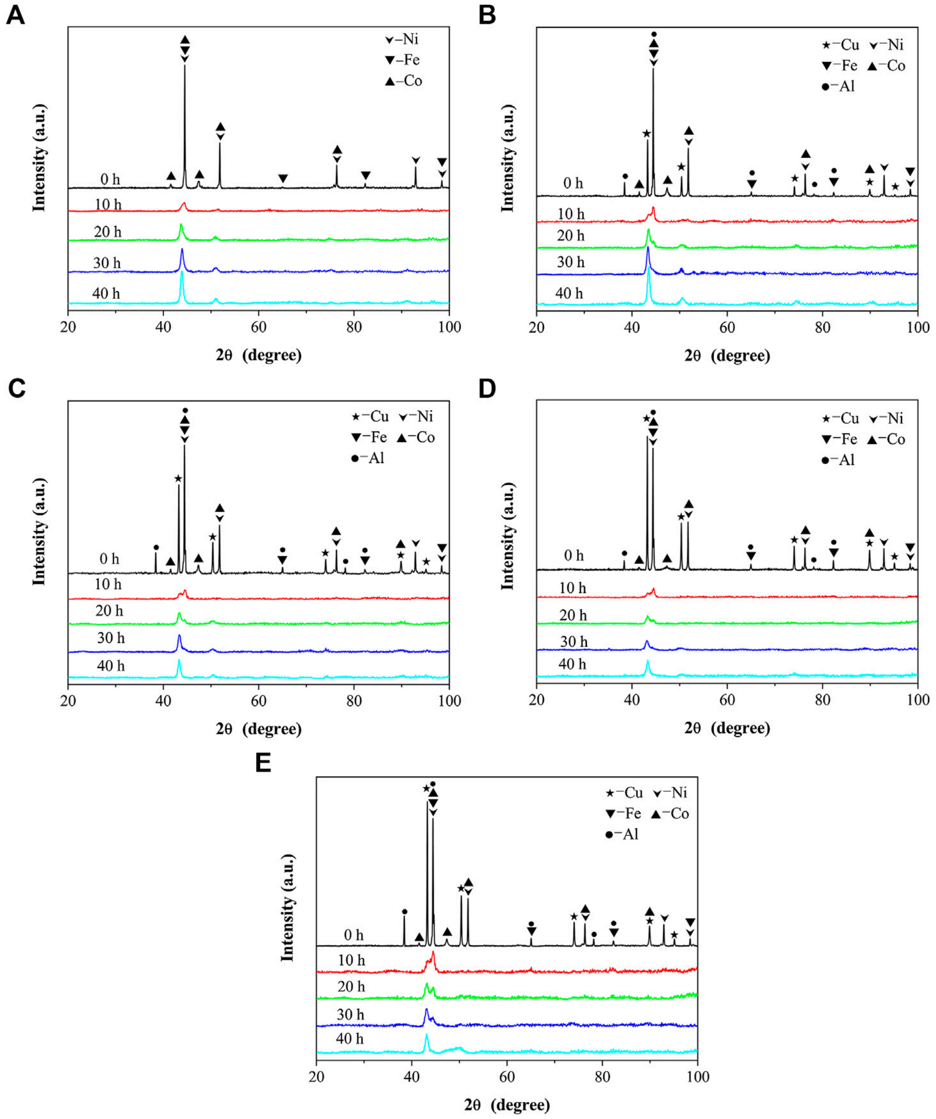

FIGURE 1 | XRD patterns of FeCoNi(CuAl)$_x$ MEA and HEA powders with different milling times: **(A)** x = 0; **(B)** x = 0.4; **(C)** x = 0.6; **(D)** x = 0.8; **(E)** x = 1.0.

TABLE 3 | Average grain sizes, lattice strains and lattice constants of 40 h-milled FeCoNi(CuAl)$_x$ MEA and HEA powders.

Alloy	Grain size (nm)	Lattice strain ε (%)	Lattice constant (nm)
x = 0	29.83	0.95	0.35725
x = 0.4	12.71	0.95	0.36009
x = 0.6	18.47	0.91	0.36196
x = 0.8	20.89	1.08	0.36177
x = 1.0	14.60	1.56	0.36311

FCC + BCC dual-phase. Additionally, we can see from **Table 4**, the lattice constants of FCC and BCC phases are continuously increased with the increase of x due to the addition of Al and Cu with relatively large atomic radius. As previously reported, Al promotes the formation of BCC phase, while Cu lead to the formation of FCC phase (Tung et al., 2007; Li et al., 2010; Yang et al., 2015; Matusiak et al., 2019). When the content of Al and Cu changes at the same time in the present work, the effect is similar with that of changing the Al content alone, which demonstrates that in the competition between the two elements Al dominates the phase formation in the HEA.

The microstructure of FeCoNi(CuAl)$_x$ bulk alloys sintered at 1,100°C was observed and analyzed by Scanning Electron Microscope (SEM). The back scattering images are presented in **Figure 4**. Single FCC phase matrix and a small amount of oxides are observed at x = 0, the volume fraction of oxides is about 4.4%; and the HEA basically remains single phase structure for x = 0.4. In the specimens with x ranging from 0.6 to 1.0, it can be seen clearly that there are two kinds of phases in the microstructure, that is, light gray phase and dark phase, which are consistent with XRD results. While x = 0.6, the second phase

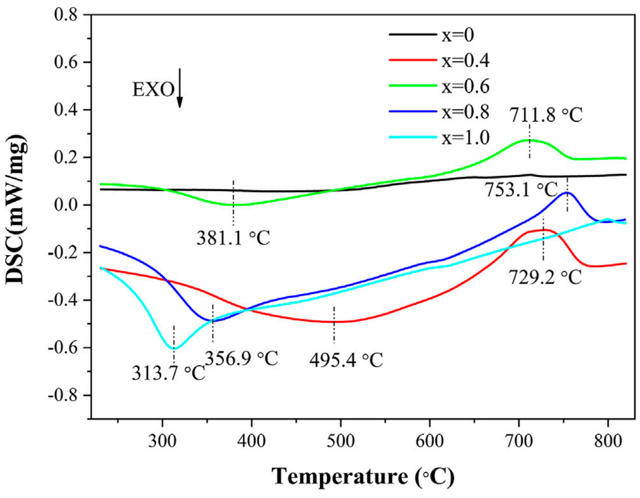

FIGURE 2 | DSC curves of 40 h-milled FeCoNi(CuAl)$_x$ MEA and HEA powders.

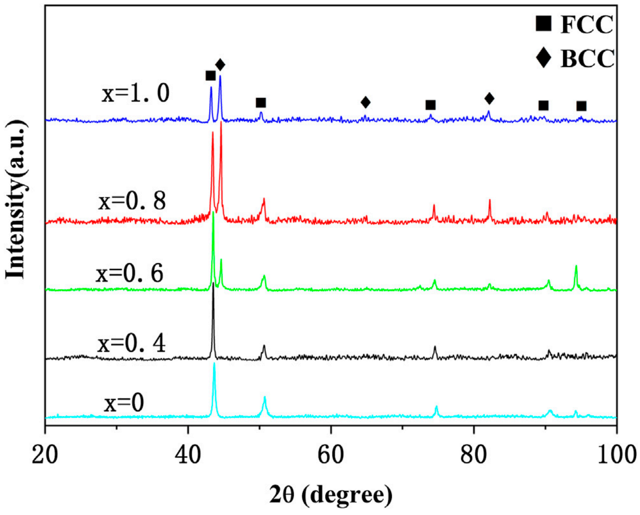

FIGURE 3 | XRD patterns of sintered bulky FeCoNi(CuAl)$_x$ MEA and HEAs.

TABLE 4 | Lattice parameters, lattice strain and phase fraction of FeCoNi(CuAl)x MEA and HEAs.

Alloy	Lattice constant (nm)		Lattice strain ε (%)	
	FCC	BCC	FCC	BCC
x = 0	0.35922	—	0.38	—
x = 0.4	0.36014	—	0.17	—
x = 0.6	0.36055	0.28718	0.32	0.27
x = 0.8	0.36076	0.28774	0.28	0.34
x = 1.0	0.36251	0.28803	0.26	0.33

disperses uniformly on the matrix in a granular morphology. With the continuous increase of the contents of Al and Cu elements, the second phase increases significantly and its distribution tends to be agglomerated and entangled gradually. It is also found from **Figure 4** that the FeCoNi (x = 0) ternary alloy contains more oxides than other alloys that containing Al and Cu elements. It is previously reported that adding Al element to FeCoNi alloy can effectively limit the formation of oxides (Butler and Weaver, 2016).

Figure 5 illustrates TEM bright-field image and selected area electron diffraction patterns (SAED) of FeCoNi(CuAl)$_x$ (x = 0, 0.4, 0.6, 0.8, 1.0) alloys. Apparently, the sintered alloys exhibit fine equiaxed microstructures. The SAED pattern in **Figure 5A** shows that the FeCoNi ternary alloy consists of single FCC phase and there are a few fine oxide particles at the grain boundary (as pointed by the arrow in **Figure 5A**). The FeCoNi alloy has a wide grain size distribution; the larger grain sizes are above 1 μm while the smaller grain sizes are less than 200 nm. After adding Cu and Al (x = 0.4), the grain sizes of sintered samples become more homogeneous, and the average grain size of FeCoNi(CuAl)$_{0.4}$ high-entropy alloy is significantly reduced, as shown in **Figure 5B**. With the following increase of Al and Cu content, the grain size of the material shows an obvious increasing trend, as seen in **Figures 5C–E**. At x = 1.0, the average grain size of FeCoNiCuAl high-entropy alloy grow up to be close to that of the FeCoNi ternary alloy. For x = 0.4, 0.6, 0.8, 1.0, oxide particles are hardly found in TEM bright-field images, suggesting that the oxidation of HEAs are suppressed by the addtion of Al. SAED analysis of FeCoNi(CuAl)$_x$ (x = 0.4, 0.6, 0.8, 1.0) HEAs shows that FCC and BCC phases both exist in bulky high-entropy alloys with the addition of Al and Cu elements. The insets in **Figure 5D** present the SAED patterns of the selected grains marked as A and B in **Figure 5D**. According to the SAED results, A is indexed to be a FCC structure, while B possesses a BCC structure. The EDS/TEM compositions of each phase for FeCoNi(CuAl)$_x$ (x = 0, 0.4, 0.6, 0.8, 1.0) MEA and HEAs are shown in **Table 5**. The BCC phase is found to be enriched in Al and Ni elements, while FCC phase is enriched in Fe, Co and Cu elements. It should be pointed out that though the existence of BCC phase is not found in the XRD result because of its low volume fraction in the FeCoNi(CuAl)$_{0.4}$ specimen, SAED patterns discovers that miner BCC has been formed in the HEA with x of 0.4.

As the content of Al and Cu increases, the percentage of BCC phase increases. It can be seen from **Table 5** that with the precipitation of BCC phase, Al and Ni are depleted in FCC phase and other elements are enriched in FCC phase, thus makes FCC phase became different from the nominal composition.

According to the theory of solid solution formation (Zhang et al., 2008; Wang et al., 2015), simple solid solution phases are supposed to form when thermodynamic parameters Ω (Zhang et al., 2008), atomic size difference δ (Zhang et al., 2008), and atomic size parameter γ (Wang et al., 2015) of the high-entropy alloys satisfy the conditions that $\Omega \geq 1.1$, $\delta \leq 6.6\%$, and $\gamma \leq 1.175$. It can be seen from **Table 6** that the sintered alloys with various compositions all satisfy this criteria. As to determination of lattice structure, Guo and Liu (2011) and Guo et al. (2011) proposed that single FCC solid solution phase will be formed if VEC > 8. As the VEC of the five high-sintered alloys are greater than 8, these five MEA and HEAs can form single FCC solid solution phase, but actually the sintered alloys prefer to form FCC + BCC two-phase

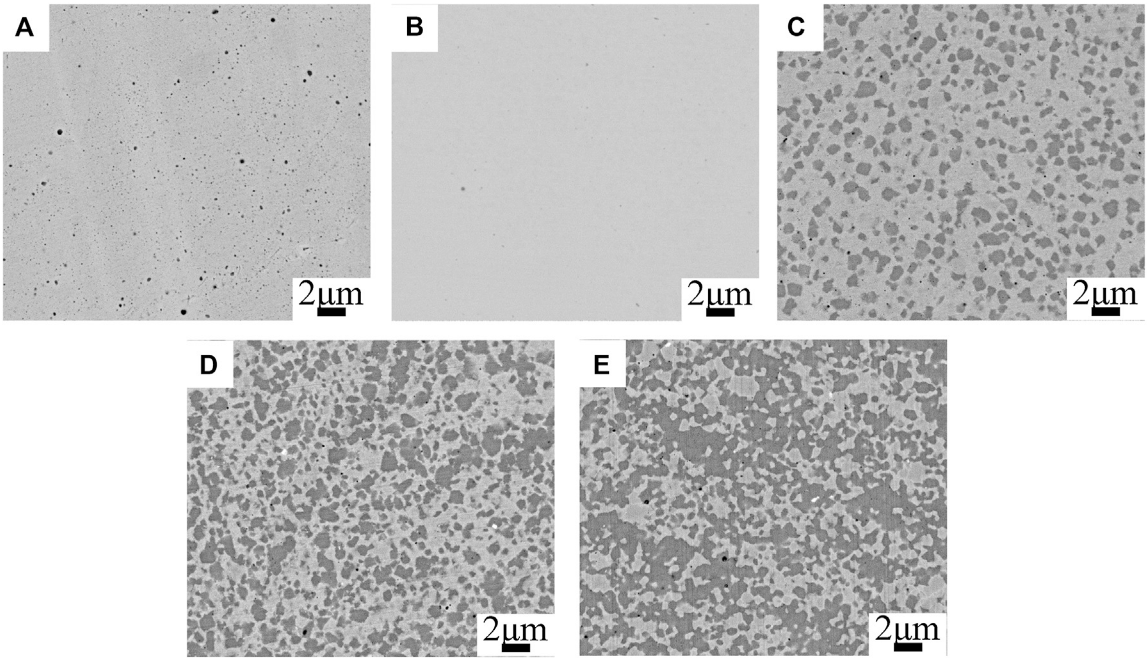

FIGURE 4 | SEM back scatter electron images of the bulk FeCoNi(CuAl)$_x$ MEA and HEAs: **(A)** x = 0; **(B)** x = 0.4; **(C)** x = 0.6; **(D)** x = 0.8; **(E)** x = 1.0.

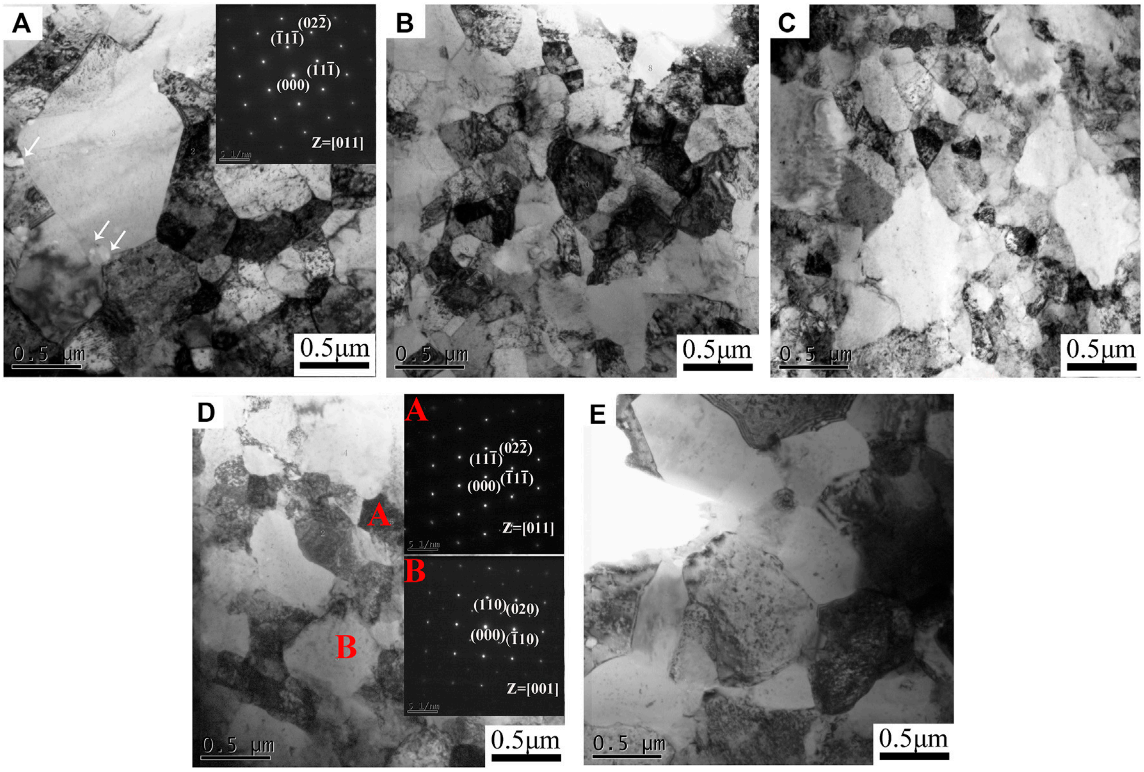

FIGURE 5 | TEM images of bright field and corresponding SAED patterns of bulk FeCoNi(CuAl)$_x$ alloys (x = 0,0.4, 0.6,0.8, 1.0): **(A)** x = 0, inset: SAED pattern of FCC matrix along [011] axis; **(B)** x = 0.4; **(C)** x = 0.6; **(D)** x = 0.8, inset A: SAED pattern of grain A corresponding to a FCC structure along [011] axis; inset B: SAED pattern of grain B corresponding to a BCC structure along [001] axis; (e) x = 1.0.

TABLE 5 | EDS/TEM results (in at%) of the phases of bulk FeCoNi(CuAl)$_x$ MEA and HEAs.

Alloy	Region	Al	Fe	Co	Ni	Cu
x = 0	Nominal composition	—	33.33	33.33	33.33	—
	FCC	—	34.19	32.51	32.30	—
	BCC	—	—	—	—	—
x = 0.4	Nominal composition	10.52	26.32	26.32	26.32	10.52
	FCC	5.60	30.59	27.31	24.52	11.98
	BCC	21.27	21.48	21.22	30.59	5.44
x = 0.6	Nominal composition	14.29	23.81	23.81	23.81	14.29
	FCC	6.67	27.82	27.11	23.16	15.24
	BCC	21.66	22.25	22.07	28.58	5.44
x = 0.8	Nominal composition	17.39	21.74	21.74	21.74	21.74
	FCC	9.68	25.89	22.59	18.78	23.06
	BCC	26.05	18.97	20.40	24.62	9.96
x = 1.0	Nominal composition	20	20	20	20	20
	FCC	11.74	26.94	16.71	17.38	27.23
	BCC	28.37	19.83	17.48	25.07	9.25

TABLE 6 | Relevant parameters of FeCoNi(CuAl)$_x$ MEA and HEAs.

Alloy	ΔS_{mix} (J K^{-1} mol^{-1})	δ (%)	Ω	T_m (K)	ΔH_{mix} (kJ mol^{-1})	VEC	γ
x = 0	9.13	0.65	12.11	1,729	−1.33	9	1.017
x = 0.4	12.70	4.36	5.09	1637.76	−4.09	8.58	1.169
x = 0.6	13.14	4.88	4.44	1590.89	−4.71	8.43	1.169
x = 0.8	13.32	5.21	4.07	1552.17	−5.07	8.30	1.169
x = 1.0	13.37	5.44	3.85	1519.65	−5.28	8.2	1.168

alloy except the ternary alloy. It is indicated that the phase formation is not only associated with the composition, but also influenced by the processing temperature. From the former DSC results, phase transformation is observed in the quinary HEAs. During the heating process of mechanically alloyed HEA powders, BCC phase is first precipitated from the supersaturated FCC matrix, and then partially dissolved into the FCC phase with the rising temperature. This result is basically consistent with the FeCoNiCuAl HEA phase diagram previously estimated by Beyramali Kivy et al. (2017) that illustrated the phase fraction changes as a function of temperature. At a temperature higher than about 950 K, FeCoNiCuAl HEA tends to exhibit a single FCC phase structure, while at a temperature below ~950 K, FCC solid solution became unstable and there exists a two-phase zone of FCC + BCC phases.

According to Gibbs free energy formula, stability of single-phase solid solution relies on mixing enthalpy and configuration entropy of an alloy system. When configuration entropy dominates in the alloy system, stable single-phase solid solution can be formed. However, in most cases, the enthalpy of mixing and other factors will affect the stability of phases in alloys to a certain extent, leading to formation of multiphase or intermetallic compounds in alloys. If the tendency of forming compounds among alloying elements is relatively large, this tendency will be reflected in the high-entropy alloy. Based on the parameter from **Table 2**, there is a relatively large negative

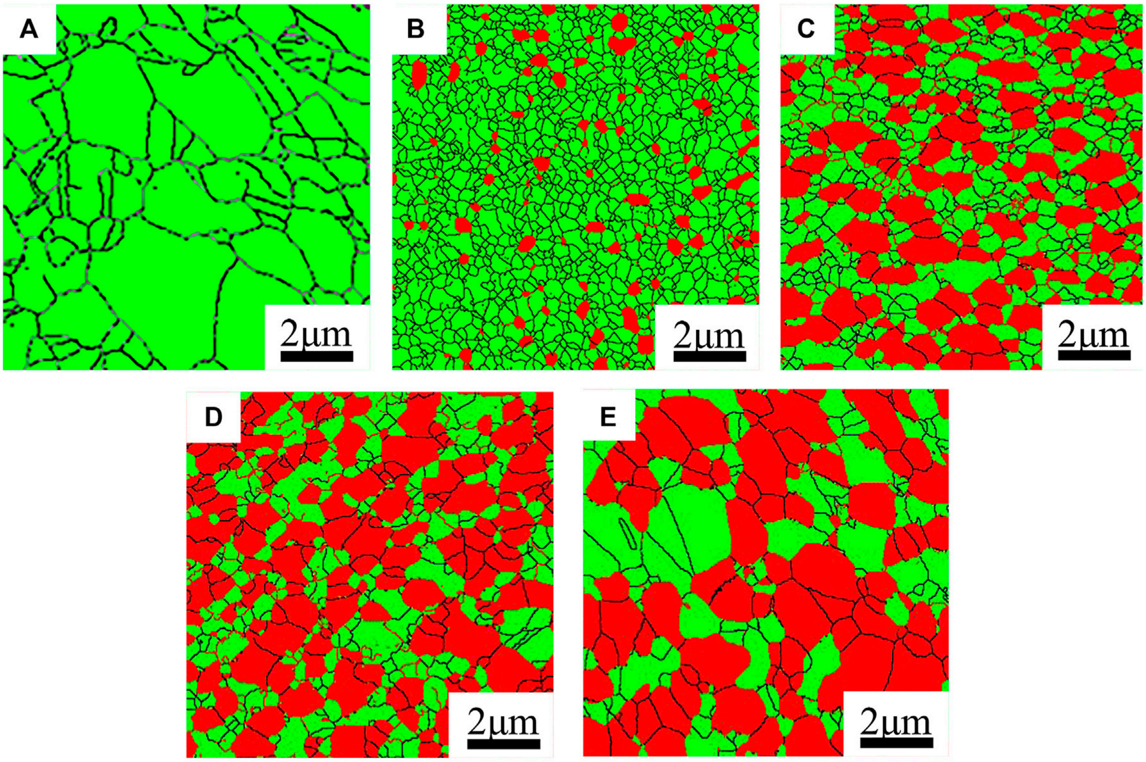

FIGURE 6 | EBSD phase maps of bulk FeCoNi(CuAl)$_x$ MEA and HEAs: **(A)** x = 0; **(B)** x = 0.4; **(C)** x = 0.6; **(D)** x = 0.8; **(E)** x = 1.0 (green-FCC, red-BCC).

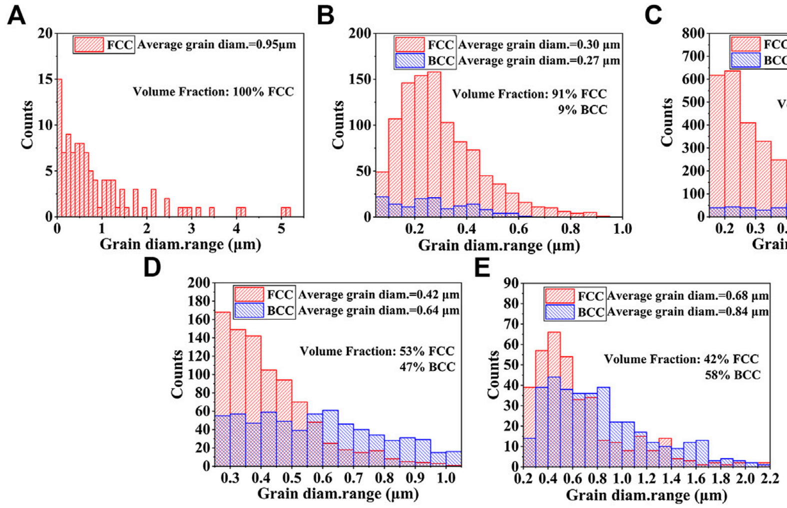

FIGURE 7 | Statistical grain diameter distribution and phase volume fraction of bulk FeCoNi(CuAl)$_x$ MEA and HEAs: **(A)** x = 0; **(B)** x = 0.4; **(C)** x = 0.6; **(D)** x = 0.8; **(E)** x = 1.0.

mixing enthalpy between Al and Ni elements. It can be predicted that in the high-entropy alloy, If the content of Al and Cu elements increases, the second phase rich in Al and Ni elements would inevitably be formed, which can explain the appearance of the second phase in FeCoNi(CuAl)$_x$ HEA samples. In addition, Al atom has the largest atomic radius of 1.43 Å in FeCoNi(CuAl)$_x$ HEAs system. In the process of SPS sintering, Al element tends to precipitate from the FCC matrix by combining with other elements, thus reducing the lattice distortion and elastic energy of the matrix. In fact, this transformation of alloy structure from single FCC phase to FCC + BCC dual-phase caused by changing Al and Cu elements at the same time is similar with the situation of changing Al elements in FeCoNiCuAl (Beyramali Kivy et al., 2017). It is suggested that though Al and Cu contents are changed simultaneously in FeCoNi(CuAl)$_x$ high-entropy alloys, Al element may play a dominant role in the phase transformation. In the process of sintering, the internal stress in the high-energy ball-milled powders is released, the lattice defects are greatly reduced, phase transformation occurs in the supersaturated solid solution by atomic inter-diffusion. Moreover, the ball-milled powders exhibit a severely-plastic-deformed nanocrystalline structure, and a large amount of lattice defects and grain boundaries can promote the diffusion of atoms, thus facilitating the occurrence of phase transformation.

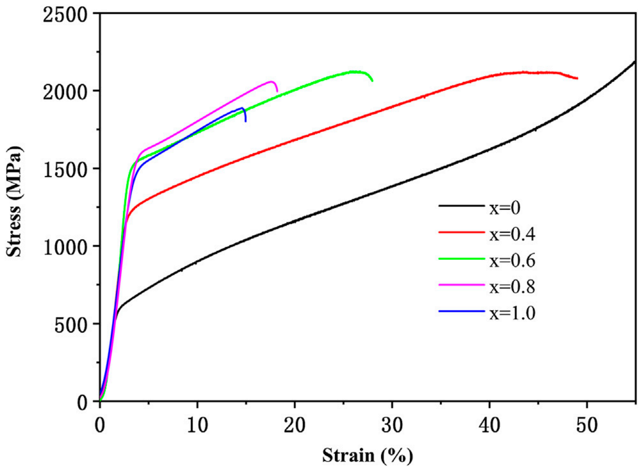

FIGURE 8 | Compressive engineering stress-strain curves of the bulk FeCoNi(CuAl)$_x$ MEA and HEAs.

In order to determine the grain size and distribution of each phase, EBSD examination were carried out on FeCoNi(CuAl)$_x$ MEA and HEAs. EBSD results are shown in **Figure 6** and corresponding grain distribution statistical charts and phase volume fraction are illustrated in **Figure 7**. For x = 0, only a single FCC phase structure is observed, and there are a certain number of twin boundaries in the grains. Its average grain size is measured to be 0.95 μm. For x = 0.4, there are a few BCC phase dispersed in the matrix with FCC structure, and the average grain sizes for FCC and BCC phase are dramatically reduced to only 0.30 and 0.27 μm, respectively. When x increases from 0.4 to 1, the volume fraction of second phase increases continuously, and the second phase begins to agglomerate and form connected regions. At x value of 1.0, its volume fraction arrives at 58%, even exceeding the proportion of FCC phase. Additionally, the grain sizes of two phases grow up with the addition of Al and Cu content. As x increased up to 1.0, the average grain sizes of FCC and BCC phases rise to 0.68 and 0.84 μm, respectively.

While the content of Al and Cu (x) is 0.4, an interesting phenomenon could be seen that the grains of the HEA are refined remarkably in comparison to the ternary alloy (as shown in **Figures 6A,B**). This grain refinement is probably caused by the sluggish diffusion effect due to the addition of Al and Cu, which is previously proposed by Yeh and TONG et al. to explain the

TABLE 7 | Mechanical properties of sintered FeCoNi(CuAl)$_x$ alloys and casting FeCoNi(CuAl)$_{0.8}$ HEA.

Process	Alloy	$\sigma_{0.2}$ (MPa)	σ_{max} (MPa)	ε_p (%)	Hardness (Hv)	Relative density (%)	Reference
MA + SPS	x = 0	574.9	—	—	234.9	96.5	This work
	x = 0.4	1165.1	2122.5	45.2	356.9	95.4	
	x = 0.6	1467.7	2123.2	24.9	412.8	98.4	
	x = 0.8	1470.4	2058.0	14.7	501.1	99.4	
	x = 1.0	1381.2	1887.8	12.4	462.6	96.6	
Cast	x = 0.8	601	1935	37.2	280	—	Li et al., 2018

nano-grained microstructure in HEAs (TONG et al., 2005; Yeh, 2013). Diffusion of elements might be hindered in multi-principle-component alloys because of the large fluctuation of lattice potential energy (LPE) between lattice sites. There may exist plenty of low LPE sites that act as traps for atomic diffusion, and also some high LPE sites that are hard for atoms to jump into, thus leading to the sluggish diffusion effect. The reduced diffusion rate would retard the grain boundary migration and slows down the grain growth during the sintering process. However, with the increase of the content of Al and Cu (x), the grain size increases gradually, and the FeCoNiCuAl specimen with equiatomic ratio has an average grain size almost close to the ternary FeCoNi alloy. This result suggests that the atomic diffusion rate of FeCoNiCuAl HEA can also be affectted by the concentration of Al and Cu elements. When x increase in FeCoNiCuAl HEA, content of Al and Cu elements which have lower melting points keep increasing, thus the activation energy of atomic diffusion is reduced and the diffusion rate in HEAs may be developed, subsequently the grain growth rate is increased in the sintered alloy. Meanwhile, the measured average grain sizes of BCC phases is a bit larger than those of FCC phases due to the higher content of Al in BCC phase and the difference in crystal structure. Anyway, statistical analysis results in **Figure 7** show that all the average grain sizes of the quinary HEA samples are still smaller than the ternary MEA sample, suggesting a reduced atomic diffusion rate in HEAs, if the difference in original grain sizes in the ball milled powders could be ignored.

Mechanical Properties

Figure 8 depicts the compressive engineering stress-strain curves of the as-sintered FeCoNi(CuAl)$_x$ (x = 0, 0.4, 0.6, 0.8, 1.0) MEA and HEA specimens at room temperature. The densities and mechanical properties of FeCoNi(CuAl)$_x$ alloys fabricated by SPS and conventional casting FeCoNi(CuAl)$_{0.8}$ HEA (Li et al., 2018) are summarized in **Table 7**. After SPS, all the alloy samples are sintered to near-full densities (95.4~99.4%). For the FeCoNi MEA specimen, its yield strength is only 574.9 MPa. While the content of Al and Cu is 0.4, a small amount of BCC phase is formed in the matrix, and the grain sizes of the matrix are significantly refined, which doubles the yield strength (from 574.9 to 1,165.1 MPa) and meanwhile remains a good plasticity. When x increases from 0.4 to 0.8, the yield strength ($\sigma_{0.2}$) for as-sintered HEA increases continuously and reaches the maximum value of 1,470.4 MPa, but the plastic strain to fracture (ε_p) exhibits a descending trend. According to previous studies, FCC-structured HEAs always show high plasticity and low strength, while BCC-structured HEAs tend to exhibit relatively high strength and poor plasticity. Thus the increase of the yield strength and decrease of the plasticity can be attributed to the increased volume fraction of BCC phase in the HEAs specimens due to the increase of x. Compared with the as-cast counterpart with the same composition, the sintered FeCoNi(CuAl)$_{0.8}$ HEA specimen exhibits a notable increases of 145% on the yield strength, as a result of the much finer grain size in the sintered alloy. At x = 1.0, though the fraction of BCC phase is increased, the yield strength of the FeCoNiCuAl high-entropy alloy slightly declined. This decrease in strength can be explained by the grain growth in the HEA specimen and the aggregation of the second phase, as seen in **Figure 6**.

As the phase composition of FeCoNi(CuAl)$_x$ alloys varies with the content of Cu and Al, the mechanical properties of this alloy can thus be tailored by designing the microstructure through changing x value. It is seen in **Table 7** that at an x value of 0.6 a combination of relatively high strength and good plasticity is achieved in the sintered HEA. The FeCoNi(CuAl)$_{0.6}$ specimen shows a yield strength of 1,467.7 MPa, plastic strain to failure of 24.9% and hardness of 412 Hv.

CONCLUSIONS

In the present work, fine-grained and high-strength FeCoNi(CuAl)$_x$ (x = 0, 0.4, 0.6, 0.8, 1.0) MEA and HEAs were successfully fabricated by MA and SPS, the microstructure, phase formation and mechanical properties of FeCoNi(CuAl)$_x$ have been systematically investigated.

1) Quinary FeCoNi(CuAl)$_x$ alloys have slower mechanical alloying speeds than the ternary FeCoNi alloy, and the ball milling time for FeCoNi(CuAl)$_x$ alloys to accomplish the mechanical alloying process increases with the increase of x. Supersaturated solid solution with single FCC structure is formed in the mechanically alloyed powders with various compositions after ball milling for 20~40 h. After SPS, the sintered alloys exhibit different microstructures depending on the contents of Cu and Al (x). The FeCoNi MEA without addition of Cu and Al remains the single FCC phase structure, while the HEAs with x range from 0.4 to 1.0 transform into FCC + BCC dual-phase structure, with the BCC phase rich in Al and Ni elements while the FCC phase rich in Fe, Co and Cu elements.
2) EBSD observation results show that the average grain size of sintered samples is significantly reduced with a minor addition of Al and Cu into FeCoNi alloy (x = 0.4). When

the Al and Cu content (x) in FeCoNi(CuAl)$_x$ increases from 0.4 to 1.0, the volume fraction of BCC phase increases, the average grain sizes of FCC and BCC phases grow up continuously and the distribution of two phases turns to be more aggregated. It is suggested that the atomic diffusion and grain growth in FeCoNi(CuAl)$_x$ HEAs during the sintering process are affected by the sluggish diffusion effect as well as the change in melting point of the alloy.

3) When x increases from 0 to 0.8, the compressive yield strength and hardness for FeCoNi(CuAl)$_x$ increase dramatically while the plasticity of the materials decreases gradually, owing to the increased volume fraction of BCC phase. The FeCoNi(CuAl)$_{0.6}$ HEA shows a balanced mechanical properties, with its yield strength and plastic strain to failure arriving at 1,467.4 MPa and 24.9%, respectively.

DATA AVAILABILITY STATEMENT

All datasets generated for this study are included in the article.

AUTHOR CONTRIBUTIONS

YL conceived and designed the experiments. GL, XL, and HP performed the experiments. YL, GL, XL, and HP analyzed the data. YL and GL wrote the paper.

FUNDING

This work was supported by the National Natural Science Foundation of China with grant No. 51104066.

REFERENCES

Beyramali Kivy, M., Asle Zaeem, M., and Lekakh, S. (2017). Investigating phase formations in cast AlFeCoNiCu high entropy alloys by combination of computational modeling and experiments. *Mater. Des.* 127, 224–232. doi:10.1016/j.matdes.2017.04.086

Butler, T. M., and Weaver, M. L. (2016). Oxidation behavior of arc melted AlCoCrFeNi multi-component high-entropy alloys. *J. Alloys Compd.* 674, 229–244. doi:10.1016/j.jallcom.2016.02.257

Fu, Z., Chen, W., Wen, H., Zhang, D., Chen, Z., Zheng, B., et al. (2016). Microstructure and strengthening mechanisms in an FCC structured single-phase nanocrystalline Co25Ni25Fe25Al7.5Cu17.5 high-entropy alloy. *Acta Mater.* 107, 59–71. doi:10.1016/j.actamat.2016.01.050

Fu, Z., Jiang, L., Wardini, J. L., Macdonald, B. E., Wen, H., Xiong, W., et al. (2018). A high-entropy alloy with hierarchical nanoprecipitates and ultrahigh strength. *Sci. Adv.* 4, eaat8712. doi:10.1126/sciadv.aat8712

Fujieda, T., Shiratori, H., Kuwabara, K., Hirota, M., Kato, T., Yamanaka, K., et al. (2017). CoCrFeNiTi-based high-entropy alloy with superior tensile strength and corrosion resistance achieved by a combination of additive manufacturing using selective electron beam melting and solution treatment. *Mater. Lett.* 189, 148–151. doi:10.1016/j.matlet.2016.11.026

Guo, S., and Liu, C. T. (2011). Phase stability in high entropy alloys: Formation of solid-solution phase or amorphous phase. *Prog. Nat. Sci.: Materials International.* 21, 433–446. doi:10.1016/s1002-0071(12)60080-x

Guo, S., Ng, C., Lu, J., and Liu, C. T. (2011). Effect of valence electron concentration on stability of fcc or bcc phase in high entropy alloys. *J. Appl. Phys.* 109, 103505. doi:10.1063/1.3587228

Han, Z., Ren, W., Yang, J., Du, Y., Wei, R., Zhang, C., et al. (2019). The deformation behavior and strain rate sensitivity of ultra-fine grained CoNiFeCrMn high-entropy alloys at temperatures ranging from 77 K to 573 K. *J. Alloys Compd.* 791, 962–970. doi:10.1016/j.jallcom.2019.03.373

Lei, Z., Liu, X., Wu, Y., Wang, H., Jiang, S., Wang, S., et al. (2018). Enhanced strength and ductility in a high-entropy alloy via ordered oxygen complexes. *Nature* 563, 546–550. doi:10.1038/s41586-018-0685-y

Li, C., Li, J. C., Zhao, M., and Jiang, Q. (2010). Effect of aluminum contents on microstructure and properties of AlxCoCrFeNi alloys. *J. Alloys Compd.* 504, S515–S518. doi:10.1016/j.jallcom.2010.03.111

Li, X., Feng, Y., Liu, B., Yi, D., Yang, X., Zhang, W., et al. (2019). Influence of NbC particles on microstructure and mechanical properties of AlCoCrFeNi high-entropy alloy coatings prepared by laser cladding. *J. Alloys Compd.* 788, 485–494. doi:10.1016/j.jallcom.2019.02.223

Li, Z., Tasan, C. C., Pradeep, K. G., and Raabe, D. (2017). A TRIP-assisted dual-phase high-entropy alloy: Grain size and phase fraction effects on deformation behavior. *Acta Mater.* 131, 323–335. doi:10.1016/j.actamat.2017.03.069

Li, Z., Xu, H., Gu, Y., Pan, M., Yu, L., Tan, X., et al. (2018). Correlation between the magnetic properties and phase constitution of FeCoNi(CuAl)$_{0.8}$Ga$_x$ ($0 \le x \le 0.08$) high-entropy alloys. *J. Alloys Compd.* 746, 285–291. doi:10.1016/j.jallcom.2018.02.189

Liu, W. H., Lu, Z. P., He, J. Y., Luan, J. H., Wang, Z. J., Liu, B., et al. (2016). Ductile CoCrFeNiMo$_x$ high entropy alloys strengthened by hard intermetallic phases. *Acta Mater.* 116, 332–342. doi:10.1016/j.actamat.2016.06.063

Long, Y., Liang, X., Su, K., Peng, H., and Li, X. (2019). A fine-grained NbMoTaWVCr refractory high-entropy alloy with ultra-high strength: Microstructural evolution and mechanical properties. *J. Alloys Compd.* 780, 607–617. doi:10.1016/j.jallcom.2018.11.318

Lu, Y., Dong, Y., Guo, S., Jiang, L., Kang, H., Wang, T., et al. (2014). A promising new class of high-temperature alloys: eutectic high-entropy alloys. *Sci. Rep.* 4, 6200. doi:10.1038/srep06200

Luo, H., Li, Z., Mingers, A. M., and Raabe, D. (2018). Corrosion behavior of an equiatomic CoCrFeMnNi high-entropy alloy compared with 304 stainless steel in sulfuric acid solution. *Corrosion Sci.* 134, 131–139. doi:10.1016/j.corsci.2018.02.031

Matusiak, K., Berent, K., Marciszko, M., and Cieslak, J. (2019). The experimental and theoretical study on influence of Al and Cu contents on phase abundance changes in Al$_x$Cu$_y$FeCrNiCo HEA system. *J. Alloys Compd.* 790, 837–846. doi:10.1016/j.jallcom.2019.03.162

Miracle, D. B., and Senkov, O. N. (2017). A critical review of high entropy alloys and related concepts. *Acta Mater.* 122, 448–511. doi:10.1016/j.actamat.2016.08.081

Nong, Z.-S., Lei, Y.-N., and Zhu, J.-C. (2018). Wear and oxidation resistances of AlCrFeNiTi-based high entropy alloys. *Intermetallics* 101, 144–151. doi:10.1016/j.intermet.2018.07.017

Senkov, O. N., Jensen, J. K., Pilchak, A. L., Miracle, D. B., and Fraser, H. L. (2018a). Compositional variation effects on the microstructure and properties of a refractory high-entropy superalloy AlMo$_{0.5}$NbTa$_{0.5}$TiZr. *Mater. Des.* 139, 498–511. doi:10.1016/j.matdes.2017.11.033

Senkov, O. N., Miracle, D. B., Chaput, K. J., and Couzinie, J.-P. (2018b). Development and exploration of refractory high entropy alloys-A review. *J. Mater. Res.* 33, 3092–3128. doi:10.1557/jmr.2018.153

Senkov, O. N., Rao, S., Chaput, K. J., and Woodward, C. (2018c). Compositional effect on microstructure and properties of NbTiZr-based complex concentrated alloys. *Acta Mater.* 151, 201–215. doi:10.1016/j.actamat.2018.03.065

Senkov, O. N., Wilks, G. B., Scott, J. M., and Miracle, D. B. (2011). Mechanical properties of Nb$_{25}$Mo$_{25}$Ta$_{25}$W$_{25}$ and V$_{20}$Nb$_{20}$Mo$_{20}$Ta$_{20}$W$_{20}$ refractory high entropy alloys. *Intermetallics* 19, 698–706. doi:10.1016/j.intermet.2011.01.004

Tian, Q., Zhang, G., Yin, K., Wang, W., Cheng, W., and Wang, Y. (2019). The strengthening effects of relatively lightweight AlCoCrFeNi high entropy alloy. *Mater. Char.* 151, 302–309. doi:10.1016/j.matchar.2019.03.006

Tong, C.-J., Chen, Y.-L., Yeh, J.-W., Lin, S.-J., Chen, S.-K., Shun, T.-T., et al. (2005). Microstructure characterization of Al $_x$ CoCrCuFeNi high-entropy alloy system with multiprincipal elements. *Metall. Mater. Trans.* 36, 881–893. doi:10.1007/s11661-005-0283-0

Tong, Y., Chen, D., Han, B., Wang, J., Feng, R., Yang, T., et al. (2019). Outstanding tensile properties of a precipitation-strengthened FeCoNiCrTi0.2 high-entropy alloy at room and cryogenic temperatures. *Acta Mater.* 165, 228–240. doi:10.1016/j.actamat.2018.11.049

Tung, C.-C., Yeh, J.-W., Shun, T.-t., Chen, S.-K., Huang, Y.-S., and Chen, H.-C. (2007). On the elemental effect of AlCoCrCuFeNi high-entropy alloy system. *Mater. Lett.* 61, 1–5. doi:10.1016/j.matlet.2006.03.140

Wang, Z., Huang, Y., Yang, Y., Wang, J., and Liu, C. T. (2015). Atomic-size effect and solid solubility of multicomponent alloys. *Scripta Mater.* 94, 28–31. doi:10.1016/j.scriptamat.2014.09.010

Williamson, G. K., and Hall, W. H. (1953). X-ray line broadening from filed aluminium and wolfram. *Acta Metall.* 1, 22–31. doi:10.1016/0001-6160(53)90006-6

Xiang, S., Luan, H., Wu, J., Yao, K.-F., Li, J., Liu, X., et al. (2019). Microstructures and mechanical properties of CrMnFeCoNi high entropy alloys fabricated using laser metal deposition technique. *J. Alloys Compd.* 773, 387–392. doi:10.1016/j.jallcom.2018.09.235

Yang, T., Xia, S., Liu, S., Wang, C., Liu, S., Zhang, Y., et al. (2015). Effects of AL addition on microstructure and mechanical properties of Al$_x$CoCrFeNi High-entropy alloy. *Mater. Sci. Eng., A* 648, 15–22. doi:10.1016/j.msea.2015.09.034

Ye, Y. F., Wang, Q., Lu, J., Liu, C. T., and Yang, Y. (2016). High-entropy alloy: challenges and prospects. *Mater. Today.* 19, 349–362. doi:10.1016/j.mattod.2015.11.026

Ye, Y. X., Liu, C. Z., Wang, H., and Nieh, T. G. (2018). Friction and wear behavior of a single-phase equiatomic TiZrHfNb high-entropy alloy studied using a nanoscratch technique. *Acta Mater.* 147, 78–89. doi:10.1016/j.actamat.2018.01.014

Yeh, J.-W. (2013). Alloy Design Strategies and Future Trends in High-Entropy Alloys. *JOM (J. Occup. Med.)* 65, 1759–1771. doi:10.1007/s11837-013-0761-6

Yeh, J.-W., Chen, S.-K., Lin, S.-J., Gan, J.-Y., Chin, T.-S., Shun, T.-T., et al. (2004). Nanostructured high-entropy alloys with multiple principal elements: Novel alloy design concepts and outcomes. *Adv. Eng. Mater.* 6, 299–303. doi:10.1002/adem.200300567 2004

Zhang, B., Liaw, P. K., Brechtl, J., Ren, J., Guo, X., and Zhang, Y. (2020). Effects of Cu and Zn on microstructures and mechanical behavior of the medium-entropy aluminum alloy. *J. Alloys Compd.* 820, 153092. doi:10.1016/j.jallcom.2019.153092

Zhang, H., Pan, Y., and He, Y.-Z. (2011). Synthesis and characterization of FeCoNiCrCu high-entropy alloy coating by laser cladding. *Mater. Des.* 32, 1910–1915. doi:10.1016/j.matdes.2010.12.001

Zhang, Y., Yang, X., and Liaw, P. K. (2012). Alloy Design and Properties Optimization of High-Entropy Alloys. *JOM (J. Occup. Med.)* 64, 830–838. doi:10.1007/s11837-012-0366-5

Zhang, Y., Zhou, Y. J., Lin, J. P., Chen, G. L., and Liaw, P. K. (2008). Solid-Solution Phase Formation Rules for Multi-component Alloys. *Adv. Eng. Mater.* 10, 534–538. doi:10.1002/adem.200700240

Zhang, Y., Zuo, T. T., Tang, Z., Gao, M. C., Dahmen, K. A., Liaw, P. K., et al. (2014). Microstructures and properties of high-entropy alloys. *Prog. Mater. Sci.* 61, 1–93. doi:10.1016/j.pmatsci.2013.10.001

Zhou, Q., Sheikh, S., Ou, P., Chen, D., Hu, Q., and Guo, S. (2019). Corrosion behavior of Hf0.5Nb0.5Ta0.5Ti1.5Zr refractory high-entropy in aqueous chloride solutions. *Electrochem. Commun.* 98, 63–68. doi:10.1016/j.elecom.2018.11.009

Zhuang, Y. X., Liu, W. J., Chen, Z. Y., Xue, H. D., and He, J. C. (2012). Effect of elemental interaction on microstructure and mechanical properties of FeCoNiCuAl alloys. *Mater. Sci. Eng., A* 556, 395–399. doi:10.1016/j.msea.2012.07.003

Zhuang, Y. X., Xue, H. D., Chen, Z. Y., Hu, Z. Y., and He, J. C. (2013). Effect of annealing treatment on microstructures and mechanical properties of FeCoNiCuAl high entropy alloys. *Mater. Sci. Eng., A* 572, 30–35. doi:10.1016/j.msea.2013.01.081

Conflict of Interest: The authors declare that the research was conducted in the absence of any commercial or financial relationships that could be construed as a potential conflict of interest.

frontiers in Materials

ORIGINAL RESEARCH
published: 11 November 2020
doi: 10.3389/fmats.2020.572005

Synthesis of Ti/TiB Composites via Hydrogen-Assisted Blended Elemental Powder Metallurgy

Yuchao Song[1,2]*, *Shucheng Dong*[1,2], *Oleksandr Stasiuk*[1,2,3], *Dmytro Savvakin*[1,2,3] *and Orest Ivasishin*[1,2,3]

[1]College of Materials Science and Engineering, Jilin University, Changchun, China, [2]International Center of Future Science, Jilin University, Changchun, China, [3]G.V. Kurdyumov Institute for Metal Physics, Kyiv, Ukraine

Titanium–titanium boride (Ti/TiB) metal matrix composites have been widely identified as promising materials for various applications. The traditional ingot metallurgy processing strategies used to fabricate these materials are energy intensive and have fallen short of their perceived mass production potentials. Powder metallurgy processing, especially that aimed at *in-situ* synthesis of Ti/TiB composites from titanium and TiB_2 powder blends, is currently widely used for the cost-efficient production of such composites. However, this approach usually results in excessive sintered porosities and associated mechanical property degradation. Therefore, further thermomechanical or hot isostatic pressing steps are required for porosity reduction. In the present study, low-porosity Ti/TiB composites were synthesized using TiH_2 and TiB_2 powders via a simple press-and-sinter hydrogen-assisted blended elemental powder metallurgy route. The manufacturing route included two stages. Compaction and vacuum sintering of the noted blended powders was followed by hydrogenation and ball milling of the pre-sintered product to produce a hydrogenated, pre-alloyed powder. This was followed by compaction and final sintering. X-ray diffraction, light microscope, and scanning electron microscope were employed to investigate the powder morphology and material microstructures after various processing steps. The role of temporary alloying with hydrogen was established in tailoring the microstructure. When an optimized particle size distribution that was carefully controlled using a Malvern Mastersizer laser analyzer was combined with optimized hydrogenated pre-alloyed Ti/TiB powder compaction and sintering parameters, a nearly dense, uniform composite was formed. The above approach can be considered a promising solution for economical manufacturing of Ti/TiB parts with improved properties, such as a high performance-to-cost ratios.

Keywords: titanium matrix composite, titanium boride, blended elemental powder metallurgy, hydrogenation, densification, microstructure

Edited by:
Chao Yang,
South China University of Technology, China

Reviewed by:
Liang-Yu Chen,
Jiangsu University of Science and Technology, China
Deliang Zhang,
Northeastern University, China

Correspondence:
Yuchao Song
songyc19@mails.jlu.edu.cn

Specialty section:
This article was submitted to Structural Materials, a section of the journal Frontiers in Materials

Received: *15 June 2020*
Accepted: *30 September 2020*
Published: *11 November 2020*

Citation:
Song Y, Dong S, Stasiuk O, Savvakin D and Ivasishin O (2020) Synthesis of Ti/TiB Composites via Hydrogen-Assisted Blended Elemental Powder Metallurgy. Front. Mater. 7:572005. doi: 10.3389/fmats.2020.572005

INTRODUCTION

Titanium alloys have been thoroughly investigated and are used in intensive aerospace, military, biomedicine, and automotive materials applications because of their superior intrinsic properties, such as high specific strengths, excellent corrosion resistance, and high-temperature characteristics. Nevertheless, inferior hardness, poor wear resistance, and unaffordable final-product prices have limited the commercial success of these materials. Ceramic-reinforced titanium matrix composites may offset the physical property shortcomings of conventional titanium alloys (Abkowitz et al., 2004; Morsi and Patel, 2007; Hayat et al., 2019).

Of the various hard reinforcement materials available, such as TiB_2, Al_2O_3, SiC, and TiC, in-situ-formed titanium boride (TiB) is considered the most compatible because it offers a chemically stable composition and its density is similar to that of the titanium matrix. It also exhibits distinctive metallurgical bonding with the titanium matrix (Hu et al., 2017). In addition, since the thermal expansion coefficients of TiB and the matrix are similar, little residual stress forms at their interface. This further enhances the mechanical properties of the material (Yamamoto et al., 1997; Huang et al., 2015).

TiB-reinforced, titanium-based metal matrix composites can be produced via a traditional ingot metallurgy (IM) approach (Chandravanshi et al., 2011; Prasad et al., 2011; Sarkar et al., 2013). A mixture of titanium and boron sources in titanium diboride (TiB_2) or elemental forms dissolves and transforms into a titanium-boron alloy during the melt heating cycle. The *in-situ* TiB phase precipitates in the matrix during solidification via a eutectic reaction at elevated temperatures. Usually, secondary thermal work, such as rolling or extrusion, is introduced to help modify the inevitable as-cast defects in the cast products and convert coarse as-cast grains into finer microstructures.

Powder technologies are effective alternative manufacturing methods. However, pre-alloyed (PA) powder technology involves a melting stage during powder fabrication and subsequent complex powder consolidation operations. Thus, this processing route is relatively complicated. For example, the Ti-B alloy melt can be fast-cooled to obtain PA Ti-B powders via inert gas atomization (Tamirisakandala et al., 2004). Thus, the TiB phase forms and is evenly distributed among the particles. After outgassing to remove volatile impurities, the PA powders can be pressed into green parts and subjected to the abovementioned thermo-mechanical processes to produce wrought products. Advanced alloy production technologies could also be candidates in the fabrication of Ti/TiB composites with enhanced mechanical properties. Selective laser melting (SLM) is proven to be able to fabricate biomedical materials with a superb anti-corrosion ability, while spark plasma sintering (SPS) is time-saving, taking advantage of combining sintering and post treatment with the assistance of current and pressure (Zhang and Chen, 2019). With melt filling into clearance in between the reinforcements and the matrix, semi-solid sintering (SSS) can be adopted to tailor the composite densification (Yang et al., 2017).

However, the abovementioned technologies all face the same dilemma between property and cost efficiency, resulting in the limitation of industrial acceptance. Moreover, there are problematic metallurgical issues. The application of hot deformation is a key problem in ingot metallurgy (IM) processing. The growth of coarse primary TiB phases in hypereutectic compounds is the main obstacle that restricts both the IM and PA approaches (Tamirisakandala et al., 2010).

Unlike conventional IM and PA powder routes for Ti/TiB composite fabrication, blended elemental powder metallurgy (BEPM) is well known to provide a large processing "window" for microstructure control, improved TiB particle distribution uniformity in the metallic matrix, and better cost efficiency because of the lack of melting operations.

To produce composites via the BEPM route, TiB_2, boron, and boron carbide (B_4C) (Gorsse and Miracle, 2003; Saito, 2004; Tamirisakandala et al., 2004; Tjong and Mai, 2008; Tamirisakandala et al., 2010; Kumar et al., 2012; Huang et al., 2015; Li et al., 2016; Baglyuk et al., 2017; Ivasishin et al., 2017; Ivasishin et al., 2019) powders are used as starting materials. They are blended with either titanium or titanium hydride (Saito, 2004; Baglyuk et al., 2017; Ivasishin et al., 2017; Ivasishin et al., 2019) powders to form monoboride TiB particles via a high-temperature reaction between titanium and the abovementioned powders (Tjong and Mai, 2008). However, solid-state reactive sintering of such blends with the *in-situ* formation of Titanium–titanium boride (Ti/TiB) composites generally leads to excessive porosity, which is detrimental to mechanical behavior. Thus, BEPM processing routes always include complex hot deformation operations designed to reduce porosity and produce nearly dense Ti/TiB materials with an improved set of properties. Abkowitz et al. (2004) included hot isostatic pressing (HIP), forging, or extrusion of sintered products in the processing scheme, while Saito (2004) extruded, forged, and annealed sintered semi products to produce materials with properties sufficient for practical application. Li used hot extrusion to eliminate the massive pores that formed during sintering between the Ti matrix and boron powder at the expense of reinforcement aggregation (Li et al., 2016). Kumar compared HIP, spark plasma sintering, and vacuum sintering when making high-density Ti/TiB composites. The denser sintered compacts were acquired by following the first two expensive fabrication techniques; however they could not meet application requirements (Kumar et al., 2012). In the study by Gorsse and Miracle (2003), heat treatment after HIP was conducted for up to 100 h to improve the microstructure and reinforcement distribution of Ti/TiB composites.

The state-of-the-art strategies designed to reduce Ti/TiB composite porosity in most published papers typically required tedious post-thermal mechanical work or long-term heat treatment. These processes are not ideal with respect to economic factors and actual engineering demands. Only studies by Abkowitz et al. (2004) and Saito (2004) were directly aimed at the practical application of titanium-based composites.

Undoubtedly, if residual porosity can be abated, simple compaction and sintering of elemental powder blends could be one of the most fundamental and industrially viable approaches to cost-efficient fabrication of near-net-shape Ti/TiB composites. Such a process could overcome the financial obstacles driven by high material waste and the complex, expensive thermomechanical procedures that other methods require (Geng et al., 2004).

Titanium hydride TiH_2 powders have been demonstrated to be substantial substitutes for conventional CP-Ti powders that do not suffer from the abovementioned severe problems associated with press-and-sinter BEPM fabrication of titanium alloys (Ivasishin and Moxson, 2015). Because of the temporary presence of hydrogen in titanium powder, residual pores can be reduced up to 1%–2% and the contents of interstitials, such as oxygen and chlorine, can be decreased to acceptable levels via dehydrogenation and sintering (Savvakin et al., 2012). However, unlike with titanium alloys, the titanium hydride approach is less effective in producing *in-situ* Ti/TiB and Ti-6Al-4V/TiB composites via the BEPM route (Baglyuk et al., 2017; Ivasishin et al., 2017). Better densification of TiH_2-based blends than Ti-based blends has been observed only at low TiB-phase contents. However, because of the significant porosity induced by the $Ti + TiB_2 \rightarrow 2TiB$ reaction, its overall value increases by 7%–9%, as observed in Ti powder-based blends with reasonable TiB contents. Such poor results require that researchers develop a better understanding of factors that affect the densification of BEPM compacts with boride powder additions in order to more effectively use the positive potential of hydrogenated powders.

The objective of this study was to develop a manufacturing approach for *in-situ* production of nearly dense Ti/TiB composites via hydrogen-assisted BEPM using an economically friendly cold compaction and sintering approach. Sintering of TiH_2 and TiB_2 blends was investigated to establish a better understanding of the role of hydrogen in microstructure evolution during the formation of a nearly dense Ti/TiB composite.

Peculiarities of Densification of TiH_2 + TiB_2 Blends and the Microstructures of the Resulting Ti/TiB Composites

Powder blends of TiH_2 with 5 and 10 wt% TiB_2 corresponding to Ti/8.4 vol% TiB and Ti/16.8 vol% TiB composites, respectively, were used in the present investigation to elucidate the general peculiarities of *in-situ* formation of Ti/TiB materials via BEPM. TiB inclusions were expected during the sintering process due to the reaction $TiB_2 + Ti \rightarrow 2TiB$.

As the dominant starting component, single-phase titanium hydride TiH_2 (3.5 wt% H) powder was sieved to less than 100 μm and blended with corresponding amounts of fine TiB_2 powder less than 25 μm in size. **Figure 1** shows the particle size distributions of the initial powders, as determined using a Malvern Mastersizer 3,000 laser analyzer. The maximum size of titanium hydride particles sieved through an 100 μm cell sieve is approximately 120 μm because the particles are not spherical. The peak of the TiH_2 powder size distribution curve appears at approximately 40 μm. The average TiB_2 particle is approximately 8 μm in size. The powders were blended in a drum container for 6 h. Once the elemental blends were prepared, cold pressing (600 MPa) was used to fabricate cylindrical (10 mm in diameter, 10 mm long) and prismatic (60 × 9 × 9 mm) preforms. Sintering was performed in vacuum at 1,250°C (heating rate 10°C/min), followed by 4 h of isothermal exposure. Vacuum heating up to sintering temperature resulted in hydrogen emission from TiH_2 and formation of

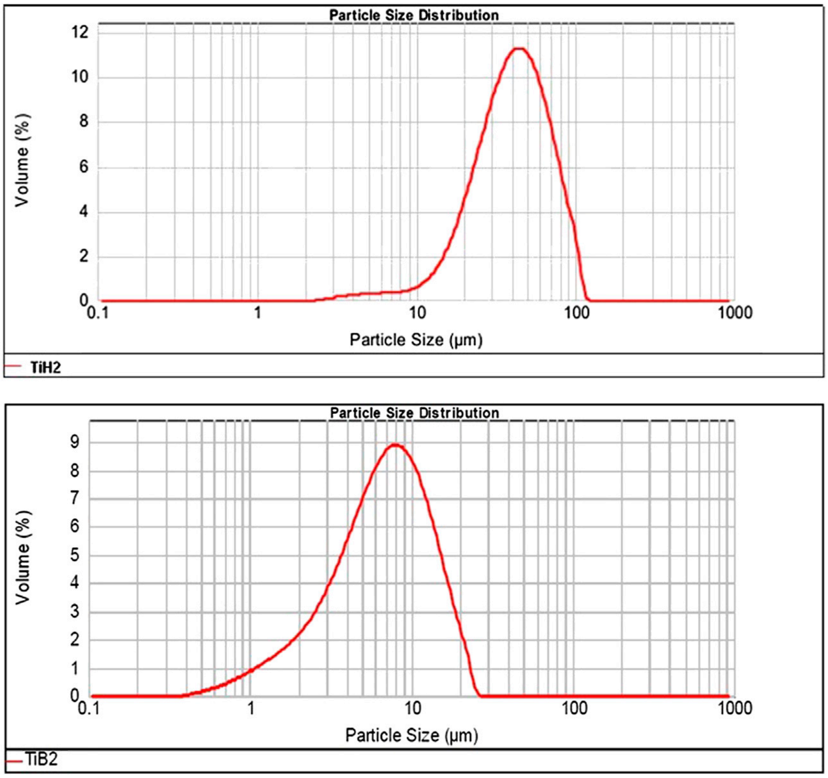

FIGURE 1 | Particle size distributions of starting powders: **(A)** TiH_2 and **(B)** TiB_2.

dehydrogenated titanium powder particles. The negative Gibbs free energy ensures that the TiB formation reaction occurs with the development of boron diffusion into the Ti matrix (Singh et al., 2019).

The microstructure of sintered Ti/8.4% TiB material is shown in **Figure 2** (TESCAN VEGA3). Images of the sintered samples indicate the presence of local microstructural inhomogeneity and substantial residual porosity. The porosity level was determined to be 7.5% via analysis of polished cross sections of the material. This is similar to early residual porosity values obtained in Ivasishin et al. (2017). The density of the sintered compact as determined via Archimedes's technique is 4.16 g/cm^3. The phase composition of the powder blends and sintered materials (**Figures 3A,B**) was analyzed using an "Ultima IV" diffractometer (Rigaku, Japan) that used monochromatic CuKα radiation. The sintered material consists of completely dehydrogenated α titanium matrix with orthorhombic TiB as the main boride phase and trace amounts of unreacted TiB_2 phase (**Figure 3B**). **Figure 2** clearly reveals that the reaction of TiB_2 particles with titanium and the diffusion of boron inside the matrix during high-temperature sintering forms boride crystals with various morphologies. The *in-situ* nucleated TiB phase exhibits coarse needle-like or lamellar crystals that are located mainly between and inside large titanium grains. Some irregularly-shaped gatherings of disperse boride particles exist locally, as shown in **Figure 2B**. Relatively large equiaxed boride particles, like those presented in **Figure 2C**, are identified as intermediate reaction products consisting of a mixture of TiB_2 and TiB phases (Ivasishin et al., 2019). Inhomogeneous boride redistribution within the titanium matrix produces relatively large areas (up to 60–80 μm in size) that are free of boride precipitation. The sizes of such areas correlate with that of the initial titanium hydride powder. This implies that finer starting titanium hydride powders might achieve better sintered composite microstructural homogeneity. Considerable porosity appears near boride crystals. Most pores form and aggregate directly alongside large boride clusters at the locations of initial TiB_2 particles and intermediate Ti-B reaction products.

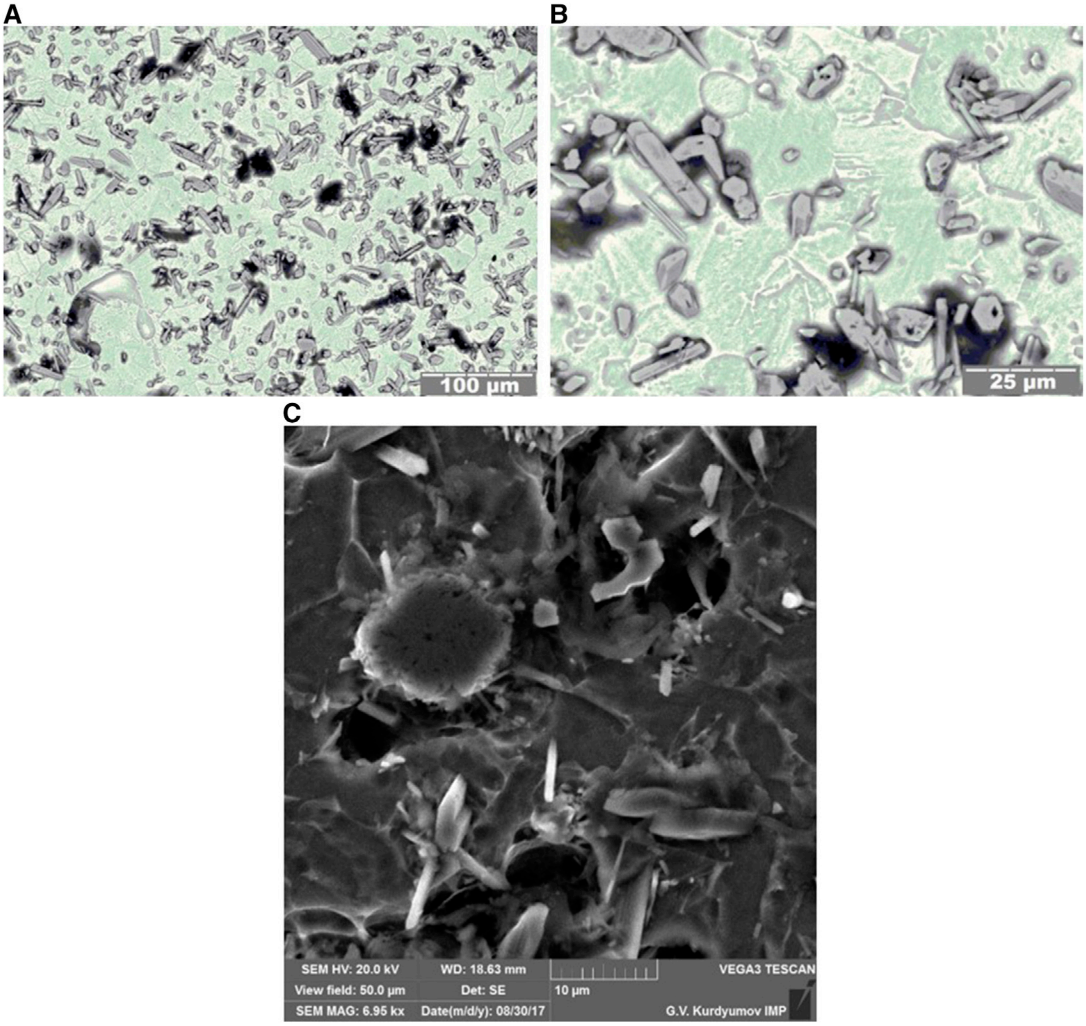

FIGURE 2 | Microstructures of Ti/8.4 vol% TiB samples fabricated via sintering at 1,250°C for 4 h **(A,B)** and typical morphology of boride inclusions showing not completely transformed equiaxed TiB_2 particle **(C)**. SEM.

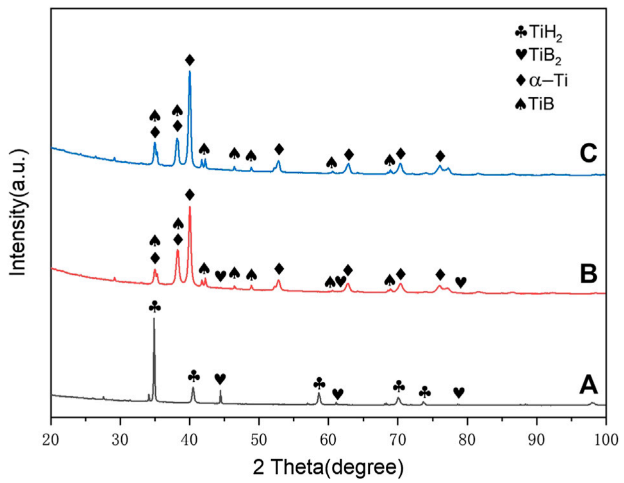

FIGURE 3 | X-ray diffraction patterns of initial TiH_2 + 10% TiB_2 powder blends **(A)**, material after first sintering **(B)** and after second hydrogenation and sintering stage **(C)**.

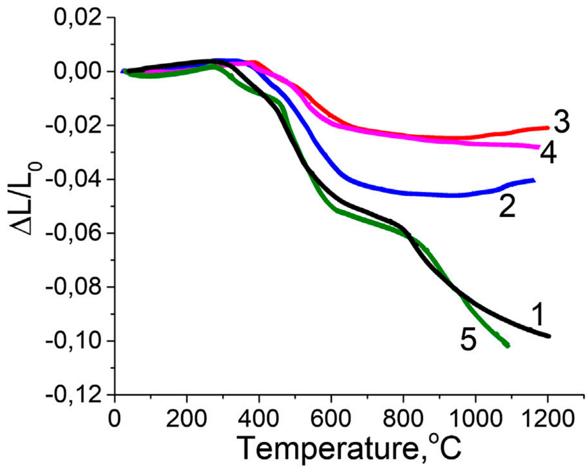

FIGURE 4 | Dilatometric heating curves for (1) compacted TiH_2 powder; (2) TiH_2 + 5% TiB_2 powder blend; (3,4) TiH_2 + 10% TiB_2 powder blends; and (5) hydrogenated, pre-alloyed Ti/TiB powder compacts. The TiB_2 particles are (2, 3) <25 μm and (4) <8 μm in size.

To investigate the sintering kinetics and to understand the reasons for increased Ti/TiB composite porosities, *in-situ* shrinkage curves (**Figure 4**) were measured during vacuum heating (rate of 10°C/min) of powder compacts using a special dilatometric complex (Ivasishin et al., 2010). It is clearly seen (**Figure 4**) that the densification kinetics of the TiH_2 + 5% TiB_2 (curve 2) blend are worse than those of a pure TiH_2 compact (curve 1). This indicates that excess porosity forms during the heating stage. When the TiB_2 content is further increased to 10% in the powder blend (curve 3), less shrinking occurs. This indicates that there is an inverse relationship between the amount of TiB_2 used and the extent of densification. Most TiH_2 densification occurs during the dehydrogenation period. Starting when the vacuum heating process has reached approximately 300°C, the release of hydrogen atoms results in the reconstruction of the crystal lattice and significant shrinkage of each powder particle and of the entire sample due to a specific compaction mechanism that is exhibited between the particles (Ivasishin and Savvakin, 2010). Dehydrogenation is nearly complete for all samples at around 600–650°C. Phase transformations δ-TiH_2 to β-Ti and then to α-Ti creates a large number of crystalline defects (Ivasishin et al., 2011). This factor activates an overall diffusion that is accompanied by intensive powder sintering and ~10% linear reduction in total. However, as seen when comparing curve 1 with curves 2 and 3, the addition of TiB_2 particles to the titanium hydride strongly affects the shrinkage processes of the corresponding compacts, retarding densification. The presence of TiB_2 particles results in the loss of compact integrity during dehydrogenation, as well as the formation of additional gaps and voids between compacted particles at 300–650°C. When the temperature exceeds 650°C, the boride blend shrinkage intensity decreases substantially. Minor swelling even occurs when the temperature exceeds 1,000°C. These differences can be attributed to the presence of titanium diboride particles in the blend, which, unlike hydride particles, are not subject to dehydrogenation-related shrinkage. Reactions between dehydrogenated Ti particles and TiB_2 are another reason for poor densification. Although calculations based on the densities of reacting materials indicate minor volume reductions (~1%) during *in-situ* formation of the TiB phase, swelling occurs because of increased porosity formation at higher boride contents. As shown in Ivasishin et al. (2019)' the interfaces between TiB_2 particles and the Ti matrix are important sintering-related pore formation locations. The swelling effect observed due to this reaction strongly hinders the overall densification upon powder sintering, decreasing overall linear shrinkage from ~10% for TiH_2 to ~4% for TiH_2 admixtures that contain 5% TiB_2 and to 2% for blends that contain 10% TiB_2.

Bulk shrinkage of TiH_2 powder particles upon hydrogen release during heating cycles creates extra interstitial spaces between the dehydrogenated titanium matrix and TiB_2 particles. These spaces further impede direct contact between the reactants, diminishing the TiB formation rate and sometimes stopping the reaction during its intermediate stages. Two more reasons for the noted excess porosity are the gap between the diffusion capabilities of titanium and boron at elevated temperatures (Baglyuk et al., 2017) and the difference between the boron diffusion velocities in TiB and TiB_2 phases. These factors can cause the formation of Kirkendall porosity during boron redistribution (Panda et al., 2003). The TiB crystals grow to form needle-like shapes via unidirectional diffusion of atomic boron. This creates a flux of vacancies in the opposite direction and forms pores, which also contribute to the swelling of the compact and the formation of residual porosity.

The presence of a particular boride cluster structure surrounded by a number of pores (**Figure 2C**) and the remnants of TiB_2 phase in the sintered material prove that titanium diboride is not completely reacted to single-phase titanium monoboride even after treatment at 1,250°C for 4 h. Similar effects were observed in Ivasishin et al. (2019). Incomplete transformation of TiB_2 powder to the TiB phase can also be induced via occasional formation of relatively coarse TiB_2 aggregates during powder blending. This also promotes the porous structure developed during heating.

Increased porosity, remnants of borides that are not fully transformed into TiB, and boride particle distribution irregularities in the titanium matrix harm the mechanical properties of the resulting composites. For example, Ti/8.4 vol% TiB with 7.5% porosity has a moderate Vickers hardness (260–270 HV) and moderate tensile characteristics (UTS = 770 MPa, elongation 2.4%). The Ti/16.8% TiB composite is completely brittle without the expected hardness increase due to its higher (~9%) porosity. For comparison, commercially pure titanium (CP-Ti) produced by sintering TiH_2 powder exhibits a hardness of 220 HV–230 HV, UTS of 570–600 MPa, and elongation of 16%–22% at a low (1.5%) residual porosity. Excessive porosity of Ti/TiB material is the main cause of premature fracture because pores serve as stress concentrators during tensile loading and hide the strengthening effect of boride particles during hardness testing. The strengthening potential of TiB particles cannot be used when the resulting composites exhibit excessive porosities.

EFFORTS TO REDUCE POROSITIES BY VARYING BLENDED ELEMENTAL POWDER METALLURGY PROCESSING PARAMETERS

Since high porosity of sintered Ti/TiB composite porosities, incomplete $TiB_2 \rightarrow TiB$ transformation, and non-uniform distribution of TiB crystals in the titanium matrix all contribute to property degradation, significant efforts were dedicated to improving as-sintered microstructures by varying press-and-sinter BEPM parameters. Smaller starting powders, higher temperatures, and longer sintering durations were tested. All such efforts are summarized in **Table 1**, taking Ti/8.4% TiB composite as an example. A basic set of parameters was taken, as described above.

Changing the types and sizes of starting powders did not result in a noticeable microstructural improvement. Since TiB_2 powder is responsible for compromised densification, a finer starting TiB_2 powder (<8 μm) was tested via dilatometric experiments (**Figure 4**, curve 4). Although the decreased boride powder size leads to some better shrinkage behavior at high temperatures (compare curves 3 and 4 in **Figure 4**), the final porosity is not considerably reduced (**Table 1**, #2). A minor decrease in as-sintered porosity is also observed in Stasiuk (2019) when smaller TiH_2 powder particles are used (**Table 1**, #3). These experiments cannot reduce the average residual porosity below 5%–6%. As expected, the use of HDH titanium powder sieved to less than 100 μm (i.e., with a particle size distribution similar to that of the TiH_2 powder presented in **Figure 1**) results in even worse densification, similar to that observed in Baglyuk et al. (2017), and an increase in residual porosity to 9% for the Ti/8.4% TiB composite (**Table 1**, #6).

Increasing the temperature to 1,350°C and extending the sintering cycle duration to 8 h has a minor effect on porosity reduction (**Table 1**, #4–#5), while completion of TiB formation improves only slightly. To conclude, substantial improvement of Ti/TiB composite microstructures requires a different technique that includes more revolutionary changes to the manufacturing process.

PRODUCTION OF LOW-POROSITY COMPOSITES VIA THE BLENDED ELEMENTAL POWDER METALLURGY + PRE-ALLOYED DOUBLE HYDROGENATION/DOUBLE SINTERING METHOD

The idea for this process modification comes from the relatively good Ti/TiB composite PA powder metallurgy results in Tamirisakandala et al. (2004). It has already been mentioned that the disadvantage of the PA approach is that it requires melting for powder fabrication and further complex operations to consolidate hard, crystallized powders. In contrast, processing can be simplified significantly if the above-described BEPM solid-state sintered Ti/TiB composites are used as a specific grade of PA material for further production of PA powders and these resulting PA powders are then used in a second press-and-sinter stage.

In two-stage BEPM + PA processing, the non-uniform Ti/TiB obtained during the first sintering stage is further mixed via crushing. This promotes better boride-phase distribution uniformity in the resulting PA powder. Moreover, the absence of the $TiB_2 \rightarrow TiB$ reaction during subsequent sintering of the PA powder can improve densification as compared to the initial TiH_2 + TiB_2 powder blends. However, the problem with this processing route is the insufficient sintered Ti/TiB composite crushing ability. This hinders the production of PA powders of desirable sizes. Despite the considerable porosities of the Ti/TiB composites produced during the first sintering stage and the presence of brittle boride particles, the titanium matrix plasticity allows the material to be deformed instead of crushed. Transformation of bulk

TABLE 1 | Microstructural characteristics of Ti/8.4% TiB composites produced with various press-and-sinter BEPM parameters.

#	Parameter variation	Average residual porosity, %	Effect on completion of TiB formation	Effect on TiB uniformity improvement
1	Basic set of parameters	7.5	—	—
2	Finer TiB_2 powder (<8 μm)	5	+	-
3	Finer TiH_2 powder (<63 μm)	6	-	+
4	Increased sintering temperature (1,350°C)	6	+	-
5	Longer sintering time (8 h)	7	+	-
6	Substitution of TiH_2 with Ti HDH powder of the same size	9	-	-

as-sintered product into PA powders smaller than 100 μm requires long, intensive milling processes that lead to excessive contamination of the powders.

Hydrogenation of the Ti/TiB composite obtained during the first sintering stage was proposed to overcome the problems described above. This operation was intended to be the main feature of the modified process. Hydrogenation would make the Ti/TiB composite material brittle and reduce its strength, just as it affects titanium. Non-uniform, porous composite materials saturated with hydrogen would be crushed easily into composite powders of desirable sizes. Utilization of a hydrogenated, pre-alloyed powder in a second press-and-sinter stage would promote a positive influence of hydrogen on densification and hydrogen cleaning of powder once more to produce uniform, low-porosity composite structures. This approach is validated via the experimental results described below.

The Ti/TiB material hydrogenation process was thoroughly investigated and optimized based on Sieverts method, which demonstrated active hydrogen consumption above 425°C. The Ti/TiB composite obtained by sintering of the TiH_2 + 5 wt% TiB_2 blends (1,250°C for 4 h) was saturated with hydrogen at 600°C and 0.6 MPa. Thus, the titanium matrix reverts to a δ-TiH_X lattice structure according to the X-ray data. The substantial volume change associated with this leads to stress accumulation and crack nucleation in the bulk sintered composites. As shown in **Figure 5**, wide cracks extend throughout the sintered compacts and fractures form and grow along intergranular positions.

Because of the brittle, low-strength nature of the hydride composite and ceramic reinforcement of the titanium boron compound, the sintered compacts were readily broken up and ground into powders with desirable dimensions after quick (10 s) milling in a planetary mill. **Figure 6** shows the resulting hydrogenated pre-alloyed powders after milling. The particles of irregular morphologies are fractured during further compaction and mechanically locked to each other with the formation of dense compacts via close powder stacking. Furthermore, large TiB whiskers and incompletely reacted remnants of the initial TiB_2 powders are crushed and blended with the matrix phases, creating a prerequisite for the complete formation and homogeneous distribution of the titanium monoboride phase during the second sintering stage. The resulting PA powder was pressed into compacts at 600 MPa and sintered again using the same parameters (1,250°C for 4 h) to form the final Ti/TiB composite.

Neither TiB_2 nor other Ti-B phases were identified after the second sintering step (**Figure 3**). The intensities of the TiB peaks are enhanced after the second sintering step. This indicates that transformation to TiB is complete. Titanium hydride phases are not found in the composite after the second sintering step. This demonstrates that hydrogen has completely escaped from the base material during heating. The above X-ray findings are in accordance with our microstructure observations.

As shown in **Figure 7**, after hydrogenation of pre-sintered material and the second press-and-sinter operation, porosity is reduced from over 7.5% to nearly 2.2%, which is acceptable. The density improvement from 4.16 to 4.41 g/cm^3 corroborates this observation. The average pore size also decreases. This promising result is in line with dilatometric studies where hydrogenated, pre-alloyed powder compacts (**Figure 4**, curve 5) exhibit shrinkage trends similar to those for pure TiH_2 (curve 1). Hydrogen desorption from hydrogenated, pre-alloyed Ti/TiB compacts is observed at the same temperature range as for

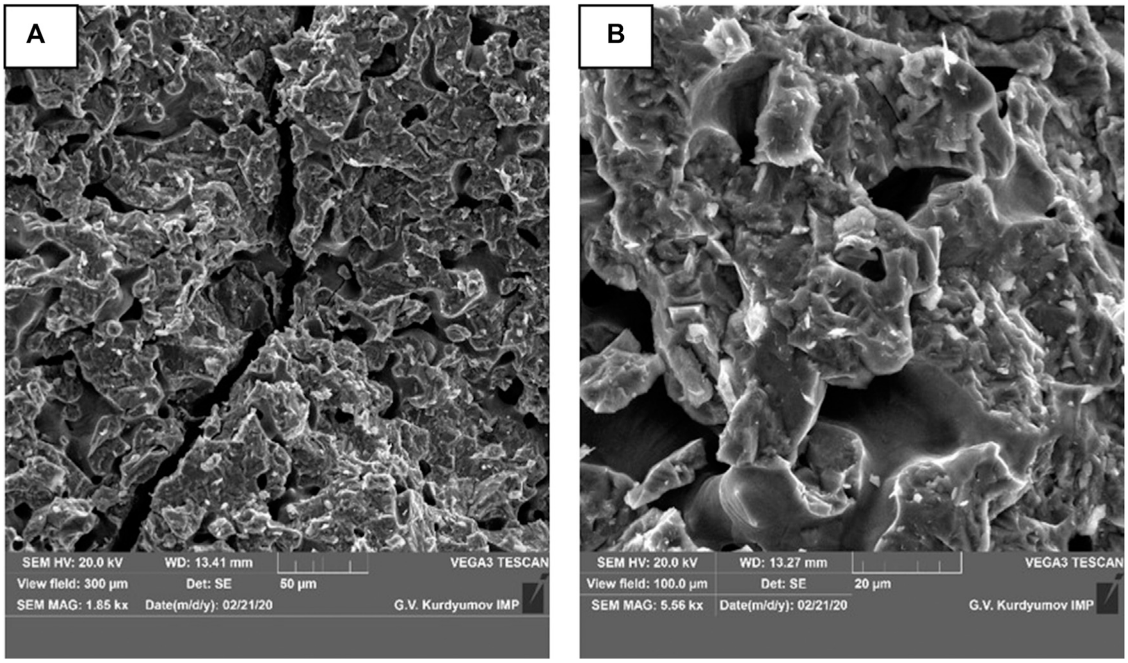

FIGURE 5 | SEM images of bulk sintered samples after hydrogenation.

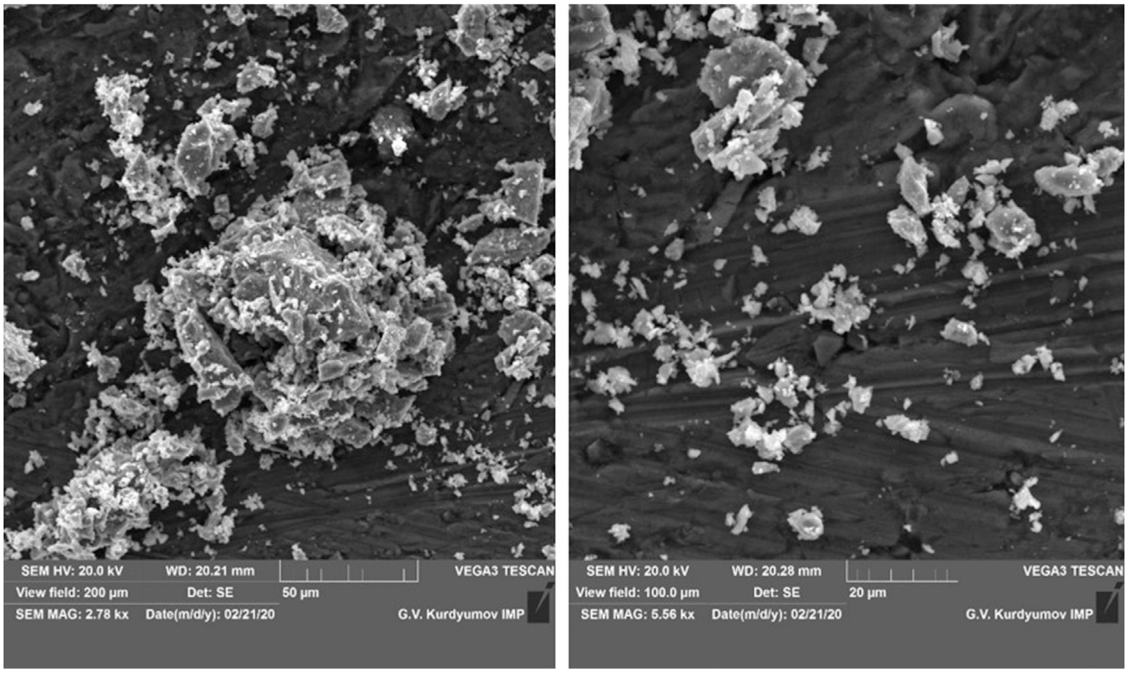

FIGURE 6 | SEM images of hydrogenated pre-alloyed powders.

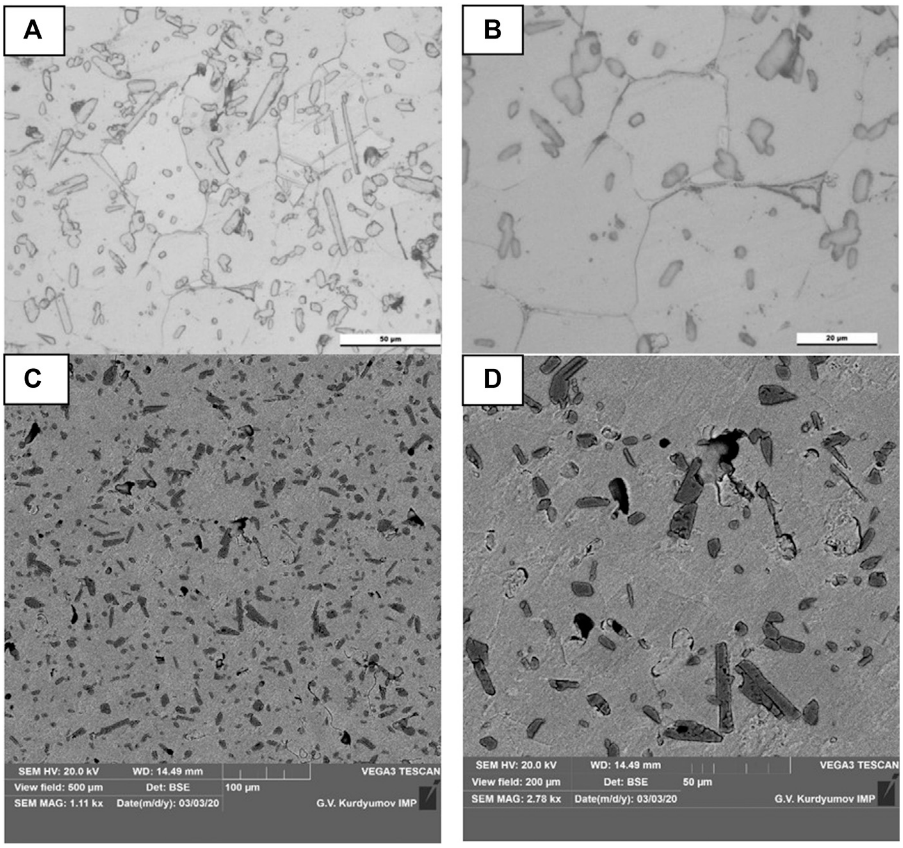

FIGURE 7 | Low-porosity microstructure of the Ti/8.4 vol% TiB composite after a second sintering stage performed at 1,250°C for 4 h.

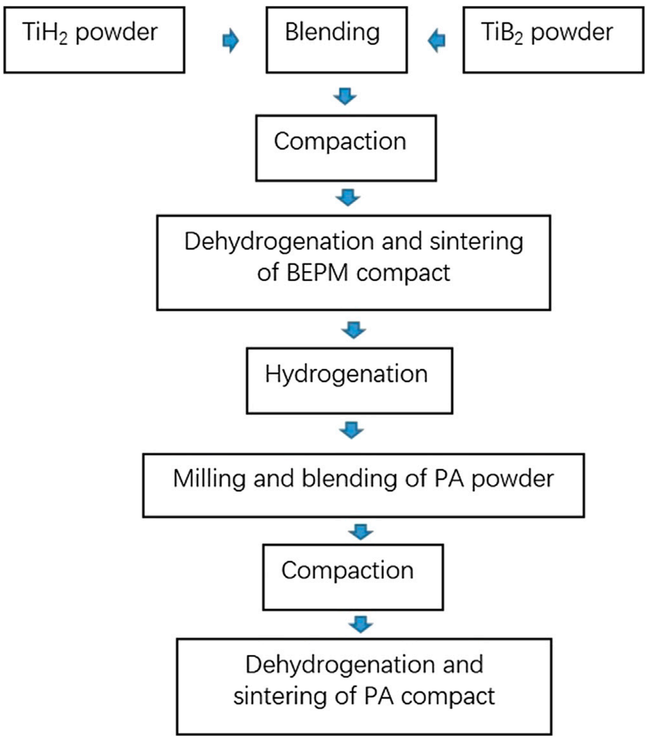

FIGURE 8 | Scheme of the two-stage BEPM + PA press-and-sinter manufacturing process used to make Ti/TiB composites.

titanium hydride powder (300–700°C) and results in analogous compact shrinkage during dehydrogenation (curves 5 and 1 in **Figure 4**). The apparent shrinkage difference between curve 5 and curves 2–4 demonstrates that the considerably more intense densification of the hydrogenated pre-alloyed powder compact naturally results in low residual porosities after isothermal exposure at 1,250°C. The presence of boron mainly as a TiB phase embedded into hydrogenated titanium powder provides better densification kinetics than those observed with the TiB_2 + TiH_2 powder blend during dehydrogenation (curves 5 and 2 in **Figure 4**). The absence of a pronounced $Ti + TiB_2 \rightarrow 2TiB$ reaction above 900°C in the pre-alloyed Ti/TiB compact minimizes factors that negatively affect densification and reduce porosity.

The second sintering stage improves the TiB reinforcement distribution uniformity in the Ti matrix considerably and produces a grain size of approximately 40 μm (**Figure 7**). Finer TiB particles are attained and uniformly distributed among the α-Ti grains in equiaxial or whisker morphologies, as shown in **Figure 7**. The markedly reduced residual porosity is observed with few voids near single TiB particulates (**Figure 7D**). The two-stage hydrogen-assisted processing schematically summarized in **Figure 8** significantly contributes to the tailored microstructures and composite homogeneity.

Vickers hardness tests were carried out using a Wolpert Wilson 452 SVD hardness meter in order to provide preliminary evaluations of the mechanical properties of the Ti/8.4 vol% TiB composites fabricated using the present approach. The hardness values obtained demonstrate that the proposed hydrogen-assisted two-stage BEPM + PA approach contributes to a nearly 50% increase in hardness (390–410 HV) relative to the traditional one-step BEPM press-and-sinter route (260–270 HV). This is a clear reflection of the finer grain size, minimized residual porosity, and better TiB redistribution uniformity in Ti/TiB composites fabricated via the hydrogen-assisted BEPM + PA technique. The Ti/TiB composite hardness values suggest the feasibility of this manufacturing approach for practical use.

CONCLUSIONS

(1) BEPM press-and-sinter manufacturing of Ti/TiB composites using TiH_2 + TiB_2 powder blends results in highly porous structures, non-uniform distribution of borides throughout the titanium matrix, and incomplete *in-situ* transformation of TiB_2 into the TiB phase. Addition of TiB_2 particles to TiH_2 powder hinders densification kinetics because of the loss of compact integrity that results from differences in the powder constituent volume changes that occur during the hydrogen emission stage. Development of a high-temperature *in-situ* $Ti + TiB_2 \rightarrow TiB$ reaction is another reason for poor densification.

(2) The microstructures of BEPM-produced Ti/TiB composites could not be markedly improved via optimization of press-and-sinter processing parameters, such as powder size or the sintering time-temperature regime.

(3) A new approach was developed based on the hydrogen-assisted two-stage press-and-sinter BEPM + PA method. The microstructurally and chemically non-uniform, highly porous Ti/TiB composite received after the first sintering stage was hydrogenated again to produce PA powder. The second stage of processing focuses on sintering the hydrogenated PA powder. This finally produces a Ti/TiB composite with improved densification kinetics, as well as the desired chemistry and microstructure.

DATA AVAILABILITY STATEMENT

The raw data supporting the conclusions of this article will be made available by the authors, without undue reservation.

AUTHOR CONTRIBUTIONS

YS and OS conceived and designed the study and experiment plan and performed the experiments. YS wrote the paper. YS and SD analyzed the experiment result. DS and OI reviewed and edited the manuscript. All authors read and approved the manuscript.

FUNDING

This study was funded by Jilin University, China and the National Academy of Sciences of Ukraine.

REFERENCES

Abkowitz, S., Abkowitz, S. M., Fisher, H., and Schwartz, P. J. (2004). CermeTi discontinuously reinforced Ti-matrix composites: manufacturing, properties, and applications. *J. Mater. Sci.* 56, 37–41. doi:10.1007/s11837-004-0126-2.

Baglyuk, G. A., Ivasyshyn, O. M., Stasyuk, O. O., and Savvakin, D. G. (2017). The effect of charge component composition on the structure and properties of titanium matrix sintered composites with high-modulus compounds. *Powder Metall. Met. Ceram.* 56, 45–52. doi:10.1007/s11106-017-9870-z.

Chandravanshi, V. K., Sarkar, R., Kamat, S. V., and Nandy, T. K. (2011). Effect of boron on microstructure and mechanical properties of thermomechanically processed near alpha titanium alloy ti-1100. *J. Alloys Compd.* 509, 5514. doi:10.1016/j.jallcom.2011.02.114.

Geng, K., Lu, W., Qin, Y., and Zhang, D. (2004). *In situ* preparation of titanium matrix composites reinforced with TiB whiskers and Y_2O_3 particles. *Mater. Res. Bull.* 39, 873–879. doi:10.1016/j.materresbull.2003.11.008.

Hayat, M. D., Singh, H., He, Z., and Cao, P. (2019). Titanium metal matrix composites: an overview. *Compos. Appl. Sci. Manuf.* 121, 418–438. doi:10.1016/j.compositesa.2019.04.005.

Hu, Y., Ning, F., Wang, X., Wang, H., Zhao, B., Cong, W., et al. (2017). Laser deposition-additive manufacturing of *in situ* TiB reinforced titanium matrix composites: TiB growth and part performance. *Int. J. Adv. Manuf. Technol.* 93, 3409–3418. doi:10.1007/s00170-017-0769-0.

Huang, L. J., Geng, L., and Peng, H.-X. (2015). Microstructurally inhomogeneous composites: is a homogeneous reinforcement distribution optimal? *Prog. Mater. Sci.* 71, 93–168. doi:10.1016/j.pmatsci.2015.01.002.

Ivasishin, O. M., Bagliuk, G. A., Stasiuk, O. O., and Savvakin, D. G. (2017). The peculiarities of structure formation upon sintering of TiH_2+TiB_2 powder blends. *Phys. Chem. Solid State.* 18, 15–20.

Ivasishin, O. M., Cherepin, V. T., Kolesnik, V. N., and Gumenyak, N. M. (2010). An automated dilatometric system. *Instrum. Exp. Tech.* 53, 457–460. doi:10.1134/s0020441210030255.

Ivasishin, O. M., Markovsky, P. E., Savvakin, D. G., Stasiuk, O. O., Rad, M. N., and Prikhodko, S. V. (2019). Multi-layered structures of Ti-6Al-4V alloy and TiC and TiB composites on its base fabricated using blended elemental powder metallurgy. *J. Mater. Process. Technol.* 269, 172–181. doi:10.1016/j.jmatprotec.2019.02.006.

Ivasishin, O. M., and Moxson, V. S. (2015). Low-cost titanium hydride powder metallurgy. *Titanium Powder Metall.* 2015, 117–148. doi:10.1016/b978-0-12-800054-0.00008-3.

Ivasishin, O. M., Savvakin, D. G., and Gumenyak, N. M. (2011). Dehydrogenation of powder titanium hydride and its role in the activation of sintering. *Metallofiz. Noveish. Tekhnol.* 33, 899–917.

Ivasishin, O. M., and Savvakin, R. G. (2010). The impact of diffusion on synthesis of high-strength titanium alloys from elemental powder blends. *Key Eng. Mater.* 436, 113–121. doi:10.4028/www.scientific.net/kem.436.113.

Morsi, K., and Patel, V., V. (2007). Processing and properties of titanium–titanium boride (TiBw) matrix composites—a review. *J. Mater. Sci.* 56, 42–48.

Kumar, M. S., Chandrasekar, P., Chandramohan, P., and Mohanraj, M. (2012). Characterisation of titanium–titanium boride composites processed by powder metallurgy techniques. *Mater. Char.* 73, 43–51.

Li, S., Kondoh, K., Imai, H., Chen, B., Jia, L., and Umeda, J. (2016). Strengthening behavior of *in situ* -synthesized (TiC-TiB)/Ti composites by powder metallurgy and hot extrusion. *Mater. Des.* 95, 127–132. doi:10.1016/j.matdes.2016.01.092.

Panda, K. B., and Chandran, K. S. R. (2003). Synthesis of ductile titanium-titanium boride (Ti-TiB) composites with a beta-titanium matrix: the nature of TiB formation and composite properties. *Metall. Mater. Trans.*, 34, 1371–1385. doi:10.1007/s11661-003-0249-z.

Prasad, K., Sarkar, R., Ghosal, P., Satyanarayana, D. V. V., Kamat, S. V., and Nandy, T. K. (2011). Tensile and creep properties of thermomechanically processed boron modified timetal 834 titanium alloy. *Mater. Sci. Eng. A* 528, 6733–6741. doi:10.1016/j.msea.2011.05.069.

Saito, T. (2004). The automotive application of discontinuously reinforced TiB-Ti composites. *J. Mater. Sci.* 56 (5), 33–36. doi:10.1007/s11837-004-0125-3.

Sarkar, R., Ghosal, P., Nandy, T. K., and Ray, K. K. (2013). Structure-property correlation of a boron and carbon modified as castβtitanium alloy. *Phil. Mag.* 93, 1936–1957. doi:10.1080/14786435.2013.765979.

Savvakin, D. H., Humenyak, M. M., Matviichuk, M. V., and Molyar, O. H. (2012). Role of hydrogen in the process of sintering of titanium powders. *Mater. Sci.* 47 (5), 651–661. doi:10.1007/s11003-012-9440-y.

Gorsse, S., and Miracle, D. B. (2003). Mechanical properties of Ti-6Al-4V/TiB composites with randomly oriented and aligned TiB reinforcements. *Acta Mater.* 51, 2427–2442. doi:10.1016/s1359-6454(02)00510-4.

Singh, H., Hayat, M., Zhang, H., Das, R., and Cao, P. (2019). Effect of TiB_2 content on microstructure and properties of *in situ* Ti-TiB composites. *Int. J. Miner. Metall. Mater.* 26, 915–924. doi:10.1007/s12613-019-1797-6.

Stasiuk, O. O. (2019). The general laws of high-modulus refractory compounds influence on structure and properties of sintered titanium alloys. Dissertation (Kyiv: National Technical University of Ukraine, Ihor Sikorsky Kyiv Polytechnical Institute).

Tamirisakandala, S., Bhat, R. B., Ravi, V. A., and Miracle, D. B. (2004). Powder metallurgy Ti-6Al-4V-xB alloys: processing, microstructure, and properties. *J. Mater. Sci.* 56 (5), 60–63. doi:10.1007/s11837-004-0131-5.

Tamirisakandala, S., and Miracle, D. B. (2010). Microstructure engineering of titanium alloys via small boron additions. *Int. J. Adv. Eng. Sci. Appl. Math.* 2, 168–180. doi:10.1007/s12572-011-0033-z.

Tjong, S. C., and Mai, Y.-W. (2008). Processing-structure-property aspects of particulate- and whisker-reinforced titanium matrix composites. *Compos. Sci. Technol.* 68, 583–601. doi:10.1016/j.compscitech.2007.07.016.

Yamamoto, T., Otsuki, A., Ishihara, K., and Shingu, P. H. (1997). Synthesis of near net shape high density TiB/Ti composite. *Materials Science and Engineering: A*, 239-240, 647–651. doi:10.1016/s0921-5093(97)00643-6.

Yang, C., Kang, L. M., Li, X. X., Zhang, D. T., Fu, Z. Q., et al. (2017). Bimodal titanium alloys with ultrafine lamellar eutectic structure fabricated by semi-solid sintering. *Acta Mater.* 132, 491–502. doi:10.1016/j.actamat.2017.04.062.

Zhang, L. C., and Chen, L. Y. (2019). A review on biomedical titanium alloys: recent progress and prospect. *Adv. Eng. Mater.* 21, 1801215. doi:10.1002/adem.201801215.

Conflict of Interests: The authors declare that the research was conducted in the absence of any commercial or financial relationships that could be construed as a potential conflict of interest.

The handling editor declared a past co-authorship with one of the authors OI.

frontiers
in Materials

ORIGINAL RESEARCH
published: 25 November 2020
doi: 10.3389/fmats.2020.560569

Microstructure and Property of Sintered Fe-2Cu-0.8C-0.6Mo-2W Materials Prepared From Prediffused Powders

Wenchao Chen[1,2], *Jinghui Wang*[1,2], *Pengqi Chen*[1,2] and *Jigui Cheng*[1,2]*

[1]*School of Materials Science and Engineering, Hefei University of Technology, Hefei, China,* [2]*Research Centre for Powder Metallurgy Engineering and Technology of Anhui Province, Hefei, China*

Prediffused Fe-W powder with 2 wt% of tungsten was prepared by heating Fe-W powder mixes at 800°C for 45 min in H_2 atmosphere. Two kinds of Fe-2Cu-0.8C-0.6Mo-2W powder mixtures were obtained by mechanically mixing the prediffused Fe-W powders with the other elemental powders. After pressing and sintering, the sintered Fe-2Cu-0.8C-0.6Mo-2W materials were obtained from the two powder mixtures. The effects of the introducing methods of tungsten element and sintering conditions on microstructure, mechanical and wear properties of the sintered samples were investigated. The results show that with the increase of sintering temperature and time, hardness and strength of sintered samples increase. Prediffused treatment of Fe-W powder can improve density of green compacts and sintered samples. When W element introduced in the form of prediffused Fe-W powders, the compacts pressed at 700 MPa have a green density of 7.13 g/cm^3, and after sintered at 1,150°C, the density, hardness, tensile strength and radial crushing strength of the sintered samples are 7.16 g/cm^3, 95 HRB, 547 and 791 MPa, respectively, which are higher than those of the samples prepared from powder mixtures by mechanically mixing the elemental powders. Furthermore, the prediffused treatment of Fe-W powders can improve the distribution of W element and enhance wear resistance.

Keywords: ferrous powder metallurgy, prediffused Fe-W powders, sintering, microstructure, property

Edited by:
Chao Yang,
South China University of Technology,
China

Reviewed by:
Hua Li,
Shanghai Jiao Tong University, China
Jidong Ma,
Xiamen University of Technology,
China

Correspondence:
Jigui Cheng
jgcheng@hfut.edu.cn

Specialty section:
This article was submitted to
Mechanics of Materials,
a section of the journal
Frontiers in Materials

Received: *09 May 2020*
Accepted: *28 October 2020*
Published: *25 November 2020*

Citation:
Chen W, Wang J, Chen P and Cheng J
(2020) Microstructure and Property of
Sintered Fe-2Cu-0.8C-0.6Mo-2W
Materials Prepared From
Prediffused Powders.
Front. Mater. 7:560569.
doi: 10.3389/fmats.2020.560569

INTRODUCTION

Iron-copper-carbon (Fe-Cu-C) alloy is the most widely used sintered iron-based materials, accounting for more than 50% of in the sintered ferrous powder metallurgy parts (Lee et al., 2012; Annamalai et al., 2013; Azevedo et al., 2018). With the developments of modern industry and manufacturing technology, the performance of sintered ferrous components is more required rigorously. Researchers have found that the performance can be improved by adding alloying elements, such as Mo, Ni, and Cr and so on. These elements not only have the effect of solution strengthening, but can also refine the grain size of pearlite. (Wu et al., 2016; Wang et al., 2019; Zhang et al., 2019). Among these, tungsten as a novel alloying element has an excellent hardening effect, which can be used to enhance the matrix and improve the high temperature strength (Deng et al., 2014; Xuan et al., 2019). The sintered PM materials with W addition show good wear resistance due to the forming of carbides (Silva et al, 2009), and reduce the stress concentration at high temperature

(Meng et al., 2020). However, the particle size of tungsten elemental powders used in PM process is almost smaller than of the raw iron powders, and the density difference between W and Fe is large. During mixing it is easy to agglomerate and segregate, resulting in non-uniformity of element distribution in both powder mixtures and sintered materials (Daumann et al., 2011; Aditya et al., 2015; Oka et al., 2017). Therefore, an investigation toward introducing new methods for alloying powders and the preparation process has significance in promoting application for W-containing ferrous PM materials.

Nowadays, researchers have tried to introduce alloying elements in some other forms to improve the homogeneity and process properties of the powder mixtures (Narasimhan, 2001; Cristofolini et al., 2018). One such approach, known as adding prediffused powders, is an effective way to realize the improvement of PM industry (Semel, 1990; Xiao et al., 2009; Lee et al., 2012). The main advantages of prediffused powders compared to mechanically mixing powder mixtures and prealloyed powders are better fluidity and bulk density, uniform alloy elements distribution, and microstructure homogeneity, which can improve performance and consistency of sintered parts (Chawla et al., 2001; Wu et al., 2013; Pope et al., 2019). On the other hand, prediffused powders usually contain Ni, Mo, and Cu elements, but the preparation of W-containing prediffused powders and their sintering properties are rarely reported.

In this paper, prediffused Fe-W powders were prepared by prediffused treatment, Fe-2Cu-0.8C-0.6Mo-2W powder mixtures were then obtained by mechanically mixing the prediffused Fe-W powders with the other elemental powders (PD powder mixtures), and for comparison, mechanically-prepared powder mixtures were prepared by mechanically mixing all the elemental powders (EL powder mixtures). The sintered Fe-2Cu-0.8C-0.6Mo-2W materials with different methods of introducing tungsten and sintering processes were prepared subsequently. The microstructure, mechanical and wear properties of sintered samples were systematically tested to investigate the effects of W addition forms on properties of the sintered samples.

EXPERIMENTAL

Sample Preparation

Preparation of the Prediffused Fe-W Powder

Reduced iron powders (average particle size of 75 μm) and ultrafine tungsten powders were used as raw materials. The tungsten powders have an average particle size of about 0.8 μm and near spherical shape. Tungsten and iron powders were mixed in a double-cone mixer in air for 20 min. The mechanically mixed powders were then heat treated with a pipe furnace at 800°C for 45 min in H_2 atmosphere. After being crushed and screened through a 100 mesh sieve, the prediffused Fe-W powder were obtained subsequently.

Preparation of the Sintered Fe-2Cu-0.8C-0.6Mo-2W Samples

Reduced iron powders, water atomized copper powders (average particle size of 32 μm), molybdenum powders (average particle size of 12 μm), flaky graphite powders (average particle size of 28 μm) and tungsten powders were used as raw materials. Two kinds of Fe-2Cu-0.8C-0.6Mo-2W powder mixtures were obtained by mixing the prediffused Fe-W powder with the other elemental powders, and mixing all the elemental powders, respectively. Zinc stearate powders were added into the powder mixtures with an addition amount of 0.6 wt% as lubricant. After compaction under 500–700 MPa uniaxially, the green compacts were sintered at 1,050–1,200°C for 60–100 min in H_2 atmosphere without pressure.

Characterization of the Powders and Sintered Samples

The microstructure and tungsten element distribution of powders and sintered samples were carried out by using a scanning electron microscope (SEM) and energy-dispersive spectroscopy (EDS). Density of the green compacts and sintered samples was measured by the Archimedes' method according to ASTM B328-2003 standards. For sintered samples, the tensile strength test was performed by using a universal material testing machine by the dumbbell specimen with a length of 90 mm at a crosshead speed of 0.5 mm/min. The hardness was measured by using the rockwell hardness tester under a load of 100 kg at room temperature. The radial crushing strength was measured by using the pendulum impact testing machine under a load of 401.93 Nm. Wear tests were carried out by an end face wear tester, Cr12 with a hardness of 58–60 HRC was used as a counter-part with oil lubrication, the fixed load was 100 N, the plate rotated was 1 m/s and the test time was 5 min.

RESULTS AND DISCUSSION

Microstructure and Property of the Powders

Figure 1 shows SEM images of the raw iron, tungsten powders, and prediffused Fe-W powders with EDS result and XRD patterns of prediffused Fe-W. The prediffused powders have an average particle size of about 75 μm (**Figures 1C**), which is the same as that of raw iron powder (**Figures 1A**), so the prediffused treatment process had no effect on the particle size. It also can be seen that small tungsten particles (raw particles as show in **Figures 1B**) attached to the iron particles, which have a homogeneous distribution with less segregation (**Figures 1D**) in the prediffused powders. As shown in **Figures 1E**, the EDS analysis confirms that the superfine tungsten particles attached to iron particles. **Figures 1F** shows the XRD patterns of the Fe and prediffused Fe-W powders. The patterns can be indexed for W (JCPDS No. 47-1319, marked by black squares) and Fe (JCPDS No. 50-1275, marked by white squares). Only diffraction peaks (110), (200), (211) of Fe and (110) of W are observed in **Figures 1F**, and the peaks of prediffused Fe-W powders shifted slightly due to the solid solution of tungsten element. The prediffusion treatment promotes partial diffusion of tungsten and iron, which can make small particles of tungsten adhere firmly and avoid segregation.

Figure 2 shows green density of Fe-2Cu-0.8C-0.6Mo-2W compacts by pressing different powder mixtures. It shows that

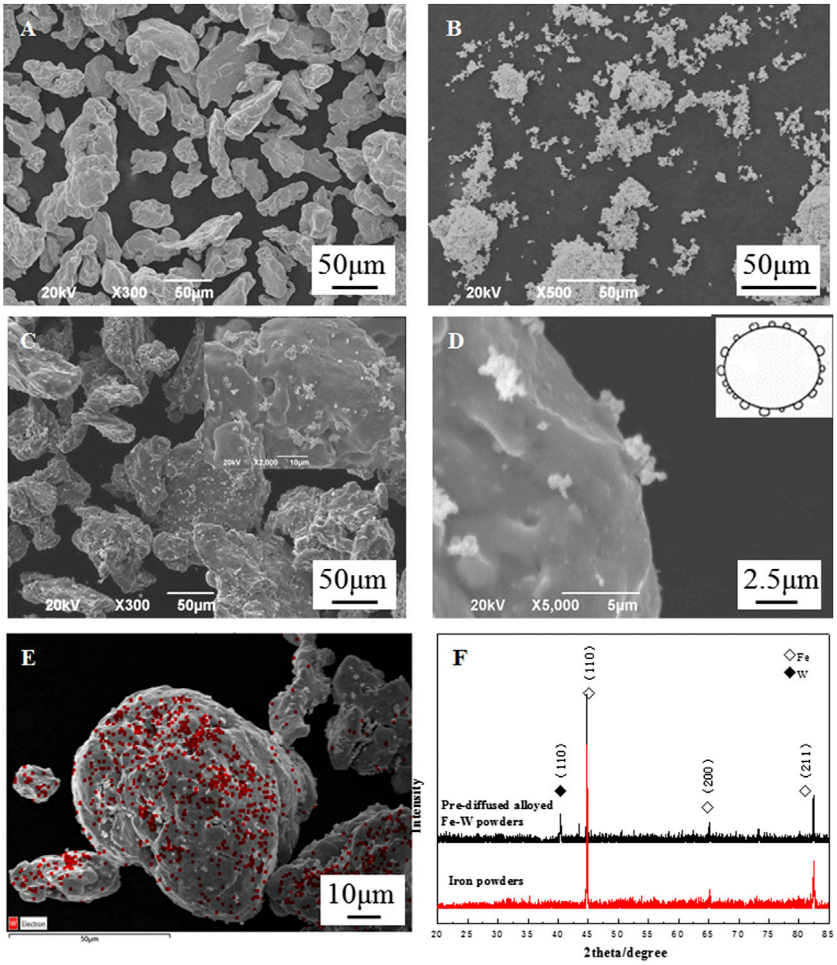

FIGURE 1 | SEM images of iron powders **(A)**, tungsten powders **(B)** and prediffused Fe-W powders **(C, D)**; EDS results **(E)** and XRD patterns **(F)** of prediffused Fe-W powders.

the prediffused treatment influences the compressibility of PD powder mixtures, and a maximum green density of 7.13 g/cm^3 is obtained at compaction pressure of 700 MPa. The green density of the compacts from EL powder mixtures is 7.11 g/cm^3 at the same pressure. When tungsten is introduced in the forms of elemental powders, the powder mixtures have low flowability and are easy to aggregate, resulting in the green density of powder compacts reducing. The prediffused Fe-W powders keeps the compressibility of reduced iron powder and the fine W powder sticks to the surface of iron powder, so the PD powder mixtures have better flowability and higher compressibility.

Density and Microstructure of the Sintered Fe-2Cu-0.8C-0.6Mo-2W Samples

Figure 3 shows density of the sintered Fe-2Cu-0.8C-0.6Mo-2W samples. With the increase of sintering temperature, density of sintered samples first increases, and then changes less. From **Figure 3**, it can be seen that when the sintering temperature is 1,150°C and sintering time is 90 min, the sintered samples

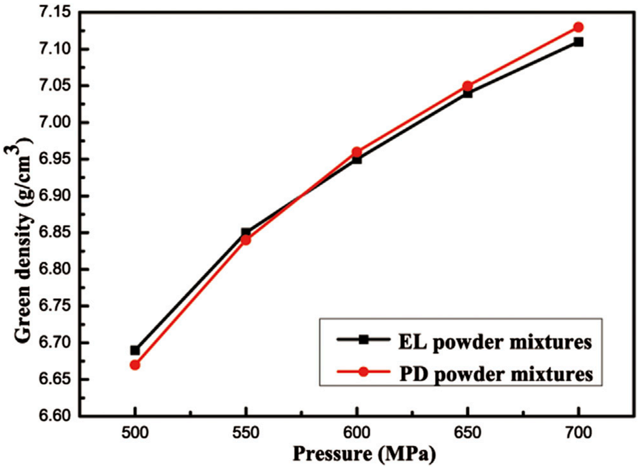

FIGURE 2 | Green density of the Fe-2Cu-0.8C-0.6Mo-2W compacts as a function of compaction pressure of 500–700 MPa.

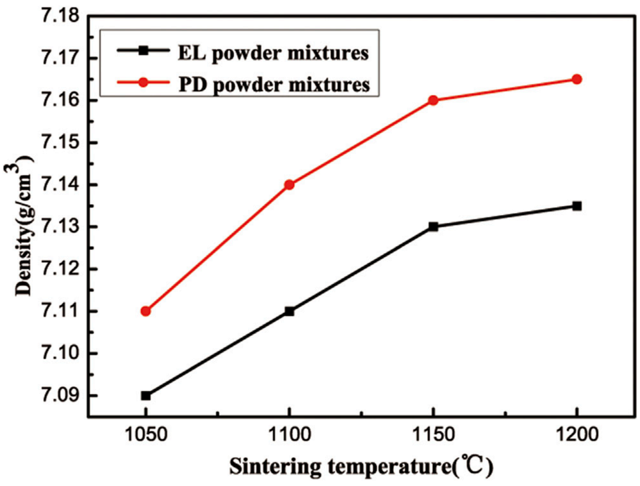

FIGURE 3 | Density of the Fe-2Cu-0.8C-0.6Mo-2W samples sintered at different temperatures.

prepared from PD powder mixtures have a maximum density of 7.16 g/cm^3, while this value of EL powder mixtures is 7.13 g/cm^3. The advantage on density improvement of introducing W element in the form of prediffused Fe-W powder is proved again.

Figure 4 shows density of the samples sintering at 1,150°C for 60–100 min. It can be seen that with the increase of sintering time, density of sintered samples first increases and then remains unchanged, while the density of sintered samples from EL powder mixtures shows a slight decline. When the sintering time exceeds, not only the grain will grow abnormally, but also a small amount of copper would be lost, so the optimal of sintering time is also important. From **Figures 3**, **4**, it can be seen that the optimal sintering condition of Fe-2Cu-0.8C-0.6Mo-2W samples is 1,150°C for 90 min in H_2 atmosphere, and under this sintering condition, samples prepared from PD powder mixtures have a higher density.

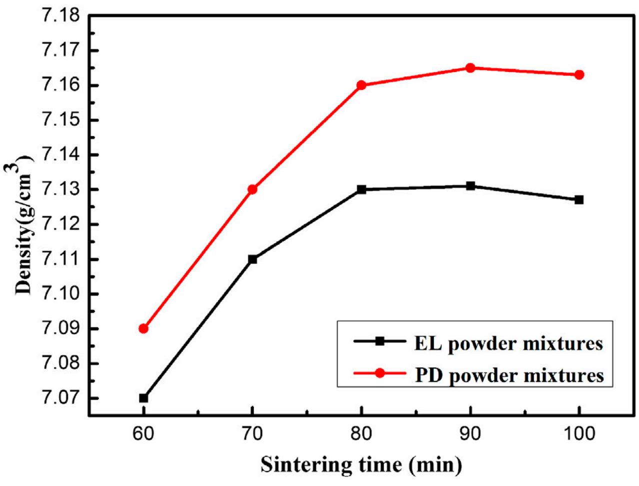

FIGURE 4 | Density of the Fe-2Cu-0.8C-0.6Mo-2W samples sintered for different times.

Figure 5 shows the morphology of the Fe-2Cu-0.8C-0.6Mo-2W samples with different addition forms of W sintered at 1,150°C for 90 min. **Figures 5A**,**B** present the morphology of sample prepared from EL powder mixtures, and **Figures 5C**,D correspond to the microstructure of that prepared from PD powder mixtures. The microstructure of the sintered sample from PD powder mixtures is more uniform with smaller grain size of ferrite (F) and pearlite (P), and the carbide is more evenly ferrite dispersed on the grain boundary. This microstructure effectively restricted the growth of pearlite, which is also critical for the performance of sintered iron-based materials.

Figure 6 shows the surface SEM image and EDS results of the samples sintering at 1,150°C for 90 min in H_2 atmosphere. Compared with samples prepared from EL powder mixtures (**Figures 6A**,**B**), the microstructure of sintered samples prepared from PD powder mixtures (**Figures 6C**,D) is more uniform, and the W element is better-distributed. Due to the adhesion of element W to iron particles before sintering, the diffusion of W element during the sintering densification process was improved. As the EDS results showing, W-rich region (WR) appeared in the sintered samples prepared from EL powder mixtures. By using PD powder mixtures, a diffusion layer between tungsten and iron before sintering is formed, which promote the diffusion of tungsten element during the sintering process. Different from other alloying elements for ferrous alloys like Ni, Cr, and Mn (formation of Ni (Cr, Mn)-rich ferrite), the microstructure of tungsten segregation area (W-Rich region (WR)) is blocky or granular in **Figure 6**.

Mechanical and Tribological Properties of Fe-2Cu-0.8C-0.6Mo-2W Samples

Figure 7 shows the effect of sintering temperature and time on tensile strength of sintered samples. With the increase of sintering temperature and time, tensile strength of sintered samples first increases, and then changes less. A maximum tensile strength of 547 MPa is obtained for the specimens from PD powder mixtures, sintered at 1,150°C and 90 min. When W element added in the form of prediffused Fe-W powder, the solid-state diffusion of W and Fe during sintering is promoted, thus the mechanical properties of sintered samples are improved. The diffusion and uniform distribution of the tungsten element improve the strength of matrix, so the sintered samples prepared from PD powder mixtures have a higher tensile strength.

The diffusion of alloying elements in the powder mixtures directly affects the tensile strength properties of the sintered material, and the improvement of properties is related to diffusion degree and densification during the sintering process. In this experiment, the tensile strength of the sintered materials can be considered as a function of the sintering temperature and time. A predictor is based on the following equation (Ddeoix et al., 2000):

$$f(t, T) = t exp\left(-Q/_{RT}\right) \qquad (1)$$

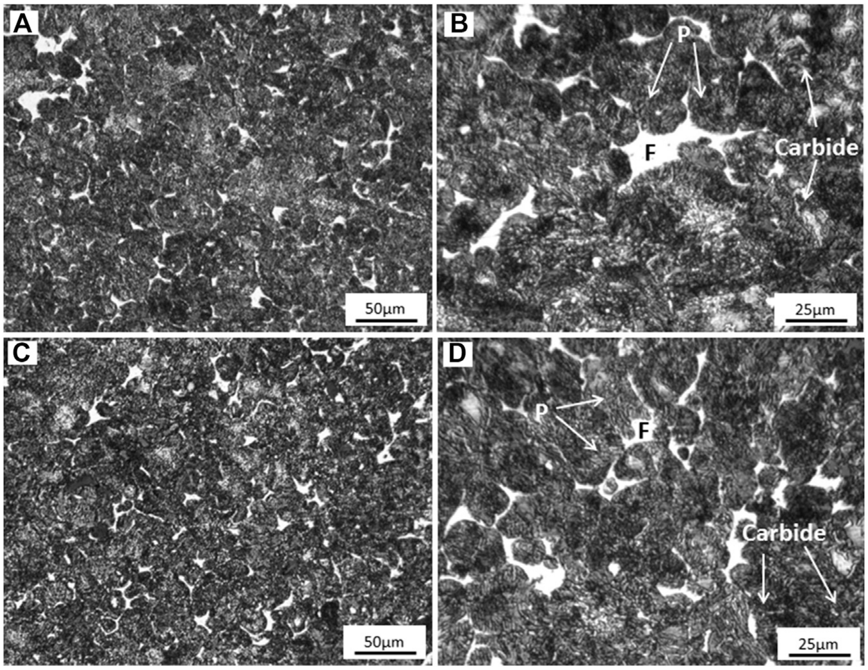

FIGURE 5 | Microstructure of sintered Fe-2Cu-0.8C-0.6Mo-2W materials from different powder mixtures. **(A, B)** EL powder mixtures; **(C, D)** PD powder mixtures

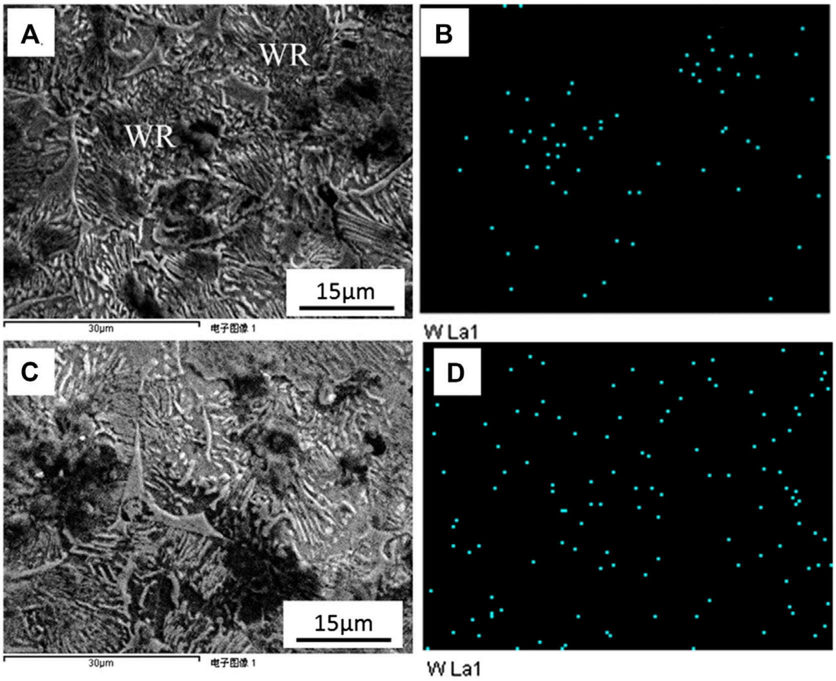

FIGURE 6 | SEM images and EDS results of sintered Fe-2Cu-0.8C-0.6Mo-2W materials from different powder mixtures. **(A, B)** EL powder mixtures; **(C, D)** PD powder mixtures

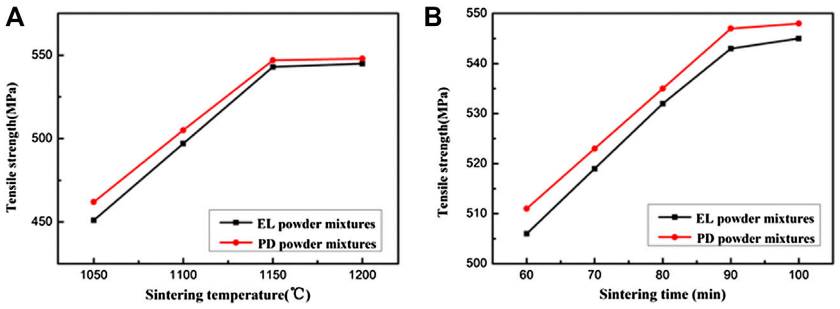

FIGURE 7 | Effect of sintering condition on tensile strength of sintered Fe-2Cu-0.8C-0.6Mo-2W samples. **(A)** sintering temperature; **(B)** sintering time.

TABLE 1 | Value of $f(t, T)$.

Sintering condition	1,050°C 90 min	1,100°C 90 min	1,150°C 60 min	1,150°C 70 min	1,150°C 80 min	1,150°C 90 min	1,150°C 100 min	1,200°C 90 min
Value (s, 10^{-4})	0.69	1.33	1.63	1.91	2.17	2.45	2.72	4.37

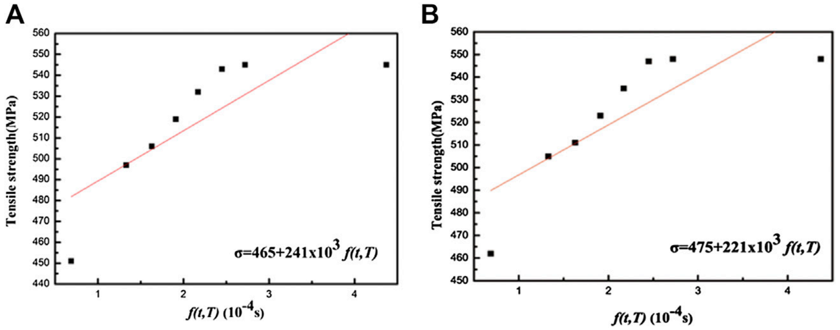

FIGURE 8 | Relationship between tensile strength and *f(t, T)* of sintered Fe-2Cu-0.8C-0.6Mo-2W materials from different powder mixtures. **(A)** EL powder mixtures; **(B)** PD powder mixtures

Where T is the sintering temperature (Kelvin), t is the sintering time, is the gas constant and the value is 8.314 J/(mol·K), and Q is the activation energy which was chosen to be 200 kJ/mol. **Table 1** shows the value of in this experiment.

Figure 8 shows the relationship between tensile strength and the function of sintered materials. The tensile strength (σ) of sintered samples sintered at 1,200°C for 90 min exists a big deviation mainly because of the abnormally grain growth with excessive sintering temperature. By analyzing the experimental data of the sintered samples prepared from EL powder mixtures and PD powder mixtures, **Eqs 2**, **3** are obtained respectively. These two equations allow the tensile strengths of different sintered samples to be estimated based on the sintering conditions. From the data, it can be found that within a reasonable sintering temperature range, with the increase of , the tensile strength of the sintered materials increases linearly.

$$\sigma = 465 + 241 \times 10^{3} f(t, T) \tag{2}$$

$$\sigma = 475 + 221 \times 10^{4} f(t, T) \tag{3}$$

Table 2 lists the properties and comparison of Fe-2Cu-0.8C-0.6Mo-2W materials sintered at 1,150°C for 90 min. A maximum hardness of 95 HRB of the sintered samples were obtained from PD powder mixtures, higher than the value of MPIF standard and other Fe-Cu-C (W-containing) materials. A radial crushing strength of 791 MPa were obtained for the sintered samples from PD powder mixtures which the value of EL powder mixtures is 753 MPa. The diffusion of the tungsten can improve the hardness and strength of the matrix, and the tungsten carbide formed also can increase hardness, but for EL

TABLE 2 | Properties comparison of sintered Fe-2Cu-0.8C-0.6Mo-2W materials.

Composition	Density (g/cm^3)	Tensile Strength (MPa)	Hardness (HRB)	Ref.
Fe-2Cu-0.8C-0.6Mo-2W (EL/PD powder mixtures)	7.13/7.16	543/547	93/95	This work
Fe-2Cu-0.8C	7.1	520	84	MPIF standard 35
Fe-2Cu-0.8C	7.14	410	59	3
Fe-1.5Cu-0.7C-1WC	6.63	317.3	72.6	8

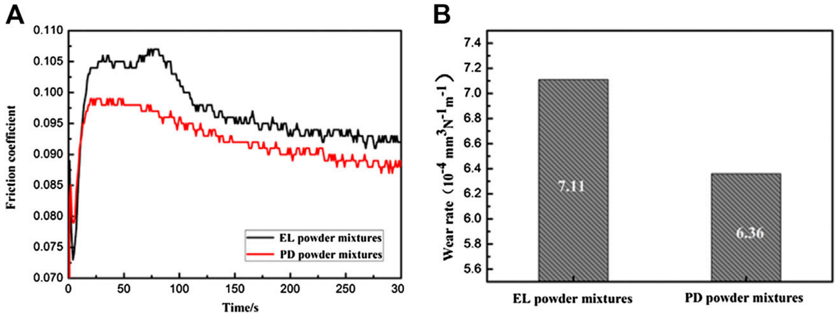

FIGURE 9 | Friction coefficient and wear rate of the sintered samples from different powder mixtures. **(A)** EL powder mixtures; **(B)** PD powder mixtures.

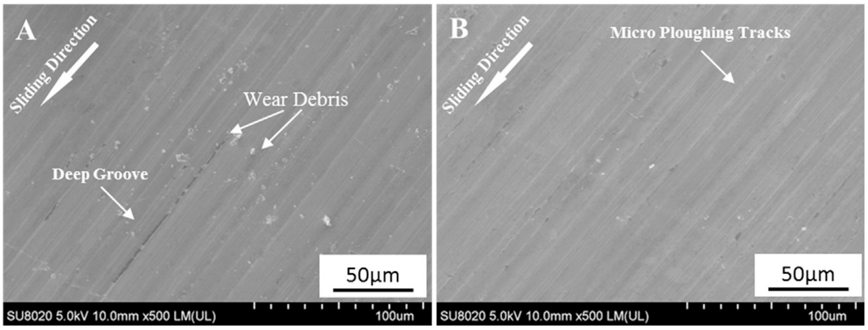

FIGURE 10 | SEM images of the worn surface of sintered samples from different powder mixtures. **(A)** EL powder mixtures; **(B)** PD powder mixtures.

powder mixtures, the agglomerated carbides or W element will lead to stress concentration and elevate the brittleness.

The influence of W addition forms on coefficient of friction during the end-face wear test is shown in **Figure 9**. The coefficient of friction of the sample prepared from EL powder mixtures is 0.096, while the value of the sample prepared from PD powder mixtures is 0.092. Different microstructural features, hardness and strength values of the sintered samples lead to different friction behavior. The wear rate of the sample prepared from PD powder mixtures is 6.36 × 10^{-4} mm^3 N^{-1}m^{-1} while the samples of the sample prepared from PD powder mixtures is 7.11 × 10^{-4} mm^3 N^{-1}m^{-1}. The sintered sample from PD powder mixtures shows uniform microstructure, higher hardness and lower value of coefficient of friction.

Figure 10 shows the worn surfaces of the sintered samples prepared from different powder mixtures. **Figures 10A** shows the worn surface of the sintered samples prepared by EL powder mixtures, with some pores and deep grooves parallel to the sliding direction. The SEM image of the sintered samples from PD powder mixtures only shows some micro ploughing tracks on the worn surface (**Figures 10B**). The above features demonstrate that the tribological behavior improves by higher hardness and uniform microstructure.

The test results of tribological behavior show the samples prepared by adding PD powder mixtures own better properties. The reasons for forming abrasion scratch contain lubrication conditions, high contact stress and relative slip on the contact surface. The formula as following can be used to analyze the relationship between the hardness and wear property (Chen et al., 2003).

$$H = \frac{KWL}{CAP} \tag{4}$$

Where H is the wear depth, is the friction coefficient relating to the wear condition of surface, W is the load on the sliding surface, is the sliding distance, C is a constant, A is the contact area, and is the hardness of the contact surface. From the **Eq. 4**, it can be seen that the wear depth is directly proportional to the coefficient of friction, the size of load at each point on the contact surface and the sliding distance, but inversely proportional to the area of contact surface and hardness. With the increase of area and the hardness of the matrix, the adhesive wear reduced. With more diffusion during sintering after prediffused treatment for PD powder mixtures, the value of P is also improved.

CONCLUSION

Prediffused Fe-W powders were prepared using prediffused bonding treatments. The firmly metallurgical bonding between tungsten and iron particles could avoid the segregation of the W element. the optimal sintering condition was beneficial to sintering densification and the improvement of properties. When the sintering condition was 1,150°C for 90 min, a maximum tensile strength of 547 MPa, a hardness of 95 HRB and a radial crushing strength of 791 MPa were obtained for the specimens from PD powder mixtures, and the tribological behavior was also improved. The present results provided a potential way to improve the density and mechanical properties of ferrous powder metallurgy structure materials.

DATA AVAILABILITY STATEMENT

The original contributions presented in the study are included in the article/supplementary material, further inquiries can be directed to the corresponding author.

AUTHOR CONTRIBUTIONS

WC: designed and performed the experiments, manuscript draft and revising. JW: properties test. PC: experimental work, data analysis. JC: revised the manuscript, and final approval. All authors agree to be accountable for all aspects of the work.

ACKNOWLEDGMENTS

We gratefully acknowledge experimental support by our colleagues Yonghong Xia (sintering equipments), Jianhua Zhang (samples characterization), Yu Hong (SEM), and Jingcheng Zhang (XRD).

REFERENCES

Aditya, K., Peter, L., Magdalena, B., Dino, C., and Gaurav, S. (2015). On the application of inertial microfluidics for the size-based separation of polydisperse cementitious particulates. *Front. Mater.* 2, 48. doi:10.3389/fmats.2015.00048

Annamalai, R., Upadhyaya, A., and Agrawal, D. (2013). An investigation on microwave sintering of Fe, Fe–Cu and Fe–Cu–C alloys. *Bull. Mater. Sci.* 36 (3), 447–456. doi:10.1007/s12034-013-0477-9

Azevedo, J. M. C., Serrenho, A. C., and Allwood, J. M. (2018). Energy and material efficiency of steel powder metallurgy. *Powder Technol.* 328, 329–336. doi:10.1016/j.powtec.2018.01.009

Chawla, N., Murphy, T. F., Narasimhan, K. S., Koopman, M., and Chawla, K. K. (2001). Axial fatigue behavior of binder-treated versus diffusion alloyed powder metallurgy steels. *Mat. Sci. Eng. A* 308, 180–188. doi:10.1016/S0921-5093(00)01990-0

Chen, W. X., Tu, J. P., Wang, L. Y., Gan, H. Y., Xu, Z. D., and Zhang, X. B. (2003). Tribological application of carbon nanotubes in a metal-based composite coating and composites. *Carbon* 41, 215–222. doi:10.1016/S0008-6223(02)00265-8

Cristofolini, I., Molinari, A., Pederzini, G., and Rambelli, A. (2018). From experimental data, the mechanics relationships describing the behaviour of four different low alloyed steel powders during uniaxial cold compaction. *Powder Metall.* 61, 1–11. doi:10.1080/00325899.2017.1361507

Daumann, B., Weber, J. A., Anlauf, H., and Nirschl, H. (2011). Discontinuous powder mixing of nanoscale particles. *Chem. Eng. J.* 167, 377–387. doi:10.1016/j.cej.2010.12.033

Ddeoix, C. N., Griffo, A., and German, R. M. (2000). Effects of sintering parameters on the mechanical properties of a Fe-2Cu-2Ni-0.9M-0.8C steel. *Int. J. Mater. Prod. Technol.* 15, 409–426. doi:10.1504/ijmpt.2000.001248

Deng, X. T., Wang, Z. D., Han, Y., Zhao, H., and Wang, G. D. (2014). Microstructure and abrasive wear behavior of medium carbon low alloy martensitic abrasion resistant steel. *J. Iron Steel Res. Int.* 21, 98–103. doi:10.1016/S1006-706X(14)60015-7

Lee, J. G., Lim, C. H., Kim, H. S., Hong, S. J., Kim, M. T., Kang, B. C., et al. (2012). Highly dense steel components prepared by magnetic pulsed compaction of iron-based powders. *Powder Technol.* 228, 254–257. doi:10.1016/j.powtec.2012.05.027

Meng, H. J., Wang, J., Wang, L., Fang, X., Donga, N., Zhanga, C., et al. (2020). The precipitation control in aged alumina-forming austenitic stainless steels Fe-15Cr-25Ni-3Al-NbWCu by W addition and its effect on the mechanical properties. *Mater. Char.* 163, 110–233. doi:10.1016/j.matchar.2020.110233

Narasimhan, K. S. (2001). Sintering of powder mixtures and the growth of ferrous powder metallurgy. *Mater Chem Phys.* 67, 56–65. doi:10.1016/S0254-0584(00)00420-X

Oka, S., Sahay, A., Wei, M., and Muzzio, F. (2017). Diminished segregation in continuous powder mixing. *Powder Technol.* 309, 79–88. doi:10.1016/j.powtec.2016.11.038

Pope, J. J., Calvert, E. L., Weston, N. S., and Jackson, M. (2019). FAST-DB: a novel solid-state approach for diffusion bonding dissimilar titanium alloy powders for next generation critical components. *J. Mater. Process. Technol.* 269, 573–599. doi:10.1016/j.jmatprotec.2019.02.011

Semel, F. J. (1990). Properties of parts made from an Ancorbond processed Fe-Ni-C powder mix. *Met. Powder Rep.* 45, 193–197. doi:10.1016/S0026-0657(10)80088-8

Silva, P. A., Weber, S., Inden, G., and Pyzalla, A. R. (2009). Influence of hard particle addition and chemical interdiffusion on the properties of hot extruded tool steel compounds. *Mater. Sci. Eng.* 516, 193–200. doi:10.1016/j.msea.2009.03.048.

Wang, X. D., Chen, Y. B., Wei, S. Z., Zuo, L. L., and Mao, F. (2019). Effect of carbon content on abrasive impact wear behavior of Cr-Si-Mn low alloy wear resistant cast steels. *Front. Mater.* 6, 153. doi:10.3389/fmats.2019.00153

Wu, M. W., Tsao, L. C., and Chang, S. Y. (2013). The influences of chromium addition and quenching treatment on the mechanical properties and fracture behaviors of diffusion-alloyed powder metal steels. *Mater. Sci. Eng.* 565, 196–202. doi:10.1016/j.msea.2012.12.032

Wu, Y. F., Hui, W. J., Chen, S. L., Xu, L., Yong, Q. L., and Zhou, S. T. (2016). Influence of vanadium on microstructure and mechanical properties of medium carbon forging steel. *J. Iron Steel Res.* 28, 56–62. doi:10.13228/j.boyuan.issn1001-0963.20160073

Xiao, Z. Y., Ke, M. Y., Fang, L., Shao, M., and Li, Y. Y. (2009). Die wall lubricated warm compacting and sintering behaviors of pre-mixed Fe-Ni-Cu-Mo-C powders. *J. Mater. Process. Technol.* 209, 4527–4530. doi:10.1016/j.jmatprotec.2008.10.018

Xuan, Y., Hua, T., Ling, Q., and Yuxiang, L. (2019). Properties of Fe-Cu-C composite reinforced by different WC content[J]. *IOP MSE* 688, 033025. doi:10.1088/1757-899X/688/3/033025

Zhang, C., Li, P., Wei, S. Z., You, L., Wang, X., and Mao, F. (2019). Effect of tempering temperature on impact wear behavior of 30Cr3Mo2WNi hot-working die steel. *Front. Mater.* 6, 149. doi:10.3389/fmats.2019.0014

Conflict of Interest: The authors declare that the research was conducted in the absence of any commercial or financial relationships that could be construed as a potential conflict of interest.

frontiers
in Materials

ORIGINAL RESEARCH
published: 03 June 2021
doi: 10.3389/fmats.2021.534407

Mechanical Properties of WC-Si_3N_4 Composites With Ultrafine Porous Boron Nitride Nanofiber Additive

Ting Cao[1], Xiaoqiang Li[1], Jingmao Li[1], Yang Huang[2], Shengguan Qu[1], Chao Yang[1], Liang Liang[1] and Tao Song[2]*

[1] National Engineering Research Center of Near-Net-Shape Forming for Metallic Materials, South China University of Technology, Guangzhou, China, [2] School of Materials Science and Engineering, Hebei University of Technology, Tianjin, China

WC-10 wt.% Si_3N_4 composites toughened with ultrafine porous boron nitride nanofiber (0, 0.01, 0.05, 0.1, and 0.15 wt.%) were prepared for the first time by spark plasma sintering. Compared with the WC-Si_3N_4 composite sintered in the same condition, the obtained WC-10 wt.% Si_3N_4 composites with ultrafine porous boron nitride were found to possess better hardness and fracture toughness. In addition, the Si_3N_4 phase in the UPBNNF toughened composites did not exhibit traditional catastrophic fracture as indicated in most investigations. In this study, the phenomena are discussed, and a probable mechanism is elucidated. It is deduced that the approach could be extended to materials with a feature of internal liquid phase during the sintering process and could improve hardness and fracture toughness.

Keywords: porous nanofiber, WC, Si3N4, Young's modulus, fracture mode

Edited by:
Suryanarayana Challapalli,
University of Central Florida,
United States

Reviewed by:
Mehdi Shahedi Asl,
University of Mohaghegh Ardabili, Iran
Zhi Wang,
South China University of Technology,
China
Francesco Colangelo,
University of Naples Parthenope, Italy
Pasquale Vena,
Politecnico di Milano, Italy
Ehsan Ghasali,
Materials and Energy Research
Center, Iran

****Correspondence:***
Xiaoqiang Li
lixq@scut.edu.cn

Specialty section:
This article was submitted to
Mechanics of Materials,
a section of the journal
Frontiers in Materials

Received: *14 February 2020*
Accepted: *16 April 2021*
Published: *03 June 2021*

Citation:
Cao T, Li X, Li J, Huang Y, Qu S,
Yang C, Liang L and Song T (2021)
Mechanical Properties of WC-Si_3N_4
Composites With Ultrafine Porous
Boron Nitride Nanofiber Additive.
Front. Mater. 8:534407.
doi: 10.3389/fmats.2021.534407

INTRODUCTION

Tungsten carbide (WC) has numerous advantages, including high Young's modulus, high hardness, and excellent wear-resistance (Zhang et al., 2009; Kumar et al., 2011; Namini et al., 2019; Sakkaki et al., 2019; Fattahi et al., 2020a,b). However, the shortcoming of WC is brittleness. Therefore, most industrial WC-based materials are WC-Co composites, which are typically applied as cutting tools and molds (Chang et al., 2015; Norgren et al., 2015). Co is beneficial for improving fracture toughness because of its ductility and wettability to WC. In addition, binderless WC-based materials continue to be investigated due to their merits of corrosion-resistance and red hardness in comparison to binder-containing composites. In this manner, carbides are mostly used (e.g., VC, Cr_2C_3, TaC, and TiC (Kim et al., 2008; Poetschke et al., 2012; Nino et al., 2019). The toughening effects of oxides such as MgO, Al_2O_3, and ZrO_2 are also investigated on the WC matrix (El-Eskandarany, 2000, 2005; Basu et al., 2004; Zheng et al., 2012, 2013b).

Carbon (CNT) and boron nitride (BNNT) nanotubes have outstanding mechanical properties, which have attracted attention in materials reinforcement (Wang et al., 2011; Yadhukkulakrishnan et al., 2012; Tatarko et al., 2014; Vasudevan et al., 2016; Jin et al., 2017; Li et al., 2018). CNT with exceptionally high Young's modulus in the terapascal (TPa) range and tensile strength of as much as 60 GPa has been investigated as a toughening phase for a long time (Han et al., 2018). BNNT possesses high chemical stability in addition to previously mentioned advantages. However, difficulties remain in BNNT synthesis with large quantities and low costs (Golberg et al., 2007, 2010). As an alternative for environmental chemistry and hydrogen storage, Lin et al. (2016)

prepared an ultrafine porous boron nitride nanofiber (UPBNNF) with a high specific surface area of 515 m^2/g and a total pore volume of 0.566 cm^3/g using freeze-drying and pyrolysis processes. But studies on the toughening effect of the porous fiber are rare yet.

WC-Si_3N_4 composites have been considered in detail with respect to the sintering process, phase transformation, microstructure, and mechanical properties using spark plasma sintering (SPS) (Li et al., 2013; Zheng et al., 2013a, 2015). In this study, the WC-10 wt.% Si_3N_4 composites with addition of UPBNNF were prepared using SPS to investigate UPBNNF's effects on the overall mechanical properties. The mechanical phenomena after testing were discussed on experimental data and fracture theory.

EXPERIMENTAL PROCEDURE

For starting materials, we used WC (200 nm, purity $>$ 99.9%, Xuzhou Jiechuang New Material Technology Co., Ltd., China), Si_3N_4 ($\sim$1 μm, $>$95% α-phase, Xuzhou Jiechuang New Material Technology Co., Ltd., China), Y_2O_3 (5–10 μm, purity $>$ 99.9%, Sinopharm Chemical Reagent Co., Ltd., China) and Al_2O_3 ($\sim$1 μm, purity $>$ 99.9%, Beijing Mountain Technological Development Center, China), UPBNNF (diameter: 20–60 nm, length: tens of micrometers; Boron Nitride Research Center, Hebei University of Technology, China). The WC-10 wt.% Si_3N_4 ($93Si_3N_4 + 6Y_2O_3 + 1Al_2O_3$, wt.%) powder mixtures with the addition of 0, 0.01, 0.05, 0.1, and 0.15 wt.% UPBNNF ultrasonically dispersed in ethanol in advance were wet-mixed on a planetary ball mill. Then they were dried, sieved, poured into a cylindrical graphite die, and heated to 1750°C (monitored by infrared thermometer) without soaking time under applied pressure of 30 MPa in $\leq$6 Pa vaccum. Other processing details have been shown in Li et al. (2013) and Zheng et al. (2013a, 2015). Thereafter, the five obtained WC–UPBNNF specimens were named 10S, 10S0.01B, 10S0.05B, 10S0.1B, and 10S0.15B, respectively, in terms of their UPBNNF content. For necessary supporting details, an over-sintering 10S0.1B specimen was prepared with the sintering parameters of 1750°C and 5-min soaking time.

The density of the specimens ($\Phi 20 \times 10$ mm) was measured using water before being calculated by the Archimedes principle. The hardness (HV_{10}) was evaluated on a Vickers hardness tester (430SVA, Wilson Wolpert Co., Ltd., China) with a load of 10 kg. An indentation with a load of 30 kg was produced to illustrate crack details on the 10S0.05B specimen. The fracture toughness (K_{Ic}) was calculated based on the radial crack produced by Vickers indentation according to the Anstis formula (for half-penny crack):

$$K_{\mathrm{I}c} = 0.016 \times \left(\frac{E}{H}\right)^{\frac{1}{2}} \times \frac{P}{c^{3/2}},$$

where E is Young's modulus, H is hardness, P is peak load, and c is the characteristic dimension (Anstis et al., 1981). The reported values were the averages of the data obtained from five indentation tests. Using the pulse-echo overlap ultrasonic technique (ultrasonic generator CTS-32, SIUI, China; data collection system DPO5034, Tektronix, United States; longitudinal wave detector K 10K-52832, GE, United States; transverse wave detector MB2Y, KK, Germany), we determined the elastic modulus of all samples. Sound velocity is measured to inversely calculate Young's modulus, which is based on influence of intrinsic properties of materials like elastic properties on sound propagation. As a reference, the Young's modulus of specimens shown in **Table 1** was also calculated according to Voigt's formula (upper boundary):

$$E = \sum E_i V_i,$$

where E_i and V_i represent the Young's modulus and volume fraction of every phase, respectively (Meyors and Chawla, 1999).

Phase identification was conducted using an X-ray diffractometer (XRD, D8 Advance, Bruker Co., Germany) with Cu Kα radiation. The wt. fraction of the β phase in Si_3N_4 was calculated based on the α (200)/β (200) ratio of the diffraction peak heights (PH) based on the method reported by Pigeon and Varma (1992). The PH data were collected at a 0.02° step^{-1} between 25 and 29° of 2theta (time constant 2 s) with the contribution subtracted due to background noise:

$$\alpha/\beta \text{ phase ratio} = 4.9381(\mathrm{PH}) + 0.1144(\mathrm{PH})^2 + 0.08106(\mathrm{PH})^3,$$

$$\text{wt. fraction} = 1/(1 + \alpha/\beta).$$

The microstructure as well as the Vickers indentations was examined using high-resolution scanning electron microscopy (HRSEM, Nova Nano 430, FEI, United States).

RESULTS AND DISCUSSION

The displacement of the lower punch, which reflects the densification process of the sample, and the temperature were automatically recorded during sintering. **Figure 1** shows shrinkage rate curves of the specimens heated to 1750°C without soaking time. As the shrinkage rate became positive, the powders were densified until the shrinkage rate was again reduced to zero. For the fine grain WC-10 wt.% Si_3N_4 and those specimens with the addition of UPBNNF, the densification process started at approximately 900°C. Much faster densification rates were observed for all specimens when the sintering temperature rose to 1400°C. Finally, the densification process ended at approximately 1600°C.

Figure 2 shows the XRD patterns of WC-10 wt.% Si_3N_4 with and without UPBNNF specimens. The wt. fraction of the β phase calculated from the XRD data in **Figure 3** are listed in **Table 1**. The specimens containing UPBNNF had a higher wt. fraction of the β phase than the specimens without the fiber. The microstructures of composites containing UPBNNF that can be seen in **Figure 4** are not different from the WC-10 wt.% Si_3N_4 reported in our previous works (Li et al., 2013; Zheng et al., 2013a, 2015). In the microscopy examination processes that we performed, UPBNNF was hardly

TABLE 1 | Characteristics of WC-Si_3N_4-UPBNNF specimens.

Specimen	Density (g/cm^3)	β-Si_3N_4 (100%)	Hardness (GPa)	Elasticity modulus (GPa, calculated)	Elasticity modulus (GPa, tested)	Fracture toughness (MPa·m$^{1/2}$)
10S	11.45	16.96	17.76 ± 0.25	572	521	7.70 ± 0.56
10S0.01B	11.39	20.44	18.32 ± 0.33	567	793	10.99 ± 0.41
10S0.05B	11.40	18.79	20.56 ± 0.87	556	779	10.57 ± 0.38
10S0.1B	11.41	27.51	19.04 ± 0.39	544	775	10.50 ± 0.68
10S0.15B	11.37	24.83	19.12 ± 0.56	532	755	10.09 ± 0.76

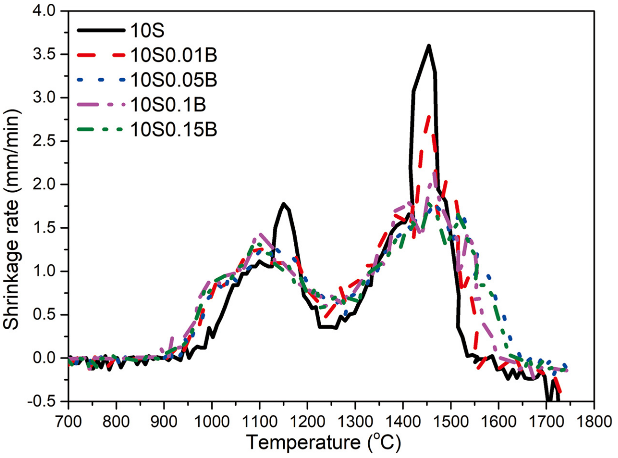

FIGURE 1 | Densification curves of the composite specimens.

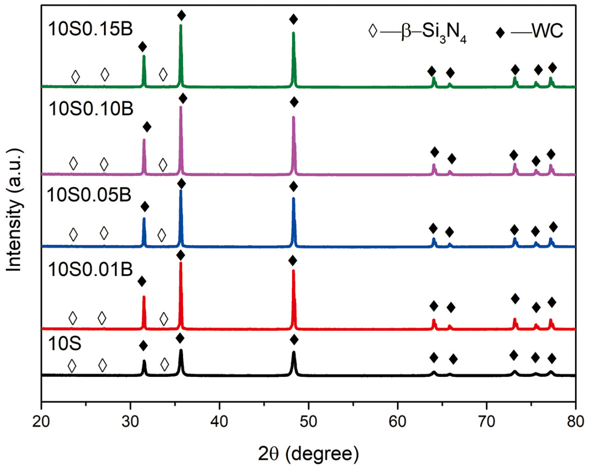

FIGURE 2 | XRD patterns of the composite specimens.

to be observed, which could be attributed to the low contrast of BN in the composites.

Values for the hardness and fracture toughness of WC-10 wt.% Si_3N_4 with different ratios of UPBNNF composites are listed in **Table 1**. All specimens containing UPBNNF were better in terms of both hardness and fracture toughness as compared to the WC-10 wt.% Si_3N_4. **Table 1** also shows the tested Young's modulus values of specimens as well as the theoretical upper boundary calculated from Voigt's formula, and the UPBNNF-containing specimens had abnormally high values (the highest reached 793 GPa) that were superior to the value of pure WC (700 GPa), with nearly changeless density. If the calculated values are obtained based on tested value of 10S, the calculated values along with growth of UPBNNF additive amount are 520, 519, 518, and 517 GPa, respectively. The crack path details of all composites are presented in **Figure 5**, where tearing and scratch patterns on Si_3N_4 in the composites containing UPBNNF are visible. The crack pattern of Si_3N_4 grains in composites is different from the transgranular crack pattern of Si_3N_4 with clean edges. When the crack passes the Si_3N_4 grains in the composites, it appears healed, which is also unlike the traditional crack pattern of ceramic matrices. Under a 10-kg load, UPBNNF is rarely observed. Therefore, a 30-kg load is employed to produce a bigger crack. In the crack images of **Figure 6**, UPBNNF can be observed in the UPBNNF-containing specimens. In particular, single fibers can be seen between the broken parts of Si_3N_4.

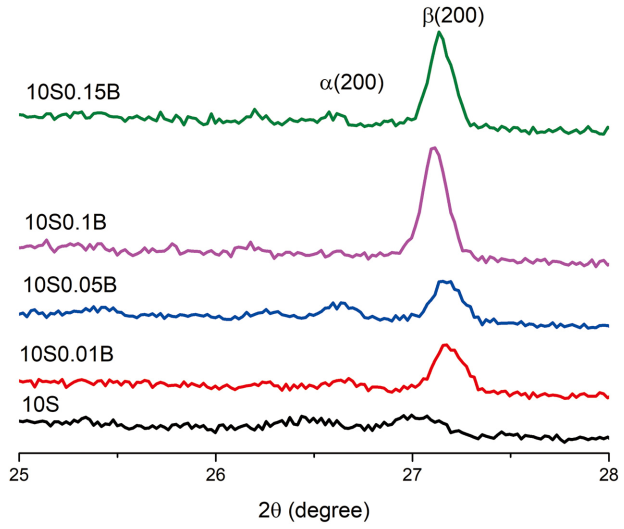

FIGURE 3 | XRD patterns for α-Si_3N_4 (100) and β-Si_3N_4 (200) crystal planes of the composite specimens.

In the aforementioned results, the fracture mode identified in the results can be noticeable. In general, Si_3N_4 ceramics are known for catastrophic fracture, and thorough fracture of Si_3N_4 grains with clean edge is observed (a fine image of fracture

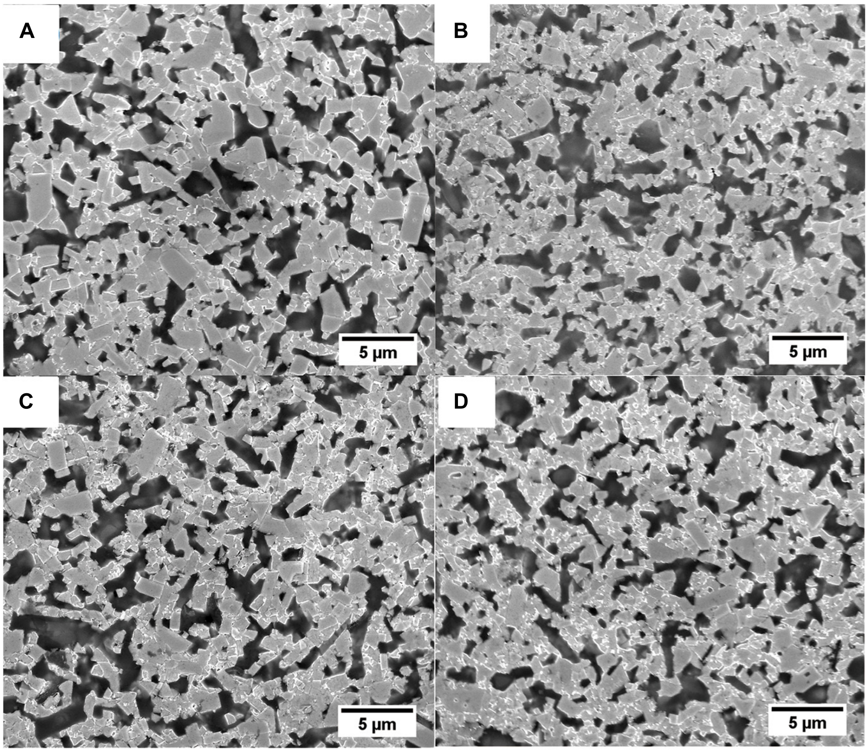

FIGURE 4 | SEM micrographs of the indentation crack paths in **(A)** 10S0.01B, **(B)** 10S0.05B, **(C)** 10S0.1B, and **(D)** 10S0.15B.

of Si_3N_4 grains is provided in Riley (2000), Ii et al. (2004), Klemm (2010), Zhou et al. (2014), and Hu et al. (2019). However, different cases of tears and scratches emerge on the Si_3N_4 grains in the composites with UPBNNF, as shown in **Figure 5**, which means fractures of Si_3N_4 occur partly under a given load. The phenomena has been barely observed in other Si_3N_4-containing composites. It can be deduced that the whole fracture process involves two steps at least during a given time interval under a limited load. Therefore, these crack patterns are not the traditional catastrophic fracture mode of Si_3N_4.

Theories on fracture and toughening can be simply divided two theoretical categories: the microstructural and the atomic. Fracture and toughening phenomena are usually elucidated by microstructure theory with respect to interface energy that is sufficient in most cases (Marshall and Evans, 1985; Becher et al., 1988; Becher, 1991). Furthermore, analysis on fracture is based on thermodynamics. According to second law of thermodynamics, there must be extra work to block the crack propagation in the traditional way. As reported, deformation work of UPBNNF cannot lead the different fracture mode of WC (Li et al., 2020). Combining mentioned analysis on UPBNNF, the probable reason is extra elastic work in the process of crack propagation of Si_3N_4 grains containing UPBNNF. The source of the elastic work cannot be found in the microstructure scale. Therefore, atomic theory is necessary when the fracture mode of materials is concerned in this case. A simple theory is the cohesive strength model. In this model, fracture is determined based on the cohesive strength of atoms, which is proportional to Young's modulus (Lawn, 1993). The Si_3N_4 in a nanopore could possess higher cohesive strength as a result of being restrained by the nanopore based on the previously mentioned elevated Young's modulus of parts of Si_3N_4. Thus, the fracture mode of Si_3N_4 in the composites with UPBNNF is consistent with an increase in Young's modulus. Young's modulus and fracture at the atomic scale are both the variations in force and distance between atoms (Lawn, 1993; Hsieh and Tuan, 2005).

As shown in results, one unusual observation is that the Young's modulus of the composites was even higher than the highest value, which is rarely present in other composites regardless of whether the second phase exists as a particle or fiber. Examples of these types of composites include Si_3N_4-*SiC*, Si_3N_4-TiN, Si_3N_4-ZrO_2, TaC-TaB_2, and ZrB_2-TiC (Akimune, 1990; Pezzotti, 1993; Blugan et al., 2005; Zhang et al., 2008; Guicciardi et al., 2010; Bódis et al., 2017). It is known that Young's modulus of materials as an intrinsic property is determined by the bonding between the individual atoms, which means Young's modulus is a characterization of force and distance between atoms (Meyors and Chawla, 1999). For materials containing pores, Young's modulus descends with higher porosity (Pabst and Gregorová, 2004). On evaluating Young's modulus of composites, the mixture rule is usually applied, and the value is located between the high and low values regardless of the calculation methods (Meyors and Chawla, 1999; Hsieh and Tuan, 2005). In addition, different methods are also applied to obtain this value. However, results derived from the examination methods or calculated by the mixture rule show only minimal differences. Therefore, all

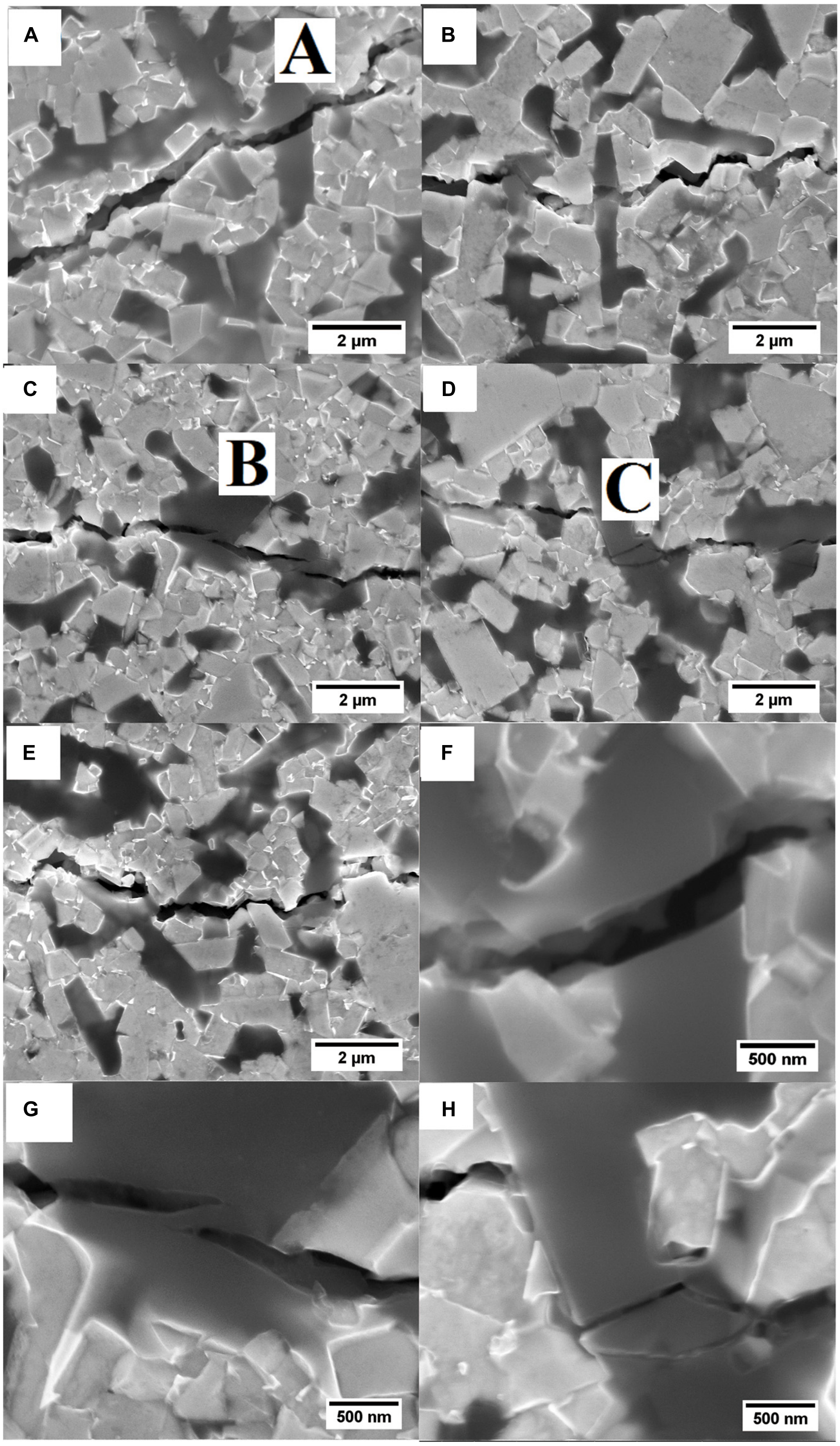

FIGURE 5 | HRSEM images of the indentation crack paths in of **(A)** 10S, **(B)** 10S0.01B, **(C)** 10S0.05B, **(D)** 10S0.1B, **(E)** 10S0.15B, **(F)** A area in **(A)**, **(G)** B area in **(C)**, and **(H)** C area in **(D)**.

methods are adopted in materials investigations (Koopman et al., 2002; Cha et al., 2003; Basu et al., 2004; Wang et al., 2012; Xia et al., 2020). In brief, the addition of a phase with a low Young's modulus leads to decreasing value of composites. UPBNNF possesses two features that result in negligible Young's modulus in WC-Si$_3$N$_4$ composites: high porosity and a turbostratic

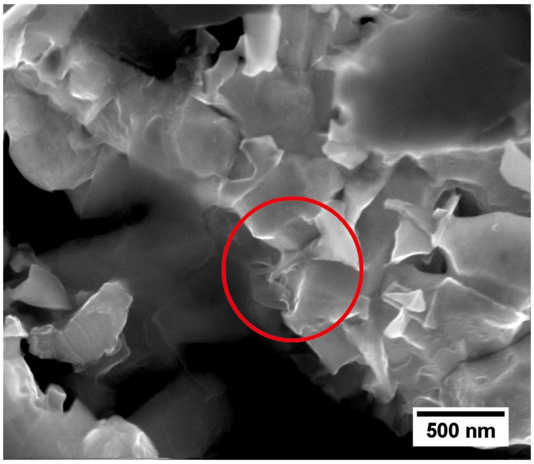

FIGURE 6 | Elongated Si_3N_4 grain pinned by UPBNNF in WC matrix.

structure that is related to a low Young's modulus of high tensile strength (HT) carbon fiber (Frank et al., 2012; Lin et al., 2016). In fact, the value of a BN fiber with a normal structure is only tens of GPa (Economy and Anderson, 1967). Therefore, the Young's modulus of UPBNNF itself has no effect on the composites. The only probable explanation is based on the most fundamental mechanism whereby the bonding of atoms is affected.

Meanwhile, there is no increase of Young's modulus found in WC-UPBNNF composites (Li et al., 2020). Young's modulus of some WC composites reported in published papers are listed in **Table 2**, which were all tested by the pulse-echo overlap ultrasonic technique. There are no abnormal phenomena, too. Thus, we consider that in addition to the liquid phase in the Si_3N_4 sintering process, the major point of influence is the nanosized pores of UPBNNF. For nanocrystalline materials (grain size < 50 nm), the properties could be modified at an atomic scale, but most of the modification is employed on functional ceramics (Gleiter, 1989; Jin and Bao, 1996; Maglia et al., 2013). It is rarely observed that Young's modulus of ceramics can be modified to increase thereafter, as no effective means are available to intervene at the atomic scale. Restricting the sizes of grains to less than 50 nm during the sintering process is difficult. However, it is possible that the bonding of atoms of Si_3N_4 can be affected after sintering by the presence of UPBNNF. As reported in the papers about WC-Si_3N_4 materials (Li et al., 2013; Zheng et al., 2013a, 2015), a liquid phase is generated during sintering, and then pores of UPBNNF can be filled with the liquid phase. In fact, reordering happened on groups of atoms in liquid phase sintering, and some groups were trapped in nanopores of UPBNNF. The bonding of atoms of Si_3N_4 in a pore is restrained after sintering, which means that the force and distance between atoms are also restricted. As a result, the Young's modulus of parts of Si_3N_4 increases, and in turn the values of whole Si_3N_4 and composites increase. Because of agglomeration, excess fraction of the fiber results in another decrease in Young's modulus. By contrast, directly observing the phenomenon is difficult. Regarding interaction between nanopores and filler materials, numerical modeling is mostly used. Even though accurate observation is employed on nanopores, there are too many requirements on the specimen itself (Lee et al., 2018; Gu et al., 2019; Hou et al., 2019; Nehra et al., 2019). WC-Si_3N_4 bulks after ball milling and sintering are too crude to meet the requirements. In addition, although some BN phases like BN nanoplates observed were reported (Ahmadi et al., 2017; Germi et al., 2018; Mahaseni et al., 2018), the turbostratic structure and pore leading to bad contrast hindered the intention of observation for UPBNNF in this case.

Eventually, synergic toughening is evident on the WC matrix, which is based on toughened Si_3N_4 and UPBNNF, as shown in **Figure 6**. By contrast, the synergic mechanism is not consistent with traditional ceramic-ceramic toughening theory. According to the traditional toughening model, weak interfacial bonding between non-binder second phases and the matrix is beneficial due to the fragile second phases without toughening effects in complex stress environments (Mahaseni et al., 2018). Energy is consumed by debonding, interfacial friction, and so on. In brief, energy must be consumed by generating new interfaces, but must not be alongside main cracks. Why the synergetic toughening is possible in this study? It was observed that Si_3N_4 is strongly bonded to the matrix by UPBNNF, so do UPBNNF itself. As a result, debonding between WC matrix and Si_3N_4 was more difficult, and the energy had to be consumed in other approaches like Si_3N_4 fracture. Usually, fracture in the ceramic second phase does not have considerable attribution to the toughening matrix due to the transitory nature of the fracture (Germi et al., 2018). However, as observed and elucidated, the ultimate fracture of Si_3N_4 grain in the composites can occur during a certain time interval. The aforementioned effects may consume more energy than traditional methods that lead to toughening.

The following is a brief summary of the previous discussion. First, it is possible that Young's modulus of ceramics is elevated using nanopores. High specific stiffness, which is a ratio of

TABLE 2 | Young's modulus of some WC composites reported in published papers.

Specimen	**0[a]**	**6Co[b]**	**1CNT[c]**	**6ZrO_2[b]**	**8ZrO_2[d]**	**1Si_3N_4[e]**	**3Si_3N_4[e]**	**6Si_3N_4[e]**	**8Si_3N_4[e]**
Young's modulus	704	649	658	575	559	650	596	542	522
Specimen	**10Si_3N_4[e]**	**12Si_3N_4[e]**	**15Si_3N_4[e]**	**0.05UPBNNF[a]**	**0.075UPBNNF[a]**	**0.1UPBNNF[a]**	**0.125UPBNNF[a]**		
Young's modulus	517	486	470	684	666	642	630		

The specimens' names are in terms of second phases with weight fraction in WC matrix.
Data sources: a, Li et al., 2020; b, Basu et al., 2004; c, Cao et al., 2018; d, Cao et al., 2021; e, Zheng et al., 2015.

Young's modulus to density, is often desired in mechanical design. However, the rule of mixture is a theoretical limitation, and no elevation exists beyond the intrinsic properties of materials that are simply affected at the atomic scale. Materials with high Young's modulus usually have a high density and result in increasing density after the addition into the matrix of a low Young's modulus. Second, ceramics with an internal liquid phase during sintering such as Si_3N_4 can employ a different fracture mode at the micrometer scale. Although no ductility can occur on the ceramics, serial and multiple fractures during a certain time interval may be closed to ductility in analogy with series approximation to a smooth function in calculus. Finally, a fiber with a deformation ability and modified ceramic phase such as those of the aforementioned Si_3N_4 enables the toughening of other ceramics jointly.

CONCLUSION

In this study, WC-10 wt.% Si_3N_4-x ($x = 0$, 0.01, 0.05, 0.1, and 0.15) wt.% UPBNNF composites were prepared by SPS. The following conclusions were drawn and thus present a means of improving the mechanical properties of ceramics.

(1) The addition of UPBNNF to WC-10 wt.% Si_3N_4 could be effective at enhancing hardness and maintaining fracture toughness.
(2) Tears and scratches patterns appear on Si_3N_4 grains in indentation crack paths of WC-Si_3N_4 composites with the addition of UPBNNF, an observation that is different from that of the traditional fracture mode of Si_3N_4 in which a catastrophic fracture occurs with clean edges.
(3) A collaborative toughening effect of UPBNNF and Si_3N_4 in WC-Si_3N_4 composites works under strong interfacial bonding.

DATA AVAILABILITY STATEMENT

The datasets generated for this study are available on request to the corresponding author.

AUTHOR CONTRIBUTIONS

TC: idea conceiving and writing. XL: supervising and project leader. SQ: supervising on mechanical tests. JL: assistant on preparing composites. LL: providing hardness tester. YH: supervising on porous fiber preparing. TS: preparing porous fiber. All authors contributed to the article and approved the submitted version.

FUNDING

This study was supported by the National Natural Science Foundation of China (Nos. 51474108, 51575193, and 51402086), the Hundred Talents Program of Hebei Province (E2014100011), the Key Project of Guangdong Natural Science Foundation (No. 2018B030311051), and the Heyuan Science and Technology Project (heke2018009).

REFERENCES

Ahmadi, Z., Nayebi, B., Asl, M. S., Kakroudi, M. G., and Farahbakhsh, I. (2017). Sintering behavior of ZrB_2-SiC composites doped with Si_3N_4: a fractographical approach. *Ceram. Int.* 43, 9699–9708. doi: 10.1016/j.ceramint.2017.04.144

Akimune, Y. (1990). Impact damage and strength degradation in a silicon carbide reinforced silicon nitride composite. *J. Am. Ceram. Soc.* 73, 3019–3025. doi: 10.1111/j.1151-2916.1990.tb06710.x

Anstis, G. R., Chantikul, P., Lawn, B. R., and Marshall, D. B. (1981). A critical evaluation of indentation techniques for measuring fracture toughness: I, direct crack measurements. *J. Am. Ceram. Soc.* 64, 533–538. doi: 10.1111/j.1151-2916.1981.tb10320.x

Basu, B., Lee, J. H., and Kim, D. Y. (2004). Development of WC-ZrO_2 nanocomposites by spark plasma sintering. *J. Am. Ceram. Soc.* 87, 317–319.

Becher, P. F. (1991). Microstructural design of toughened ceramics. *J. Am. Ceram. Soc.* 74, 25–69.

Becher, P. F., Hsueh, C. H., Angelini, P., and Tiegs, T. N. (1988). Toughening behavior in whisker-reinforced ceramic matrix composites. *J. Am. Ceram. Soc.* 71, 1050–1061. doi: 10.1111/j.1151-2916.1988.tb05791.x

Blugan, G., Hadad, M., Janczak-Rusch, J., Kuebler, J., and Graule, T. (2005). Fractography, mechanical properties, and microstructure of commercial silicon nitride-titanium nitride composites. *J. Am. Ceram. Soc.* 88, 926–933. doi: 10.1111/j.1551-2916.2005.00186.x

Bódis, E., Molnár, K., Mucsi, A., Károly, Z., Móczó, J., Klébert, S., et al. (2017). Silicon nitride-based composites reinforced with zirconia nanofibers. *Ceram. Int.* 43, 16811–16818. doi: 10.1016/j.ceramint.2017.09.078

Cao, T., Li, X., Li, J., Zhang, M., and Qiu, H. (2018). Effect of sintering temperature on phase constitution and mechanical properties of WC-1.0 wt.% carbon nanotube composites. *Ceram. Int.* 44, 164–169. doi: 10.1016/j.ceramint.2017.09.154

Cao, T., Li, X., and Li, J. (2021). Improvements of mechanical properties of WC-ZrO_2 composites with addition of ultrafine porous boron nitride nanofiber. *Rare Metal Mat. Eng.* 50, 802–806.

Cha, S. I., Hong, S. H., and Kim, B. K. (2003). Spark plasma sintering behavior of nanocrystalline WC-10Co cemented carbide powder. *Mater. Sci. Eng. A* 351, 31–38. doi: 10.1016/s0921-5093(02)00605-6

Chang, S. H., Chang, M. H., and Huang, H. T. (2015). Study on the sintered characteristics and properties of nanostructured WC-15 wt% (Fe-Ni-Co) and WC-15 wt% Co hard metal alloys. *J. Alloy Compd.* 649, 89–95. doi: 10.1016/j.jallcom.2015.07.119

Economy, J., and Anderson, R. V. (1967). Boron nitride fibers. *J. Polym. Sci. C.* 19, 283–297.

El-Eskandarany, M. S. (2000). Fabrication of nanocrystalline WC and nanocomposite WC-MgO refractory materials at room temperature. *J. Alloy Compd.* 296, 175–182. doi: 10.1016/s0925-8388(99)00508-3

El-Eskandarany, M. S. (2005). Fabrication and characterizations of new nanocomposite WC/Al_2O_3 materials by room temperature ball milling and subsequent consolidation. *J. Alloy Compd.* 391, 228–235. doi: 10.1016/j.jallcom.2004.08.064

Fattahi, M., Asl, M. S., Delbari, S. A., Namini, A. S., Ahmadi, Z., and Mohammadi, M. (2020a). Role of nano-WC addition on microstructural, mechanical and thermal characteristics of TiC-SiC_w composites. *Int. J. Refract. Met. Hard Mater.* 90:105248. doi: 10.1016/j.ijrmhm.2020.105248

Fattahi, M., Delbari, S. A., Babapoor, A., Namini, A. S., Mohammadi, M., and Asl, M. S. (2020b). Triplet carbide composites of TiC, WC, and SiC. *Ceram Int.* 46, 9070–9078. doi: 10.1016/j.ceramint.2019.12.155

Frank, E., Hermanutz, F., and Buchmeiser, M. R. (2012). Carbon fibers: precursors, manufacturing, and properties. *Macromol. Mater. Eng.* 297, 493–501. doi: 10.1002/mame.201100406

Germi, M. D., Mahaseni, Z. H., Ahmadi, Z., and Asl, M. S. (2018). Phase evolution during spark plasma sintering of novel Si_3N_4-doped TiB_2-SiC composite. *Mater. Charact.* 145, 225–232. doi: 10.1016/j.matchar.2018.08.043

Gleiter, H. (1989). Nanocrystalline materials. *Prog. Mater. Sci.* 33, 223–315.

Golberg, D., Bando, Y., Huang, Y., Terao, T., Mitome, M., Tang, C., et al. (2010). Boron nitride nanotubes and nanosheets. *ACS Nano* 4, 2979–2993.

Golberg, D., Bando, Y., Tang, C., and Zhi, C. (2007). Boron nitride nanotubes. *Adv. Mater.* 19, 2413–2432.

Gu, C., Lu, Y., Ridgeway, C. D., Cinkilic, E., and Luo, A. A. (2019). Three-dimensional cellular automaton simulation of coupled hydrogen porosity and microstructure during solidification of ternary aluminum alloys. *Sci. Rep.* 9:13099.

Guicciardi, S., Silvestroni, L., Nygren, M., and Sciti, D. (2010). Microstructure and toughening mechanisms in spark plasma-sintered ZrB_2 ceramics reinforced by SiC whiskers or SiC-chopped fibers. *J. Am. Ceram. Soc.* 93, 2384–2391. doi: 10.1111/j.1551-2916.2010.03730.x

Han, D., Mei, H., Xiao, S., Dassios, K. G., and Cheng, L. (2018). A review on the processing technologies of carbon nanotube/silicon carbide composites. *J. Eur. Ceram. Soc.* 38, 3695–3708. doi: 10.1016/j.jeurceramsoc.2018.04.033

Hou, J., Kong, X. S., Wu, X., Song, J., and Liu, C. S. (2019). Predictive model of hydrogen trapping and bubbling in nanovoids in bcc materials. *Nat. Mater.* 18, 833–839. doi: 10.1038/s41563-019-0422-4

Hsieh, C. L., and Tuan, W. H. (2005). Elastic properties of ceramic-metal particulate composites. *Mater. Sci. Eng. A* 393, 133–139. doi: 10.1016/j.msea.2004.10.009

Hu, Y., Chen, Z., Zhang, J., Xiao, G., Yi, M., Zhang, W., et al. (2019). Preparation and mechanical properties of Si_3N_4 nanocomposites reinforced by Si_3N_4@rGO particles. *J. Am. Ceram. Soc.* 102, 6991–7002. doi: 10.1111/jace.16546

Ii, S., Iwamoto, C., Matsunaga, K., Yamamoto, T., Yoshiya, M., and Ikuhara, Y. (2004). Direct observation of intergranular cracks in sintered silicon nitride. *Phil. Mag.* 84, 2767–2775. doi: 10.1080/14786430410001671485

Jin, H., Meng, S., Xie, W., Xu, C., and Niu, J. (2017). HfB_2-CNTs composites with enhanced mechanical properties prepared by spark plasma sintering. *Ceram. Int.* 43, 2170–2173. doi: 10.1016/j.ceramint.2016.10.200

Jin, Z., and Bao, Y. (1996). *Characterization of Mechanical Properties for Brittle Materials and Ceramics*. Beijing: China Railways Publishing House, 166–168.

Kim, H. C., Kim, D. K., Woo, K. D., Ko, I. Y., and Shon, I. J. (2008). Consolidation of binderless WC-TiC by high frequency induction heating sintering. *Int. J. Refract. Met. Hard. Mater.* 26, 48–54. doi: 10.1016/j.ijrmhm.2007.01.006

Klemm, H. (2010). Silicon nitride for high-temperature applications. *J. Am. Ceram. Soc.* 93, 1501–1522. doi: 10.1111/j.1551-2916.2010.03839.x

Koopman, M., Chawla, K. K., Coffin, C., Patterson, B. R., Deng, X., Patel, B. V., et al. (2002). Determination of elastic constants in WC/Co metal matrix composites by resonant ultrasound spectroscopy and impulse excitation. *Adv. Eng. Mater.* 4, 37–42. doi: 10.1002/1527-2648(20020212)4:1/2<37::aid-adem37>3.0.co;2-n

Kumar, A. K. N., Watabe, N., and Kurokawa, K. (2011). The sintering kinetics of ultrafine tungsten carbide powder. *Ceram. Int.* 37, 2643–2654. doi: 10.1016/j.ceramint.2011.04.011

Lawn, B. R. (1993). *Fracture of Brittle Solids, 2nd Version*. New York, NY: Cambridge University Press, 144–147.

Lee, K., Park, K. B., Kim, H. J., Yu, J. S., Chae, H., Kim, H. M., et al. (2018). Recent progress in solid-state nanopores. *Adv. Mater.* 30:1704680. doi: 10.1002/adma.201704680

Li, T., Chen, Y., Li, W., Li, J., Luo, L., Yang, T., et al. (2018). Fabrication and mechanical properties of boron nitride nanotube reinforced silicon nitride ceramics. *Ceram. Int.* 44, 6456–6460. doi: 10.1016/j.ceramint.2018.01.041

Li, X., Cao, T., Zhang, M., Qiu, H., Huang, Y., Qu, S., et al. (2020). Ultrafine porous boron nitride nanofiber-toughened WC composites. *Int. J. Appl. Ceram. Technol.* 17, 941–948. doi: 10.1111/ijac.13466

Li, Y., Zheng, D., Li, X., Qu, S., and Yang, C. (2013). Cr_3C_2 and VC doped WC-Si_3N_4 composites prepared by spark plasma sintering. *Int. J. Refract. Met. Hard. Mater.* 41, 540–546. doi: 10.1016/j.ijrmhm.2013.07.004

Lin, J., Xu, L., Huang, Y., Li, J., Wang, W., Feng, C., et al. (2016). Ultrafine porous boron nitride nanofibers synthesized via a freeze-drying and pyrolysis process and their adsorption properties. *RSC Adv.* 6, 1253–1259. doi: 10.1039/c5ra23426c

Maglia, F., Tredici, I. G., and Anselmi-Tamburini, U. (2013). Densification and properties of bulk nanocrystalline functional ceramics with grain size below 50 nm. *J. Eur. Ceram. Soc.* 33, 1045–1066. doi: 10.1016/j.jeurceramsoc.2012.12.004

Mahaseni, Z. H., Germi, M. D., Ahmadi, Z., and Asl, M. S. (2018). Microstructural investigation of spark plasma sintered TiB2 ceramics with Si_3N_4 addition. *Ceram. Int.* 44, 13367–13372. doi: 10.1016/j.ceramint.2018.04.171

Marshall, D. B., and Evans, A. G. (1985). Failure mechanisms in ceramic-fiber/ceramic-matrix composites. *J. Am. Ceram. Soc.* 68, 225–231. doi: 10.1111/j.1151-2916.1985.tb15313.x

Meyors, M. A., and Chawla, K. K. (1999). *Mechanical Behavior of Materials, 2nd Version*. New York, NY: Cambridge University Press.

Namini, A. S., Ahmadi, Z., Babapoor, A., Shokouhimehr, M., and Asl, M. S. (2019). Microstructure and thermomechanical characteristics of spark plasma sintered TiC Ceramics doped with nano-sized WC. *Ceram. Int.* 45, 2153–2160. doi: 10.1016/j.ceramint.2018.10.125

Nehra, A., Ahlawat, S., and Singh, K. P. (2019). A biosensing expedition of nanopore: a review. *Sens. Actuator B Chem.* 284, 595–622. doi: 10.1016/j.snb.2018.12.143

Nino, A., Izu, Y., Sekine, T., Sugiyama, S., and Taimatsu, H. (2019). Effects of TaC and TiC addition on the microstructures and mechanical properties of binderless WC. *Int. J. Refract. Met. Hard. Mater.* 82, 167–173. doi: 10.1016/j.ijrmhm.2019.04.012

Norgren, S., García, J., Blomqvist, A., and Yin, L. (2015). Trends in the P/M hard meal industry. *Int. J. Refract. Met. Hard. Mater.* 48, 31–45. doi: 10.1016/j.ijrmhm.2014.07.007

Pabst, W., and Gregorová, E. (2004). New relation for the porosity dependence of the effective tensile modulus of brittle materials. *J. Mater. Sci.* 39, 3501–3503. doi: 10.1023/b:jmsc.0000026961.12735.2a

Pezzotti, G. (1993). Si_3N_4/SiC-platelet composite without sintering aids: a candidate for gas turbine engines. *J. Am. Ceram. Soc.* 76, 1313–1320. doi: 10.1111/j.1151-2916.1993.tb03757.x

Pigeon, R. G., and Varma, A. (1992). Quantitative phase analysis of Si_3N_4 by x-ray diffraction. *J. Mater. Sci. Lett.* 11, 1370–1372.

Poetschke, J., Richter, V., and Holke, R. (2012). Influence and effectivity of VC and Cr_3C_2 grain growth inhibitors on sintering of binderless tungsten carbide. *Int. J. Refract. Met. Hard. Mater.* 31, 218–223. doi: 10.1016/j.ijrmhm.2011.11.006

Riley, F. L. (2000). Silicon nitride and related materials. *J. Am. Ceram. Soc.* 83, 245–265. doi: 10.1111/j.1151-2916.2000.tb01182.x

Sakkaki, M., Moghanlou, F. S., Vajdi, M., Pishgar, F., Shokouhimehr, M., and Asl, M. S. (2019). The effect of thermal contact resistance on the temperature distribution in a WC made cutting tool. *Ceram. Int.* 45, 22196–22202. doi: 10.1016/j.ceramint.2019.07.241

Tatarko, P., Grasso, S., Porwal, H., Chlup, Z., Saggar, R., Dlouhý, I., et al. (2014). Boron nitride nanotubes as a reinforcement for brittle matrices. *J. Eur. Ceram. Soc.* 34, 3339–3349. doi: 10.1016/j.jeurceramsoc.2014.03.028

Vasudevan, S., Kothari, A., and Sheldon, B. W. (2016). Direct observation of toughening and R-curve behavior in carbon nanotube reinforced silicon nitride. *Scripta Mater.* 124, 112–116. doi: 10.1016/j.scriptamat.2016.06.035

Wang, B., Matsumaru, K., Yang, J., Fu, Z., and Ishizaki, K. (2012). The effect of cBN additions on densification, microstructure and properties of WC-Co composites by pulse electric current sintering. *J. Am. Ceram. Soc.* 95, 2499–2503. doi: 10.1111/j.1551-2916.2012.05218.x

Wang, W. L., Bi, J. Q., Sun, K. N., Du, M., Long, N. N., and Bai, Y. J. (2011). Fabrication of alumina ceramic reinforced with boron nitride nanotubes with improved mechanical properties. *J. Am. Ceram. Soc.* 94, 3636–3640. doi: 10.1111/j.1551-2916.2011.04821.x

Xia, C., Asl, M. S., Namini, A. S., Ahmadi, Z., Delbari, S. A., Le, Q. V., et al. (2020). Enhanced fracture toughness of ZrB_2-SiC_w ceramics with graphene nano-platelets. *Ceram. Int.* 46, 24906–24915. doi: 10.1016/j.ceramint.2020.06.275

Yadhukkulakrishnan, G. B., Rahman, A., Karumuri, S., Stackpoole, M. M., Kalkan, A. K., Singh, R. P., et al. (2012). Spark plasma sintering of silicon carbide and multi-walled carbon nanotube reinforced zirconium diboride ceramic composites. *Mater. Sci. Eng. A* 552, 125–133. doi: 10.1016/j.msea.2012.05.020

Zhang, J., Zhang, G., Zhao, S., and Song, X. (2009). Binder-free WC bulk synthesized by spark plasma sintering. *J. Alloy Compd.* 479, 427–431. doi: 10.1016/j.jallcom.2008.12.151

Zhang, X., Hilmas, G. E., and Farenholtz (2008). Densification, mechanical properties, and oxidation resistance of TaC-TaB2 ceramics. *J. Am. Ceram. Soc.* 91, 4129–4132. doi: 10.1111/j.1551-2916.2008.02780.x

Zheng, D., Li, X., Ai, X., Yang, C., and Li, Y. (2012). Bulk WC-Al_2O_3 composites prepared by spark plasma sintering. *Int. J. Refract. Met. Hard. Mater.* 30, 51–56.

Zheng, D., Li, X., Li, Y., Qu, S., and Yang, C. (2013a). In-situ elongated β-Si_3N_4 grains toughened WC composites prepared by one/two-step spark plasma sintering. *Mater. Sci. Eng. A* 561, 445–451. doi: 10.1016/j.msea.2012.10.059

Zheng, D., Li, X., Li, Y., Qu, S., and Yang, C. (2013b). ZrO_2 (3Y) toughened WC composites prepared by spark plasma sintering. *J. Alloy Compd.* 572, 62–67. doi: 10.1016/j.jallcom.2013.03.259

Zheng, D., Li, X., Tang, Y., and Cao, T. W. C. - (2015). Si_3N_4 composites prepared by two-step spark plasma sintering. *Int. J. Refract. Met. Hard. Mater.* 50, 133–139.

Zhou, Y., Ohji, T., Hyuga, H., Yoshizawa, Y., Murayama, N., and Hirao, K. (2014). Fracture resistance behavior of high-thermal-conductivity silicon nitride ceramics. *Int. J. Appl. Ceram. Technol.* 11, 872–882. doi: 10.1111/ijac.12109

Conflict of Interest: The authors declare that the research was conducted in the absence of any commercial or financial relationships that could be construed as a potential conflict of interest.

The reviewer ZW declared a shared affiliation, with no collaboration, with several of the authors, TC, XL, JL, SQ, and LL, to the handling editor at the time of the review.

Advantages of publishing in Frontiers

OPEN ACCESS
Articles are free to read
for greatest visibility
and readership

FAST PUBLICATION
Around 90 days
from submission
to decision

HIGH QUALITY PEER-REVIEW
Rigorous, collaborative,
and constructive
peer-review

TRANSPARENT PEER-REVIEW
Editors and reviewers
acknowledged by name
on published articles

Frontiers
Avenue du Tribunal-Fédéral 34
1005 Lausanne | Switzerland

Visit us: www.frontiersin.org
Contact us: frontiersin.org/about/contact

REPRODUCIBILITY OF RESEARCH
Support open data
and methods to enhance
research reproducibility

DIGITAL PUBLISHING
Articles designed
for optimal readership
across devices

FOLLOW US
@frontiersin

IMPACT METRICS
Advanced article metrics
track visibility across
digital media

EXTENSIVE PROMOTION
Marketing
and promotion
of impactful research

LOOP RESEARCH NETWORK
Our network
increases your
article's readership